Experimental analysis of the efficiency of carbon fiber anchors applied over CFRP to firebrick bonded joints

Carmelo Caggegi

UNIONE EUROPEA

UNIVERSITÀ ITALO FRANCESE | UNIVERSITÉ FRANCO ITALIENNE

ÉCOLE DOCTORALE UNIVERSITÉ PARIS-EST
Sciences, Ingénierie et Environnement

Università degli Studi di Catania

Ministero dell'Istruzione dell'Università e della Ricerca

Experimental analysis of the efficiency of carbon fiber anchors applied over CFRP to firebrick bonded joints

CARMELO CAGGEGI

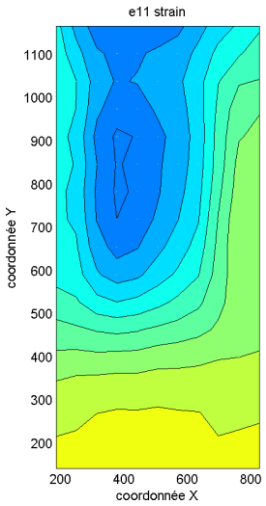

PHD SCHOOL ON "**INGEGNERIA STRUTTURALE E GEOTECNICA**" - **XXV CICLO**

UNIVERSITY OF CATANIA (ITALY)

PHD SCHOOL ON "**SCIENCE, INGENIERIE ET ENVIRONNEMENT**"

UNIVERSITY PARIS-EST (FRANCE)

Experimental analysis of the efficiency of carbon fiber anchors applied over CFRP to firebrick bonded joints

Phd Thesis

*CARMELO CAGGEGI**

Italian Supervisor - University of Catania

Professor Massimo Cuomo

French Supervisor - University of Paris-Est Marne-La-Vallée

Professor Luc Chevalier

Others members of thesis group

Ass. Prof. Vincent Pensée (UPE MLV), Ass. Prof. Loredana Contrafatto (UNI CT)

PHD SCHOOL ON "**INGEGNERIA STRUTTURALE E GEOTENICA**" - **XXV CICLO**

UNIVERSITY OF CATANIA (ITALY)

PHD SCHOOL ON "**SCIENCE, INGENIERIE ET ENVIRONNEMENT**"

UNIVERSITY PARIS-EST (FRANCE)

* EMAIL ADDRESS: caggegict@gmail.com TEL. MOBILE : +39 3286215262, +33(0)750848622

Experimental analysis of the efficiency of carbon fiber anchors applied over CFRP to firebrick bonded joints

Phd Thesis

Discussed and defended in public by

*CARMELO CAGGEGI**

on 21 MARCH 2013 in the University of Catania

Commission:

***Reporter**:*	*SACCO Elio (Professor),* *University of Cassino and of the meridional Lazio.*
***Reporter**:*	*MEFTAH Fekri (Professor),* *INSA Rennes.*
***Examiner**:*	*ASCIONE Luigi (Professor),* *University of Salerno.*
***Examiner**:*	*FAGONE Mario (Ass. Professor),* *University of Florence.*
***Examiner**:*	*PENSEE Vincent (Ass. Professor),* *University of Marne-La-Vallée Paris-Est.*
***French Supervisor** :*	*CHEVALIER Luc (Professor),* *University of Marne-La-Vallée Paris-Est.*

* EMAIL ADDRESS: caggegict@gmail.com TEL. MOBILE: +39 3286215262, +33 (0)750848622

To Mariella

This research has been financed by

the Italian Ministry of Education, University and Research (Phd scholarship).

A scholarship "Vinci_2010" has been conferred by

the University "Italo-francese" (UFI) to this research work.

Two annual scholarships (2011_2012) of "soutiene à la co-tutele" have been conferred by

the Phd School SIE (University Paris Est) to this research work.

The experimental session in France has been financed by

the ESIPE (Ecole Supérieure d'ingénieurs Paris-Est Marne-la-Vallée) and

the laboratory MSME (Modélisation et Simulation Multi échelle).

I would like to thank:

Prof. Massimo Cuomo
For his guidance during my Phd studies, the encouragement and for the aid to generate the scientific collaborations

Prof. Luc Chevalier
For his supervision, for the sound advices, for the confidence and for the warm welcoming

Ass. Prof. Vincent Pensée
For his encouragement, continual support and for his great availability

Ass. Prof. Mario Fagone
For the collaboration in the experimental session and for the great availability.

Ass. Prof. Giovanna Ranocchiai
For the work implemented in the experimental session in Florence

Prof. Silvia Briccoli Bati
For her contribution in the experimental phases in Florence

Ass. Prof. Anas Batou
For the assistance in the use of the"Code Aster – Salome Meca" software

Ass. Prof. Loredana Contrafatto
For the assistance and guidance in some difficult situations

Benoit Proust
For the passion that he showed during the construction of the steel experimental apparatus

Giuliana Di Iacovo
For the meticulously construction of the test specimens

I want also to thank Prof. Giuseppe Oliveto, for the passion that he showed in the coordination of the doctoral school of Catania, the Ass. Prof. Rosa Caponetto, for her continual encouragement, and Madame Cecile Blanchemonche for her availability.

I'm very grateful to my girlfriend Mariella, that encourage me also from 2000 km of distance with love and patience (TJ). A big "grazie" to my sister Anna Maria that gave me aid and a lot of energy. I would like to thank also my mother and my father for their support and to my grandparents their cheer.

During the three years of phd studies I had the luck to meet very special people that helped me and encouraged me during the most difficult phases of my research; each one of them can find his/her "Thank you" below:

grazie *merci* cám an gracias 谢谢 ευχαριστώ

UNIONE EUROPEA

UNIVERSITÀ ITALO FRANCESE | UNIVERSITÉ FRANCO ITALIENNE

ÉCOLE DOCTORALE UNIVERSITÉ PARIS-EST
Sciences, Ingénierie et Environnement

Università degli Studi di Catania

Ministero dell'Istruzione dell'Università e della Ricerca

English abstract

Thesis title

Experimental analysis of the efficiency of carbon fiber anchors applied over CFRP to firebrick bonded joints

Author - Caggegi Carmelo

IN THESE RECENT YEARS, THE STRENGTHENING OF MASONRY BUILDING HAS KNOWN A MASSIVE USE OF CFRP SHEETS. THOSE COMPOSITE MATERIALS GLUED ON THE ELEMENTS TO REINFORCE ARE EXPOSED TO PREMATURELY DEBONDING CRISIS DUE TO A TENSION LOAD WHICH IS MUCH SMALLER THAN THE TENSILE STRENGTH OF THE CFRP. ONE WAY TO UPGRADE FAILURE LOAD OF CFRP-TO-SUPPORT BONDED JOINT IS TO REINFORCE THE COHESION BETWEEN THE FIBERS AND THE SUPPORT BY THE USE OF MECHANICALS ANCHORS BUILT WITH THE SAME FIBERS OF THE COMPOSITE AND FASTENED IN THE SUPPORT LIKE "NAILS". RESEARCH ON THE USE OF ANCHORS FOR MASONRY SUPPORTS HAS BEEN LIMITED AND, IN THIS FRAMEWORK, THERE ARE NO EXPERIMENTAL ANALYSES RELATED TO THE DESIGN AND THE PLACEMENT OF FIBER ANCHORS.

THE AIM OF THIS THESIS IS TO PROVIDE EXPERIMENTAL DATA TO QUANTIFY THE EFFICIENCY OF THE CARBON FIBER ANCHORS APPLIED ON A REINFORCED FIRE BRICK. THIS IS A GROUND WORK TO STUDY CFRP TO MASONRY BONDED JOINT FASTENED BY FIBER "NAILS". SPECIFICALLY, THE ANALYSIS OF THE DISPLACEMENT AND THE STRAIN FIELDS OF THE REINFORCED SURFACE HAVE BEEN REALIZED BY MEANS OF DIGITAL IMAGE CORRELATION (DIC), AN OPTICAL APPEALING METHOD NEVER USED TO STUDY A FRP TO SUPPORT BONDED JOINT FASTENED BY FRP ANCHOR.

THE RESEARCH DEMONSTRATES THAT THE USE OF THE CFRP ANCHORS INCREASES THE RESISTANCE AND THE DUCTILITY OF THE REINFORCEMENT.

UNIONE EUROPEA

UNIVERSITÀ ITALO FRANCESE | UNIVERSITÉ FRANCO ITALIENNE

ÉCOLE DOCTORALE UNIVERSITÉ PARIS-EST
Sciences, Ingénierie et Environnement

Università degli Studi di Catania

Ministero dell'Istruzione dell'Università e della Ricerca

Italian abstract

Titolo della tesi

Analisi sperimentale dell'efficienza degli ancoraggi in fibre di carbonio applicati su mattoni rinforzati tramite bande in CFRP

Autore: Caggegi Carmelo

NEGLI ULTIMI ANNI IL RINFORZO DELLE STRUTTURE IN MURATURA HA CONOSCIUTO UN USO MASSIVO DELLE BANDE IN CFRP. QUESTI MATERIALI FIBROCOMPOSITI, INCOLLATI SUGLI ELEMENTI DA RINFORZARE, SONO ESPOSTI A UNA CRISI CAUSATA DA DEBONDING A TENSIONI MOLTO PIÙ PICCOLE DELLA RESISTENZA A TRAZIONE DEL COMPOSITO. UNA POSSIBILE SOLUZIONE PER INCREMENTARE IL CARICO ULTIMO DI QUESTI SISTEMI RINFORZATI È MIGLIORARE L'ADERENZA TRA LE FIBRE E IL SUPPORTO USANDO PARTICOLARI ANCORAGGI MECCANICI. QUESTI ULTIMI, REALIZZATI CON LE STESSA TIPOLOGIA DI FIBRE DEL MATERIALE DI RINFORZO, VENGONO INFISSI ALL'INTERNO DEL SUPPORTO COME DEI VERI E PROPRI "CHIODI". LA RICERCA INERENTE L'USO DI QUESTA TIPOLOGIA DI ANCORAGGI SU SUPPORTI IN MURATURA È MOLTO LIMITATA E, IN QUESTO CONTESTO, NON ESISTONO ANALISI SPERIMENTALI CONNESSE AL PROGETTO E ALLA COLLOCAZIONE SPAZIALE DI QUESTI DISPOSITIVI MECCANICI.

L'OBIETTIVO DI QUESTA TESI È DI PROVVEDERE DEI DATI SPERIMENTALI ATTI A QUANTIFICARE L'EFFICIENZA DEGLI ANCORAGGI IN FIBRE DI CARBONIO APPLICATI SU MATTONI PIENI RINFORZATI TRAMITE BANDE IN CFRP. QUESTA È UNA RICERCA PRELIMINARE A UN PIÙ AMPIO STUDIO SU SUPPORTI IN MURATURA. NELLO SPECIFICO, L'ANALISI DEI CAMPI DI SPOSTAMENTO E DI DEFORMAZIONE SULLA SUPERFICE RINFORZATA È STATA EFFETTUATA UTILIZZANDO LA CORRELAZIONE DI IMMAGINI, UN METODO OTTICO MAI USATO PRIMA PER LO STUDIO DI SUPPORTI RINFORZATI DA FRP E CHIODATI CON FRP ANCHOR.

IL LAVORO DI TESI DIMOSTRA CHE L'USO DEGLI CFRP ANCHOR AUMENTA LA DUTTILITÀ E LA RESISTENZA ULTIMA DEI RINFORZI.

UNIONE EUROPEA

UNIVERSITÀ ITALO FRANCESE | UNIVERSITÉ FRANCO ITALIENNE

ÉCOLE DOCTORALE — UNIVERSITÉ PARIS-EST
Sciences, Ingénierie et Environnement

Università degli Studi di Catania

Ministero dell'Istruzione dell'Università e della Ricerca

French abstract

Titre de la thèse

Analyse expérimentale de l'efficacité des systèmes d'ancrage en fibre de carbone appliqués sur briques renforcées par CFRP

Auteur - Caggegi Carmelo

DANS LES DERNIERS ANNEES, LE RENFORCEMENT DES BATIMENTS EN MAÇONNERIE A CONNU UN USE MASSIVE DES CFRP BANDS. CES MATERIAUX COMPOSITE, ATTACHES SUR LES ELEMENTS A RENFORCER, ONT EXPOSES A UNE FRACTURE PREMATURE POUR DELAMINAGE DU A TENSION PLUS PETIT DE LA RESISTANCE A TRACTION MAXIMAL DU CFRP. UNE FAÇON POUR ACCROITRE LA RESISTANCE MAXIMALE DU SYSTEM RENFORCE PAR CFRP EST AMELIORER LA COHESION ENTRE SUPPORT ET COMPOSITE EN UTILISANT ANCRAGES MECANIQUES. CES DERNIERS SONT REALISES EN UTILISANT LE MEMES TYPOLOGIE DE FIBRES DU RENFORCE ET EN LES INSERANT DANS LE SUPPORT COMME DES « CLOUS ». LES RECHERCHES SCIENTIFIQUES SUR L'USE DE CETTE FAÇON D'ANCRAGE SUR SUPPORT EN MAÇONNERIE A ETE TRES LIMITE ET, DANS CETTE CONTEXTE, IL N'Y A PAS DES ETUDES EXPERIMENTALES SUR LE PROJET ET LE PLACEMENT DES ANCRAGES.

L'OBJECTIF PRINCIPAL DU PRESENT TRAVAIL DE THESE EST QUANTIFIER L'EFFICACITE DES ANCRAGES EN FIBRE DE CARBONE APPLIQUES SUR BRIQUE CUIT PLEIN RENFORCE PAR CFRP BANDS. CETTE RECHERCHE EST LA PREMIERE PHASE D'UNE ETUDE PLUS VASTE SUR LES SYSTEMES MAÇONNERIE-CFRP RENFORCE PAR « CARBON FIBER ANCHOR ». DANS L'ETUDE, L'ANALYSE DES DEPLACEMENT ET DES DEFORMATION DE LA SURFACE RENFORCE A ETE FAIT EN UTILISANT LA CORRELATION DES IMAGES (DIC), UNE AVANTAGEUSE METHODE OPTIQUE JAMAIS UTILISE POUR L'ETUDE DES SYSTEMES « SUPPORT-CFRP BAND- ANCRAGES ».

LE PRESENT TRAVAIL DE THESE DEMONTRE QUE LES ANCRAGES EN CFRP AUGMENTENT LE RESISTANCE MAXIMAL ET LA DUCTILITE DES RENFORCEMENTS PAR BANDE DE COMPOSITES.

Contents

Introduction

In Europe the main construction materials used to build historic neighborhoods were stones, bricks and mortar. The social and economic value of these structures is high for several reasons: a) the old buildings (church, palace, houses) are frequently the soul of a city, they are a solid recollection of the history of a community; b) they could have artistic qualities or simply be part of a landscape (middle or lower class dwellings); c) they are very important for tourism (some masonry building are attractions while others are simply the best place to have a Hotel or a restaurant); d) they have high acoustic and thermal qualities and, therefore, they are suitable as comfortable civil habitations. That is why the study and the improvement of strengthening masonry methods to ensure people's safety and to conserve the architectural historic heritage for the future generations is so important.

Recently, the reinforcement of masonry building has seen a massive use of Carbon Fiber Reinforced Polymers sheets (CFRP). These are composite materials constituted by reinforcing fibers embedded in a polymeric matrix. The FRP are characterized by a high tensile strength, a thin thickness and a low weight; properties which are optimal to create a reinforcement. Frequently, in the field of civil engineering, the fiber reinforced polymers are realized in situ by gluing dry fiber fabric by means of epoxy resins on the structural member to strengthen. This typology of reinforcement is exposed to prematurely debonding crisis due to a tension load which is much smaller than the tensile strength of the CFRP. Specifically the reinforced system FRP-support often fails in a brittle manner not because the fibers achieve their tensile limit, but because a cohesive fracture is developed in a superficial layer of the strengthened element.

A way to upgrade failure load of CFRP-to-support bonded joint is to reinforce the cohesion between the fibers and the support by the use of mechanical anchors built with the same fibers of the composite and fastened within the support like "nails". Research on the use of anchors for masonry supports has been limited and, in this framework, there are no experimental analyses related to the design and the placement of fiber anchors.

The principal aim of this thesis is to provide experimental data to quantify the efficiency of the carbon fiber anchors applied on a fire brick reinforced by CFRP sheet. This is a ground work for the study of CFRP to masonry bonded joint fastened by fiber "nails".

Specifically, the analysis of the displacement and the strain fields of the reinforced surface have been realized by means of Digital Image Correlation (DIC), an optical method which has never been used to study a FRP to support bonded joint fastened by FRP anchor.

The work presented in this thesis has been realized within the framework of an interuniversity accord ("co-tutela") between the University of Catania and the University Paris-Est Marne-La-Vallée and with the collaboration of the university of Florence. In the research, the French experience in the field of Digital Image Correlation (DIC) has been applied to Italian knowledge of the behavior of masonry structures reinforced by FRP when undergoing earthquakes.

The thesis is divided into five chapters. The first is devoted to a literature review on FRP properties, design parameters and reinforcement improvement techniques. Experimental and numerical aspects are discussed. Several observations on the state of art are specified at the end of this part.

In the second chapter, motivations, goals and methodologies of the experimental research are defined. In this section the design of the specimen's configurations is presented specifying the properties of the materials used to make the sample. Moreover, the experimental procedure is described and details about the project of the testing machine are addressed.

The third chapter deals with general aspects of the digital image correlation technique. Literature references are presented in the opening paragraphs of this section. In the same chapter the correlation algorithm used to define the displacement field is presented. Moreover, the experimental procedure followed to realize the Digital Image Correlation is defined by means of a study case on rubber.

Results and main considerations are presented in the fourth chapter. In the first part the nomenclature of the quantity measured and the various suggestions made to interpret the raw data are explained. After that, the results of each series and the comparison between the series are presented. The check of the DIC accuracy and a general discussion of the results is proposed in the same chapter.

The general conclusions of the research are drawn in the last chapter. A comparison between the experimental results obtained and the normative design parameter is presented. The several perspectives of this research work are presented at the end of the thesis.

Chapter 1

FRP reinforced systems: from debonding fracture to mechanical anchors

1. FRP reinforced systems: from debonding fracture to mechanical anchors

An analysis of the literature on the reinforcement of masonry structures by means of FRP (Fiber Reinforced Polymers) is proposed in this chapter. A description of the properties of the reinforcement (FRP) and of the support (masonry) is presented in the first part of this section. Subsequently, the parameters and the design criteria of the straightened FRP systems are defined. Attention is then focused on the premature debonding failure of the systems FRP-to-support bonded joints. The final part of the chapter deals with the mechanical anchors (FRP anchors and U Wraps) and their capacity to improve the peak resistance of the straightened systems. The last paragraph underlines the gaps in the literature that validate the research presented in this thesis.

1.1 Materials

1.1.1 Mechanical property of FRP

The Fiber reinforced polymers, or FRP, are composite materials constituted by reinforcing fibers embedded in a polymeric matrix. The fibers are responsible for carrying the load acting on the composite; the matrix protects the fibers from the environment, distributes the load and links the composite to the support [1]. The FRP have heterogeneous and anisotropic properties and a prevalent linear elastic behavior up to failure unlike steel (yield behavior). In the field of civil engineering the fiber reinforced polymers can be built in the factory (pre-impregnated fabric) or directly in situ applying special resins over the dry fabric (non-impregnated fabric).

Three main types of fibers are used: glass (GFRP), aramid (AFRP) and carbon fibers (CFRP) (*fig. I.1*). They are assembled in a filiform geometry, they are continuous and their diameter is in the range of 4 to 10 micrometers [2]. The mechanical properties of fibers are sketched in the *figure I.2*. Among the three typologies already mentioned, the CFRP have the greatest values of maximal stress and the greatest value of stiffness. In the structural strengthening field the fibers are assembled in unidirectional, bidirectional or multiaxial fabrics. The *unidirectional* tissue is characterized by fibers all oriented in the direction of the length, the *bidirectional* fabric is made of an orthogonal weft-warp weaving and the *multiaxial* tissue is characterized by fibers oriented in different directions.

The matrix of FRP composites is commonly realized with thermoset resins. These are characterized by a low viscosity, good adhesive properties, a good resistance to chemical agents and an absence of melting temperature. In the field of civil engineering the epoxy resin is commonly used; it has a good resistance to moisture, to chemical agents and excellent adhesive properties. The epoxy resin

undergoes a change of its mechanical properties at a temperature greater than 60°C, this is an essential characteristic in the design project of reinforcements.

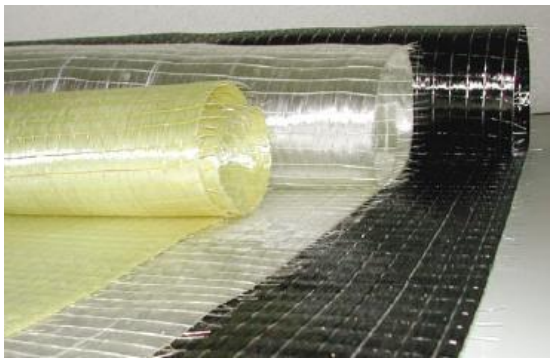

fig. I.1 - Fabric fibers(aramidic, glass, carbon)

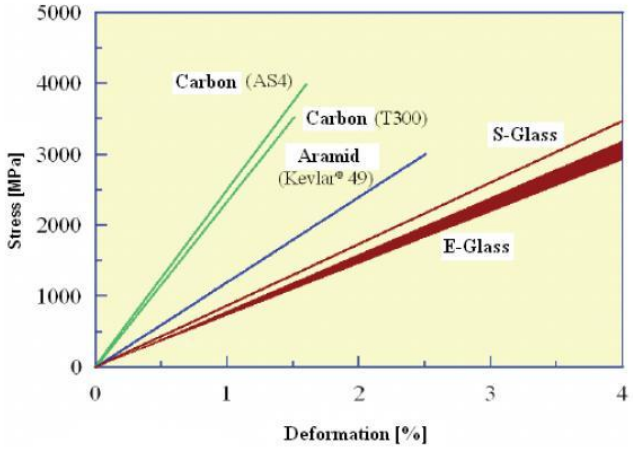

fig. I.2 - Stress-strain diagram for different fibers [1]

tab. 1.I - Comparison between the properties of FRP components and steel [1]

	Young's modulus E	Tensile strength σ_r	Strain at failure ε_r	Coefficient of thermal expansion α	Density ρ
	[GPa]	[MPa]	[%]	$[10^{-6}\ °C^{-1}]$	$[g/cm^3]$
E-glass	70 – 80	2000 – 3500	3.5 – 4.5	5 – 5.4	2.5 – 2.6
S-glass	85 – 90	3500 – 4800	4.5 – 5.5	1.6 – 2.9	2.46 – 2.49
Carbon (high modulus)	390 – 760	2400 – 3400	0.5 – 0.8	-1.45	1.85 – 1.9
Carbon (high strength)	240 – 280	4100 – 5100	1.6 – 1.73	-0.6 – -0.9	1.75
Aramid	62 – 180	3600 – 3800	1.9 – 5.5	-2	1.44 – 1.47
Polymeric matrix	2.7 – 3.6	40 – 82	1.4 – 5.2	30 – 54	1.10 – 1.25
Steel	206	250 – 400 (yield) 350 – 600 (failure)	20 – 30	10.4	7.8

In *table 1.I* there is a comparison between the properties of fibers, matrix and steel.

The mechanical properties of FRP materials are due to the composite geometry (shape, thickness), fibers orientation (unidirectional, bidirectional or multiaxial fabric) and concentration. The composite does not have the same mechanical properties as the fibers, in fact the presence of the matrix lowers the level of the stress resistance (see *fig. I.3* and *table 1.II*). For FRP materials characterized by unidirectional fibers the mechanical property of the composite may be estimated using the rule of mixtures.

Obviously the increase of fiber volumetric fraction improves the mechanical quality of the composite (*fig. I.4*).

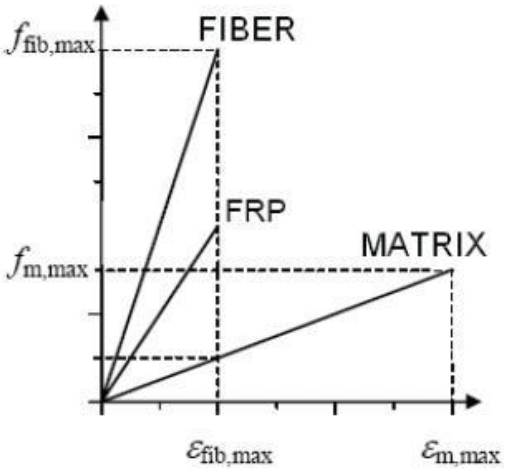

fig. I.3 -Stress-strain diagram for fibers and matrix [1]

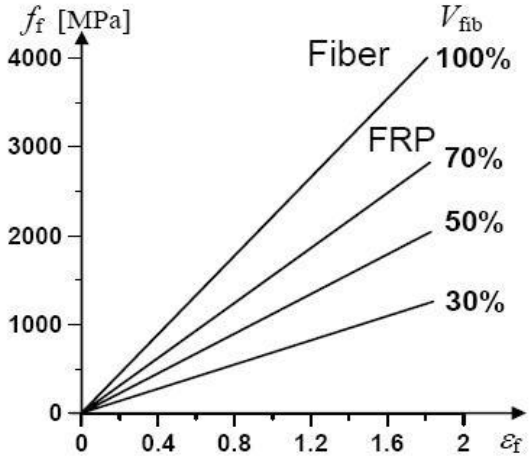

fig. I.4 - Fibers and mechanical properties [1]

tab. 1.II - CFRP and carbon fibers [1]

Pre-cured systems	Modulus of elasticity [GPa]		Ultimate strength [MPa]		Ultimate strain [%]	
	FRP E_f	Fiber E_{fib}	FRP f_f	Fiber f_{fib}	FRP ε_{fu}	Fiber $\varepsilon_{fib,u}$
CFRP (low modulus)	160	210-230	2800	3500-4800	1.6	1.4-2.0
CFRP (high modulus)	300	350-500	1500	2500-3100	0.5	0.4-0.9

The properties of steel (traditional material used in civil engineering for its high tensile resistance) and those of FRP composites can be compared thanks to analyses of plots of FRP rods (*fig. I.5*). The stiffness of FRP is smaller than that of steel. The behavior of steel is ductile, unlike the failure of FRP composite which is fragile after an elastic stroke. The stress tensile limit of CFRP is more than five times higher than that of steel. Among the composite materials in the *figure I.5* FRP made by carbon fibers has the highest value of stiffness.

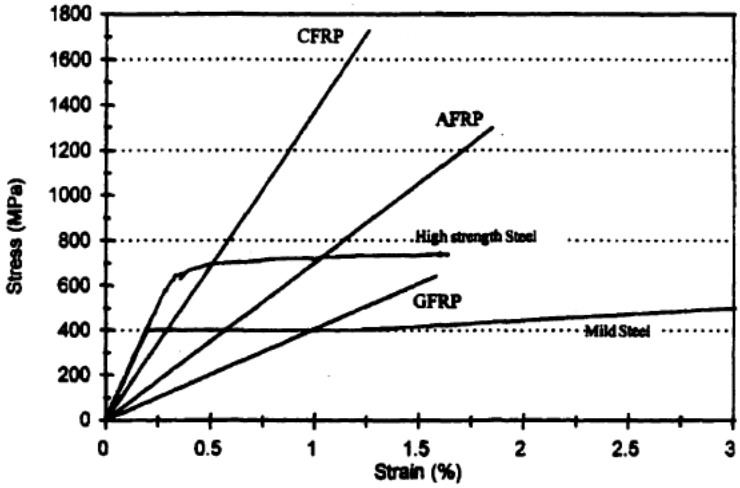

I.5 - Behavior of fibers rod [2]

1.1.2 Mechanical property of masonry

Traditional masonries are composed of prismatic blocks and mortar. The former give the system mechanical resistance, the latter is applied among the blocks to distribute the load and to prepare the surface to apply other layers of prismatic elements. Normally the blocks could be natural (stone) or artificial (fire brick, cinder block.). Each geographical territory is characterized by typical typologies of masonry since in each zone there are typical materials and typical construction techniques. The principal typologies of stone used in civil engineering are: igneous rocks (granite, basalt, pumice, tuff), metamorphic stone (marble) and sedimentary stone (limestone, sandstones). Instead, the main typologies of masonry are: the rubble masonry, the ashlar masonry, the slipform stone masonry, the dry set masonry, the solid brick work (*fig. I.6* and *I.7*). Masonry characterized by rubble elements employs a large quantity of mortar and has poorer mechanical quality than the ashlar masonry.

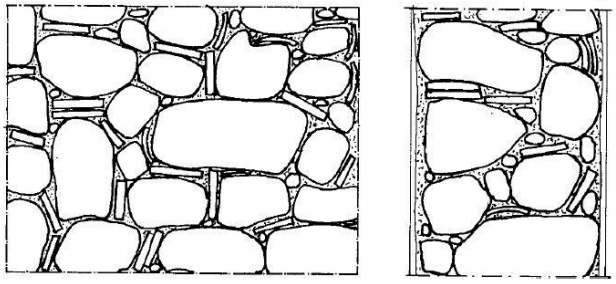

fig. I.6 - Stone rubble masonry (territory of Catania) [3]

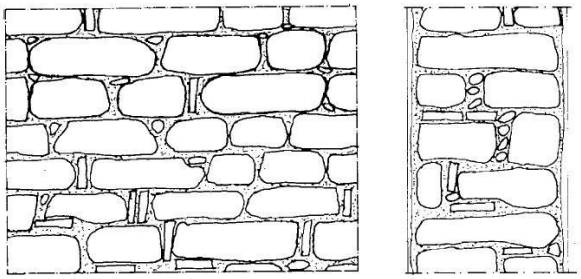

fig. I.7 - Stone ashlar masonry (territory of Catania) [3]

The large field of wall typologies and materials make a global and synthetic analysis of the masonries impossible. The technical Italian law *D.M. 14 January 2008* [4] provides a classification of mortar types (*table 1.III*); the number of these classes (M2,5, M5…) corresponds to the compression strength in N/mm^2. In the same state regulation, there is a table of the masonry compression strength values in relation to mortar quality and stone typologies (*table 1.IV*).

Classe	Tipo di malta	Composizione				
		Cemento	Calce aerea	Calce idraulica	Sabbia	Pozzolana
M 2,5	Idraulica	--	--	1	3	--
M 2,5	Pozzolanica	--	1	--	--	3
M 2,5	Bastarda	1	--	2	9	--
M 5	Bastarda	1	--	1	5	--
M 8	Cementizia	2	--	1	8	--
M 12	Cementizia	1	--	--	3	--

tab. 1.III - Composition and classification of mortar [4]

Characteristic strength in compression (f_{bk}) of the stone element	Mortar typologie			
	M15	M10	M5	M2,5
2,0	1,0	1,0	1,0	1,0
3,0	2,2	2,2	2,2	2,0
5,0	3,5	3,4	3,3	3,0
7,5	5,0	4,5	4,1	3,5
10,0	6,2	5,3	4,7	4,1
15,0	8,2	6,7	6,0	5,1
20,0	9,7	8,0	7,0	6,1
30,0	12,0	10,0	8,6	7,2
≥ 40,0	14,3	12,0	10,4	--

tab.1.IV - Masonry compressive strength fk [N/mm^2] in relation to mortar class and stone resistance [4]

The compressive characteristic strength f_{bk} of the elements (first column of the *table 1.IV*) is defined as:

$$f_{bk} = 0{,}75\ x\ f_{bm} \tag{1.1}$$

where f_{bm} is the average value of the compressive strength of the stone element.

Table 1.IV shows that the masonry *compressive characteristic strength* f_k is included between 1 MPa and 14,3 MPa.

Indeed the tensile resistance of masonry wall is approximately equal to 1/10 of f_{bm} [1]. This low value is frequently considered null by engineers.

Unlike FRP materials masonries have good permeability property and good fire resistance.

1.2 Strengthening design criteria, application and failure modes

The strengthening of civil structures by FRP consists in applying the composite over the support that must be reinforced (concrete, masonry). In the framework of masonry buildings the use of the fiber reinforced polymer (laminates, sheets, grids and bars) is oriented to increase the capacity of each structural member as well as the global capacity of the structure [1]. In particular, the main reason that justify the use of FRP are:

- To carry the tensile stress within the structural members or between adjoining members:
- To connect more structural members (orthogonal walls, walls and vault…);
- To stiffen the horizontal elements (vault, floor…);
- To limit the crack width; and
- To confine the columns for enhancing their resistance.

The application of FRP to the member to reinforce is carried out by adhesion or by means of mechanical anchorage devices. Often, in the civil engineering field, the non-impregnated fabric (carbon, glass or aramid) is bonded directly over the support surface using epoxy resins. The result is the realization of the FRP composite directly "in situ".

The adhesion between support and FRP is fundamental for the efficiency strength. Unlike concrete elements, masonries have commonly rough external surfaces due to the presence of blocks and mortar. This surface configuration makes it necessary to apply a leveling mortar to the roughened layer. In synthesis the phases of application of a FRP strength system are:

- Cleaning the surface of application;
- Applying, if necessary, a leveling mortar [1];
- Spreading a layer of epoxy bi-component resin;
- Spreading the dry-fabric on the resin; and
- Spreading another layer of epoxy resin on the fabric by a roller brush.

A roller brush is used to eliminate the empty air within the fabric and the resin. The *photos I.8* show the FRP application procedure carried out during the reinforcement of the vaults of the church "Spirito Santo" in Nicolosi (CT-Italy).

fig. I.8 - Steps of FRP application (strengthening of the vaults of the church "Spirito Santo" in Nicolosi - CT): application on a leveling mortar of a layer of epoxy resin (photo 1), placing of the dry monodirectional glass fabric (photo 2), application by roller brush of a epoxy resin layer (photo 3)

The failure of the FRP reinforced masonry occurs in one or in a mixture of the following modalities [1]:

- Excessive cracking in the wall (tensile stress);
- Crushing of masonry structural element;
- Shear slip of masonry;

- FRP rupture; and
- FRP debonding.

Among these failure typologies, the debonding is one of the most critical because it occurs at tension much smaller than the tensile capacity of the composite. The study of this brittle modality of failure is the starting point of the research of this thesis.

1.3 The debonding crisis

1.3.1 Definitions

Debonding failure consists in the detachment of FRP from the support. It occurs with a brittle expansion of a crack between the reinforcement and the substrate.

The fracture can be [1]: adhesive, cohesive, mixed (see *fig.I.9*). Adhesive fracture takes place in the interface between adhesive and support material, it is characterized by a smooth surface. Frequently, it occurs when the application of the reinforcement is inaccurate. Cohesive fracture takes place inside the support, it is characterized by a rubble surface. The same material (concrete, mortar) is present on both sides of the crack. This kind of fracture is often noted when the debonding occurs. Mixed fracture is registered when both cohesive and adhesive failure happen. In this case, the crack surface is characterized by the coexistence of support and FRP composite materials.

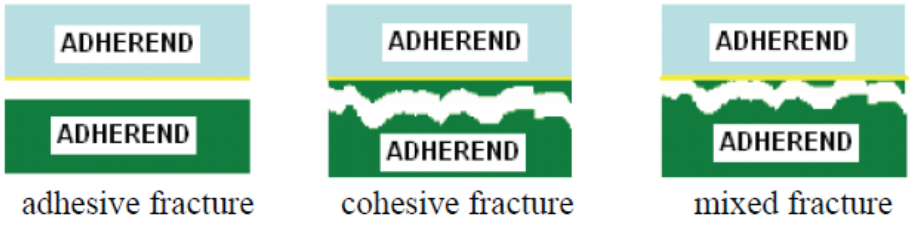

fig I.9 - The main typologies of fracture (adhesive, cohesive, mixed) [1]

The debonding may occur in two main failure modes [1]: plate end debonding (mode 1) and intermediate crack debonding (mode 2). The first failure type occurs when the detachment between FRP and support takes place in the extremity of the reinforcement (*fig. I.10*). Instead, the intermediate crack debonding takes place in the proximity of the existing crack on the support (*fig. I.11*). In this case a stress concentration develops the debonding. When not only stresses in the direction of the fibers but also significant tensile stresses perpendicular to the composite surface (peeling) are applied to the reinforcement, the forces that can be transferred by the adhesive layer are reduced and the debonding occurs prematurely [1].

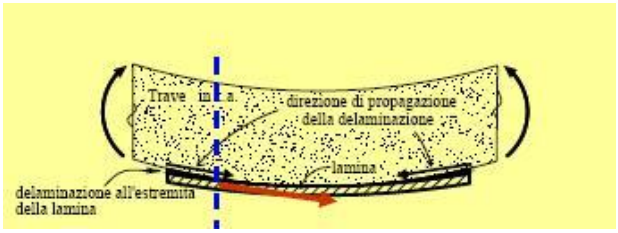

fig. I.10 - Failure mode 1; "plate end debonding"

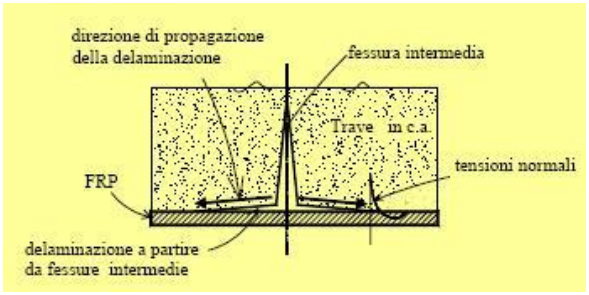

fig. I.11 - Failure mode 2; "intermediate crack debonding"

The phenomenon of the debonding is ruled by some physical parameters: the fracture energy (Γ), the effective bond length (l_e) and the design bond strength (f_{fdd}). We refer to *figure I.12* for the geometric properties of a simple reinforcement.

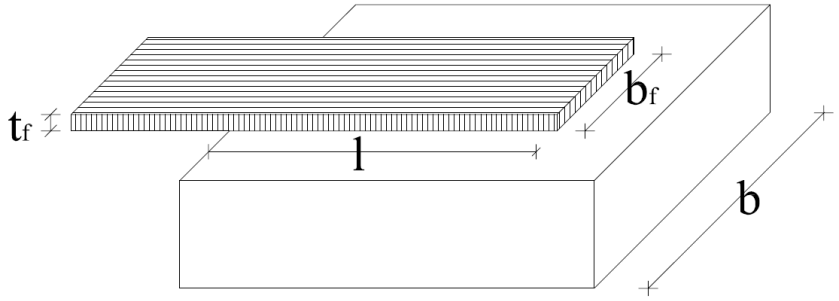

fig I.12 -Support reinforced by a FRP sheet (the same nomenclature of [1] is used)

The fracture energy Γ is the energy dissipated during the debonding failure; it could be quantified in [J] as the area underlying the curve *displacement [mm] – Load [kN]* that describe a shear test.

In the design of a reinforcement the ultimate stress that can be transferred from the FRP reinforcement to the support prior to FRP debonding must be calculate, this stress is named f_{fdd} , for the first debonding mode, and $f_{fdd,2}$, for the second debonding mode.

Experimental and numerical studies show that an increase in the bond length l up to the length l_e causes an increase of f_{fdd}; a further increase in the bonded area does not increase the value of the force transferred. The length l_e is called *optimal bond length* [1] or *effective bond length* [5]. Therefore in the simple case of *fig. I.12* the stresses are transferred between the FRP and the support in a short area nearest to the applied load; the length of the latter is l_e. An increment in load gives rise to the apparition of the first cracks in the zone of length l_e and to the displacement of the stress transfer area toward the unloaded side of the reinforcement. This phenomenon justifies that if $l > l_e$ the system has a residual ductility after the development of the first crack (before the debonding,

the stress transfer zone has to move toward the extremity of the unloaded side). If $l = l_e$ the appearance of the first crack is simultaneous with the total debonding fracture. Yuan et al. [5] defined l_e as the value corresponding to 97% of the load carrying capacity if l is infinite.

In order to define the debonding parameters several fracture mechanics based models founded on experimental results have been carried out. Niedermaier R. in 1996 [5] studied the bond strength between a steel plate and a concrete support by means of a nonlinear fracture mechanics and defined the following relations of P_u (bond strength), l_e and Γ. Denoting by E_f the Young modulus of composite, the ultimate bond strength is given by:

$$P_u = \begin{cases} 0{,}78 b_f \sqrt{2\,\Gamma\, E_f t_f} \quad [N] & if \quad l \geq l_e \\ 0{,}78 b_f \sqrt{2\,\Gamma\, E_f t_f}\,\frac{l}{l_e}\left(2 - \frac{l}{l_e}\right) \quad [N] & if \quad l \leq l_e \end{cases} \tag{1.2}$$

where the effective bond length l_e is written as:

$$l_e = \sqrt{\frac{E_f t_f}{4 f_{ctm}}} \quad [mm] \tag{1.3}$$

and the fracture energy Γ is:

$$\Gamma = c_f k_p^2 f_{ctm} \quad \left[\frac{N\ mm}{mm^2}\right] \tag{1.4}$$

With c_f is a constant obtained in a linear regression analysis using the results of double shear or similar tests, f_{ctm} an average surface tensile strength of the concrete determined in a pull-off test [5] and K_p is a geometrical factor defined by:

$$k_p = \sqrt{1{,}125\,\frac{2 - \frac{b_f}{b}}{1 + \frac{b_f}{400}}} \tag{1.5}$$

Where :

$t_f = thickness\ of\ composite\ [mm]$

$b_f = width\ \ of\ composite\ [mm]$

$b = width\ of\ the\ concrete\ block\ [mm]$

$c_f = constant\ determined\ in\ a\ linear\ regression\ analysis\ using\ the\ resuts\ of\ double\ shear\ or\ similar\ tests$

In these expressions the value of ultimate load is proportional to: the width of the bonded composite, the energy fracture, the stiffness of the composite and the thickness of the FRP. Instead the effective bond length is proportional to the stiffness and the thickness of the composite and inversely proportional to the strength tensile capacity of the concrete support. It's interesting to note that the value of Γ is connected to the ratio between b_f and b.

Neubauer U. and Rostàsy (1997) [5] studied the debonding problem by means of a series of double shear tests on CFRP applied to a concrete support. They affirmed that, for both cohesive failure and adhesive failure, the shear-slip relationship may be represented by a bilinear model (*fig. I.13*).

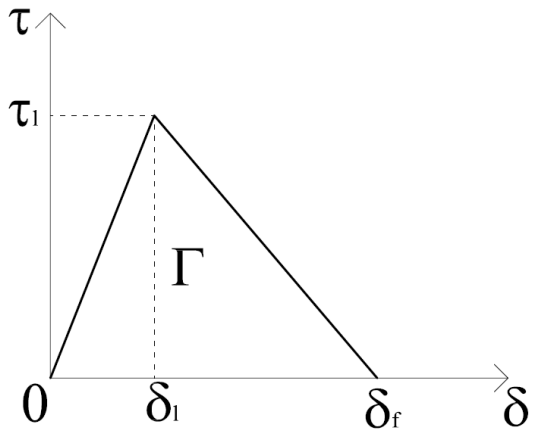

fig. I.13 - Shear-slip relationship model [5]

They defined an average value of c_f, corresponding to 0,204 [mm] and proposed the following new expressions of the parameters:

$$P_u = \begin{cases} 0{,}64 k_p b_f \sqrt{E_f t_f f_{ctm}} & se\ l \geq l_e \\ 0{,}64 k_p b_f \sqrt{E_f t_f f_{ctm}}\ \frac{l}{l_e}\left(2 - \frac{l}{l_e}\right) & se\ l < l_e \end{cases}$$

(1.6)

$$\Gamma = c_f f_{ctm} \left[\frac{N\ mm}{mm^2}\right] \tag{1.7}$$

$$l_e = \sqrt{\frac{E_f t_f}{2 f_{ctm}}}\ [mm] \tag{1.8}$$

In the equation (1.6) of P_u the value of Γ, present in (1.2), is replaced by $f_{ctm}k^2_p$. It is possible to underline that the value of the bond length of equation (1.8) is bigger than that of equation (1.3).

To design a reinforcement Neubauer and Rostasy [5] proposed using 75% of the ultimate bond strength.

The CNR DT 200/2004 [1], in the case of $l > l_e$, provides the following equations of design debonding strength for the mode 1 (f_{fdd}), design debonding strength for the mode 2 ($f_{fdd,2}$) and characteristic fracture energy (Γ_{FK}):

$$f_{fdd} = \frac{1}{\gamma_{f,d}\sqrt{\gamma_M}}\sqrt{\frac{2E_f\Gamma_{FK}}{t_f}} \left[\frac{N}{mm^2}\right] \quad (1.9)$$

$$f_{fdd,2} = \frac{K_{cr}}{\gamma_{f,d}\sqrt{\gamma_M}}\sqrt{\frac{2E_f\Gamma_{FK}}{t_f}} \left[\frac{N}{mm^2}\right] \quad (1.10)$$

$$\Gamma_{Fk} = c_1\sqrt{f_{mk}f_{mtm}} \left[\frac{N}{mm}\right] \quad (1.11)$$

Where $\boldsymbol{\gamma_{f,d}}$ is a partial factor depending on the FRP application, $\boldsymbol{\gamma_M}$ is a partial factor of the masonry, $\mathbf{c_1}$ is an experimental determined coefficient, $\mathbf{f_{mk}}$ is the masonry average compressive strength, $\mathbf{f_{mtm}}$ is the masonry average tensile strength and $\mathbf{K_{cr}}$ is the amplification coefficient of mode 2. The equation of the optimal anchor length (l_e) provided by the CNR [1] for the masonry is similar to that of eq. (1.8) and it is proposed as follows:

$$l_e = \sqrt{\frac{E_f t_f}{2f_{mtm}}} \ [mm] \quad (1.12)$$

Where f_{mtm} is the average tensile strength of masonry support.

1.3.2 Analytical considerations

In the framework of industrial mechanics the adhesion problem has been extensively studied. In 2008 Jongsma J. [7] proposed a model for analyzing the shear stress distribution in the adhesive layer of an "easy peel" system (*fig. I.14*). An easy peel system is a type of closure for metal cans of food products and consists in a foil material (*easy peel sealing*) bonded over a ring (*easy peal ring*) seamed on the top of the tin (*fig. I.15*). When the closed can is sterilized, the product is heated and, consequently, it expands (*fig.I.16*).

fig. I.14 - Metal cans with easy peal system [7]

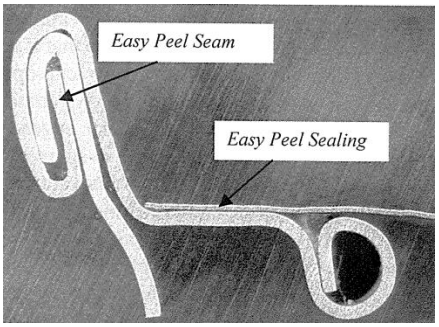

I.15 Cross section of easy-peel ring [7]

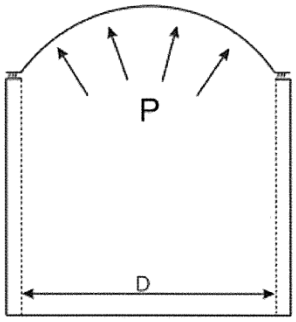

fig. I.16 - Expansion of a metal can during the sterilization [7]

During this process a shear stress is developed in the adhesive layer. Jongsma J. [7] realized an analytic elastic model for studying the shear distribution. The boundary conditions of the debonding problem studied are presented in *figure I.17*. The aluminum support is blocked at one extremity, upon it are placed, in order, a layer of adhesive and the aluminum easy peel.

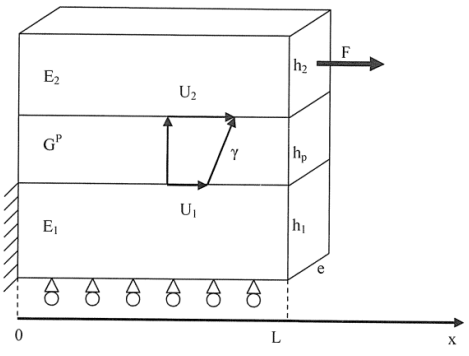

fig. I.17 - Schematic representation of simplified sealed zone (easy-peal) [7]

The value of the shear deformation $\gamma(x)$ is directly obtained from the motion induced by the lower and upper metallic layers. Resolving the differential equations describing the equilibrium on the interfaces *support-adhesive* and *adhesive-easy peel sealing*, the shear deformation $\gamma(x)$ is obtained as:

$$\gamma(x) = \frac{(u_2 - u_1)}{h_p} = \frac{1}{h_p} \frac{F}{E_1 h_1 E_2 h_2 \omega \sinh(\omega L)} [E_1 h_1 \cosh(\omega x) + E_2 h_2 \cosh(\omega(L - x))] \quad (1.13)$$

With:

$$\omega^2 = \frac{G^p}{h_p} \left(\frac{E_1 h_1 + E_2 h_2}{E_1 h_1 E_2 h_2} \right) \quad (1.14)$$

Where u_1 is the displacement in x-direction of the lower joint interface, u_2 is the displacement in x-direction of the upper joint interface, E_1 is the Young modulus of the lower aluminum part, E_2 is the Young modulus of the upper aluminum part, L is the seal width, G_p is the shear modulus of polymer joint, h_1 is the thickness of the lower aluminum part, h_2 is the thickness of the upper aluminum part, h_p is the thickness of polymer joint and F is the tensile force applied on upper aluminum part.
The results of Jongsma [7] confirm that the shear distribution is not homogeneous in the adhesive layer; there is a short area nearest to the applied load characterized by a stress concentration (the effective bond length). When the adhesive thickness (h_p) decreases the stress concentration is more remarkable (*fig. I.18*). Jongsma affirms that this proves that the phenomenon of the heterogeneous shear stress distribution is a thin layer effect.

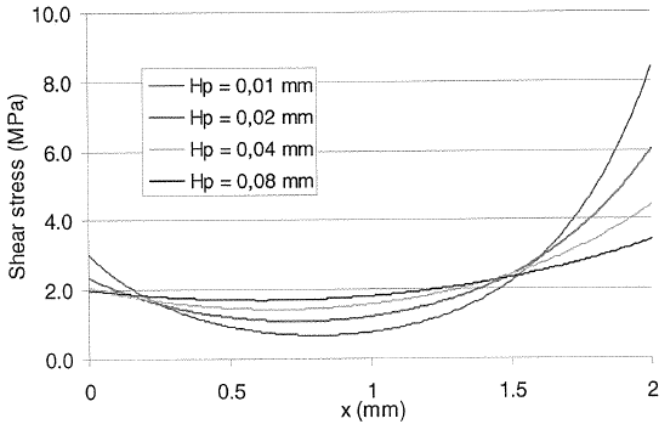

fig. I.18 - Shear stress distribution in the adhesive zone according to Jongsma analytic model for four different adhesive thicknesses [7]

Cottone and Giambanco (2010) [8] studied the stress transfer between a FRP and support bonded joint during a single shear pulling test. They modeled the composite reinforcement as an indefinitely elastic beam connected to a Winkler non-linear deformable foundation (*figures I.19 a,b*).

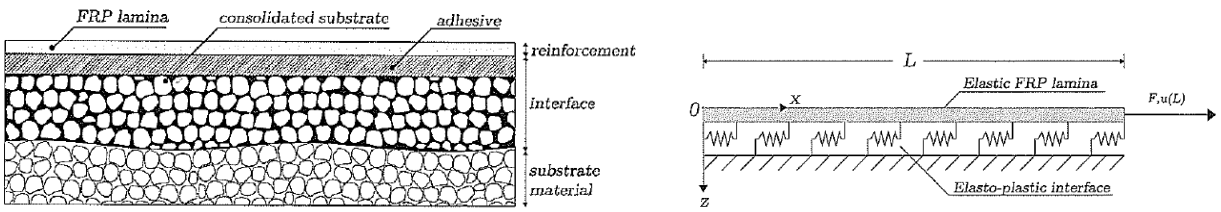

fig. I.19 - a) Physical schematization of the contact layers; b) Mechanical scheme adopted for the simulation of single shear pulling test by Cottone and Giambanco [8]

The interface layer is composed of two strata: the thin film of adhesive and a layer of consolidated material of the substrate. They chose this typology because the cohesive fracture occurs a few millimeters under the interface "adhesive-support". In [8] the behavior of the interface is described by constitutive laws derived from elasto-plasticity theory with softening (*fig. I.20*). The study focalises the pure elastic response of the FRP-substrate system, the evolution of the elasto-plastic zone and the fracture propagation.

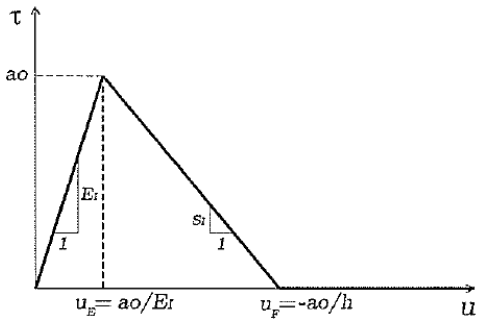

fig. I.20 - Bilinear bond-slip one-dimensional model [8]

During a single shear test, when the applied force F exceeds the elastic limit F_E, the damage process takes place in the loaded extremity. In this experimental step, the interface can be divided in two parts; the portion of length ρ where an elasto-plastic damage occurs, and the remaining portion whose behavior is elastic (figure *I.21*).

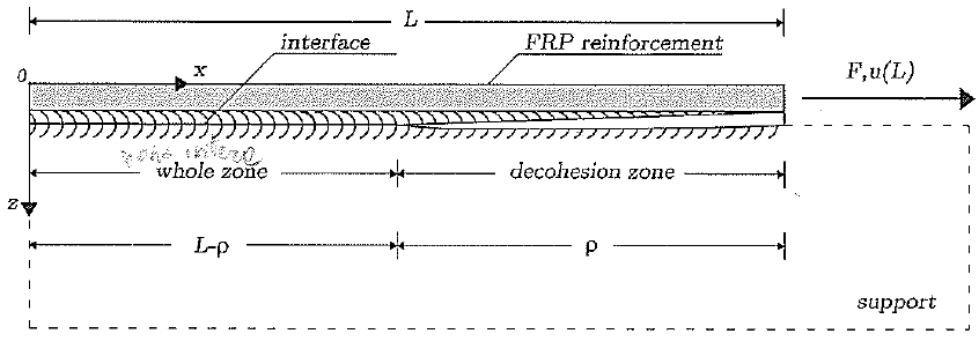

fig. I.21 - Schematic representation of the interface when $F_e < F < F_F$ (elastic whole zone and elasto-plastic decohesion zone) [8]

When the force F reaches the value of F_U (ultimate fracture load) a crack appears in the loaded extremity of the FRP to support bonded joint. In this step, in the interface there is an elastic whole zone, an elasto-plastic damaged zone and a cracked zone (*fig. I.22*).

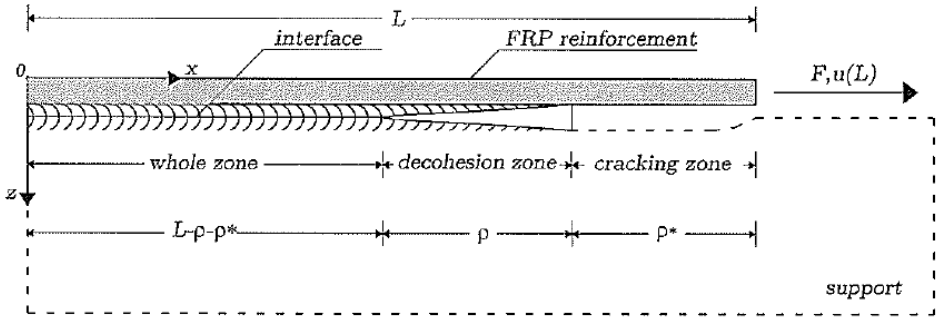

fig. I.22 - Schematic representation of the interface when u(L) > u_F [8]

Cottone and Giambanco [8] define an equation to calculate the maximum extension of the elasto-plastic zone at the interface; the length ρ_i.

$$0 \leq \rho \leq \rho_i = \frac{\pi}{2}\left(\frac{s_i b}{K_B}\right)^{-\frac{1}{2}} \tag{1.15}$$

Where s_i is the interface softening modulus and K_B is the axial stiffness of the composite. The length ρ_i coincides with the effective bond length [8]. If the bond length L is smaller than ρ_i the apparition of the first crack occurs simultaneously with the total debonding fracture. If L is bigger than ρ_i, after the first crack the elasto-plastic damage zone is displaced in the opposite direction of the applied load, this phenomenon happens without any increase in F. The advancement of the crack occurs together with a displacement of the elasto-plastic zone toward the unloaded end; when the value of $\rho = \rho_i$ and there is no longer a whole zone, the crack cannot advance further and a total debonding occurs. In synthesis if $L < \rho_i$ a brittle failure takes place without crack advancement phase. Instead, a crack phase is registered before the fracture if $L > \rho_i$.

1.3.3 Experimental and numerical study

In the literature many different experimental set-ups have been used to determine the FRP-to-concrete bond strength. A classification of the bond tests, with a clearly representation of the corresponding boundary condition is given by Yao et al. [6]. They defined the following five test

types: a) far end supported double-shear tests (FES); b) near end supported (NES) double-shear tests; c) far end supported (FES) single shear tests; d) near end supported (NES) single-shear tests; e) beam test; f) modified beam test (*figure I.23*).

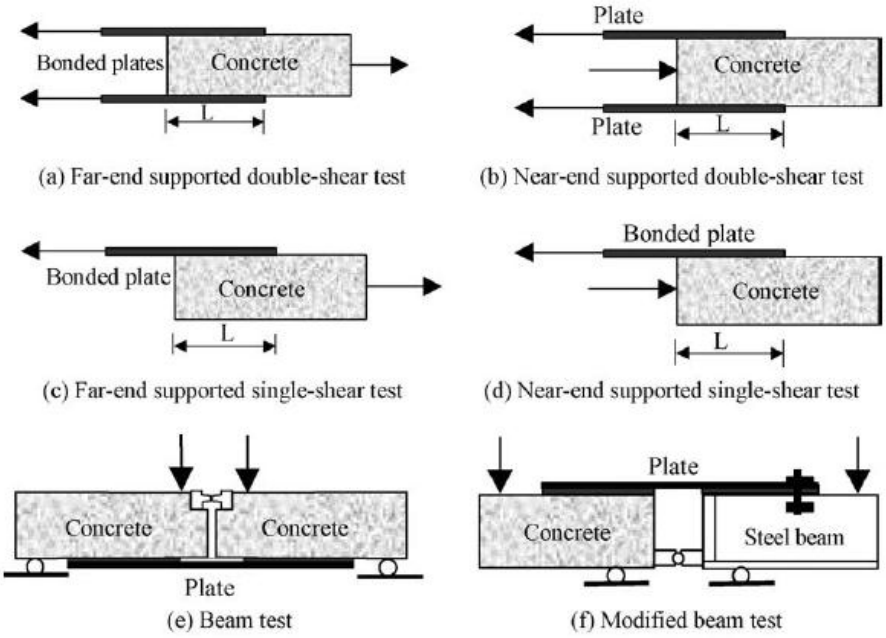

fig. I.23 - Classification of bond tests [6]

Numerical and experimental studies have shown that the different boundary conditions can lead to significantly different test results. The double shear test and the single shear pull tests have been widely used for their simplicity. Yao et al. [6] realized an experimental study using a NES single-shear pull test. They affirm that with this boundary condition the stress state in the critical region of a beam can be described when an intermediate crack induced the debonding failure (*fig. I.11*). Therefore, the near end single-shear pull test is proposed as a standard set-up for determining the FRP-to-concrete bond strength [6]. The experimental session conducted by Yao et al [6] consists in 72 shear tests on concrete prisms bonded with FRP strip. Different series of specimens were studied to analyze the follow factors: the bond length, the width ratio between the FRP strip and the concrete support (b_f/b) and the offset (δ) in the load position (*fig. I.24*).

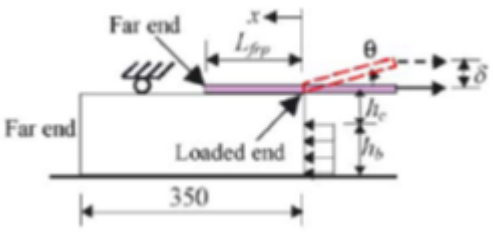

fig. I.24 - Specimen and boundary condition of Yao et al. experimental session [6]

The experiments confirm that the failure of the FRP reinforced systems occurs mainly with a cohesive fracture. Indeed, 56 out of the 72 specimens failed due to debonding in concrete, 8 specimens failed with an adhesive fracture and the remaining 8 specimens failed in the concrete by detachment of a big angular prism (concrete prism failure, see *figures I.25*).

fig. I.25 - Failure modes in the Yao et al. experimental session [6]; a) Cohesive fracture, b) Adhesive fracture, c) concrete prism failure.

The adhesive fracture occurred only in the tests series prepared by an assistant with limited experience. The concrete prism failure took place when the ratio $b_f/b \geq 0{,}8$. In the specimens characterized by a small bond length when the first crack takes place in the loaded-end a brittle debonding failure quickly occurs. The *figure I.26* shows the strain distribution in FRP during the test I-1 (specimen with l = 75mm). From the image it is evident that the strain increases with the applied load and the stress transfer zone moves from the loaded side to the unloaded side. In the test I-16, carried out on a specimen unlike from the specimen I-1 only for a larger bond length (l = 190 mm), the first crack occurs at a similar load of the test I-1 but the propagation of the fracture goes on to reach the farthest extremity. The displacement of the stress transfer zone during the test is clear in the *figures I.27*. The figure proposed by Yao et al. [6] are realized using a normalized distance from loaded end (x/l_e), where l_e is the effective bond length defined by Chen [5].

The Yao et al. [6] tests underline that an increase of the bond length does not increase the load of the first crack but the ductility of the system. In this case the displacement of the effective bond length (stress transfer zone) through the whole FRP to concrete interface permits the delay of the total debonding fracture.

Finally Yao et al. [6] found in their experiment that the existence of a loading offset reduced the ultimate bond strength significantly only when the bond length is small.

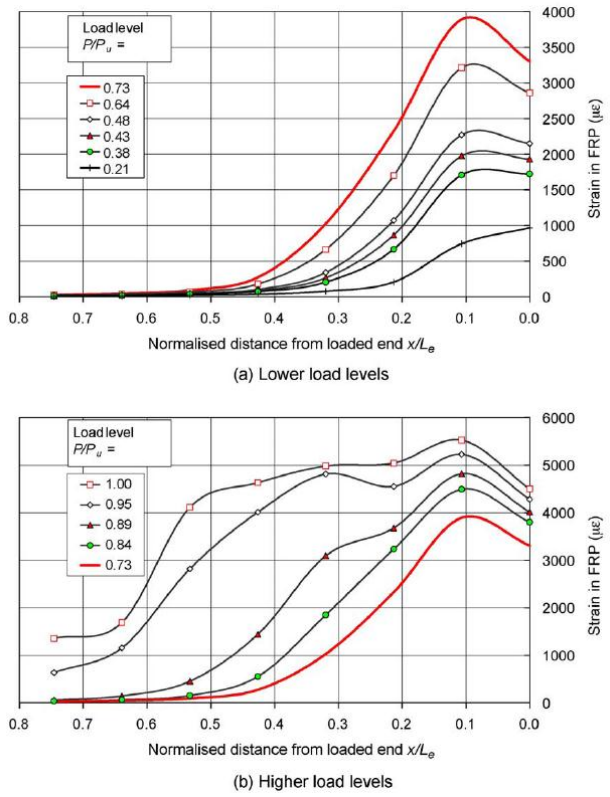

fig. I.26 - Strain distribution along the FRP, test I-1 of Yao and al. (L=75 mm) [6]

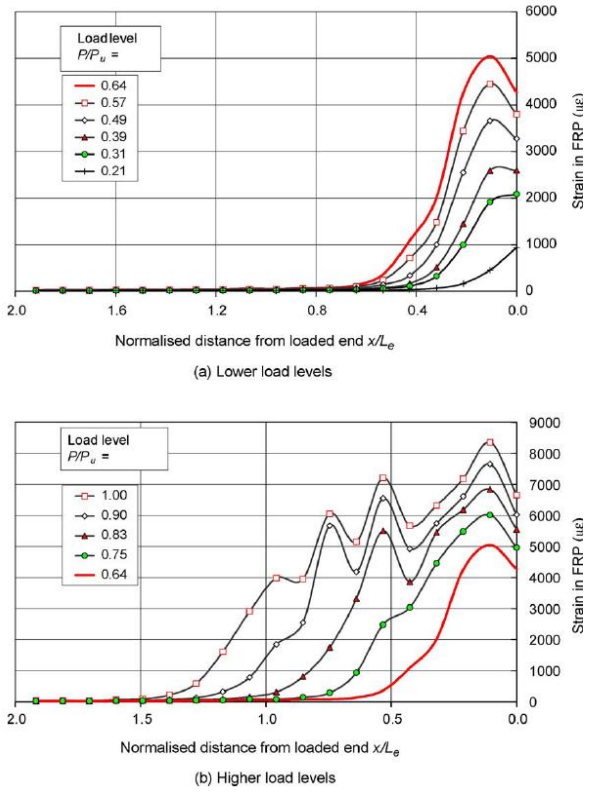

fig. I.27 - Strain distribution along the FRP, test I-16 (L=190)[6]

Research on masonry-FRP systems is much more limited. Experimental studies by means of shear tests have been managed on brick (homogeneous support), pillar and masonry walls (heterogeneous support). Briccoli Bati S. and Fagone M. [15] carried out an experimental analysis using near end supported shear tests to evaluate the collapse load of CFRP reinforcement applied to single brick specimens. The tests had a FRP width (b) varying from 10 to 100 mm and a length (l_b) varying from 10 to 240 mm. The image *I.28* shows that the increase in the bond width leads to an increase in the collapse load until an effective bond length is reached. The value of l_e is the abscissa of the point where the slope of the curves l_b-F_{max} become almost horizontal (*figure I.28*).

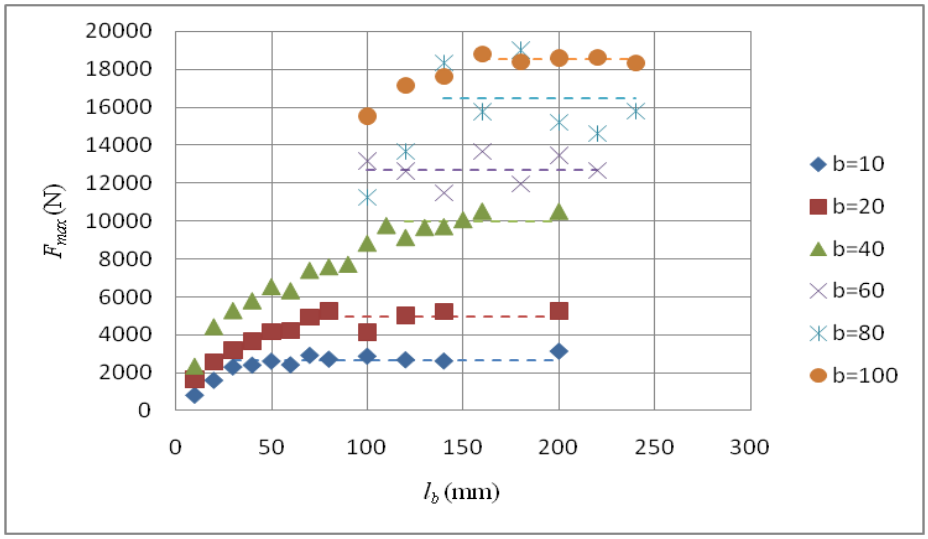

fig. I.28 - Bond length and specific maximum load varying the FRP width (courtesy of M.Fagone)

The bigger the width (*b*) of the FRP, the greeter is the value of the collapse load. The main failure mode registered during the tests described in [15][16] is the cohesive fracture (*figures I.29*).

fig. I.29 - Failure mode, NES double shear tests (a courtesy of M. Fagone)

Another experimental analysis by NES double shear test on FRP on historic brick bonded joints has been carried out by Capozzucca [17]. The reinforcements tested were made by GFRP, CFRP and SRP (Steel reinforced polymer) with a width of 50 mm and a bond length of 250 mm. The historic brick has approximately a dimension of 300x150x80 mm. The stress transfer advancement described in this work is coherent with the Yao et al. analysis [6] (*fig. I.30*).

Experimental and numerical studies show that most failure modes in the bending of masonry walls reinforced by FRP systems are due to the extremity or to the intermediate debonding [18], [19], [20].

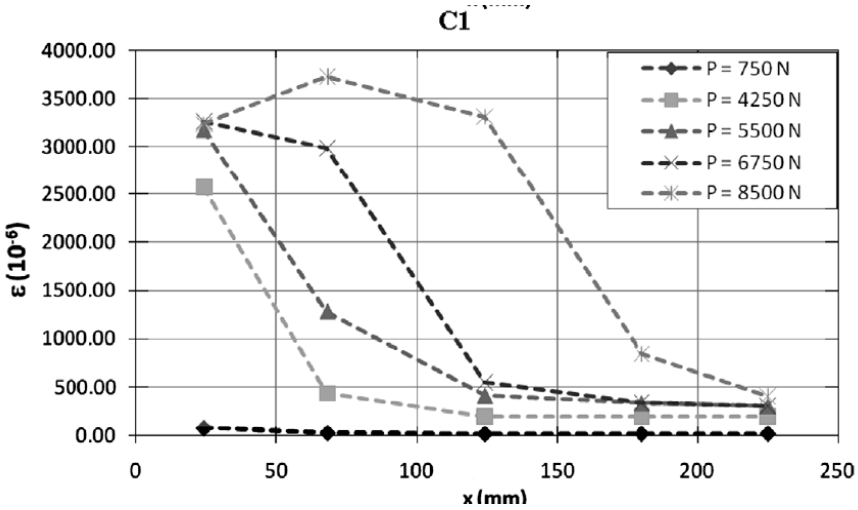

fig. I.30 - Experimental strain values for the CFRP-to-historic brick bonded joint [17]

Fedele and Milani [9] studied the debonding failure of a masonry pillar reinforced with FRP by means of a damage continuum model. The masonry element consist of three standard bricks interposed by two mortar joints. Since the fracture occurs nearly in a cohesive manner Fedele and Milani [9] carried out a numerical study with the assumption of perfect adhesion between the reinforcement and the underlying support. This hypothesis takes into account only the mechanical properties of the FRP and masonry constituents; the properties of the adhesive interface are neglected. The constitutive law used to simulate the debonding is characterized by different isotropic damage variables in tension and compression. The mortar joints and the bricks are modeled independently; each material with its internal variables and activation criteria.

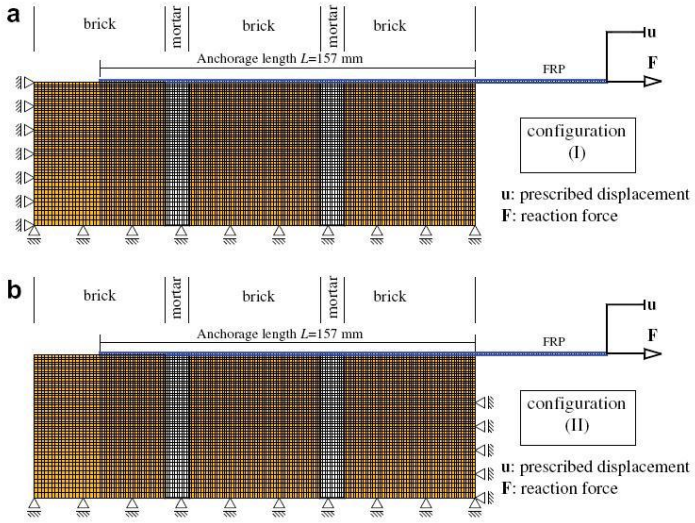

fig. I.31 - Finite element discratization; configuration I (FES double shear test), configuration II (NES double shear test) [9]

The numerical study simulates two experimental boundary conditions; a FES double shear test (configuration I) and a NES double shear test (configuration II) (*fig. I.31*). The fracture in the configuration (I) occurs close to the unloaded-end and the crack advancement starts in the left mortar joint versus the loaded side (*figures I.32 and I.33*).

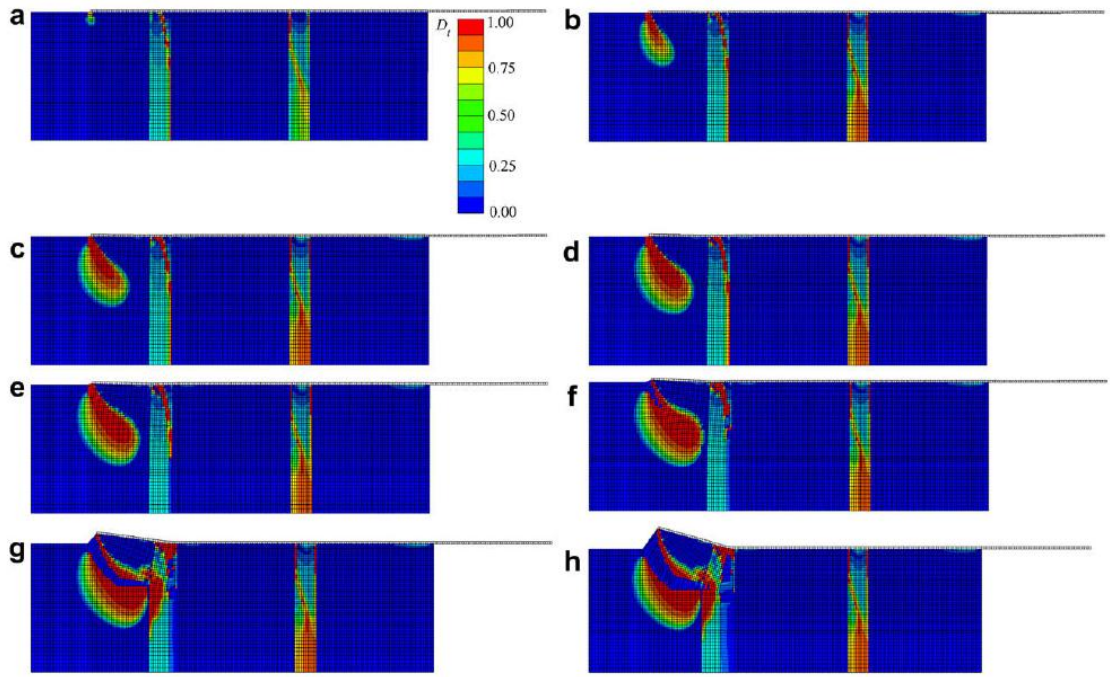

fig. I.32 - Distribution of the damage in tension (D_t) for the numerical FES double shear test (configuration I) [9]

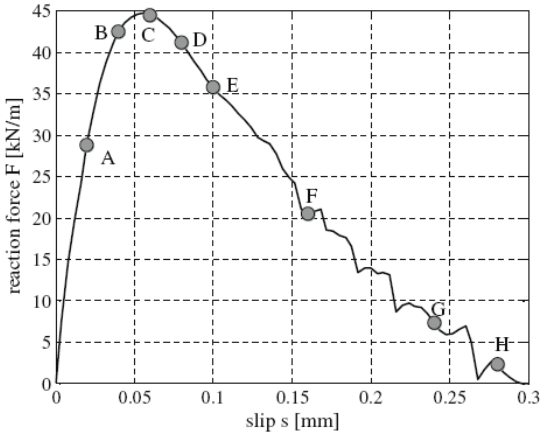

fig. I.33 - Displacement-Load curve of the numerical FES double shear test; points A-H indicate the instants selected for the damage evolution of fig. [9]

In the configuration (II), the fracture advancement takes place in proximity of the loaded end and the crack advancement passes through all the bricks and mortar joints versus the unloaded side of

the specimen (*figures I.34 and I.35*). Comparing the images *I.33* and *I.35* is evident that the peak load for the NES double shear test is five times bigger than that of the FES double shear test; this is due to the different tensile stress distribution in the support. The presence of weak joints in the substrate, like mortar in masonry, could change the crack advancement mode in the debonding fracture.

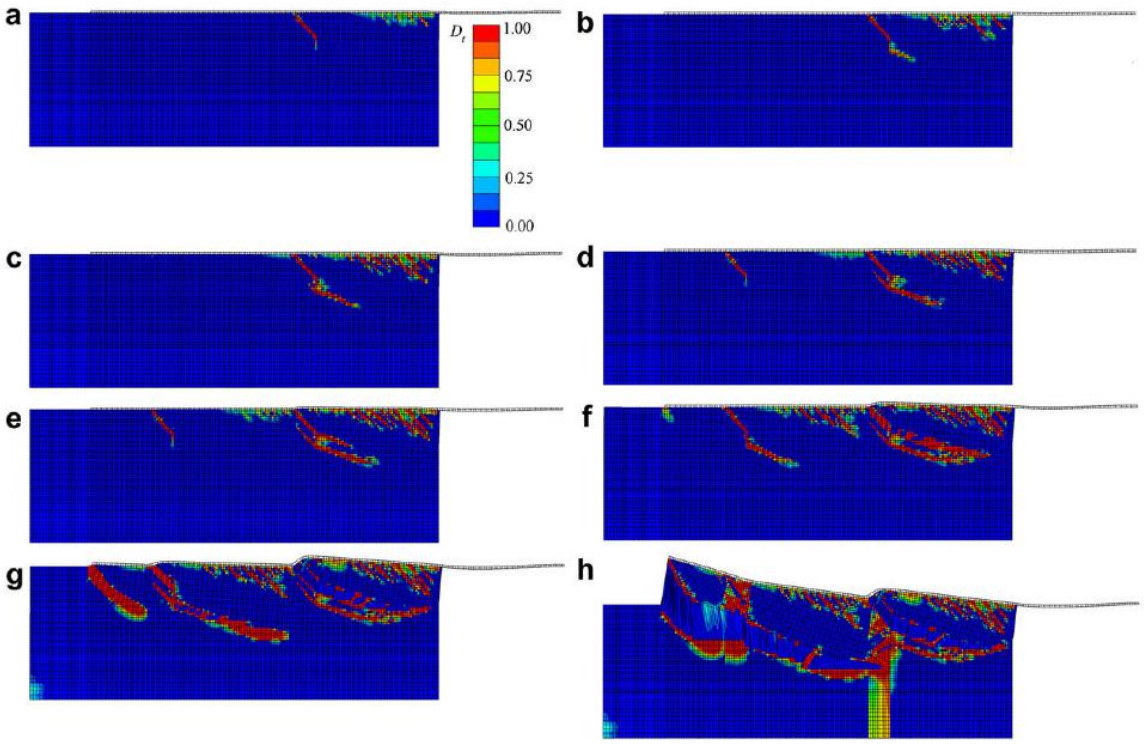

fig. I.34 - Distribution of the damage in tension (D_t) for the numerical NES double shear test (configuration I) [9]

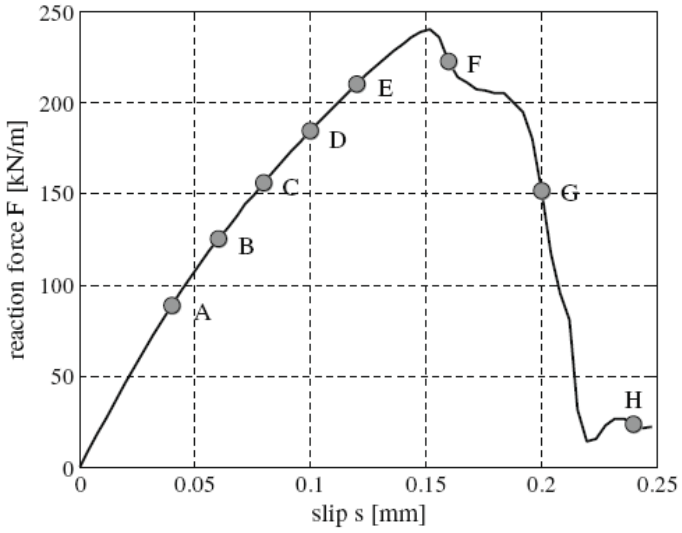

fig. I.35 - Displacement-Load curve of the numerical NES double shear test; points A-H indicate the instants selected for the damage evolution of fig.I.34 [9]

The damage mechanic appears as a good tools to study the cohesive crack advancement process inside the support. A large number of damage model exist in literature, each one characterized by a specifical constitutive law [10][11][12][13][14].

1.3.4 Debonding strength and masonry; a case study

The above literature review shows that the debonding between the composite and the support occurs before the FRP fracture. To obtain an approximate estimation of the debonding strength of a FRP to masonry bonded joint, a simple case study is proposed below. Given a geometry configuration of simple shear test (values of b_f, l), the composite property (t_f, E_f, σ_f) and the support characteristics (Γ_{FK}, f_{bk}, f_{mk}, f_{mdm}), the value of l_e and f_{fdd} (when $l > l_e$) has been calculated. The calculus carried out using the design equations proposed by the Italian National Council of Research [1]. The value of l_e and f_{fdd} have been calculated for eight different typologies of masonry support, see table *1.IV* [4] considering a class of mortar M15. The partial factors ($\gamma_{f,d}$ and γ_M) have been chosen imagining a certified application of the FRP. The value of c_1 has been selected equal to 0,015 [1]. The results of the simple calculus are summarized in *table 1.V.* The optimal bond length (l_e) is inversely proportional to the specific fracture energy of the support (Γ_{fk}) (*fig. I.36*). Therefore a masonry with good cohesive properties, needs an optimal bond length shorter than a support of poor quality. In other words, when Γ_{FK} is high the stress transfer zone is reduced. Instead the design bond strength (f_{fdd}) is proportional to the specific fracture energy Γ_{FK} (*fig. 1.V*). As expected, a support characterized by good cohesive quality increases the debonding strength of the reinforced FRP system.

Tab. 1.V - Masonries and debonding strength

Type	Masonry (M15)					FRP			FRP to masonry bonded joint				
	f_{bk} [N/mm^2]	f_{mk} [N/mm^2]	f_{mtm} [N/mm^2]	γ_M	Γ_{Fk}	E_f [N/mm^2]	t_f [mm]	s_{lim} [N/mm^2]	l_b [mm]	c_1	γ_{fd}	l_e (mm)	f_{fdd} [N/mm^2]
I	2	1,2	0,12	2	0,01	270000	0,167	2700	450	0,015	1,2	433,45	79,94
II	3	2,2	0,22	2	0,01	270000	0,167	2700	450	0,015	1,2	320,12	108,24
III	5	3,5	0,35	2	0,02	270000	0,167	2700	450	0,015	1,2	253,80	136,53
IV	7,5	5	0,5	2	0,02	270000	0,167	2700	450	0,015	1,2	212,34	163,18
V	10	6,2	0,62	2	0,03	270000	0,167	2700	450	0,015	1,2	190,69	181,71
VI	15	8,2	0,82	2	0,04	270000	0,167	2700	450	0,015	1,2	165,81	208,98
VII	20	9,7	0,97	2	0,05	270000	0,167	2700	450	0,015	1,2	152,45	227,29
VIII	30	12	1,2	2	0,06	270000	0,167	2700	450	0,015	1,2	137,07	252,80

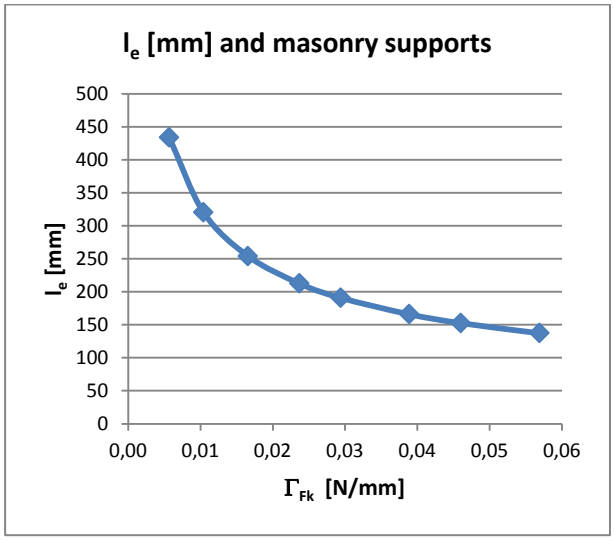

fig. I.36 - Optimal bond length (CNR) and masonries

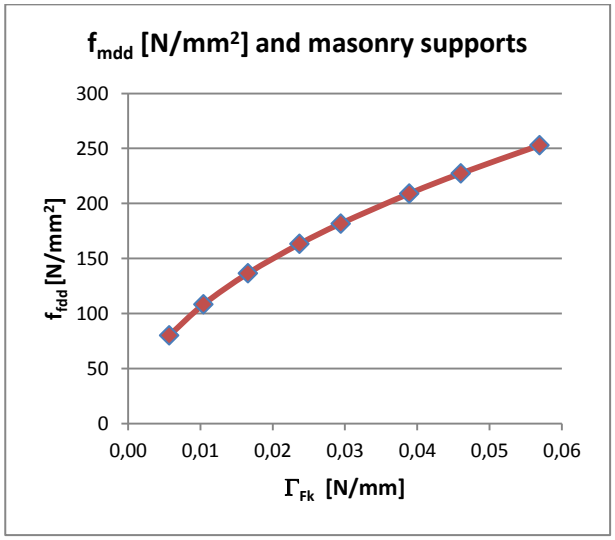

fig. I.37 - Design bond Strength (CNR) and masonries

The design bond strength (f_{fdd}) of the reinforced system with the better support quality (type VIII in table 1.V) is equal to 252,8 MPa. This value is much smaller than the tensile resistance of the composite (σ_f=2700 MPa); only a small percentage of the high quality of the FRP is used. This thesis has been developed to increase the efficiency of the FRP reinforced systems.

1.4 Mechanicals anchors

A solution to increase the tension strength and the ductility of FRP reinforced systems as well as the use of "mechanical anchors" to join support to composite sheet. In the framework of the reinforced concrete structure, some studies have been carried out recently to define the typologies of anchors and the better configuration of application.

Ha lee and al. [21] executed an experimental study on the strengthening FRP systems fastened with steel nails. They utilized Near End Supported shear tests on concrete blocks, and flexural tests on reinforced concrete beams (*fig. I.38*). The composite applied over the concrete surface was a pultruded FRP strip characterized by hybrid carbon and glass fiber in a vinylester matrix (product named Safstrip). In the NES shear test session the FRP laminate (355 x 25 mm^2) has been applied directly on the concrete block (260 x 130 x 130 mm^3) without resin, and the adhesion between the support and the composite has been ensured only by one (conf. 1) or two (conf. 2) steel nails. The latter have a diameter of 3,5 mm (the same as the hole) and a length of 32 [mm].

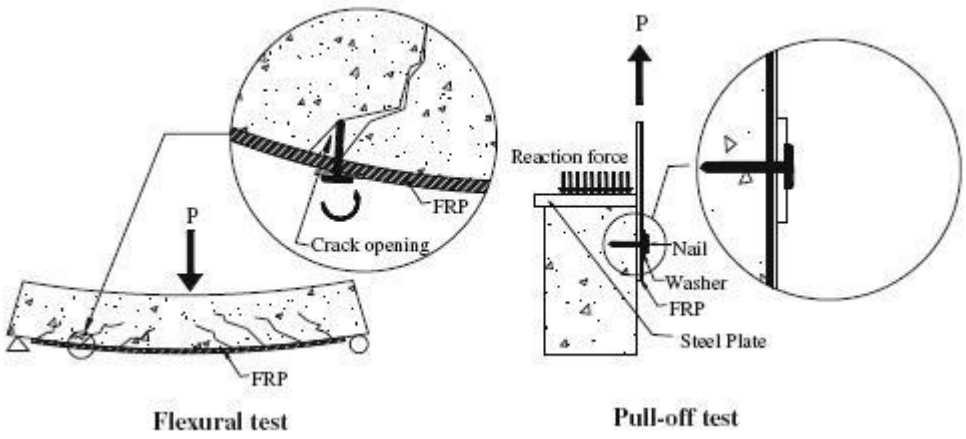

fig. I.38 - Boundary condition and failure of flexural tests and NES single shear test of Ha Lee et al. [21]

The average pull-off load for the configuration with two nails was 11,7 kN, approximately twice that for one nail (6,10 kN). During the NES shear tests bearing damage close to the anchor occurs (*fig. I.39*). In the flexure beam test, the FRP laminate was fastened with more nails, in all cases without the application of resin. The reinforced beam has an 35% increase of the ultimate moment when compared to the unstrengthened beams. During the tests the nails rotated with a limited bearing failure of the FRP (*fig. I.39 b,c*). The presence of the anchor acted as a crack initiator (*fig. I.38 and I.40*). When the FRP strip slipped off the concrete, it remained linked to the support; the fasteners led to a ductile flexural failure mode.

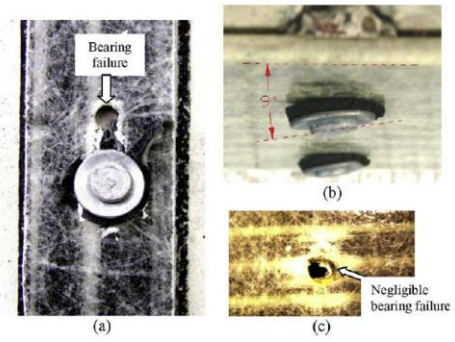

fig. I.39 - Nail and FRP interaction: a) extensive bearing failure (NES single shear test), b) nail rotation after flexure test, c) limited bearing failure after flexure test [21]

fig. I.40 - Crack and nails in a flexural test [21]

Other studies on the efficiency of the steel nails applied on FRP laminate exist in literature [22]. Moreover other anchorage devices have been proposed for the FRP laminates [23].

When the composite is made directly in situ by applying special resin over a dry fabric and bonding the FRP on the support, other typologies of mechanical anchors are used. Among those the "U WRAPS" and the "fiber anchors" are the joint systems built by means of the same fiber typologies of composite sheet (*fig. I.42*). The first system uses FRP strips applied over the reinforcement in different directions from the principal FRP [24], the second solution is similar to "nails" inserted in the strengthening system to connect mechanically the FRP sheet to the support.

fig. I.41 - U WRAPS joint system [24]

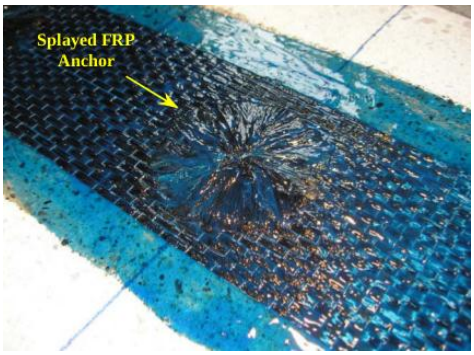

fig. I.42 - Fiber Anchors joint system [Niemitz]

Orton *et al.* [25] carried out 40 experiments to test a reinforced concrete beam in bending with a preexisting crack at midspan. The beams were strengthened with CFRP with and without the addition of anchor joints (U WRAPS or fiber anchors). Orton et al. [25] defined an indicator to define the efficiency of the CFRP material usage:

$$Efficiency = \left(\frac{V_{LS}}{V_T}\right)\left(\frac{T_{max}}{T_{cap}}\right) [\%] \quad (1.16)$$

Where V_{LS} is the volume of the longitudinal CFRP sheet, V_T is the total volume of CFRP, T_{cap} the tensile capacity of CFRP sheet, T_{max} the maximum measured tension in CFRP sheet and $\frac{T_{max}}{T_{cap}}$ the rate of the tensile capacity exploited.

In Orton's specimens the value of T_{cap} was about 130 kN. The beam strengthened by a FRP bonded joints, without mechanical anchorages, exploits only 37 % of the tensile capacity of the sheet (efficiency = 37%) (*fig. I.43*). When two single layer U-Wraps were applied the $\frac{T_{max}}{T_{cap}}$ increases to 70% (efficiency = 21%). The application of two double layers U-Wraps means 93% of the tensile capacity of the sheet can be used. However the value of efficiency became 16 % due to the large use of CFRP material.

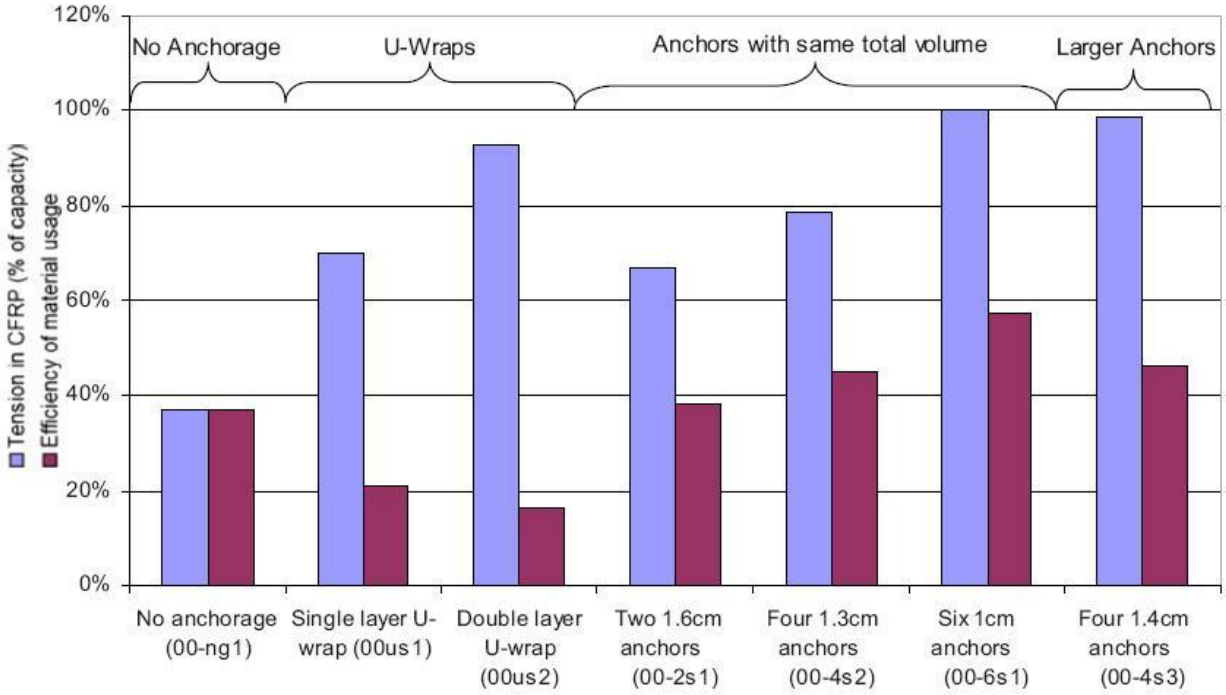

fig. I.43 - Percentage of the used CFRP sheet tensile capacity (in blue) and efficiency (in violet) of different reinforcement configuration [25]

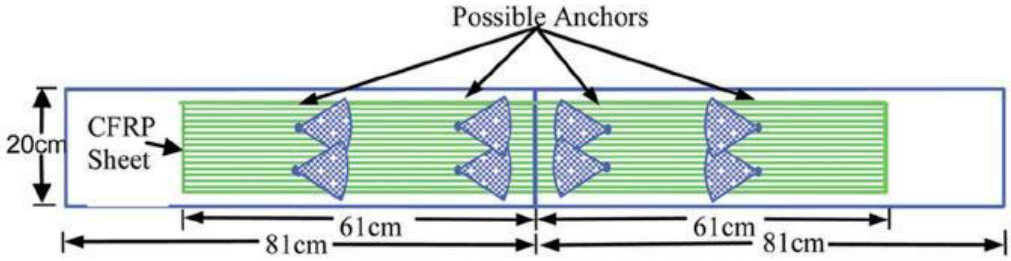

fig. I.44 - Intrados of the cracked beam tested by Orton; they are visible the four anchors rows (two in each mid-span) [25]

The FRP anchors were applied across the concrete blocks in aligned rows at 13 cm and 54 cm from the centerline of cracked beam. When two anchors of 1,6 cm diameter are applied in each mid-span row 67 % of T_{cap} is exploited. The placing of four anchors (1,3 cm diameter), two in each mid-span row, increases the value of the tensile capacity used to 79% (efficiency = 44%). The better result was obtained applying six anchors of 1 cm diameter, three in each mid-span row, and reaching the CFRP sheet's full tensile capacity ($\frac{T_{max}}{T_{cap}} = 1$). In this case the value of the efficiency was 57%; the highest value registered. It is thus evident that the fiber anchors are more efficient than the U Wraps and reduce the amount of CFRP material required to obtain a given strength.

fig I.45 - Dry fiber anchor [27]

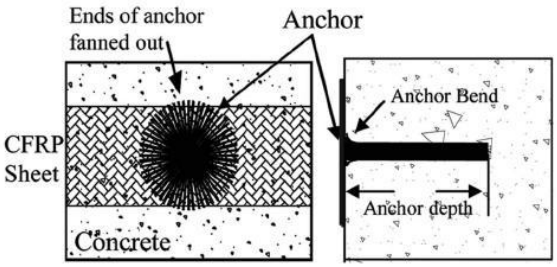

g. I.46 - Fiber Anchor applied in a support (360° splay) [25]

The fibers anchors are constructed by rolling a sheet of fiber tissue (*fig. I.45*). The lower part of this one is inserted through the composite strip, into an impregnated hole in the support (*fig. I.47*). The fibers at the top of anchor are spread over the FRP sheet like in fan shape. A layer of epoxy resin must be applied under and over the fan [25][26][27][28]. The studies of Kobayashi [25] into the stress transfer mechanism between the FRP sheet and the fan anchor define a fan opening angles limited to less than 90° to limit stress concentration [25][26][28]. However in the literature, a complete opening fan of 360° is considered [27]. The limit between the hole and the support must be rounded to reduce the stress concentration [29]; the fibers bending in this area has an important influence on the tensile capacity of the anchor.

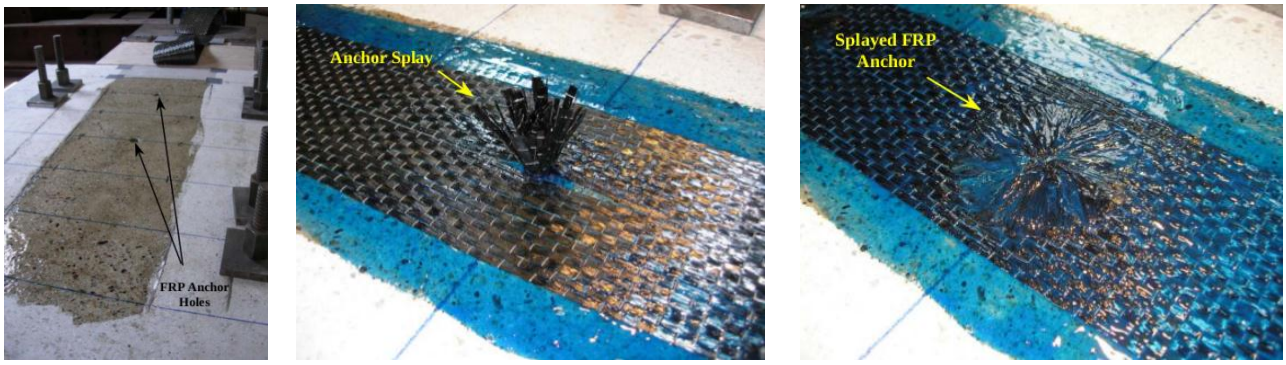

Fig. I.47 - Some phases of the fiber anchors application process, I) Covering the support surface with primer after the realization of the anchors holes, II) Insertion of the anchor through the composite strip, III) fanning of the anchor splay [27]

Niemitz [27] studied the efficiency of carbon fiber anchors by means of 12 NES single shear tests on reinforced concrete blocks (dimensions of 101.6 x 86 x 32.2 cm^3) strengthened with CFRP sheet (*fig. I.48*). Niemitz's anchors were applied dry in the support holes which were filled approximately half way with epoxy resin (*fig. I.45 and I.47*). Without anchors and for a sheet of 12.7 cm wide and 76.2 cm long, the failure of strengthened system occurred at a tension equal to 46 % of the stress limit of the composite. When there are two anchors (each-one with a diameter of 1.3 cm and 360° fan diameter of 5.1 cm) placed longitudinally, the failure occurred at a tension equal to 68 % of the limit tension of the composite. The failure occurs with the local fracture of the fibers in the

proximity of the first nail (load side), and with the debonding of the FRP sheet in the lateral sides of the reinforce (*fig. I.49*). When the two anchors are placed across the width of the sheet the ratio between the failure load of the reinforcement and the failure load of the composite in tension is equal to 71 % (*fig. I.50*). In this case, the failure occurs in the same modality as the previous case but with more limited lateral debonding zones.

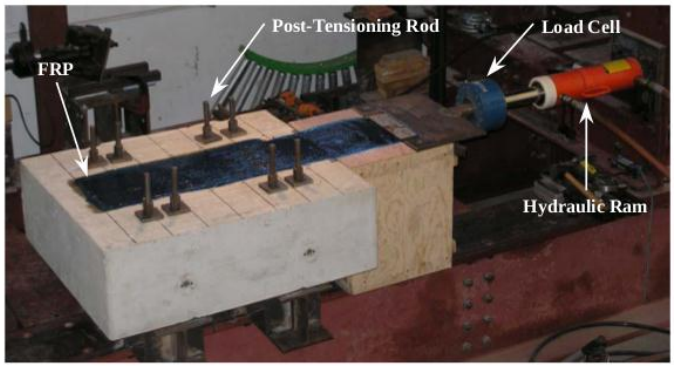

fig I.48 - Specimen test setup of Niemitz [27]

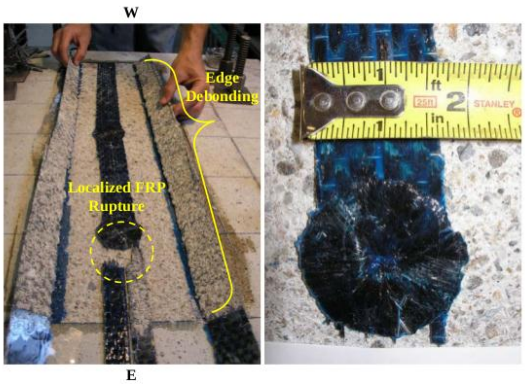

fig. I.49 - Failure of the specimen with two anchors placed longitudinally [27]

For all tests the anchor length of 5.1 cm is enough to prevent the anchor pullout. Niemitz found that the overall effectiveness of FRP anchors is related to: the ratio between the anchor diameter and the fan diameter, the anchor spacing and the anchor depth. A larger fan diameter increases the force applied to the anchor; if the amount of fibers is not sufficient a shear failure of anchor is possible, indeed, this typology of failure has occurred in a test with an anchor diameter of 0,64 [cm] (*fig. I.51*). The most efficient disposition of anchors is across the width of the composite sheet. Spacing anchors longitudinally is convenient also to increase the ductility of the system. It was not possible, in Niemitz's study [27], to record the peak stress values using a discrete number of strain gauges.

fig. I.50 - Failure of the specimen with two anchors placed across the width of the sheet [27]

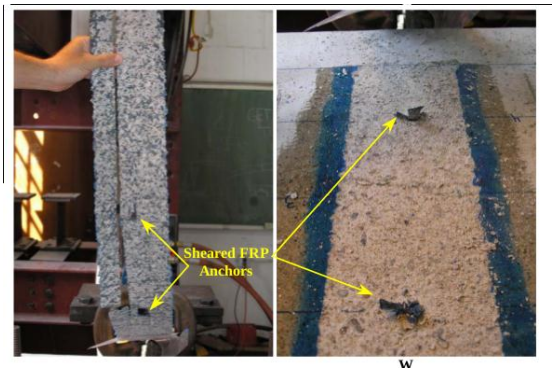

fig. I.51 - Shear failure of the reinforced system with a small anchor diameter [27]

Zhang *et al.* [28] have studied the FRP anchors by means of 27 single shear tests on reinforced concrete blocks (40x20x20 cm^3) reinforced with FRP sheet (joint surface of width 5 cm and length 25 cm). They tested two typologies of anchors: dry and impregnated (*fig. I.52*). The second, which is more efficient, is made with inferior lower extremity (dowel) of 2.5 cm pre-impregnated in the phase of rolling fiber tissue. For all the tested specimens the anchor length was equal to 4 cm and the anchor diameter to 1.2 cm.

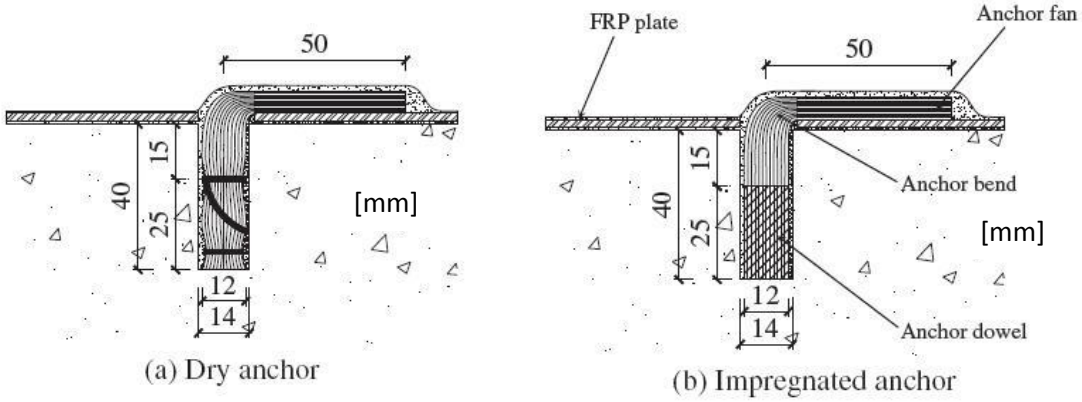

fig. I.52 - Dry and impregnated anchors of Zhang et al. [28]

The anchor fan was oriented towards the direction of load (fan open of 60°) with a radius of 5 cm.
The generic curve slip-load obtained during the tests by Zhang et al. [28] is represented in *figure I.53*; it has been subdivided in five steps. The first one corresponds to the elastic behavior of the reinforced system (stroke A-B). This phase finishes when the crack advancement process starts with the development of a first fracture in the support (loaded side). In the second step (stroke B-C) the ratio load-slip is lower than that of stroke A-B. In this phase the resistance of the reinforced system is connected to: i) the remaining portion of plate bonded to the concrete, ii) the strength and the stiffness of the anchor and iii) the friction between the roughened interfaces of debonded plate and concrete substrate. In the third step (stroke C-D) the complete debonding of the plate brings a quick decreasing of the load. The fourth step is characterized by an improvement of the load due to the contribution of the tensile resistance of anchor. It is also due to the friction between the roughened surfaces of the debonded plate and the concrete substrate. In the fifth step the load reduced rapidly for anchor rupture failure and gradually for anchor pull-out. The average load peak (at the end of second step) of unanchored FRP-to-concrete control joints is 18 kN. The application of a dry anchor 200 (built rolling a fiber sheet of 200 mm) improves the load peak of 54%. The application of an impregnated fiber anchor 200 improves the load peak of 73%. Different design arrangements of impregnated fiber anchors have been studied in bending tests on FRP-strengthened reinforced concrete slabs [30].

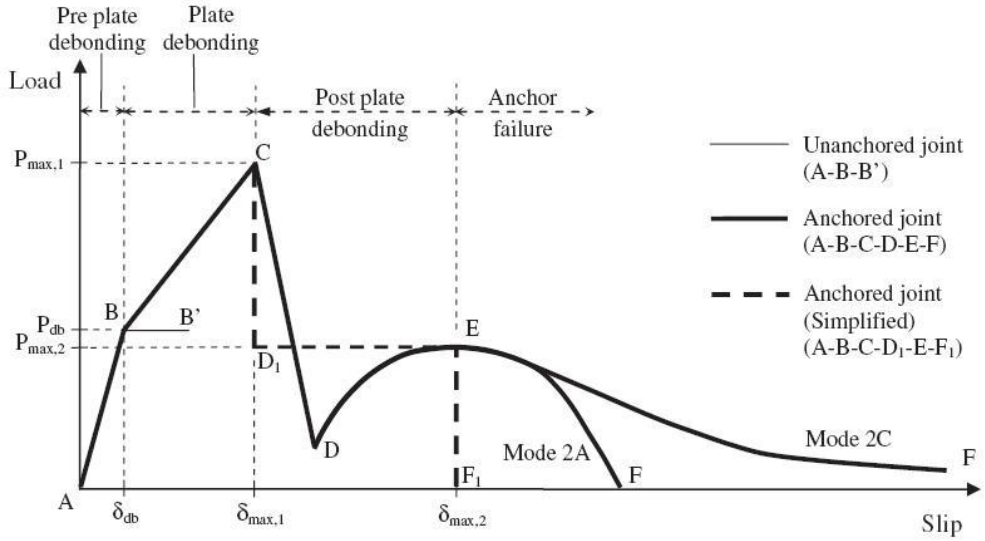

fig. I.53 - Load-slip response of FRP-to-concrete joints anchored tests [28]

1.5 The reinforcement of the masonry structures using FRP strips and anchors; a new scientific field to analyze

The literature review presented above showed that the support in concrete strengthened by FRP have studied more than in the case of masonry. This is probably due to the extensive use of concrete in the civil engineering field and to the "simplest" execution of numerical and experimental studies on a support that could be considered homogenous. Therefore, many of the civil structures to requiring reinforcement are built in masonry.

In Italy, the norms CNR DT 200/2004 have guided the engineers in the application of the fiber composite polymers onto concrete and masonry supports. However, several improvements can be added to the technical directives. Specifically, the value of the optimal anchor length defined in the DT 200/2004 does not take into account the influence of the composite width [15]. In addition the norms recommend designing the reinforcement by using the mechanical properties of the support but they do not specify how implement the calculus when a leveling mortar layer is applied between the FRP strip and the masonry (or concrete).

The carbon fiber anchors are not described in the CNR norms though some engineers already apply them without any scientific support. The use of the anchorages could be revolutionary for the reinforcement design of the FRP to masonry (and concrete) systems for several reasons:

1. The nails increase the strength of the reinforced systems [25][26][27][28];
2. The anchors increase the ductility of the reinforced systems [28][27];
3. When the anchors are applied a residual resistance is registered after the brittle debonding of the FRP plate from the support [28]; and
4. When the FRP anchors are applied the properties of the superficial support layer are negligible [25].

The experimental research presented in this thesis is a ground work of a more wider study on the efficiency of the FRP strengthening systems applied on the masonry support and fastened by FRP anchors.

Chapter 2

Experimental program

2 Experimental Program

Why realize an experimental study on CFRP to fire brick bonded joints? What are the goals of the tests? What are the problems connected with the test realization? How should the experiments be carried out? In this chapter these questions have been answered. Herein, after a presentation of the motivations, goals and methodology of the experimental program (*par. 2.1*), a detailed description of the test setup is presented (*par. 2.2*).

The logical steps carried out to project each particular of the experimental system have been: 1) focus the goals, 2) a more efficient conception of the experimental device, 3) design. This methodological process has been used to project the boundary condition, the specimen geometries, the anchor devices and the steel apparatus.

In the following pages, the most important, boundary conditions are defined (*par. 2.2.1*), the geometry of the specimens is presented (*par. 2.2.2*). All the materials used to prepare the sample are characterized and described. In particular, the results of the compression tests on the fire bricks carried out in Florence are shown. Moreover, the properties of the CFRP components are presented in line with the technical sheet BASF. A particular attention is given to the description of the carbon fiber anchors. All the phases of specimen realization are presented and commented.

Afterwards, a description of the mechanical apparatus of the boundary conditions is presented. The Universal machine Deltalab of the ESIPE (Univ. Paris Est Marne La Vallée) laboratory is analyzed in paragraph 2.2.3. The mechanical systems created to lock the brick and to grip the fibers are presented in paragraph 2.2.4. The numerical studies carried out to determine the best configuration of the apparatus are shown in the first part of this section. Then, all the devices designed and realized are presented and commented. Moreover, an experimental study of the stiffness of the new steel system is reported; in the same paragraph the results obtained have been compared with those of the numerical study. Afterwards the project and the devices of the steel grab system are described and commented. Paragraph 2.2.4 finishes with a global geometrical representation of the boundary condition apparatus.

The paragraph 2.2.5 describes all the procedures necessary to prepare the test; the insertion of the reinforced fire brick inside the steel apparatus, the gripping process of the fiber fabric, the alignment and the global assembling of the experimental system. The instrumentation applied on the apparatus is presented in paragraph 2.2.6 underlining the experimental data searched. Finally, the test procedure is described.

2.1 Motivation, goals and methodology

In the field of concrete structures many studies exist on the use of FRP anchors systems. It has been demonstrated that this mechanical anchor typology increases the strength peak and the ductility of the reinforced elements. Moreover, it is more efficient than the U-WRAPS method. Therefore, in the field of masonry, almost no study has been conducted on the FRP anchors. This lack of research leads to the absence of a scientific basis to define the correct design modality and anchor application methodologies; in this context engineers employ the new joint technologies relying only on their own experience or the FRP producer's advice.

The experimental study proposed in this work has been designed to analyze the performance of mechanical anchors applied over CFRP straightened fire brick. This support typology has been chosen becuase among the numerous different masonries, the "solid brick work" (see chapter 1) is the typology present all over the world with almost uniform characteristics, this happens for two reasons: the fire brick from different territories have similar mechanical and geometrical characteristics (this is not the case of local stone) and the constructive technique used to build the walls is the same in all the regions (joints of staggered mortar). Moreover, the fire brick structures are simple to realize. The use of this "classical" typology of masonry for the realization of the experimental tests could be "indicative" to evaluate the performance of FRP anchors on heterogeneous supports. The research program proposed consists in three progressive steps:

- Near End Support single shear tests over CFRP straightened fire brick fastened with FRP anchors (brick + CFP sheet + anchor /s);
- Near End Support single shear tests over CFRP straightened pillars fastened with FRP anchors (pillars + CFP sheet + anchor /s); and
- Flexural tests over CFRP straightened walls fastened with FRP anchors (wall + CFRP sheet + anchor /s).

The experimental study reported in this work is relative to the first research step. Specifically, the **goals** of the test sessions have been:

a) Quantify the strength enhancement that CFRP anchors can provide the strength capacity of the reinforcement;
b) Study the efficiency of different design configurations varying the anchor fan angle, the anchor fan radius, the number and the placement of anchors;
c) Observe the crack advancement and the failure modes of the FRP-to-firebrick system with and without the different anchor configurations;

d) Analyze and quantify the dissipation of energy during the crack advancement in each different design configuration;
e) Obtain the strain field on the reinforced surface in each step of the load history using the Digital Image Correlation;
f) Obtain the bond stress field on the reinforced surface in each step of the load history;
g) Define the evolution of the stress transfer zone;
h) Quantify the optimal length l_e by evaluating the maximal length of the stress transfer zone;
i) Compare the experimental value of l_e with the value of the optimal length obtained using the equation of CNR DT200/2004; and
j) Compare the experimental maximal strength with the design strength $f_{fdd,2}$ defined in CNRDT200/2004.

To achieve these goals 72 Near End Supported shear tests divided in 6 typologies of specimens were managed. The design of the tests, the reinforced systems and the FRP anchors has been done after a detailed literature research. The experimental program has been realized in collaboration with the University of Florence, Department of Construction. The "Fagone, Ranocchiai, Briccoli Bati" research group believed the proposition to study the FRP anchors interesting and has made available its confirmed experience in the fields of masonry and FRP. The tests have been carried out in parallel, in France and in Italy, to compare the results obtained with two different methodologies of strain analysis; the DIC in Paris and the use of traditional strain gauges in Florence. Specimen tests were carried out in Firenze, after that fifty percent of the samples were sent to France. The tests in Paris were carried out using the laboratory equipment of the University Paris-Est Marne-La-Vallée. The photos of the specimens during the phases of construction are a courtesy of Giuliana Di Iacovo (student intern at University of Florence).

2.2 Experimental Setup

2.2.1 Boundary conditions

The experimental analyses have been carried out with series of Near End Supported single shear tests (*fig. II.1*). This typology of boundary conditions reproduces an "intermediate crack debonding" [6]. As seen in the first chapter, the NES single shear tests are easy to reproduce and have been used in many numerical and experimental literature studies [1][5] [6][7][8][9][15][16][17][21][27][28]. The adoption of such a well-tried configuration test has permitted the comparison of the experimental results obtained in this work with those of literature.

Moreover, the equation of the debonding parameters defined in literature have been obtained starting from shear hypothesis; the choice of similar boundary conditions makes a cross-comparison between the normative and the experimental values of l_e, Γ and f_{fdd} possible.

The single shear tests (SST) have been preferred to the double shear test because the slender thickness of the brick does not permit the application of the anchors in two symmetric surfaces of the block. Indeed, in the SST, the anchor system is applied only in one side of the fire brick and the support presents a behavior more similar to that of reality.

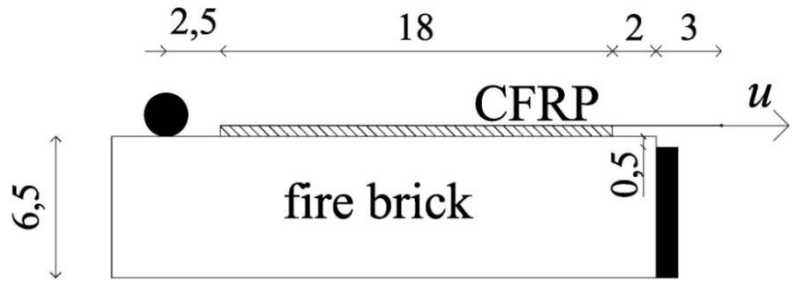

II.1 Boundary conditions; NES single shear test, in black the steel lock. Measures are in [cm].

In the figure *II.1* the boundary conditions chosen for the experimental tests are shown. The shear load is applied on the contrasting planar side of the apparatus; this is placed at 0,5 [cm] from the brick corner. A steel cylinder is positioned close to the "far loaded end" to prevent a rotation of the brick. The load is applied to the unbonded extremity of the composite.

2.2.2 Specimens

In this paragraph the features of the specimens are defined. In the first section properties of the materials used to make the samples are presented (fire bricks, the epoxy primer, the epoxy adhesive and the carbon fabric). Then, the design motivations, the nomenclature and the geometry properties of the specimens are described. Finally, the realization procedure is reported.

2.2.2.1 Materials

2.2.2.1.1 Fire brick

The support of the reinforced system is realized with fire brick (12 x 25 x 6,5 cm^3) produced by *laterizi S. Marco (terreal Italia group)* from the commercial line "*classico*". The value of compressive strength of this material was obtained by means of 24 compression tests over cubes of 5x5x5 cm^3 carried out in Florence. These cubes have been cut out from 6 different fire bricks (*fig.*

II.3 and II.4). Since the production procedure gives the blocks different mechanical properties in each orthogonal orientation, the cubes obtained from the bricks have been tested in directions x,y, z.

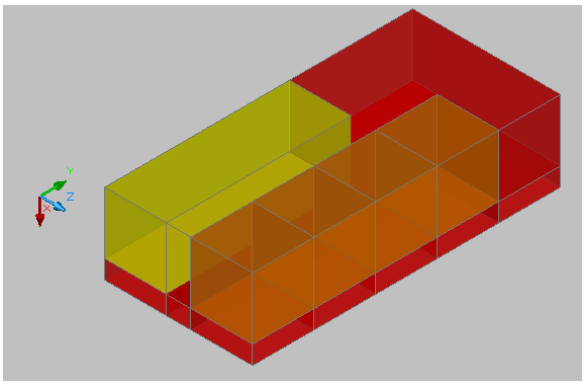

fig. II.3 - The subdivision of the firebrick to generate the cubic samples (compressive tests) and the parallelepiped specimen (Young modulus tests). It's shows also the reference axis.

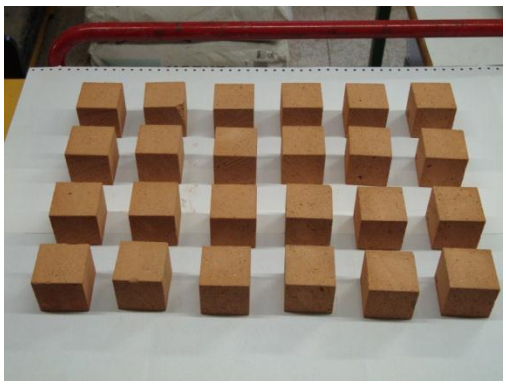

fig. II.4 - The 24 cubes tested in compression

The tests have been made using a compression testing machine characterized by a load cell of 150kN. Each cube has been placed on a steel support and loaded by means of a quadrangular compression plate; a steel sphere is interposed between the latter and the load piston. Four displacement comparators were applied on the superior surface of the compression plate (*fig. II.5*). *Figure II.6* shows the curve displacement-load for the three tests on the fire brick "1" in the directions x, y, z. The displacement in abscissa (fig. *II.6)* is the average of the values read by the four comparators. It is clear that the compression strength of the block is greater in the same direction as the clay input which occurred during the industrial shaping procedure.

fig. II.5 Compressive test on a cube

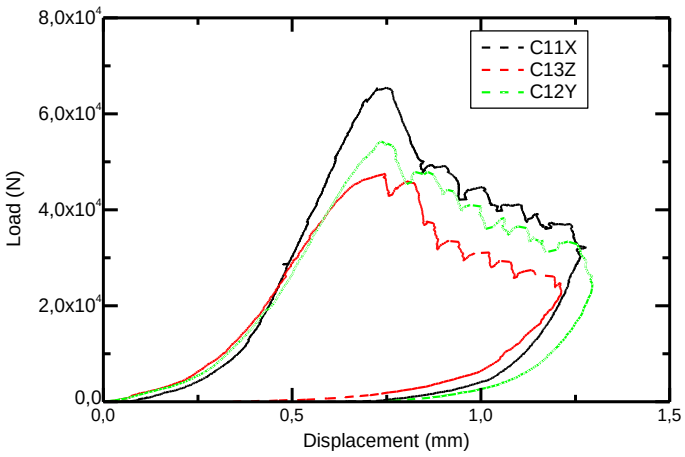

fig II.6 Graphes displacement-load for the compression tests over the firebrick 1

The results are presented in *table 2.IV*; the average value of registered compressive strength is included between 18,22 [MPa] (direction z) and 22,18 [MPa] (direction x).

To obtain the Young Modulus, six compression tests have been carried out over 6 parallelepiped specimens (5x5x15 cm^3) cut out from the same 6 fire bricks cited previously (*fig. II.3*). Four comparators Ω were applied in the center of each lateral surface (5 x 15 cm^2) of the specimens (*fig. II.7*). Reading the variation of the distance between the "foot" of the Ω, originally equal to 5 cm, it was possible to calculate the strain value. The use of Ω comparators permits the strain field farthest from the boundary support to be obtained. Once the strain field and the applied tension for each load step is obtained, the Young modulus is simple to calculate. In the stiffness tests the load is applied using the same procedure presented above for the compression test on cubes. In *figure II.8* are shown the graphics displacement-load for the Young modulus compression tests. The mean value of the stiffness modulus E obtained is equal to 8814,66 [MPa] (*table 2.IV*).

fig. II.7 - Young modulus compression test

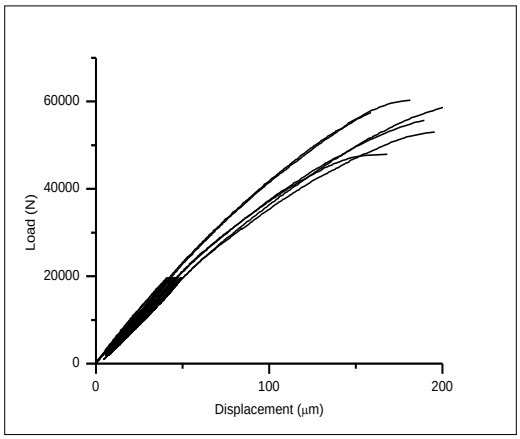

fig II.8 - Graphs displacement-load for the Young modulus compression tests

tab. 2.IV - Compressive strength and Young modulus on a sample of six fire brick "S.Marco"

	load direction	mean value	st. dev.	coefficient of variation
		(MPa)	(MPa)	(%)
Compressive strength	x	22,18	2,00	9,02
	y	19,89	1,02	5,13
	z	18,22	1,35	7,40
Young modulus	y	8814,66	610,06	6,92

2.2.2.1.2 Epoxy resin primer

The epoxy resin primer used to improve adhesion between CFRP and support is named "MBRACE Primer" and is distributed by BASF [31]. This Primer is a two-part epoxy product and it is applied on the support before the adhesive. "MBRACE Primer" is a ready to use product with high adhesive and bond strength. Moreover, it bonds to a damp surface. T*able 2.V* shows the performance data of the product defined by the construction company. In *2.V* is possible to read the properties, 7 days after the primer application in an environment with a T=20°C, of the *bonding to concrete* σ_{BTC} (UNI EN 1542), the *direct tensile strength* σ_+ (ASTM D638), the *tensile modulus of elasticity* E_+ (ASTM D638), the *flexural tensile strength* σ_f (ASTM D790), the *compressive strength* σ_- (ASTM D695) and the *compressive modulus of elasticity* E_- (ASTM D695).

table 2.V - Performance data of "MBRACE primer"

	σ_{BTM} [MPa]	σ_+ [MPa]	E_+ [MPa]	σ_f [MPa]	σ_- [MPa]	E_- [MPa]
MBRACE Primer	> 3,5	> 20	1200	> 35	> 40	1900

The MBRACE Primer is supplied in packaging of ten liters (7,5 l of component A and 2,5 l of component B). The mixing ratio is 3 parts of A with 2 parts of B. The construction company recommended the application of only one layer of primer (environ 150 micron).

2.2.2.1.3 Epoxy resin adhesive

The epoxy resin adhesive used in the specimen construction is named "MBrace Adesivo" and it is distributed by BASF [32]. This saturant is applied over the still tacky Primer to bond the fiber fabric. The "MBrace Adhesive" must be applied below and above the fiber tissue layer to guarantee the distribution of load and the protection of the composite from the environment. The resin adhesive is a two-part epoxy product with 100% solids content. It is a product "ready to use" with high adhesive and bond strength. Moreover, the low viscosity of "MBrace Adhesive" enables the use of a variety of fiber densities (glass, carbon, aramid). *Table 2.VI* shows the performance data of this epoxy adhesive defined by the construction company. The parameters presented in table *2.VI* are the same as that described in the paragraph 2.2.2.1.2 (properties 7 days after the saturant application in an environment with T=20°C).

table 2.VI - Performance data of "MBrace adhesive"

	σ_{BTM} [Mpa]	σ_+ [Mpa]	E_+ [Mpa]	σ_f [Mpa]	σ_- [Mpa]	E_- [Mpa]
MBRACE Adesivo	> 3,5	> 25	3300	> 45	> 80	3100

The "MBRACE adesivo" is supplied in packaging of ten liters (7,5 l of component A and 2,5 l of component B). The mixing ratio is 3 parts of A with 2 parts of B. The construction company recommended the application of one coat of MBrace adhesive on base substrate and one coat on the installed sheet.

2.2.2.1.4 Carbon fabric

The CFRP reinforcement is realized using a carbon unidirectional fabric named "MBRACE fibre CFRP" and distributed by BASF [33]. Fibers have the important role to carry the load acting on the composite. The principal characteristic of the "MBrace fibre CFRP" has been defined by the construction company; in the *table 2.VII* are shown the dry thickness *t*, the Young modulus *E* (ASTM D3039), the strain limit in tension ε_{lim+} (ASTM D3039) and the characteristic tensile strength (ASTM D3039). In this table it is important to underline that the properties are inherent to the dry fabric and not the composite.

table 2.VII - Geometrical and mechanical characteristic of "MBRACE fibre CFRP"

	t [mm]	***E [Mpa]***	ε_{lim+} ***%***	f_{fk} ***[Mpa]***
MBRACE fibre CFRP	*0,165*	*230000*	*> 1%*	*>1500*

The carbon fabric is supplied in rolls of 0,30 x 100 m, and it is easy to cut with scissors or a cutter. The construction company recommended the application of the fiber fabric on the surface while the adhesive is still wet.

2.2.2.2 Design of specimen's geometry

Seventy-two specimen tests have been carried out in the experimental session. The samples are divided in 6 different series; the nomenclature and the geometrical properties of each one is defined in *figure II.10* and in *table 2.VIII*. From the name of each specimen it is possible to understand where the sample has been tested. If the first letter of the name is "T" the specimen was tried in

Paris ("Trou" is the French for hole), instead if the epithet start with a "F" the sample was tested in Firenze ("Foro" is the Italian for hole). The second character of the nomenclature corresponds to the number of anchors applied. The number which follows defines the radius of the anchor in [mm]. The next character of the nomenclature underlines the fan anchor opening; if it's "O" the fan is splayed with an angle of 360°, instead if it is a "V" the fan is splayed with an angle of 75° (*table 2.VIII*). The last number of the specimen's name corresponds to the sample piece of each series. For example: the specimen T1_40_O_5 has been tested in French and it is characterized by: 1 anchor, 40 mm of fan radius and 360° opening fan angle; it is the fifth of the series.

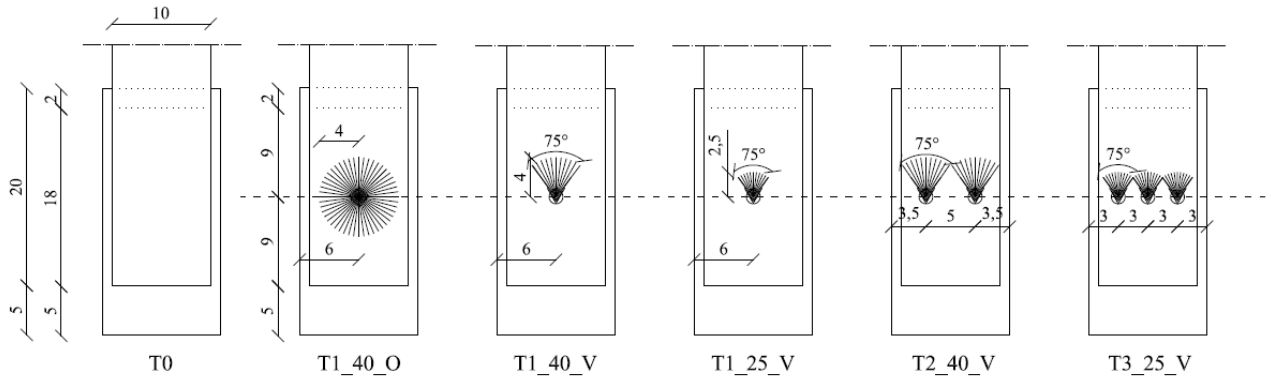

fig II.10 - The six typologies of specimen tested. Measures are in cm.

tab. 2.VIII - Geometrical properties of the samples

number of anchors	fan radius (mm)	fan angle (degree)	specimens name*	number of specimens
1	40	360	T1_40_O_n	6
			F1_40_O_n	6
		75	T1_40_V_n	6
			F1_40_V_n	6
	25		T1_25_V_n	6
			F1_25_V_n	6
2	40		T2_40_V_n	6
			F2_40_V_n	6
3	25		T3_25_V_n	6
			F3_25_V_n	6

The twelve FRP-to-fire brick bonded joints specimen of series F(T)0 are the specimen tests of reference revealing the behavior of the reinforced system without fiber anchors. The CFRP bond length (l) and the composite sheet width (b) chosen for the reference samples are equal for all specimens.

The bond length (l) has been designed to be longer than the optimal bond length defined by the CNR DT200/2004 [1]. This choice was made to analyze the advancement of the crack during the debonding failure [8][15][17][6][5]. Taking into account proprieties of the composite and of the support, the value of l_e using the equation (1.12) has been calculated. The Young modulus of the CFRP (E_p) is equal to the value of the Young modulus of the fabric (E_f) by a reduction coefficient defined by the CNR (α_{fe}=0,9) for the system impregnated in situ. The compressive strength (f_{bm}) of the fire brick is considered equal to the compressive strength in direction x measured during the Florence characterization tests. To obtain the characteristic value of compressive strength $f_{mk,}$ f_{bm} has been multiplied by the reduction coefficient 0,75 [4]. The masonry average tensile strength (f_{mtm}); since unless specific data is available, it has been assumed equal to 0,10f_{mk} [1]. The thickness (t_p) of the composite has been considered equal to 0,17 [mm].

$$l_e = \sqrt{\frac{E_p t_p}{2 f_{mtm}}} = \sqrt{\frac{(0{,}9\times 230000)\times 0{,}17}{2\times(0{,}75\times 22{,}18\times 0{,}10)}} = 102{,}85\ [mm] \qquad (2.1)$$

Therefore the optimal bond length (l_e) is about equal to 10,3 [cm] and the bond length (l) of the specimen has been designed to be longer (18 [cm]).

$$10{,}30\ [cm] = \boldsymbol{l_e} < l = 18\ [cm]$$

The width of the reinforcement was designed equal to 10 [cm] to permit the allocation of one or more anchors. In the Near End Supported side the carbon fabric is not attached to the support for a length of 2 [cm]. This expedient has been adopted to distance the bonded zone from the steel lock and so avoid a premature corner fracture. In the far end supported side, the reinforcement is not present for a 5 [cm] length to permit the contact of the steel cylinder (see the boundary condition defined above) with the fire brick. The geometrical properties of the reference specimens are shown in *figure II.11*.

All remaining specimens are characterized by the presence of anchor (s); to avoid a transversal fracture due to the presence of a nail of 5 cm in depth, a fire brick of 6,5 [cm] in thickness has been used. All the samples with anchors have a support constituted by two bricks glued together (*fig. II.12*).

The specimens of series T1_40_O have been realized to measure the improvement in strength due to one anchor with angle fan of 360° and fan radius of 40 mm (*fig. II.12*). The "nail" is applied in the center of the CFRP bonded surface; it is placed in the terminal part of the optimal bonded

length. The anchor has a section of 1,2 [cm] and it has been inserted into a hole of 1,4 [cm] in diameter and 5 [cm] in depth; the values of anchor section, hole diameter and anchor depth have been maintained constant for all the specimens with fasteners.

The series T(F)1_40_V has been carried out to evaluate the fan angle influence (*fig. II.13*). The specimens of this group have the same features as the T(F)1_40_O except the fan angle of 75°. The comparison between the results of these series has permitted the evaluation of the behavior of the reinforced system when the fibers are splayed in all directions(360° angle fan) and when the fibers are splayed only in the main direction of load (75° angle fan). It is important to underline that in the first case the bonded surface between the sheet and the fan anchor is equal to 48,92 [cm^2] and in the second case it is equal to 10,19 [cm^2].

The series T(F)1_25_V is characterized by a fan radius of 25 mm (*fig. II.14*). The specimens of this group have the fibers splayed only in the load direction with a 75° angle fan. The comparison between the results of series T(F)1_25_V and T(F)1_40_V permits the evaluation of the influence of the fan radius. In this group the bonded surface fan anchor-sheet is equal to 3,81 [cm^2].

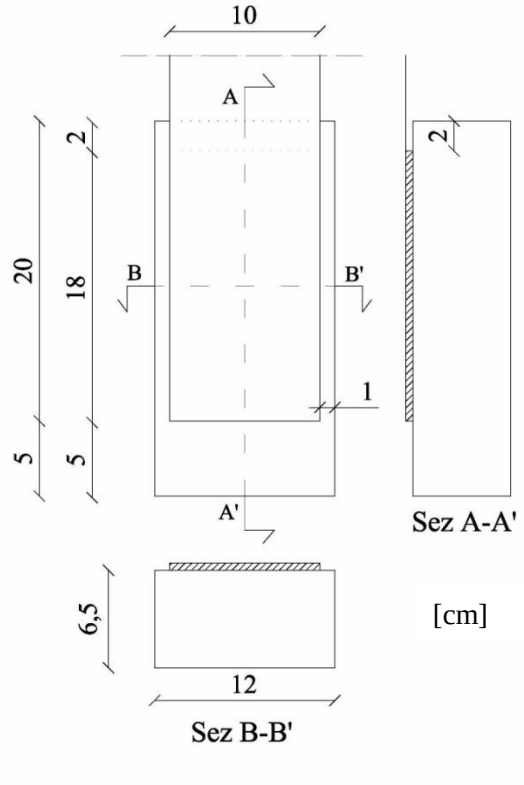

fig. II.11 - Specimen of series T(F)0

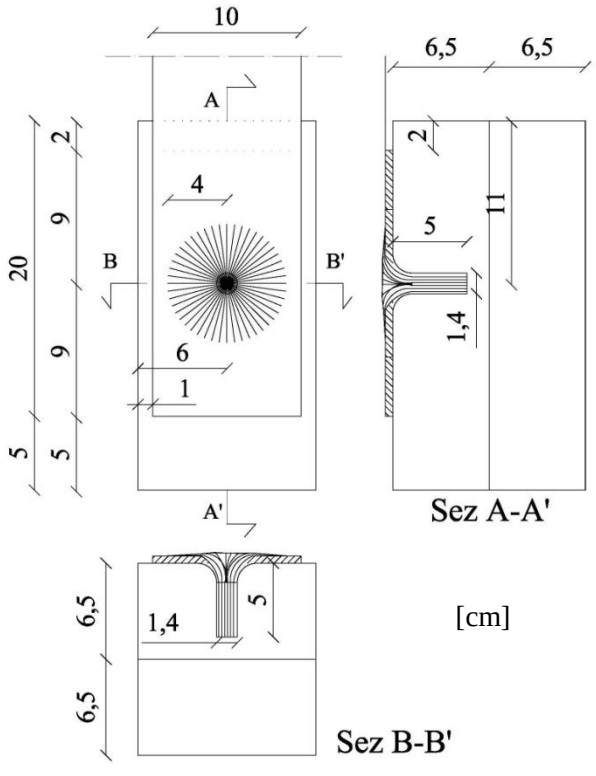

fig. II.12 - Specimen of series T(F)1_40_O

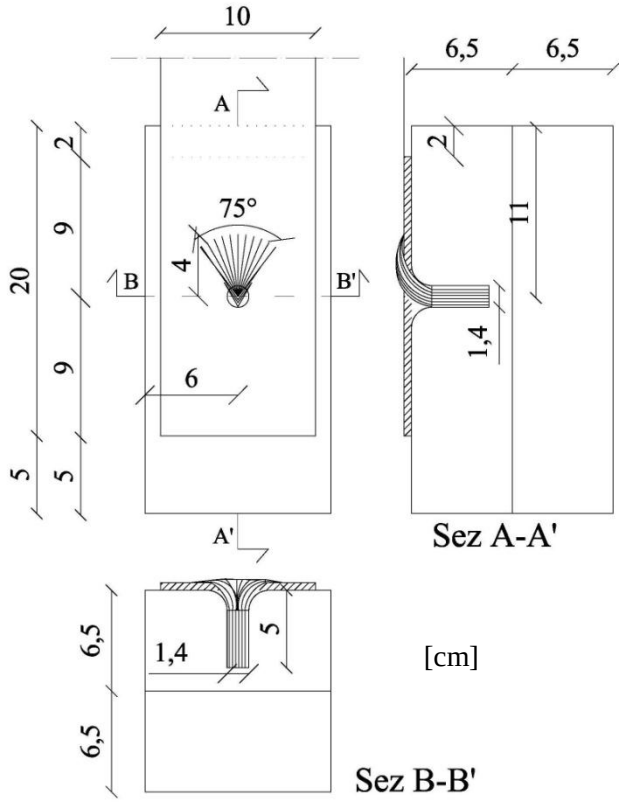

fig. II.13 - Specimen of series T(F)1_40_V

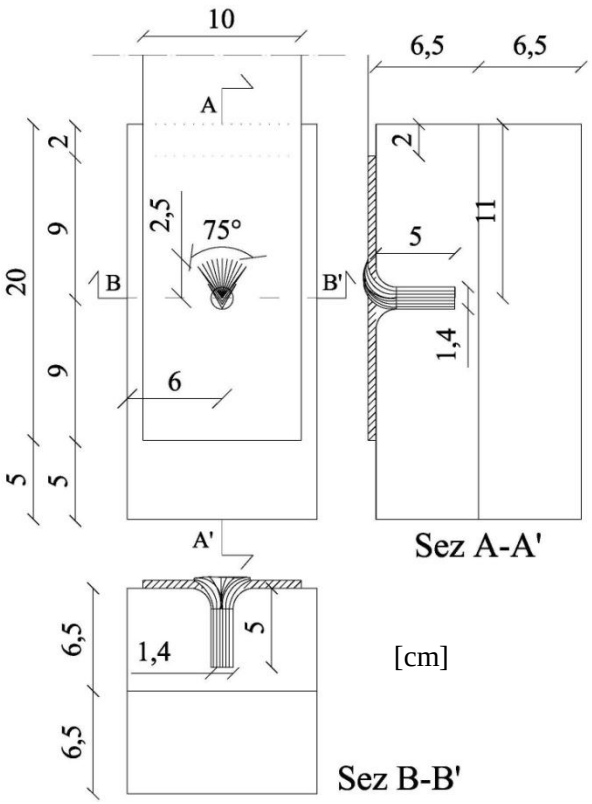

fig. II.14 - Specimen of series T(F)1_25_V

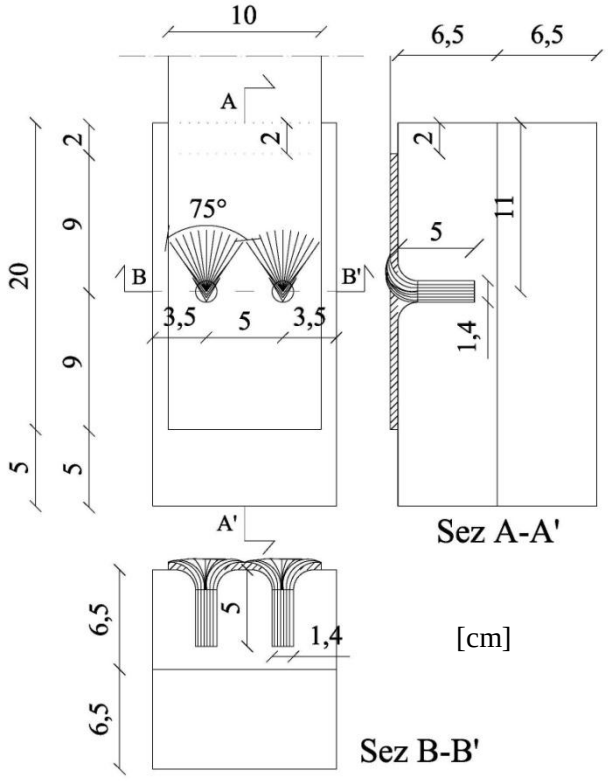

fig. II.15 - Specimen of series T(F)2_40_V

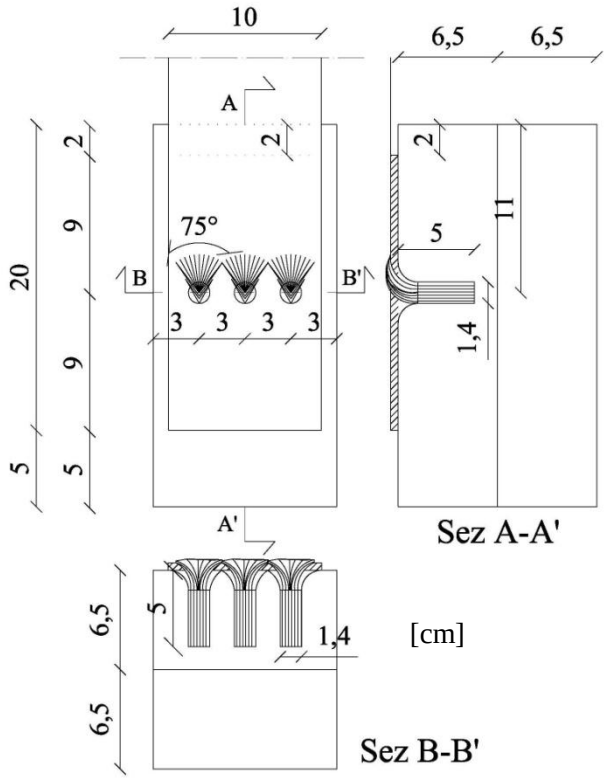

fig. II.16 - Specimen of series T(F)3_25_V

The series T(F)2_40_V has been carried out to study the efficiency of two fiber anchors placed in the same transversal line (*fig. II.15*). The "nails" have a fan radius of 40 mm and an angle fan of 75° with fan fibers directed to the load versus. The bonded area "fan-sheet" is equal to 20,38 [cm^2]. The two anchor fans cover the entire width of the CFRP.

The last series, the T(F)3_40_V, is characterized by three anchors placed in the same line along the width of CFRP. This group of specimens has been tested to measure the influence of the number of anchors. These have a fan radius equal to 25 [mm] and a fan angle equal to 75°. The overall bonded area between fans and sheet is 11,43 [cm^2]. The three anchor fans cover the entire width of the CFRP.

2.2.2.3 Anchor details

The fiber anchors have been made with the best design characteristics defined in the literature in order to measure the maximal improvement of stress capacity of the reinforced system. Therefore, we assume that the behavior of anchors in concrete support is similar to that of anchors in firebrick support and so the anchor typology used in the present experimental session is the one defined by Zhang et al. [28] "*impregnated anchor*". The anchor depth was chosen equal to 5 cm to avoid pull out crisis, since in the Niemitz [27]experimental session a similar anchorage "profundity" was sufficient to avoid the release of the "nail".

The "nail" has been built by rolling a 200 mm strip to prevent the anchor shear crisis [28]. The fan anchor has been limited to less than 90° to limit stress concentration in all series of specimen tests except one. A fan has been chosen with an opening angle of 75° because it covers, with two (r = 40 mm) or three (r=25 mm) anchors placed in parallel, the whole width of FRP sheet. The sharp limit of the anchor hole has been rounded to prevent strain concentration as recommended by ACI440(2002) [29].

Two anchor typologies have been realized; the first is characterized by a fan radius of 40 [mm] and the second by a fan radius of 25 [mm]. Since the anchor depth is equal to 50 [mm], the strips used to make the nails have a dimension of 200x90 mm^2 for the anchor of the first configuration (50+40 mm), and of 200x75 mm^2 for the anchors of the second configuration (50+25mm). The 200 mm width is cut in the direction perpendicular to the fiber orientation (*fig. II.17*).

The realization process of the CFRP anchors is constituted by the following steps [28]:1) cutting the necessary carbon fabric strips (*fig. II.17*); 2) impregnating the epoxy resin in the inferior side of tissue cut (*fig. II.18*); 3) rolling the tissue in the width direction (*fig. II.19*); 4) inserting the dowel in a pre-formed hole (12 mm of diameter) in a polystyrene mould (*fig. II.20*); 5) removing the anchor from the mould after minimum one day (*fig. II.21*).

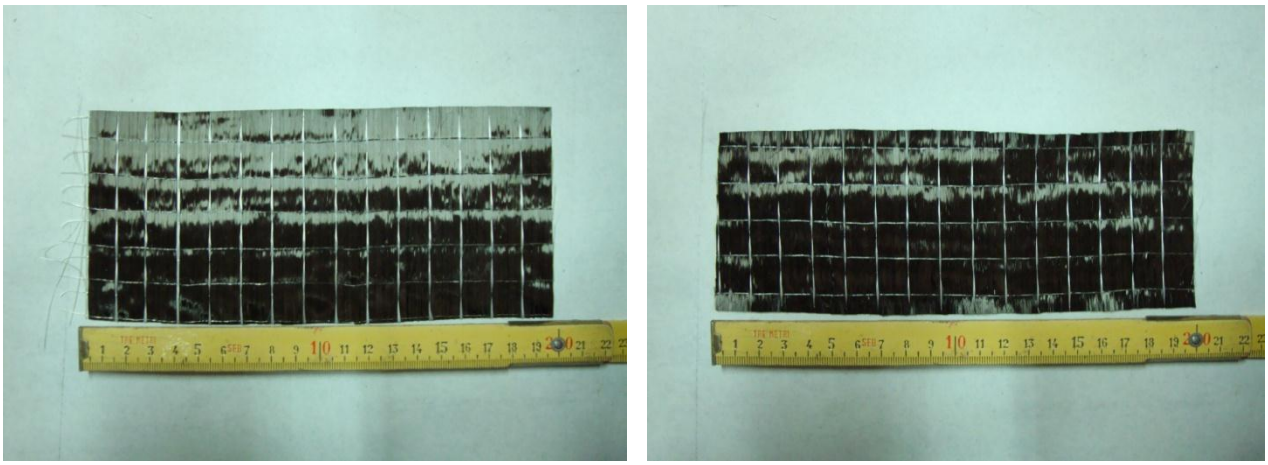

figures II.17 - The 200 mm carbon strips used to realize the two typologies of anchors; 200x90 mm^2 for the first type and 200x75 mm^2 for the second one

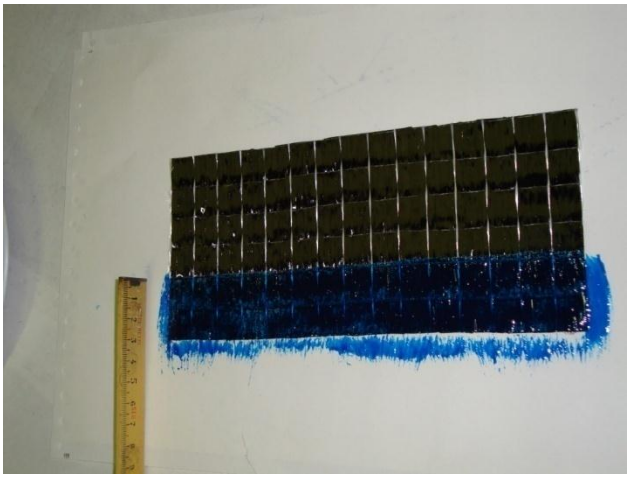

fig. II.18 - Impregnation with epoxy resin of the lower part of the carbon fabric

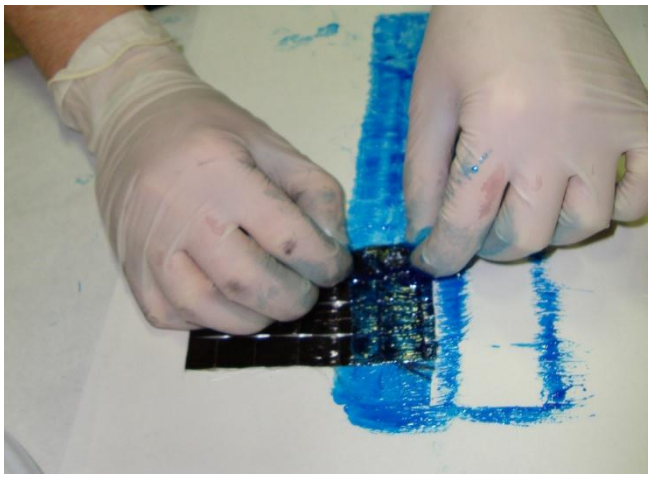

fig. II.19 - The carbon strip during the roll up phase

fig. II.20 - The anchor dowels inserted in the polystyrene mould

fig. II.21 - The impregnated anchor realized; on the right the anchor ready to be insert in the fire brick

2.2.2.4 Specimen construction details

The installation procedure of the FRP-to-firebrick bonded joint reinforced with anchors is defined by the following steps:

- drilling the hole in the fire brick (*fig. II.22*);
- rounding the hole corner to a 13 mm radius;
- bonding a second brick below the holed support (*fig. II.23*);
- cleaning the cavity and the surface of the firebrick (fig. II.24);
- filling the hole with epoxy (*fig. II.25*);
- inserting the anchor (*fig. II.26*);
- applying the primer and the epoxy resin over the surface of firebrick to reinforce (*fig. II.27*);
- laying the sheet on the epoxy resin allowing the passage of the anchor through the unidirectional fibers (*fig. II.28*);
- applying the epoxy resin on the composite sheet (*fig. II.29*);
- splaying the anchor fan over the sheet (*fig. II.30 and II.32*); and
- applying the epoxy resin over the fan anchor (*fig. II.31*).

fig. II.22 - The three typologies of support with anchor holes

fig. II.23 - The support constituted by two glued bricks

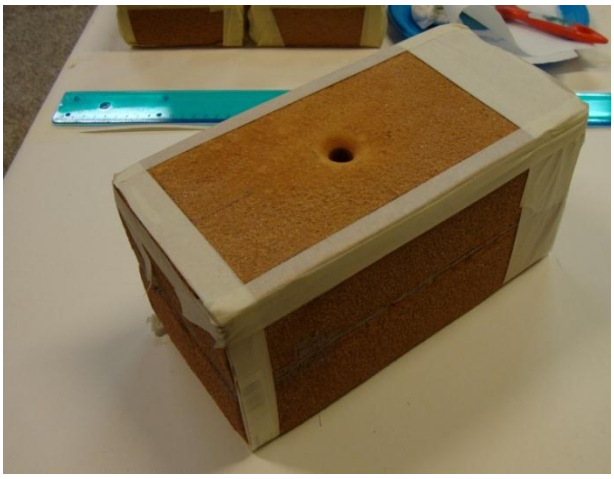

fig. II.24 - The fire brick ready to be reinforced

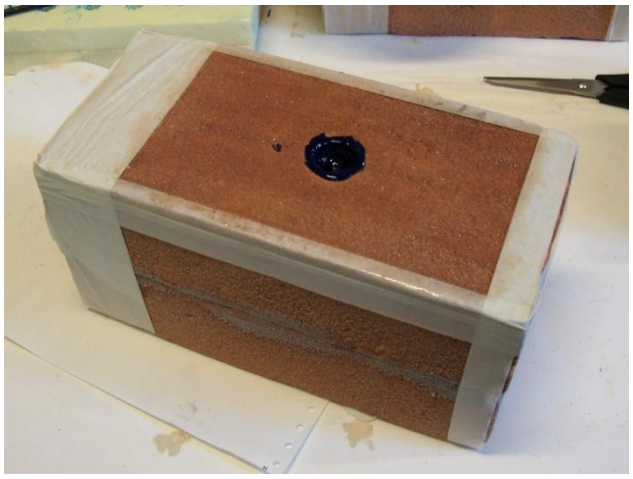

fig II.25 - Hole filled with epoxy resin

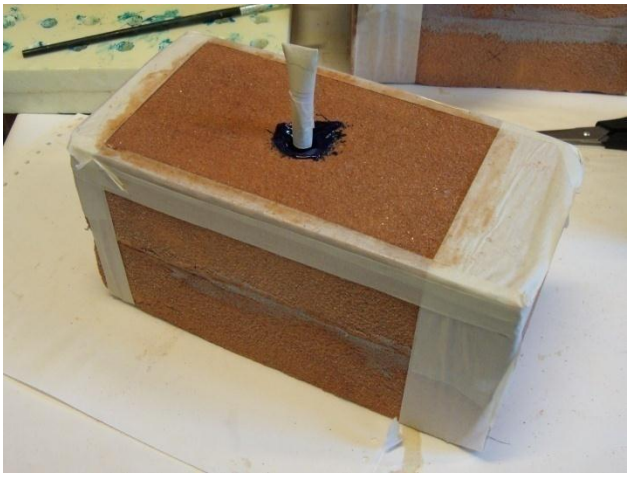

fig. II.26 - A impregnate anchor inserted in a hole support

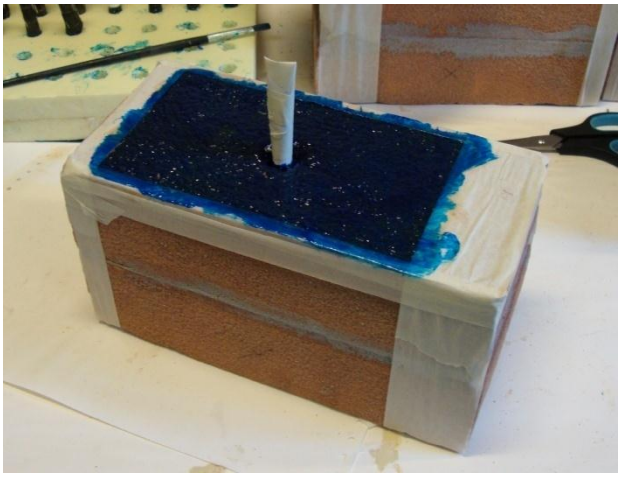

fig. II.27 - Fire brick surface covered by epoxy resin

fig. II.28 - The carbon fabric applied over the first layer of epoxy resin; the anchor pass through the unidirectional fibers

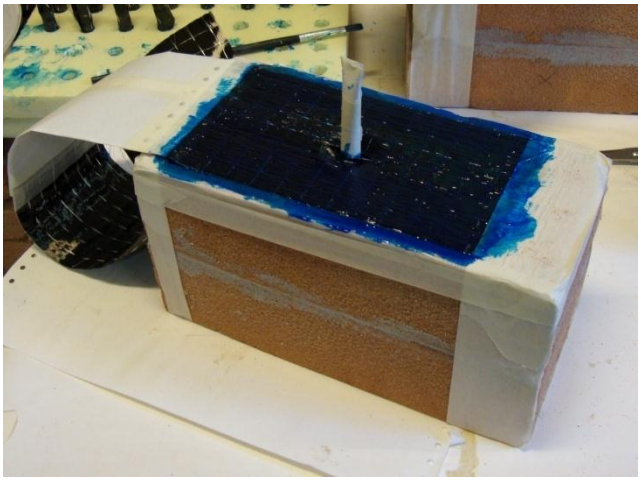

fig. II.29 - The epoxy resin applied on the carbon fabric

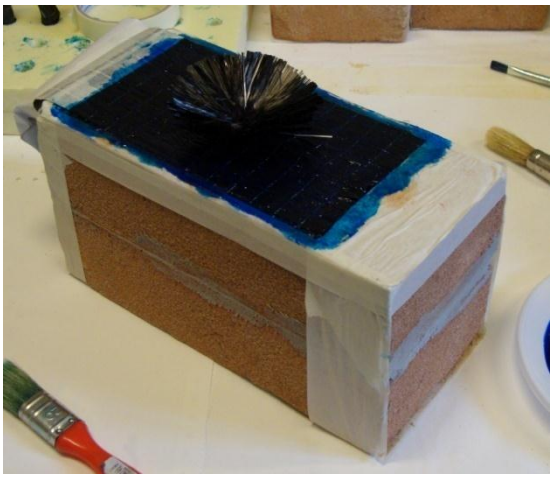

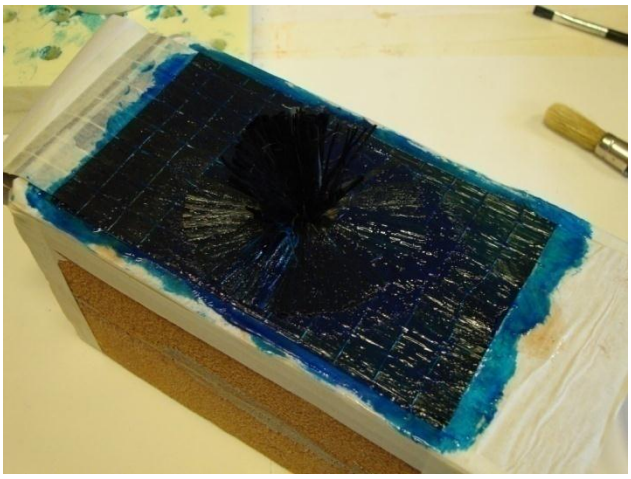

figures II.30 - Two step of the splay procedure of the fan anchor

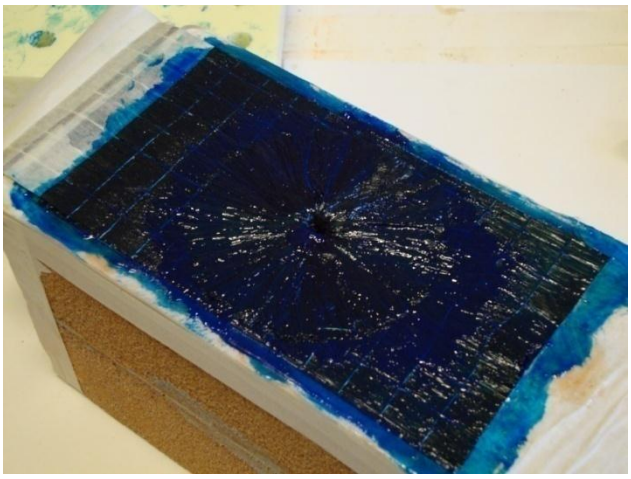

fig. II.31 - Epoxy resin applied on the fan anchor splayed

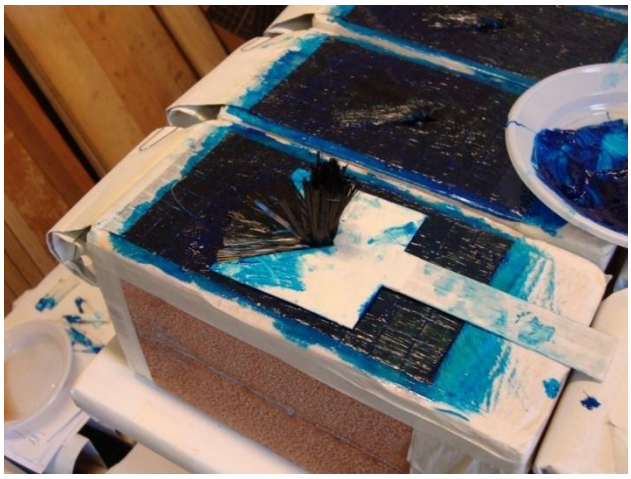

fig. II.32 - The procedure to splay the fan anchor with 75°angle

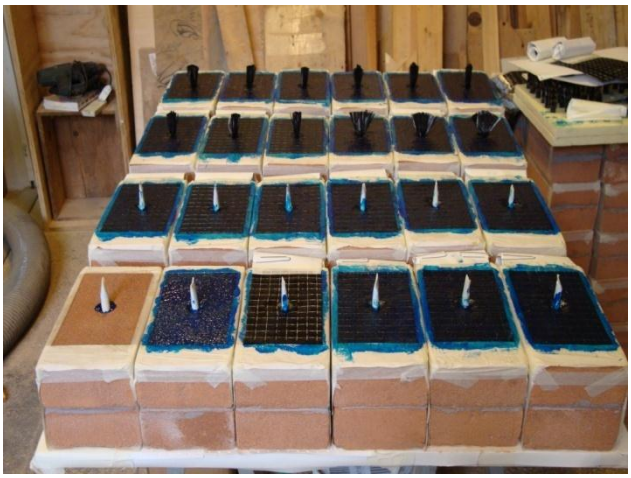

figures. II.33 - The high number of specimens during the preparation procedure

2.2.3 Universal machine

The machine used to apply the load during the tests is the "Universal Machine EM550" produced by DELTALAB (France). It is an electro-mechanical testing machine with a 50[kN] capacity in traction and compression. The EM550 is connected to a PC provided with a specific software "*deltalab*" to control, acquire and analyze data. The universal machine has a support, two columns, a cross-head and a movable traverse (*fig. II.34*). The latter can move up and down among the columns. The load cell is fixed in the center of the inferior traverse surface, defining the load axis. In the support surface six bolt joints are present around and in proximity of the load axis (*fig. II.35*). The column spacing is 42 [cm].

fig. II.34 - The universal machine EM550 DELTALAB

fig. II.35 - Detail of the universal machine (load cell and bolts joints)

2.2.4 Mechanical systems to contrast the brick and to grip the fibers

The boundary conditions of the Near Ended Supported single shear test have been reproduced in France and in Italy with different steel systems. There follows the description of the apparatus realized in Paris. Particularly this steel system has been constructed in the mechanical laboratory of ESIPE in the University Marne-La-Vallée Paris-Est. In the design phases particular attention has been given to construct a simple, versatile and compatible apparatus with the universal machine. The system must be "simple" to make the test procedure easy, accurate and fast. It must be

"versatile" to make future reuse possible in the next experimental sessions (NES single shear test on masonry pillars, 3D DIC).

2.2.4.1 Steel lock

2.2.4.1.1 Design; hypothesis and FEM studies

The apparatus that locks the brick has been constructed in steel. Its design has been influenced by the technical and geometrical properties of the universal machine. In particular, the steel system could be linked to the support only in correspondence with the six bolt joints of *figure II.35*. Moreover, the reinforced face of the specimens must be collocated along the same plane that contains the load axis of the machine.

The steel lock must carry out the follows tasks:

- applying the boundary condition defined in *figure II.1;*
- defining physically the plane where the load is applied; it is necessary to simplify the correct placement of the specimens;
- permitting the insertion of specimens characterized by different size without losing the original alignment of the system; and
- realizing the test sessions on the fire brick and on the masonry pillar supports.

Further it must be sufficiently rigid and not hide the reinforced and the lateral surfaces of the sample so that photos (Digital Image Correlation) can be taken.

A steel plate of 1,5 [cm] thickness, bolted to the universal machine, functions as the base of the apparatus; the other steel elements are fastened to it. The load plane is defined by a metallic cylinder (*fig. II.36*); the extremities of this are built-on two steel supports. The cylinder acts as the linear lock to the rotation of fire brick; to reduce the friction contact it is smooth and able to rotate around its own axis. To ensure the placement of the specimen is correctly aligned, the cylinder should not move throughout the experimental tests; the reinforced face of the specimen must be leaned against it. To reproduce the fixed surface designed in *figure II.1* a steel element, geometrically similar to a Z, is fastened onto the metallic base plate (*fig. II.37*). To permit the insertion of specimens characterized by different sizes, the "Z box" can move back and forth; if necessary it can be removed and replaced.

The length of the cylinder and the width of the Z steel element enables the testing of specimens 25 [cm] wide, 27 [cm] high and 15 [cm] thick. The sessions on fire bricks and masonry pillars can be carried out using the same apparatus.

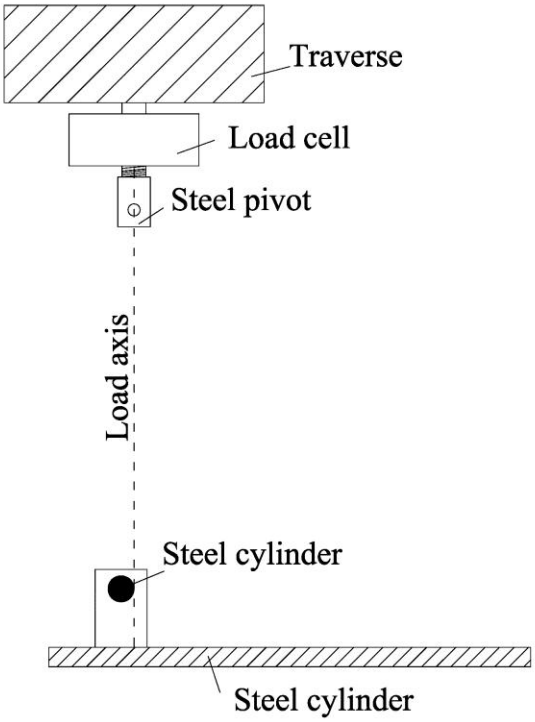

fig II.36 - Cross section design 1; placement of the cylinder

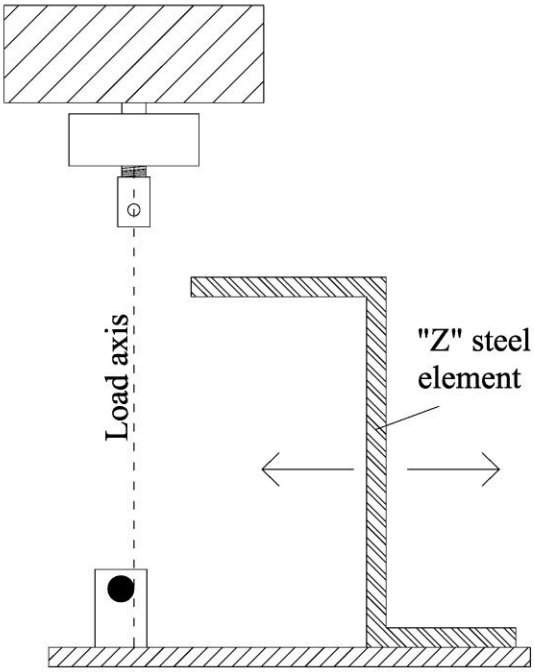

fig II.37 - Cross section design 2; placement of "Z" element

The strength capacity of various "Z box" typologies have been tested using numerical analysis FEM (Finite Element Method). The material used to make up the apparatus is the steel "E24" (S235 of the Europeans norms); the properties of the latter are presented in *table 2.IX* [35][36].

table 2.IX - Mechanical property of the steel "E24" (S235) [35][36]

Property at 20°C	**ρ [kg/m^3]**	**E [Mpa]**	**ν**	**σ_y [Mpa]**	**σ_u [Mpa]**
Steel E24 (S235)	7825	212000	0,28	170-235	340-510

The preliminary numerical study (case 1) concerned the simple configuration of lock "Z" reproduced in the geometrical cross-section of *figure II.38* and in the 3D representation of *figure II.39*.

In the case 1 the 3D mesh (*fig. II.39*) of the steel element is characterized by the following properties:

- It is subdivided in 22862 tetrahedrons
- The function shape of the elements is quadratic (9 nodes on each tetrahedron)

The mechanical properties of the solid are assigned equal to those of steel E24 (*table 2.IX*).

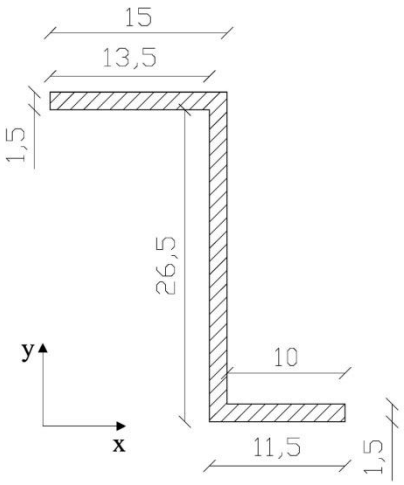

fig II.38 - Cross section of "Z" steel element and referential axis in case 1

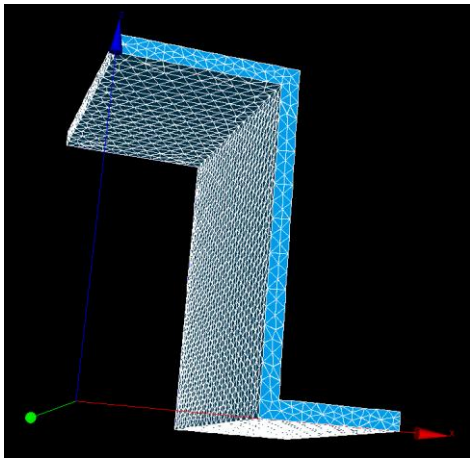

fig. II.39 - 3D mesh of case 1

The boundary conditions that characterize the case 1 are described as follows:

- A surface load L_s [MPa] is applied in the plane "A" on the direction y (*fig. II.40*). The stress L_s is equal to the maximum capacity of the Universal machine (50kN) divided by the surface of application (135 x 250 mm^2).

$$L_s = \frac{50000}{135 \times 250} = \frac{50000}{33750} = 1{,}48\ [MPa]$$

- The displacements of the surface "B" (*fig.II.41*) are blocked.

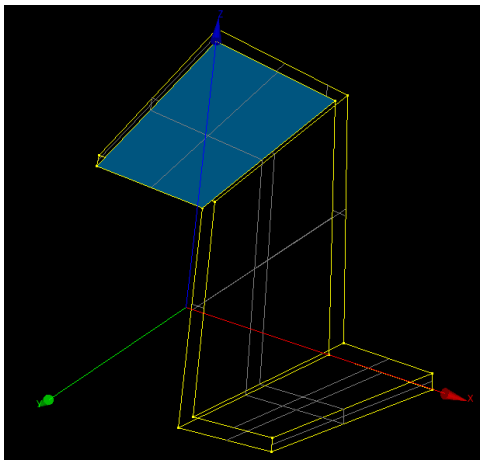

fig. II.40 - The surface of load "A"

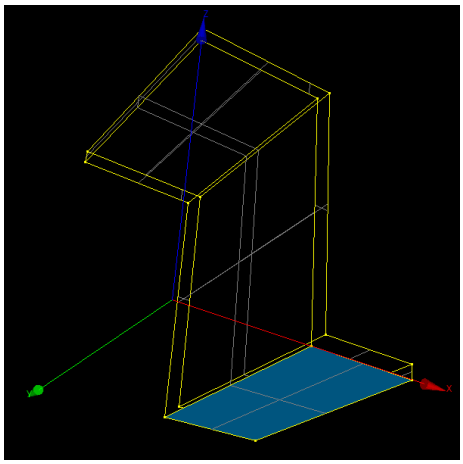

fig. II.41 - The bonded surface "B"

Calculus have been made using Code_Aster where the material is assumed to exhibit an elastic behavior. The figure of the deformed shape (*fig. II.42*) and the images relative to the Van Mises stresses σ_{id} (*fig.II.43*) have been obtained by means of *Salome-Meca*. The maximum stress value considered admissible in this design study is the yield stress of steel E24 multiplied for a reduction coefficient equal to 0,9.

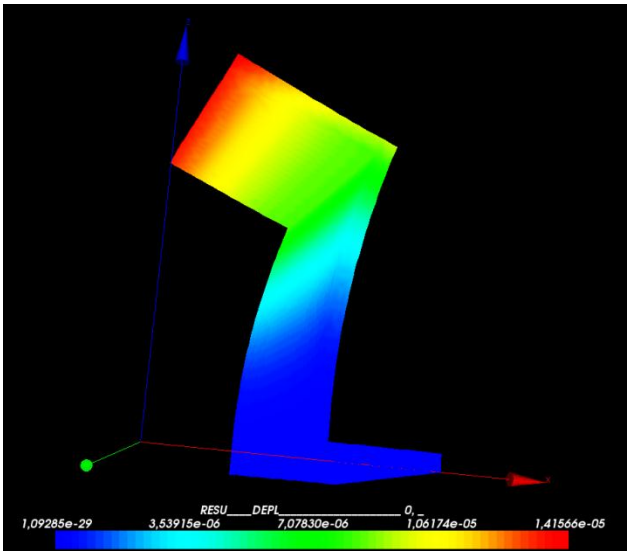

fig. II.42 - The deformed shape of case 1

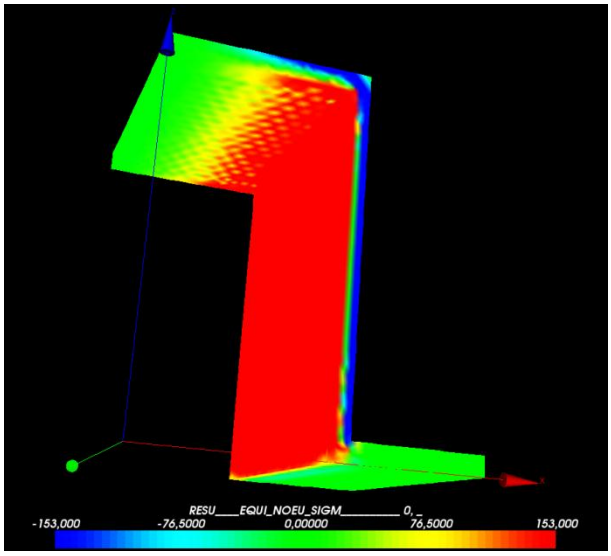

fig.II.43 - The Van Mises Stress; in dark red the zone where $\sigma_{id} > \sigma_{amm}$ and in dark blue the zone where $\sigma_{id} < -\sigma_{amm}$

$$\sigma_{amm} = \sigma_{yE24} \times 0{,}9 = 170 \times 0{,}9 = 153\ [MPa]$$

In the *image II.43* zones in red are the areas where $\sigma_{id} > \sigma_{amm}$ and in blue areas where $\sigma_{id} < -\sigma_{amm}$. It is evident that the system proposed in "*case 1*" requires reinforcement.

The second step of the design process consists in fastening both the lateral sides of the Z element with two steel plates. These have been projected not to hide the lateral views of the specimen during the test. Moreover, the steel reinforcement plates are not linked to the "fixed" side of the base but only to the Z "removable" element. The efficiency of this steel apparatus, case 2 (*fig. II.44*), has been tested with a numerical analysis. The 3D mesh realized for this purpose is reproduced in *figure II.45*. The mesh is constituted by:

- 83332 tetrahedrons
- The function shape of the elements is quadratic (9 nodes each tetrahedron)

In this test mechanical properties of the materials and the boundary conditions are equal to that assigned in "case 1". Therefore, a load L_s of 1,48 [MPa] has been applied in the direction y in the surface A (*fig. II.46*) and the surface B (*fig. II.47*) has been blocked by imposing DX=DY=DZ=0. The behavior of the material has been supposed to be elastic (att. B).

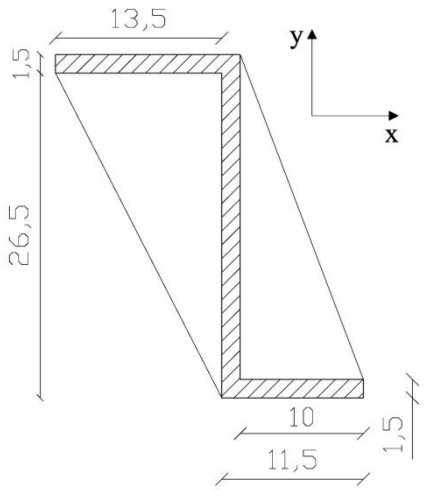

fig. II.44 - Cross-section of the steel element in "case 2"

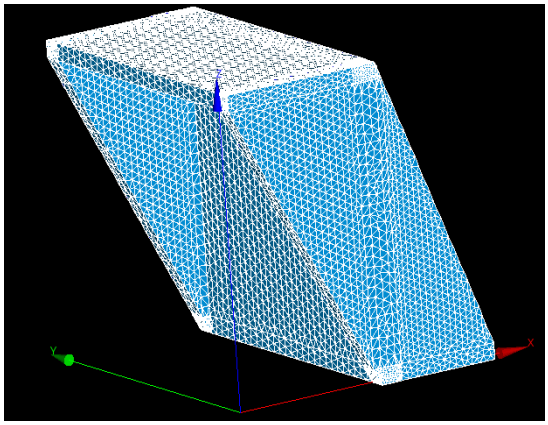

fig. II.45 - 3D mesh of the steel element in "case 2"

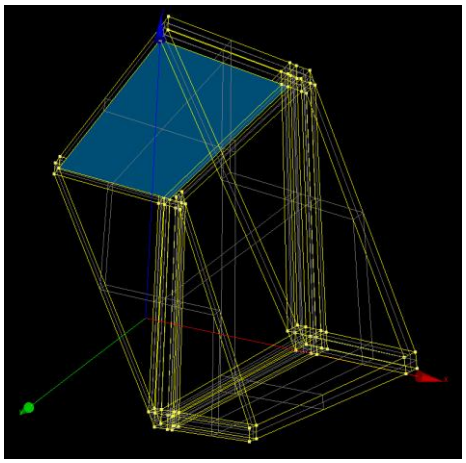

fig. II.46 - The surface A in case 2

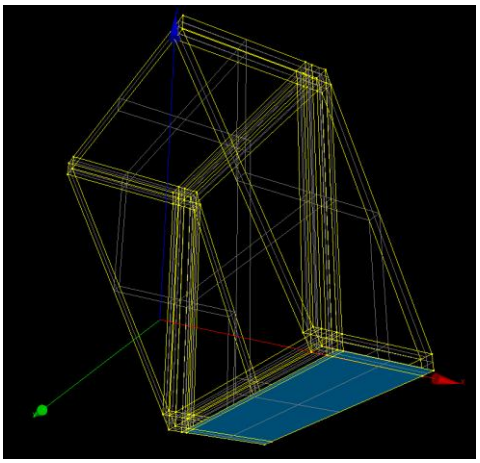

fig. II.47 - The surface B in case 2

The deformed shape (*fig. II.48*) and the Van Mises stress distribution (*fig. II.49*) are shown herein (global result sheet).

Results are sufficient to demonstrate that under the conditions of case 2 the block element Z, reinforced with the steel lateral plates, preserves its elastic behavior. Indeed, in *fig. II.49* there are not zones with $\sigma_{id} > \sigma_{amm}$ (dark red zones) and with $\sigma_{id} < -\sigma_{amm}$ (dark blue zones). However, the

steel block apparatus has been designed to be used for more typologies of specimen sizes and the numerical studies presented above reproduce only the cases when the contact surface between the specimen and the steel element is equal to the "surface A" (*fig. II.40* and *II.46*). To understand if the steel machine is stiff enough to resist the worst load conditions, another case has been studied (*case 3)* where the maximum load (50 kN) has been applied in direction y on the border of the steel apparatus (*fig. II.50*) for a line 120 [mm] length; this case reproduces the extreme contingency when the sample is a fire brick (surface of contact 120x65 [mm^2]) characterized by imperfections that lead to a linear contact.

$$L_l = linear\ load = \frac{50000}{120} = 416{,}67\ \left[\frac{N}{mm}\right]$$

The Cross section, the 3D mesh, the material properties and the bonded surface B of the case 3 are the same as those of case 2 (fig. *II.44, II.45, II.47*). The deformed shape (*fig. II.51*) and the Van Mises stress distribution (*fig. II.52*) of case 3 has been obtained considering an elastic behavior of the "Z box".

Figure *II.52* shows that the σ_{amm} is surpassed by the σ_{id} in the top zone of the steel contrast plate and in the internal sides of the lateral steel reinforces (zones in dark red). In the same image, the dark blue zones underline the surpassing of the negative admissible strength ($-\sigma_{amm}$).

To avoid the steel yielding in this critical zone a further steel plate 1,5 [cm] thick has been fastened onto the superior extremity of the "*Z box*" (*fig. II.53*). This configuration of steel apparatus with the boundary condition of case 3 has been tested in case 4. The 3D mesh is formed by 55719 tetrahedrons characterized by a quadratic function shape.

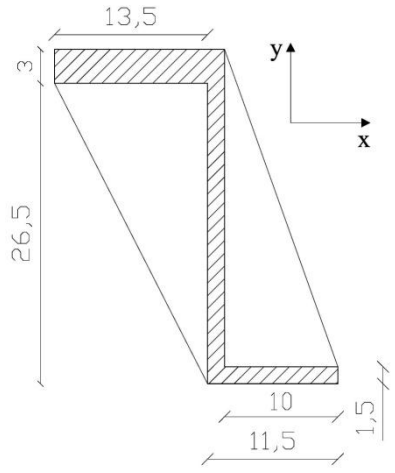

II.53 - Cross-over section of case 4

The material properties (E, v) and the boundary condition (L_l , bonded surface B) of the case 4 are the same as those of case 3. The deformed shape and the Van Mises stress distribution of case 4 are presented in figures *II.55* and *II.56*.

The image of the σ_{id} distribution shows that the geometry of the Z steel contrast analyzed in case 4 is sufficiently rigid to avoid the yielding of the metal material. In the external upper central part of the steel apparatus and the internal upper sides of the lateral reinforces the values of σ_{id} (Van Mises criterion) are close but do not exceed the σ_{amm}.

The numerical analysis has confimed that the steel apparatus configuration of case 4 is the most appropriate to reproduce the boundary condition of fig. *fig. II.1*.

Finally, the steel apparatus designed is made up of:

- a support steel plate bolted on the universal machine;
- a steel smooth cylinder linked to support plate; and
- a steel element (with a "Z" shape) bolted on the support plate. It has the same geometrical property as the configuration reproduced in case 4 (*fig. II.53*).

[mm] ***Deformed Shape*** ***/*** ***Van Mises Stress Distribution*** ***[MPa]***

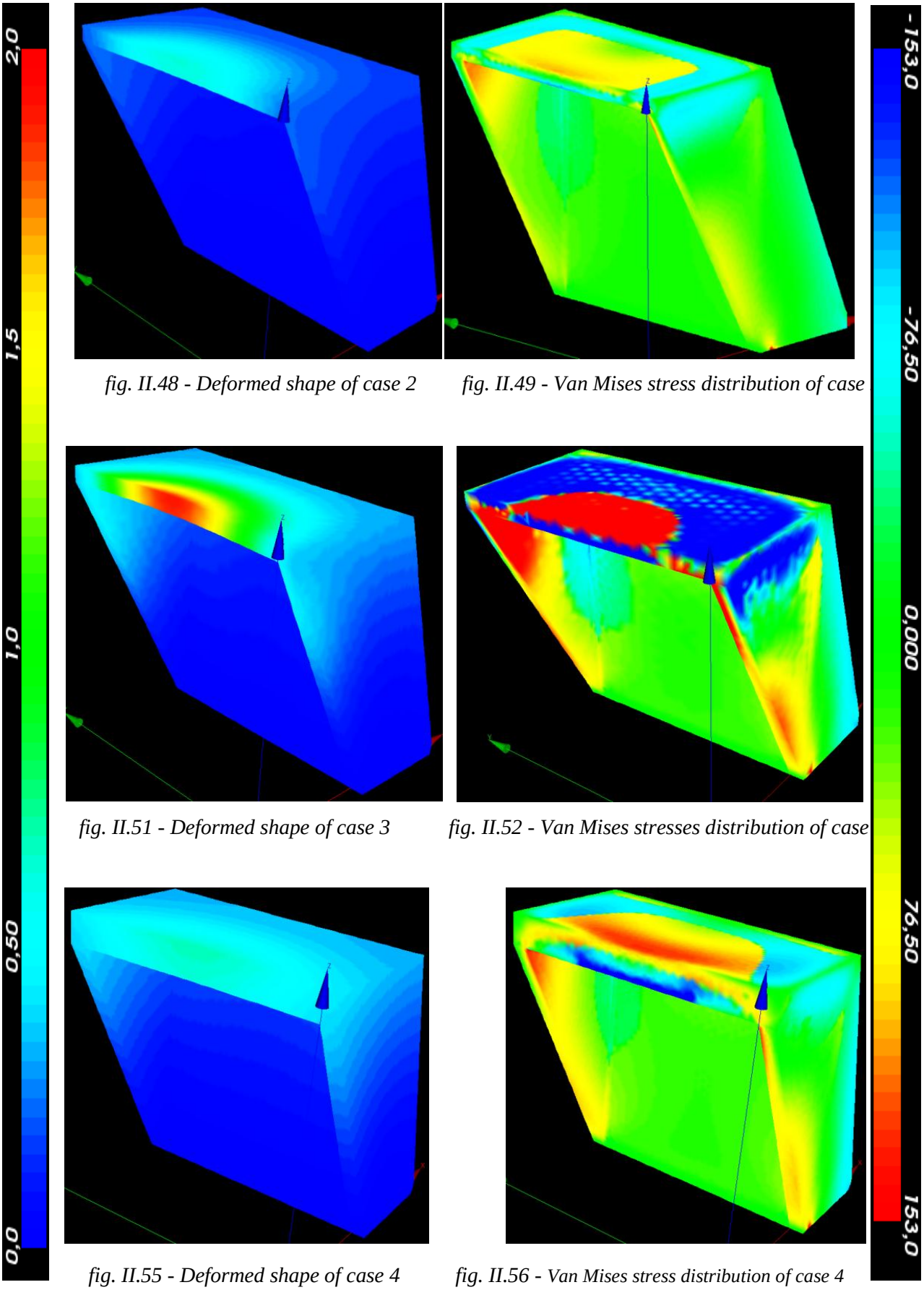

fig. II.48 - Deformed shape of case 2

fig. II.49 - Van Mises stress distribution of case

fig. II.51 - Deformed shape of case 3

fig. II.52 - Van Mises stresses distribution of case

fig. II.55 - Deformed shape of case 4

fig. II.56 - Van Mises stress distribution of case 4

2.2.4.1.2 - Realization process

To put the design described in the previous paragraph into practice, several devices were adopted. The apparatus is assembled in 10 different pieces. All the pieces are connected by bolt steel joints. The bolts used are made in steel A2 with a diameter of 8 [mm] and 10 [mm] (*table 2.X*).

The cylinder is made in steel and it is built inside two steel supports (*fig. II.58*). These are fastened to the steel plate and they could be displaced by unscrewing the bolt joints. Thus, also the cases with a offset in the load axis position [6] can be studied in the future.

The steel Z element is fastened onto the support plate; two linear openings in the base of the "Z box" function as "rails" to displace the movable apparatus back and forth (*fig. II.59*). To fix the steel Z element it is simply necessary to tighten the bolts that cross the support and the openings (*fig. II.60*).

The upper plate, 3 cm thick, has been realized by overlapping two 1,5 [cm] plates, both fastened to the lateral steel reinforcements (*fig. II.1*). These last have been realized in an industrial factory (*fig. II.61*).

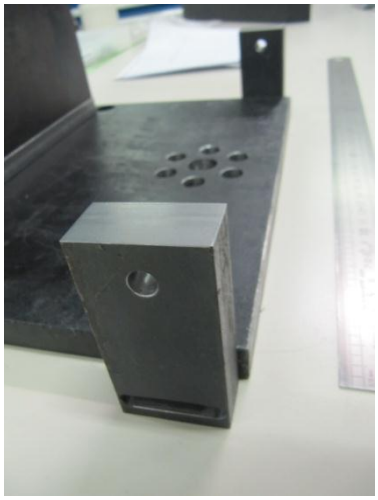

fig. II.58 - The smooth steel cylinder built in the steel apparatus

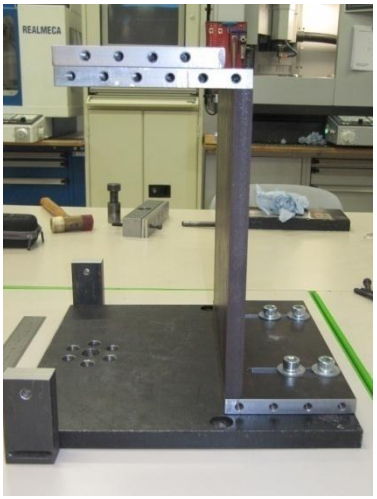

fig. II.59 - The linear openings ("rails") present in the base of the Z element

fig. II.60 - The bolt joints between the steel apparatus and the Z box.

fig. II.61- The two 1,5 [cm] plates overlapped

figures II.62 - The lateral reinforcements of the "Z box"

2.2.4.1.3 - Stiffness test

The stiffness of the steel apparatus has been measured during a laboratory test that reproduces an experimental load history. The load has been applied to the steel contrast using the upper surface of laboratory tongs (fig. *II.63*); thus the test can be carried out without having to make other pieces. The surface of the charge is equal to 40x110 mm^2 and it is geometrically similar to the lower surface of the fire brick specimen. The load has been applied by increasing the charge of 1 kN at each step, for ten steps.

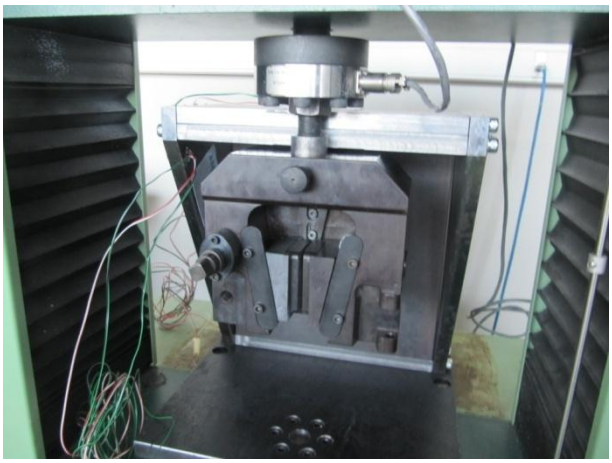

fig. II.63 - Boundary conditions of the stiffness test

Two strain gauge rosettes have been used to measure the strain in the more loaded zones of the apparatus; the location and the direction of the strain gouges have been defined using the numerical analysis (red zone in *fig. II.56*). More specifically, the rosettes are bonded onto the contrast steel plate (strain gauges 1) and onto the internal side of the lateral steel reinforcement (strain gauges 2) (*fig. II.64*).

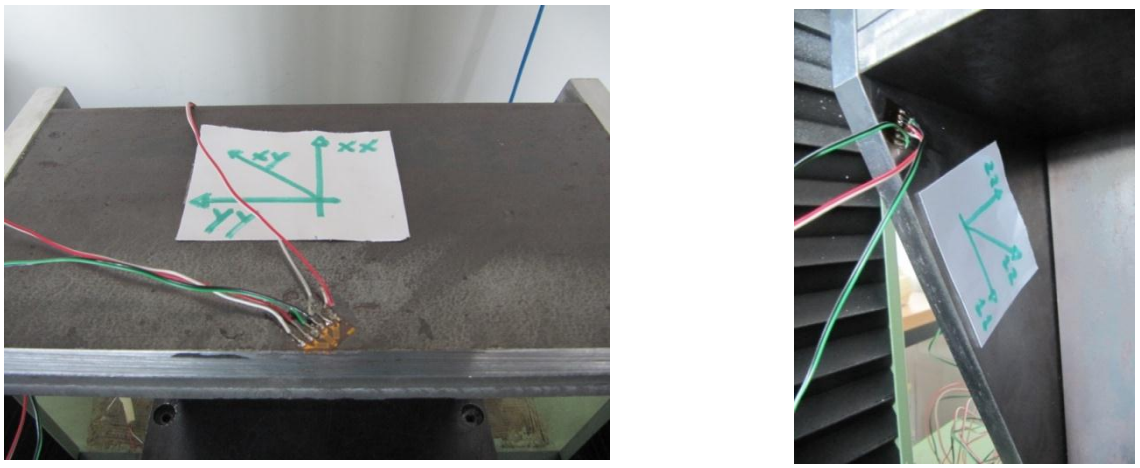

fig. II.64 - The strain gauge rosettes applied on the critical points of the apparatus. In the images are framed on the left the gauges 1 and on the right the gauges 2. Moreover the name of the axis is shown

From each rosette the value e_x, e_y and e_{xy} it has been obtained. To obtain the strains the following equations have been used.

$$\varepsilon_{xx} = e_x \,, \quad \varepsilon_{yy} = e_y \,, \quad \varepsilon_{xy} = e_{xy} - \frac{1}{2}\left(e_{xx} + e_{yy}\right) \tag{2.2}$$

The value of ε_{zz} is obtained using the Lamé coefficients (μ,λ):

$$\varepsilon_{zz} = -\frac{\mu}{2\mu+\lambda}\left(\varepsilon_{xx} + \varepsilon_{yy}\right) \tag{2.3}$$

Once the strain values are known, the tensor of stress could be obtained using the following constitutive equations [38]:

$$\sigma_{xx} = \lambda\left(\varepsilon_{xx} + \varepsilon_{yy} + \varepsilon_{zz}\right) + 2\mu\varepsilon_{xx} \tag{2.4}$$
$$\sigma_{yy} = \lambda\left(\varepsilon_{xx} + \varepsilon_{yy} + \varepsilon_{zz}\right) + 2\mu\varepsilon_{yy}$$
$$\sigma_{yx} = \lambda\left(\varepsilon_{xx} + \varepsilon_{yy} + \varepsilon_{zz}\right) + 2\mu\varepsilon_{yx}$$
$$\sigma_{zz} = \sigma_{zx} = \sigma_{zy} = 0$$

The value of σ_{zz} is equal to zero because the strain gauges is bonded upon an uncharged surface. Using the tensor stress components it is possible to calculate the Van Mises Stresses (σ_{id}).
The Van Mises stress σ_{id}, obtained for 10 kN load, has been multiplied by 5 and compared with the σ_{amm} to verify that the admissible stress of the apparatus is not reached even when the universal machine applies its maximum load (50kN).
The strain and the stresses values obtained in the stiffness test are shown in the *tables 2.XI* and *2.XII*.

table 2.XI - The strain and stress values calculated using the strain gauges 1

	[MPa]	*[MPa]*	*[MPa]*	*[MPa]*
L [kN]	σ_{yy}	σ_{yx}	σ_{xx}	σ_{id}
1	*0,04*	*0,02*	*0,00*	***0,06***
2	*0,08*	*0,05*	*-0,01*	***0,12***
3	*0,12*	*0,08*	*-0,02*	***0,19***
4	*0,16*	*0,11*	*-0,02*	***0,25***
5	*0,20*	*0,14*	*-0,03*	***0,32***
6	*0,25*	*0,16*	*-0,04*	***0,39***
7	*0,28*	*0,19*	*-0,05*	***0,45***
8	*0,32*	*0,21*	*-0,06*	***0,51***
9	*0,36*	*0,23*	*-0,06*	***0,57***
10	*0,40*	*0,26*	*-0,07*	***0,63***

table 2.XII - The strain and stress values calculated using the strain gauges 2

	[MPa]	[MPa]	[MPa]	[MPa]
L [kN]	σ_{yy}	σ_{yx}	σ_{xx}	σ_{id}
1	0,23	0,10	-0,10	**0,34**
2	0,56	0,20	-0,15	**0,74**
3	0,89	0,34	-0,20	**1,17**
4	1,21	0,45	-0,28	**1,58**
5	1,54	0,56	-0,33	**1,98**
6	1,89	0,68	-0,39	**2,42**
7	2,22	0,81	-0,47	**2,85**
8	2,55	0,90	-0,52	**3,24**
9	2,88	1,02	-0,54	**3,65**
10	3,18	1,10	-0,63	**4,02**

The graphics Load-σ_{id} presented herein (*fig. II.65*) underline that the stresses increase linearly with the applied load. The stresses measured by the strain gauges 1 at L=10 [kN] are almost ten times smaller than those of strain gauges 2. Moreover, the σ_{id} at 50 kN obtained in the two analyzed points are much smaller than the σ_{amm}.

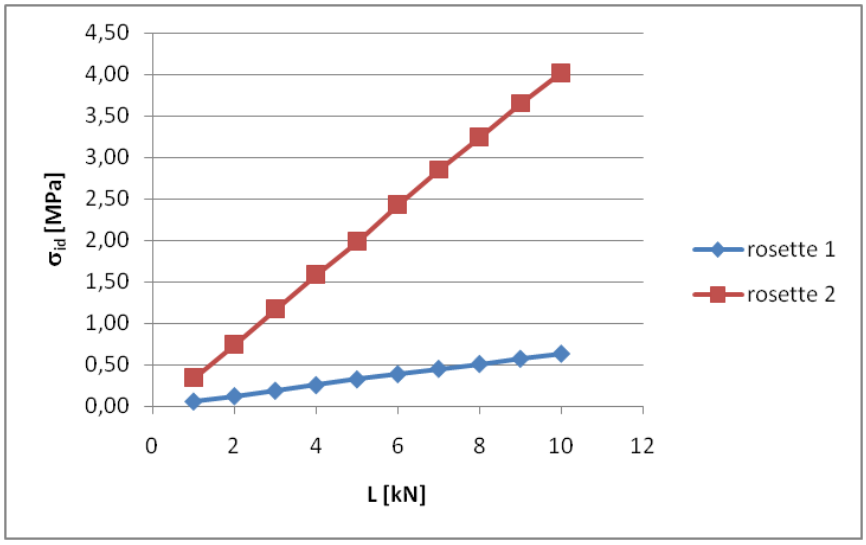

fig. II.65 - The graphic L - σ_{id} (Load – Van Mises stress) obtained in the point 1and 2

The stress values calculated by means of the stiffness test have the same sign as those of numerical analysis (case 4) but a different order of magnitude. These results are probably due to:

- The apparatus is made up of many steel pieces joined by bolts. The numerical study has been made considering a monolithic element in steel;

- In the numerical case 4, the load is applied in the extreme border of the steel contrast; in the stiffness test the charge is distributed over a surface;
- The boundary conditions supposed in the numerical study are not totally identical to the real condition. Moreover, the universal machine does not give a rigid support under the surface B; and
- The strain gauges rosette 1 is bonded onto the upper side of the two contrast plates 1,5 [cm] thick. This should be emphasized because the load is applied to the lower plate and the two steel elements are only overlapped and fastened to the lateral reinforcements.

2.2.4.2 The steel tongs

A steel system has been designed to pick up the carbon fabric and to apply the load to the specimens. Some considerations have been taken into account for the project:

- The carbon tissue is constituted by unidirectional fibers difficult to grip;
- The fabric free extremity of each specimen must be assembled in the 'grab' system before the test and removed after the experiment; and
- The roughness on the surface of brick could cause an imperfect alignment between the surface of CFRP and the grabbing carbon fabric. This distortion may cause a peeling stress concentration.

Therefore, the mechanical apparatus must carry out the following tasks:

- Grabbing the carbon fabric so as to avoid any slipping;
- Connecting the load cell to the carbon fabric;
- Placing the carbon fabric the same plane as the "load axis";
- Simplifying and accelerating the experimental phases of assembly and disassembly; and
- Permitting a rotation of the grab system around the load axis to reduce the peeling stress concentration.

The solution adopted to grab the fibers is binding the carbon fabric around a steel plate and connecting it to the load cell using two metallic jaws.

The steel plate used to bond the fibers is not a simple parallelepiped (fig. *II.67*), it has an external perimeter of 110x90 [mm] and a thickness of 5 [mm]. A slot of 5x10 [mm^2] is present on its biggest surface. Moreover, in one side of the plate a groove of 5x10 [mm^2] by 1 [mm] in thickness has been realized. One perimeter border of the plate, and one side of the slot have been rounded. The steel

plate just described is named "@" because the fiber fabric rounding the metallic element generates a shape similar to the symbol @.

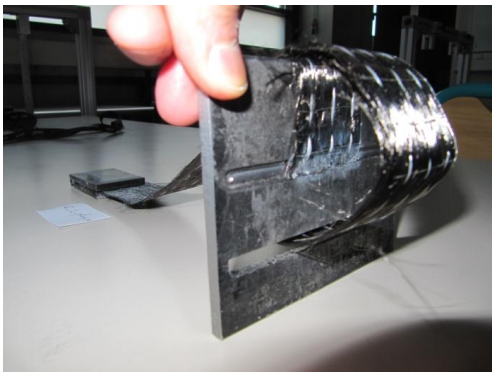

fig. II.67 - The steel plate @

The @ plate is blocked by two movable jaws in steel. These are bolted symmetrically to two metallic elements placed in the center longitudinal plane of the apparatus and connected to a horizontal steel parallelepiped (*fig. II.68 and II.69*). This is directly fastened to the load cell by a steel pivot. This cylindrical element is free to turn around its own axis.

The mechanical apparatus described above has two planes of symmetry, longitudinal and transversal, that intersect a point crossed by the load axis. The carbon fabric is collocated in the longitudinal plane.

The use of the @ plate helps to place the carbon tissue in the correct plane easily and quickly. All the adhesive procedures act only on the movables plates but not upon the steel apparatus. So, the device enables the grab mechanism to be assembled with simple actions. Thus, the realization of 4 @ plates enables the preparation of more specimens at the same time. The rotational degree of freedom of the load pivot has been provided to reduce the peeling stress concentration.

fig. II.68 - The horizontal piece realized to join the jaws to the pivot of the universal machine

fig. II.69 - The steel tongs disassembled

The grab system is composed by 16 steel pieces. All the joints of the apparatus have been made with bolts.

2.2.4.3 Test machine; a global view

The test machine consists of two parts realized using an assemblage of steel pieces;

- a lock system
- a grab system

The *figure II.71* shows a frontal and a lateral view of the mechanical system achieved to reproduce Near End Single shear tests (*fig. II.1*).

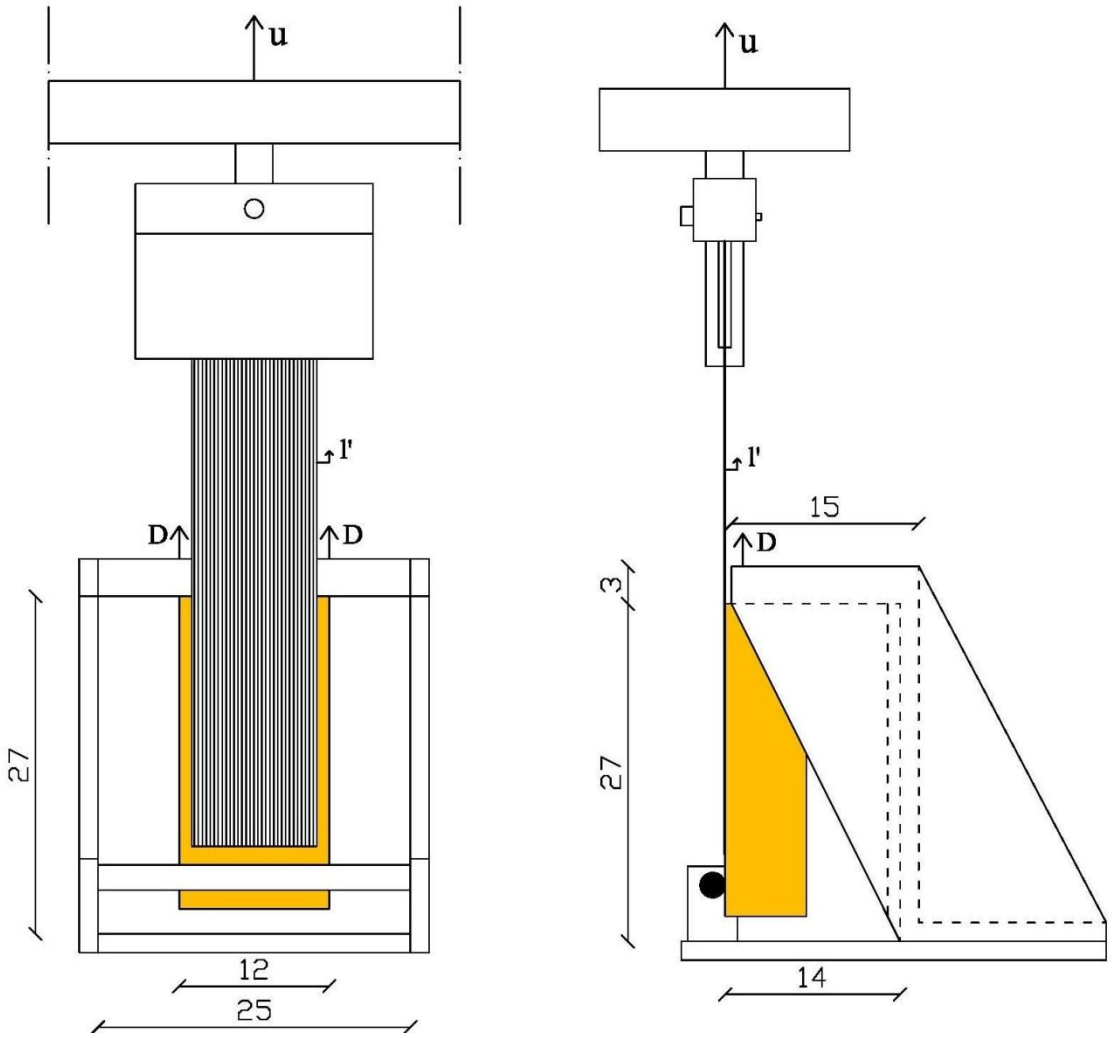

fig. II.71 - Frontal and lateral view of the mechanical system realized (measures in [cm])

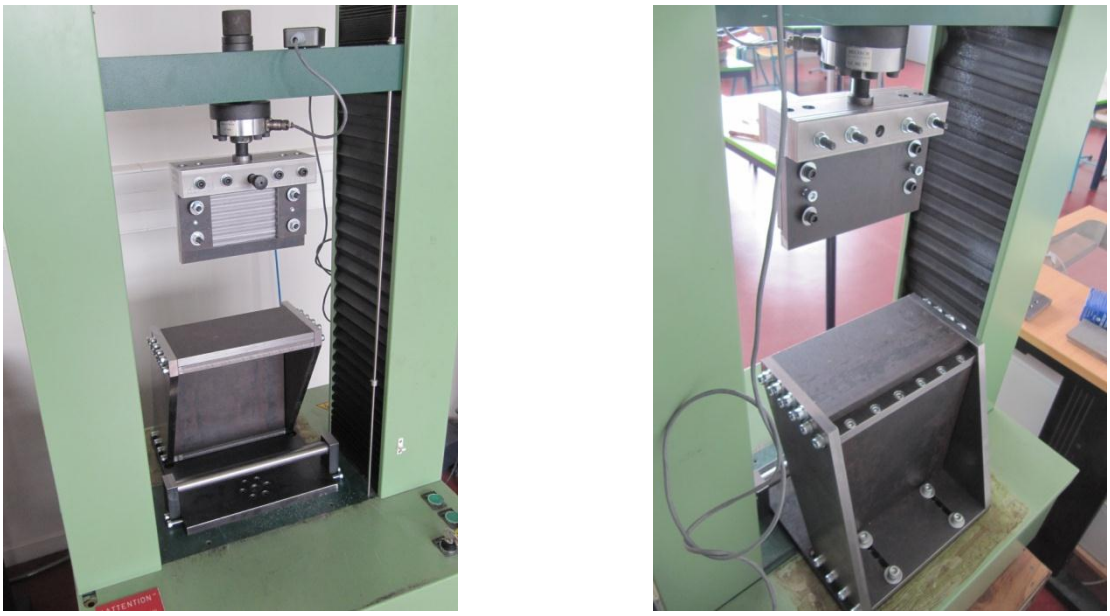

fig. II.72 - The steel apparatus assembled in the universal machine

2.2.5 Specimen installation

The specimen is placed in the suitable position, ready to be tested, using a standard procedure. The phases and the devices used during the preparation and placement of the samples are described in the following.

In the first step of preparation, the dry extremity of the fiber fabric is rolled and bonded around the steel plate @. It is important to underline that the specimens have been made with a longer carbon fabric (around 75 cm); only 18 cm of this last are bonded to the fire brick (CFRP). This is important because the rolling process around the plate "@" requires a long strip. Indeed, the free extremity of the carbon fabric was passed through the slot of the plate, turned around the perimeter blunt border of @ and bonded inside the groove on the steel surface by a quick-setting glue (phase 1 of *fig.II.73*). After the fixation of the carbon fiber extremity, an epoxy resin is applied on the surface of the plate and the fabric is stretched and placed on the support. This process occurs while rounding and bonding the fibers on the plate and on the fabric itself (*fig.II.73*). Once the gluing phases are finished the specimen connected with "its" plate is left in a particular position to allow the drying of the adhesive and ensure a perfect overlap of the fabric on the steel support. Specifically, a simple device has been conceived to block the plate without touching the wet surface of adhesive; the fire brick was placed on a table, the plate was laid on the lateral corner of the table blocked and stretched by a belt (*fig. II.74*). All the specimens were tested a minimum twenty four hours after the gluing of the tissue on the steel plate @. The epoxy resin used in this step is named "Sikadur 300" and it is a 2-component impregnation resin produced by Sika [37].

When the specimen is bonded to the plate @, it is ready to be placed inside the steel apparatus. As mentioned previously, in this experimental session specimens of two sizes have been tested: the first typology has dimensions 250x120x65 [mm^3] (single fire-brick) and the second one has dimensions 250x120x130 [mm^3] (two fire-brick bonded together). The specimens of small size (series T0) have been inserted in the steel apparatus without any displacement of the "Z" steel element. In this case, to place the movable lock at the correct distance from the cylinder (140 mm) a template of 140x200x100 [mm^3] has been utilized (*fig. II.75*). Then, the specimen was inserted in the space between the cylinder and the Z box.

To insert the specimens of big size it was necessary to unscrew 3 of the 4 bolts that fasten the Z lock with the support steel plate and displace the box as shown in *figure II.76*. After placing the sample the lock is reassembled, the distance of 140 [mm] between the Z and the cylinder is ensured by the use of two templates of 70x140x40 [mm^3] (*fig. II.77*).

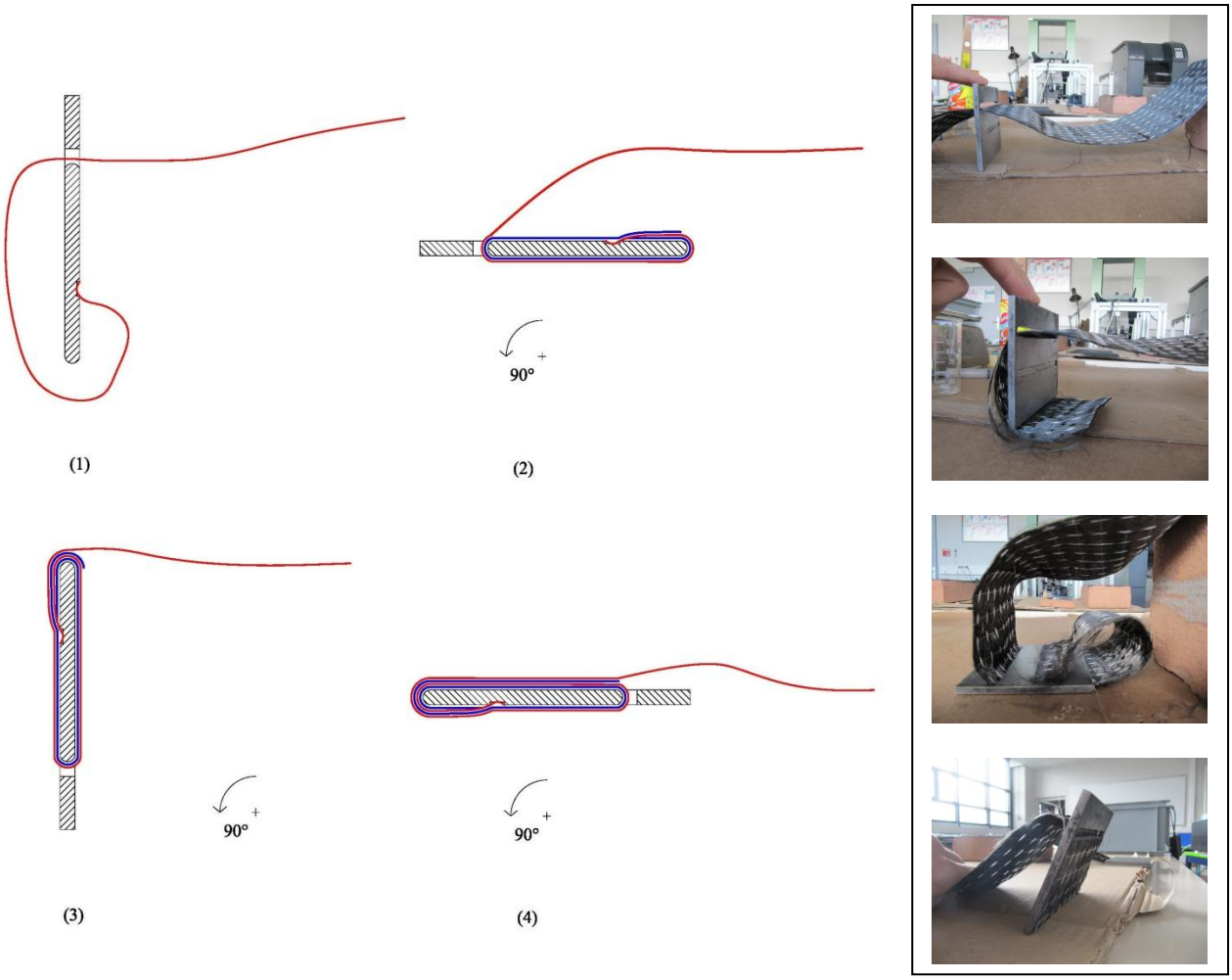

fig. II.73 - The fiber carbon to steel plate @ bonded phase; in red the fiber fabric and in blue the adhesive layer. On the right some photos of the procedure.

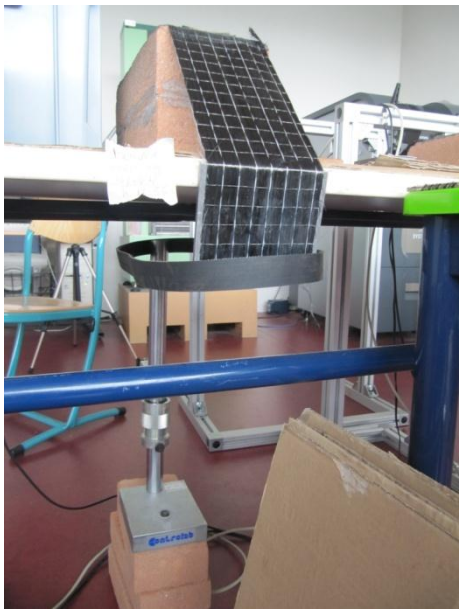

fig. II.74 - The device to stretch the fibers and block the plate without touch the adhesive

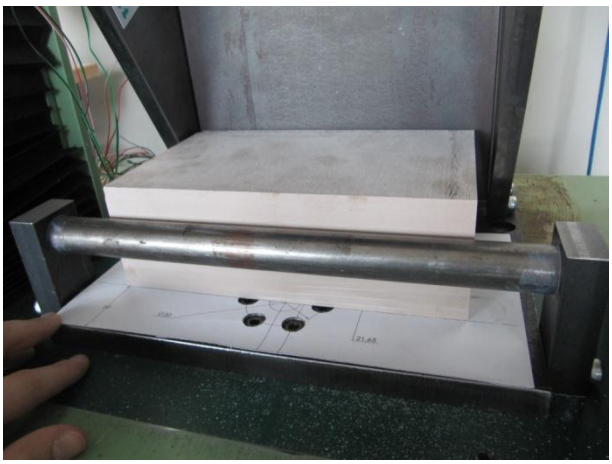

fig. II.75 - The alignment of the Z box with the template of 140x200x100 (cases T0)

fig. II.76 - The alignment procedure of the Z box during the insertion of big size specimens

It's important to underline that the internal face of the cylinder is in perfect alignment with the load plane (*fig. II.75*); to simplify the correct placing of this element a design 1:1 with the trace of the load plane is bonded on the surface of the steel support plate. The cylinder has been aligned to the trace before the start of the experimental session; its position has been maintained throughout the tests.

After the insertion of the specimen between the locks, the reinforced face of the fire brick was propped on the central part of the steel cylinder (*fig.II.77*).

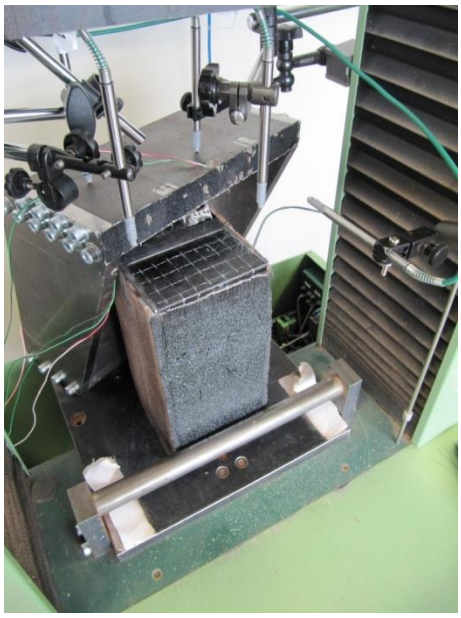

figures II.77 - The insertion of the specimen inside the steel apparatus (photo on the left) and the reassembling of the Z steel lock using the two templates 70x140x40)

The installation of the steel plate @ inside the grab system is the next phase of the procedure. To allocate the element @ inside the grab, one jaw is disassembled (*fig. II.78*); the other creates a cavity where the plate is to be placed (*fig. II.79*). After the collocation of the steel plate the grab system is reassembled (*fig. II.80*).

During the last phase of the specimen placement, the traverse of the universal machine is raised and, consequently, the grab system picks up the carbon fabric. When the sample touches the horizontal steel contrast the displacement of the traverse is stopped. Particular attention has been paid to place the specimen in the correct position, with a distance between the fibers and the lock border of 5 [mm] (*fig. II.81*). An image of the specimen placed in the test apparatus is shown in *figure II.82*.

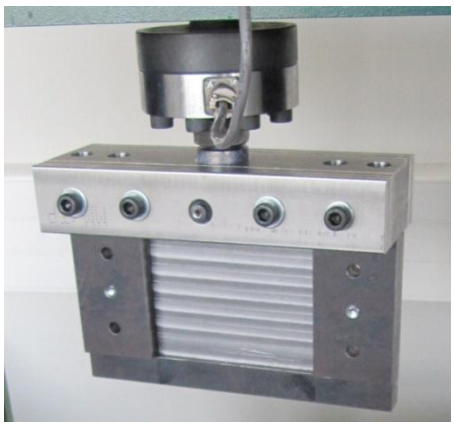

fig. II.78 - The configuration of the grab system disassembled

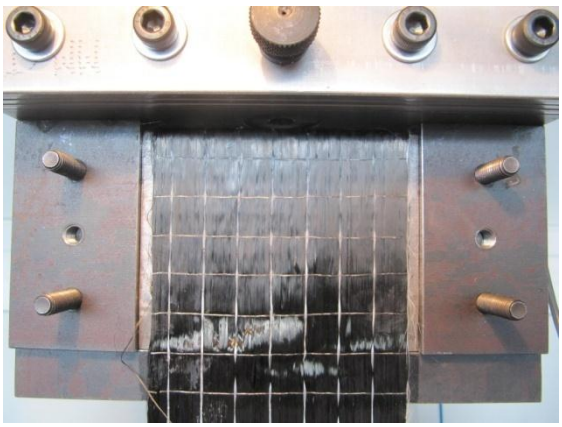

fig. II.79 - The steel plate @ inserted in the jaws cavity

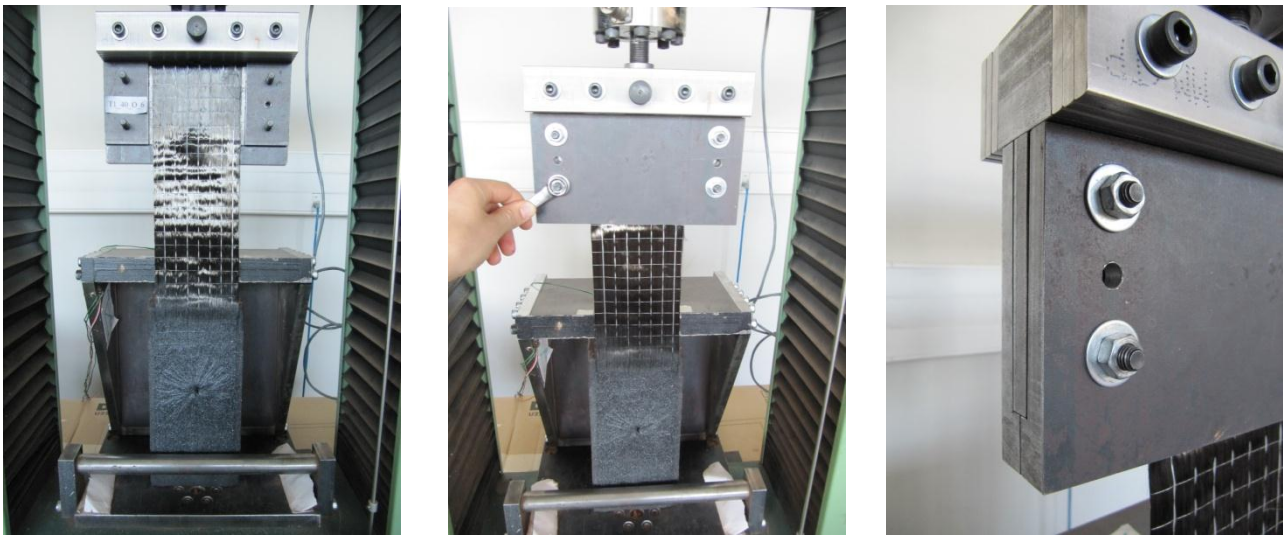

Figures II.80 - The steel grab reassembling and the @ plate clamping; three steps of the procedure

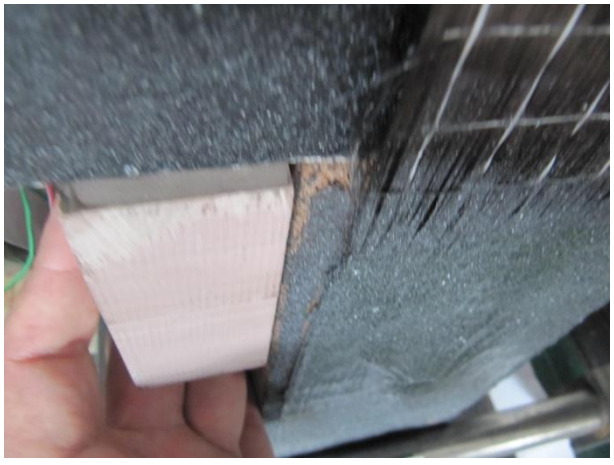

fig. II.81 - The template used to verify the 5[mm] distance between the fiber and the border of apparatus

fig. II.82 - The specimen placed in the apparatus of test

2.2.6 Test procedure; instrumentation and load history

The instrumentation placed on the universal machine consists of a load cell of 50 kN and a displacement transducer. The former quantifies the load applied to the system, the second measures the displacement of the traverse.

A set of comparators is placed over the upper surface of the steel lock Z to evaluate the displacement related to the stiffness of the metallic system (*fig. II.83*).

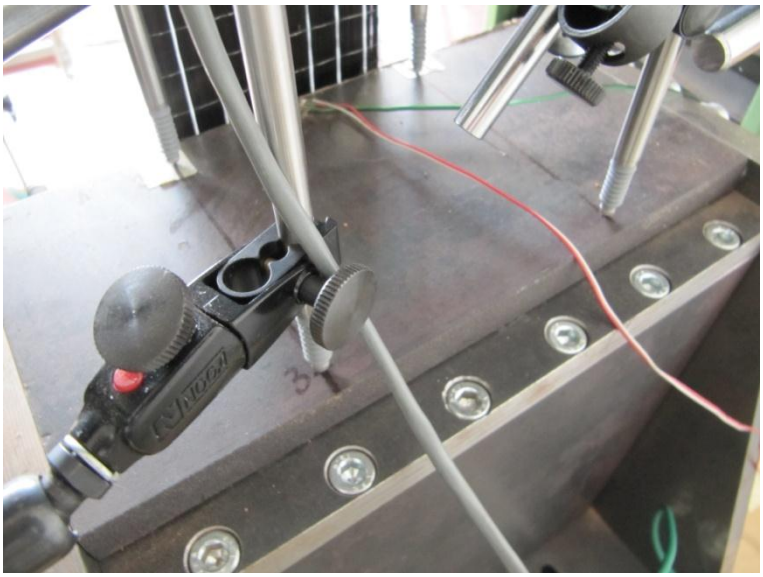

fig. II.83 - The comparators displaced on the steel contrast

A digital photo camera is positioned in front of the reinforced face of the specimen, at environ 1,20 [m], to take the necessary pictures to calculate the displacement and strain fields on the CFRP surface (Digital Image Correlation) (*fig. II.84*).

The reinforced surface of all the samples is characterized by a white texture over a black paint cover; the details related to this pretreatment (motivations and technical procedure) are described in Chapter 3 on the Digital Image Correlation. More devices have been developed to regulate the light in the test zone; specifically, a screened system has been designed to augment the contrast of the white texture.

A digital video camera has been placed close to the specimen to film the crack advancement and the sample failure from a 45° view (a lateral and a frontal face of the specimen have been framed) (*fig. II.84*). The film of each test defines the failure mode and registers the noise connected to the energy dissipation during the crack advancement. A foil of Plexiglas has been interposed between the video camera and the specimen to avoid damage of the lens during the fragile failure of the reinforced fire bricks (*fig. II.85*).

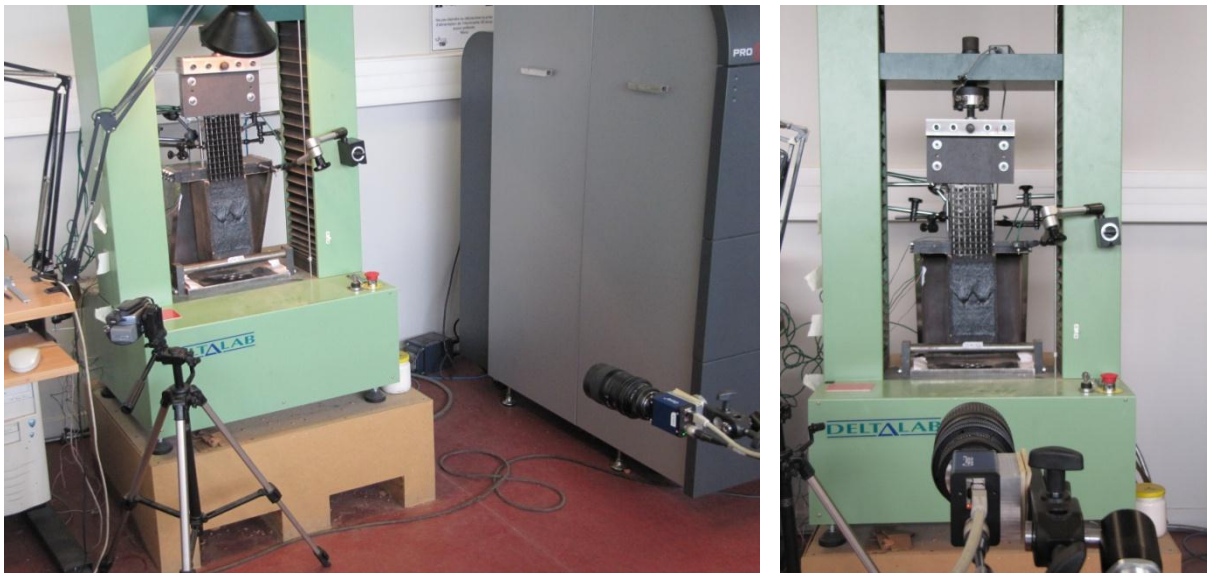

figures II.84 - Photo and video camera placement during the tests

fig. II.85 - The Plexiglas foil interposed between the video camera and the specimen

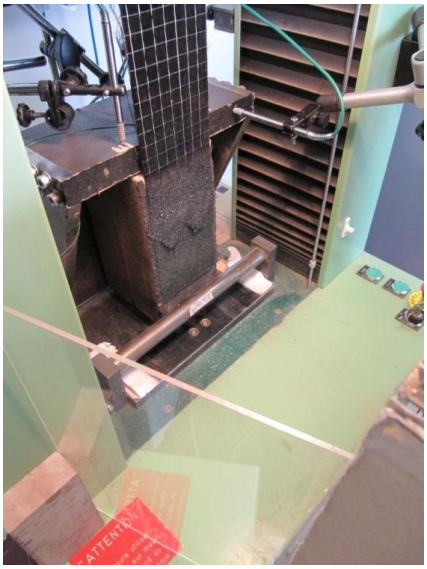

fig. II.86 - The cover used to eliminate the reflections on the Plexiglas surface

During the test the load has been applied by displacing the traverse of the universal machine at a constant rate of 0,2 mm/min (*fig. II.87*). A succession of load steps of Δu=0,2 [mm] have been applied. Between the steps a delay of 0,5 [min] has been provided to take photos and to read the values from the comparators. The universal machine Deltalab registers the value of the traverse displacement [mm] and the load applied to the system [kN] at each second [s]. The video camera films the experiment from the start of load history to the end.

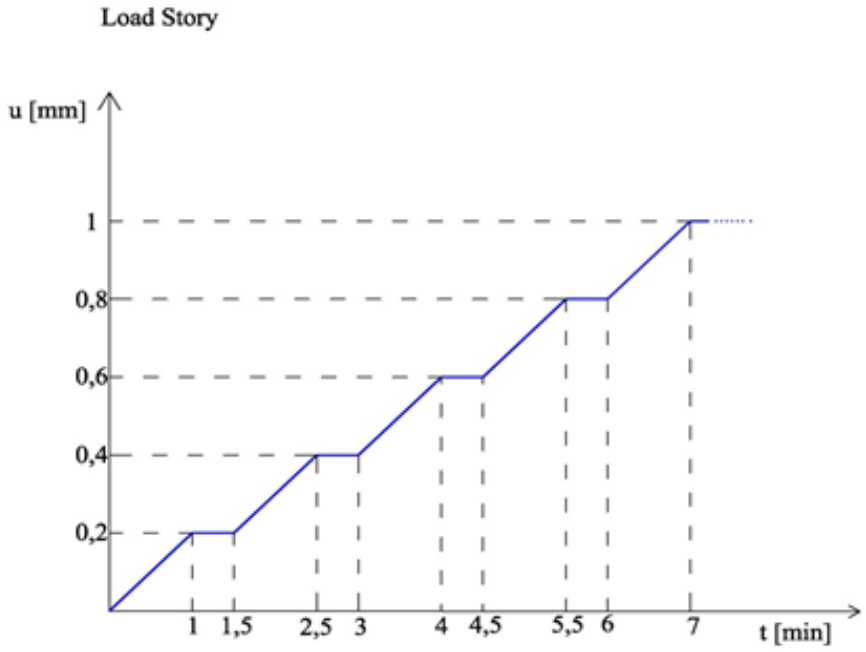

fig. II.87 - The load story in a graph time – traverse displacement

During the crack advancement, accompanied by high damage noise, additional photos have been taken. To collocate the name of these photos in time a PC screen recording software has been used. This software records the desktop of the computer where the photo-saving operations occur juxtaposed with a test video timer (*fig. II.88*).

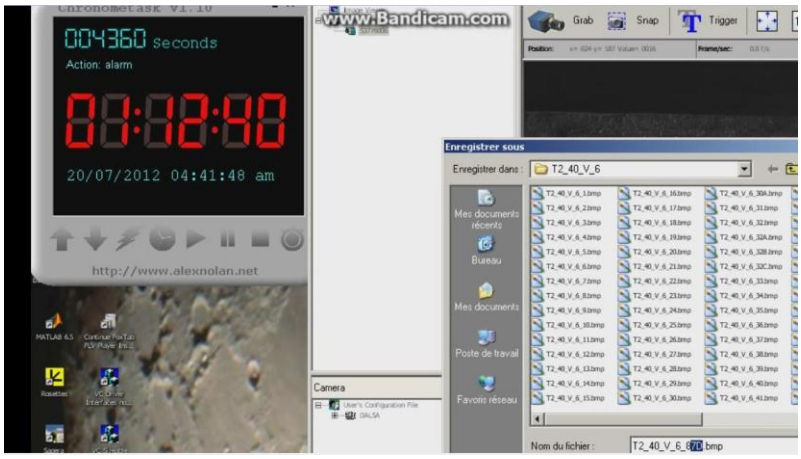

fig. II.88 - A frame of the desktop during the PC screen recording; in the left side the timer and in the right side the photo camera software

Schematically the following data have been registered during the tests:

- L [kN] - for each second of test (software DELTALAB);
- u [mm] – for each second of test (software DELTALAB);

- digital frontal photo (file *.jpeg) – for each delay of load (software camera);
- digital frontal photos (file *.jpeg) – during the last phases of the crack advancement, between the delay (software camera);
- PC screen recording (file *.MPG) – during the last phases of the crack advancement, between the delay (software Bandicam);
- D [mm] – displacement of the steel lock (comparators);
- Film video (file *.MPG) – during all the test, from start to finish (video camera); and
- photos by photo camera (file*.jpeg) – during all the test procedure.

Chapter 3

The strain field analysis by Digital Image Correlation

3 The strain field analysis by Digital Image Correlation

The Digital Image Correlation (DIC) is an attractive Optical methodology developed in the eighties to estimate the displacement and strain fields. This chapter presents the motivation that justifies the use of this technique in the framework of Civil engineering and, specifically, in the NES single shear test session carried out in this research study. A general description of the principles and of the method and advantages of the DIC is presented in *paragraph 3.1*. Subsequently, the technical characteristics of the CCD cameras and the constitutive properties of the digital photos are exposed (*par. 3.2*). The description of the DIC method and the discussion about the algorithm used in the thesis are presented in *paragraphs 3.3* and *3.4*. Then, the procedure to carry out the necessary speckle pattern onto the sample surface is shown (par. 3.5). The speckle pattern onto the firebrick reinforced specimen, the position of the CCD camera, the light exposure and the CORRELI parameters to use for the NES single shear test have been defined by a study case (*par. 3.6*). Specifically, several traction tests on rubber strips have been implemented to study the quality of the displacement and strain fields obtained by DIC. The last paragraph, the *3.7*, defines the procedure and the parameters used in the NES single shear test session to carry out the digital image correlation.

3.1 An optical measurement technique to study the 2D displacement and strain field

Usually, to estimate the two-dimensional strain fields of specimens subjected to applied load, strain gauges are glued onto the surface of the samples. When the object is deformed the gauges measure an electrical resistance change; multiplying this by a specific gauge factor it is possible to quantify the strain. With the traditional methodology just described only local values of deformation can be obtained. The strain gauges could be attached only on flat and smooth surfaces.

In the last three decades, a new method based on the optical measurement techniques has been developed to study the strain field - the Digital Image Correlation (DIC) [39][40]. This technique has been used frequently in the mechanical laboratory and, only in recent years, have some applications been realized within the Civil engineering framework [41][47][48][49].

The digital image correlation can calculate the displacement field of the surface of interest matching pictures taken during the test. The photos must be realized by a Charge-Coupled Device (CCD) camera. The digital images carried out by this instrument are constituted by a chessboard of squares (pixels), each one characterized by a monochromatic color. Before the test, the surface of interest must be treated with paint cover to realize a “texture” (speckle) of clean-cut chromatic points. Each photo used for the digital image correlation corresponds to an applied load. The displacement field

could be calculated matching the photos using a cross-correlation function that can be solved in physical space or in Fourier space [42][43][44][46]. Different approaches have been developed to identify the displacement field by comparing two different digital images; a finite element approach has been adopted by Besnard G. et al. [45].

The use of the DIC leads to several advantages: 1) the displacement and strain field can be obtained. 2) All the surface of interest covered by the chromatic texture could be analyzed. This aspect is fundamental when the zone of the strain and damage localization is not known a priori and the single measurement devices (strain gauges, extensometer) are difficult to position [46]. 3) The displacement field of heterogeneous surface could be obtained (for example the displacement between the CFRP sheet and the closer brick surface). 3) the displacement between points that do not belong to the same surface (the displacement between the splay anchor and the CFRP sheet) can be found. 4) with the photo camera instrumentation, the displacement and strain field analyze is low cost.

Several studies have applied the Digital Image Correlation in the shear test of CFRP to concrete bonded joint. Corr et al. (2006) [47] carried out an experimental study by NES single shear test using the DIC to analyze the displacement and the strain field over the reinforced surface of the specimens. The study was carried out with cross correlation between each one of the photos taken during the loading phases and the reference picture taken in the unloaded phase. In [47] the relation (3.1) has been used to calculate the bond stress $\tau(x)$. In this relation the strain values obtained by DIC are used.

$$\tau(x) = \frac{E_f A_{CFRP}(\varepsilon_{i+1} - \varepsilon_i)}{b_f \Delta x} \tag{3.1}$$

Where:

E_f = Young modulus of the composite

A_{CFRP} = Cross sectional area of the composite

b_f = the CFRP width sheet

Δx = the distance between the nodes (i+1) and i

The (3.1) requires some assumptions; the support is rigid in comparison to the reinforcement and the CFRP has an elastic behavior. The photos used for the correlation have been taken with a period of 1 second between each image. The results obtained by Corr et al. [47] shown the displacement of the stress transfer zone from the loaded side to the unloaded side (*fig. III.1*).

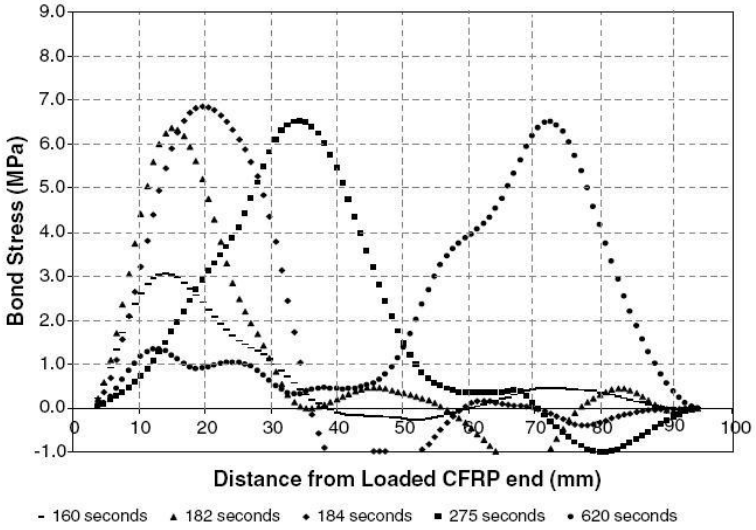

fig. III.1 - The bond stress distribution in four load step. The values of stresses are relative to the centerline of the CFRP sheet [47].

Carloni et al. [48] carried out an experimental study to obtain the through-thickness strains in the concrete reinforced by FRP during three NES single shear tests. To measure the strain below the composite layer, the traditional direct-shear configuration has been modified by bonding the FRP in line with the boundary lateral corner of the reinforced surface (*fig. III.2*). In [48], the Digital Image Correlation has been used to study the strain field onto the lateral side of the specimen. Since the thickness of the composite is insignificant in relation to the depth of the concrete block a layer of sponge 25 mm in thickness has been attached on the FRP; the displacement of this layer has been simple to measure and almost identical to those of the composite. A digital camera of 1280x1024 pixels has been used to take photos at regular intervals during the test. Before the experiment, the lateral surface of the specimen (concrete, composite and sponge) has been sprayed uniformly with white paint and stained with a speckle of black spots. The tests show that the region of concrete support through the thickness of the sample involved in the stress transfer phenomenon is approximately 15 [mm] (*fig. III.3*). Moreover, the strain distribution below the FRP is similar to the one obtained from the analysis of the composite surface. Carloni et al. conclude that the study of the fracture properties of the interface can be conducted by measuring the strain field on the surface of the FRP.

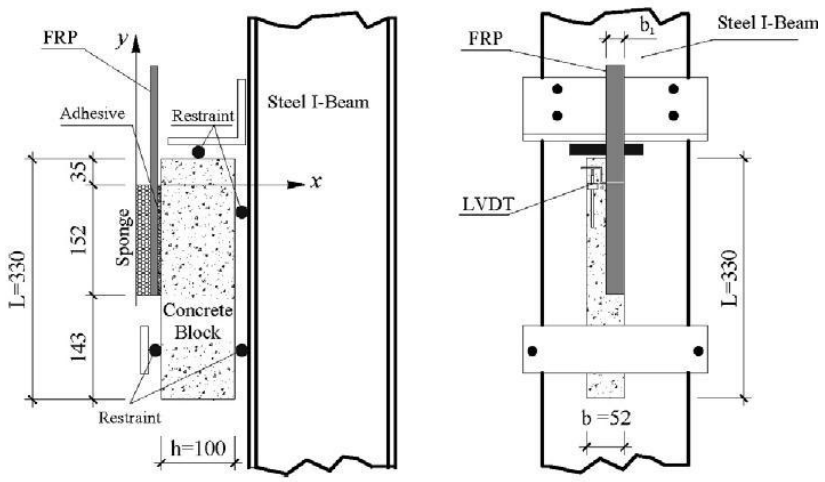

fig. III.2 - The "modified" NES single shear test executed by Carloni et al.[48].

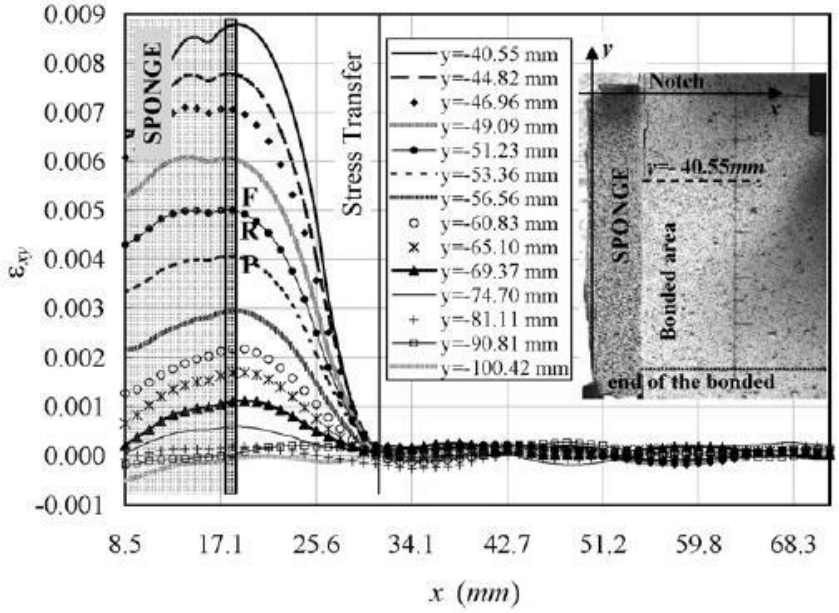

fig. III.3 - Shear strain ε_{xy} at different value of y (load step successive to the apparition of first crack)[48]

Some other studies on the FRP to concrete bonded joint have been realized using the Digital Image Correlation [49][50].

The performance of the digital image correlation is useful for studying the two dimensional displacement and strain field of the FRP to firebrick bonded joint fastened with FRP anchor and subjected to NES single shear test. The choice of this optical measurement technique has the following advantages:

- The displacement and the strain values can be obtained for all the area of the reinforced surface and not only in some points (strain gauges);
- The displacement and the strain values onto the splay anchor can be obtained;

- Detailed analysis of the strain concentration around the anchor can be carried out; and
- The displacement and the strain fields on the specimen can be obtained after the achievement of the cohesive debonding of the sheet and the activation of the FRP splay anchor (see the load-slip response of *fig. I.53*); while the brittle fracture could lead to the detachment of the strain gauges from the support.

The strain fields of the 36 specimens tested in Paris have been studied with Digital Image Correlation. The deformation values calculated during the 36 experiments held in Florence have been obtained using strain gauges. Designs of the strain gauge placements adopted in Italy are reported in *figure III.4*.

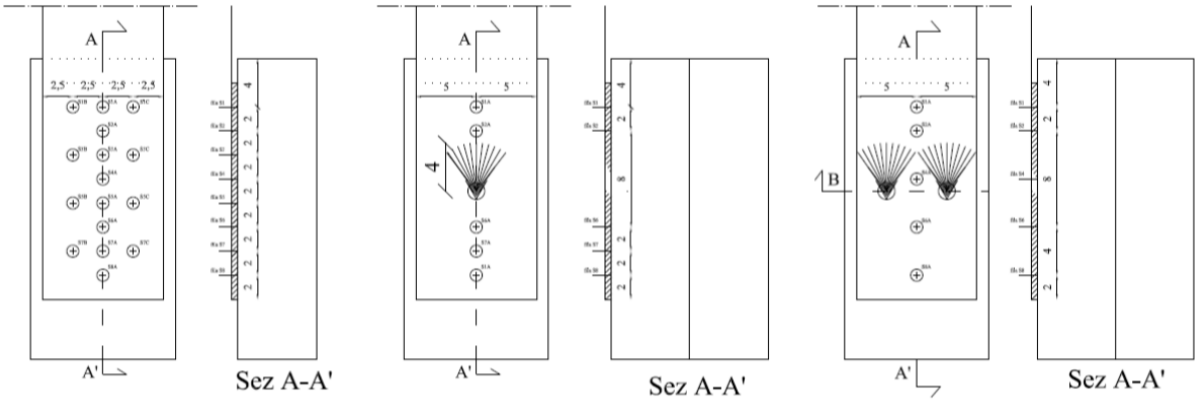

fig. III.4 – Disposition of the strain gauges adopted in Florence for the series F0, F1_40_V and F2_40_V

3.2 The CCD camera and the digital photos

The Charge Coupled Device (CCD) is a chip made in silicon designed in 1970 [51]. It is made up of an array of sensitive squares (pixels); each one stores the charge like a potential well. Therefore, when the light falls on the surface of the semiconductor, each pixel registers an electrical charge value [52]. In the CCD camera the image is projected by lens on the sensitive silicon surface and it is converted into an array of charge values. The computers can read the charge information stocked in each pixel and convert it to an intensity value. An important quality of the Charge Coupled Devices is the high speed process of recording and clearing the information detected in the pixels.
This very brief presentation of the CCD camera helps to understand that the digital images, realized with this device are intensity signals. The digital images are bi-dimensional grid, each cell of coordinate (x,y) corresponds to a pixel characterized by a specifical intensity value. For the grayscale digital images the intensity values range from 0 to 255 (*fig. III.*5). The colors of this scale change gradually from black (value 0) to white (value 255).

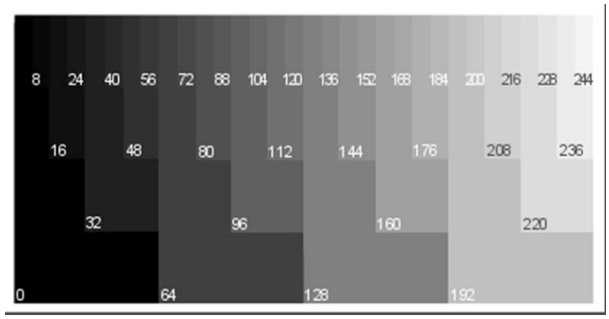

*fig. III.*5 - *The gray level scale*

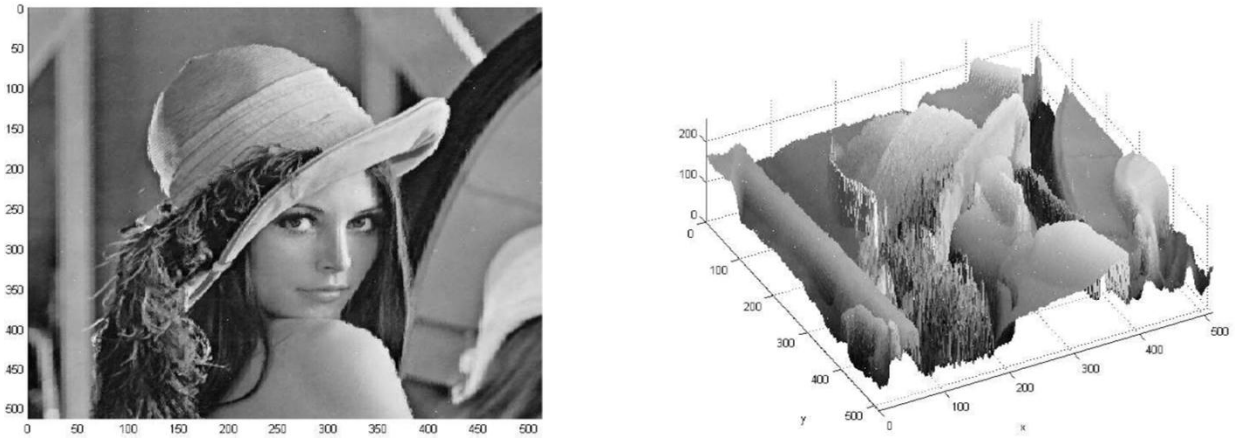

fig. III.6 - A digital image and the relative 3D graphic "x-y-gray level"

Finally, each digital image could be represented as a matrix of numbers; this possibility permits a large range of processing application on photos which could not be obtained with analogical technology. The Digital Image Correlation exploits these CCD camera performances.

3.3 The digital image correlation method

The displacement field of a deformed image with respect to a reference image is obtained by the DIC matching more sub-regions. The standard approach described below uses a correlation function [43]. To simplify the explanation of the DIC process two one-dimensional signals have been correlated herein; the signal f(x), that represents the zone of interest (ZOI) of the reference image, and the signal g(x), that represents the displaced configuration of the same zone. The f(x) is constituted by five pixels (*fig. III.*7); all the squares are black (grey level = 0) except the second, which is white (grey level = 255). The signal g(x) describes the same interest zone after a displacement u (*fig. III.8*).

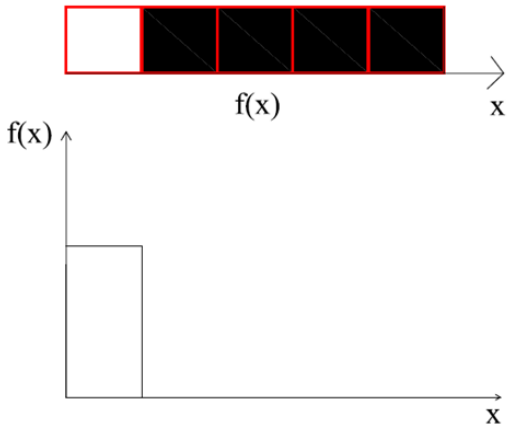

fig. III.7 - The signal f(x) and the graphic "x-f(x)"

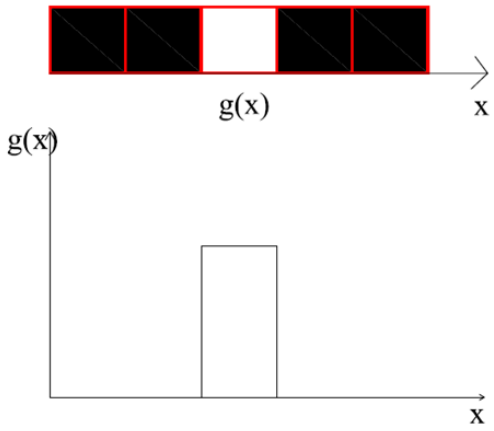

fig. III.8 - The signal g(x) and the graphic "x-g(x)"

We can write:

$$g(x) = f(x-u) + b(x) \tag{3.2}$$

Namely, the signal g(x) is equal to the shifted copy f(x-u) of the reference signal f(x) summed with a random noise b(x). The latter is due to the deformations and the optical measurements that modify slightly the speckle pattern. Changes in the ambient light during the test can also cause this noise. The value of the shift "u" is obtained using the cross correlation function h(δ) reported as follows:

$$h(\delta) = (g * f)(\delta) = \int_{-\infty}^{+\infty} g(x) f(x-\delta) dx \tag{3.3}$$

The value of δ that maximizes the cross correlation product $(g * f)(\delta)$ is the shift estimation value "u". If b(x) is nought, as in the example proposed, the estimation is perfect.

Taking into account the mono-dimensional images f(x) and g(x) presented above, a simple example of the cross correlation procedure is proposed as follows (*fig. III.9*). By increasing the value of the tentative shift δ the function h(δ) varies. The maximum value of the cross correlation product is obtained when the value of δ ensures that the f(x) overlaps the g(x) perfectly. In the example proposed the h(δ) is maximized by $\delta=\delta_4$ (*fig. III.10*).

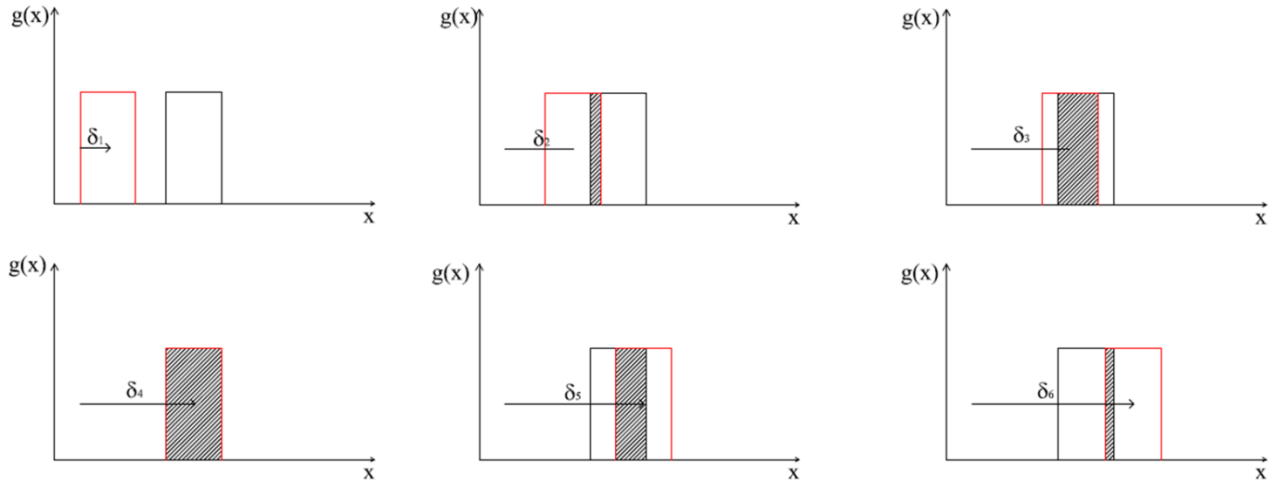

fig. III.9 - Example of cross –correlation process; the f(x) displaced by different value of tentative δ (in red).

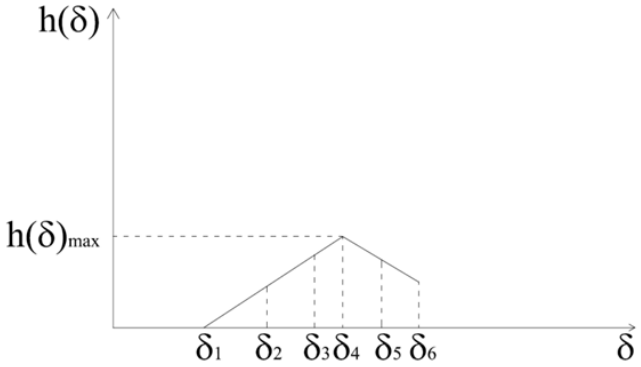

fig. III.10 - Example of cross-correlation process; the function h(δ).

The computation of h(δ) can be carried out either in the Fourier space, by using an FFT, or in the original space [43].

If the images are bi-dimensional the same process of correlation is carried out. In this case the signals will be f(x,y) and g(x,y) and the displacement of the sub-region of interest has a component in the x and y directions. In the figure a signal f(x,y) is represented with a highlighted zone of 10x10 pixels.

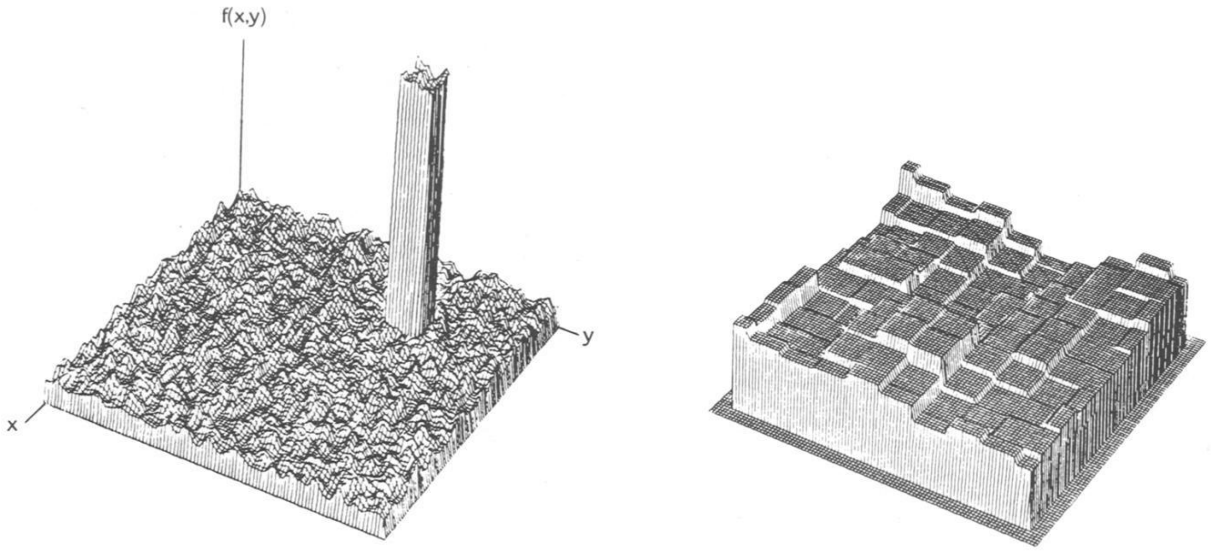

fig. III.11 - A bi-dimensional signal. In the left side the f(x,y) signal is represented. In the right side the zone of 10x10 pixels, highlighted in the left image, is zoomed. [40]

3.4 The correlation algorithm CORRELI^{GD} to study the two dimensional-signals

The correlation algorithm CORRELI^{GD} has been used to compute the displacement and strain field upon the reinforced surface of the specimens. The software version used has been developed by a research group of LMT-Cachan [42][43][44]. The algorithm is based on a multi-scale approach to increase the efficiency of the correlation process. The computation method to manage the correlation between two signals is presented as follow; a "reference" image f(x,y) and a "deformed" image g(x,y) are taken. The first step of the process is defining a region of interest (ROI) in the photo which represents f(x,y). After that, a zone of size 2^p x 2^p pixels^2 inscribed in the ROI and centered in the reference image is defined; the same region is considered in the deformed image. A first correlation is computed by a FFT to obtain the average displacement U_0 and V_0 that maximize the cross-correlation product between the ROIs of the signals f(x,y) and g(x,y). Once these values have been found, the ROI of the deformed image is moved onto the ROI of the reference image displacing its center of U_0 and V_0. The following step is choosing the parameter *s* that defines the size of the sub-regions. These sub-regions are named Zone Of Interest (ZOI) and have a dimension equal to 2^s x 2^s pixel^2. The value of parameter *s* is smaller than *p*. Then, another parameter is chosen, the shift d*x* between two consecutive ZOIs (dx=dy). The centers of the Zone of Interests, defined by the parameters *s* and *dx,* form a grid. Each ZOI of the reference signal is cross-correlated with the corresponding zone of the deformed signal. A FFT correlation gives the value of the additional in-plane displacement ΔU and ΔV for each ZOI. The displacements of the nodes of the grid, are equal to the value of U_0 and V_0 plus the ΔU and ΔV relative to each ZOI. By determining

the maximum of a parabolic interpolation of the correlation function, a sub-pixel correction of the displacement is obtained by finding the values δU and δV. The total displacement of a generic node "i,j" will be equal to:

$$U_{ZOI\ i,j} = U_0 + \Delta U_{ZOI\ i,j} + \delta U_{ZOI\ i,j} \quad (3.4)$$

$$V_{ZOI\ i,j} = V_0 + \Delta V_{ZOI\ i,j} + \delta V_{ZOI\ i,j} \quad (3.5)$$

To reduce the errors more iteration could be realized to obtain a convergence criterion. The precision of the algorithm method is of the order of 2/100 pixel for the displacement and 10^{-4} for the strain measurements. After the computation of the displacement field the strain field is obtained using simple derivations with respect to the nodes coordinates. As the displacement field is known discretely at a finite number of node, derivation is the source of noise on the strain field representation: a smoothing step (lissage) is generally useful to obtain an accurate strain field.

3.5 The speckle pattern onto the observed surface

The performances of the Digital Image Correlation are related to the grey level characteristic of the pixel array. Specifically, the best results are obtained when local gray level fluctuations are present in the images to correlate [41]. Usually, to obtain this optimal pixel characteristic, a texture is realized on the observed surface. First, we cover the surface with a homogeneous paint which is then covered with a random speckle pattern of paint. To generate a high contrast the support cover is black and the speckle is white (or inversely) [41][43][48][49]. This choice maximizes the fluctuation of the gray levels in closer pixels (black=0 and white=255). Therefore, the goal of the paint pretreatment is to simplify the production of high contrast images; namely photos with very dark shadows and very bright highlights. In this framework great attention is paid to the light that illuminates the observed surface.

In the experimental session of this thesis the homogeneous cover is sprayed with a black paint on the reinforced surface. This was then covered with a speckle pattern made with a white spray paint. The methodology used to realize the texture has already been used in the laboratory of MSME.

3.6 A preliminary case study: rubber in traction

The concepts shown above underline that the quality of the Digital Image Correlation is connected to several factors combining with each other; the speckle morphology, the photographical setup, the scale [mm]/[pixel] the parameters of the software CORRELI. A preliminary study case has been carried out to become familiar with the DIC optical measurement technique and establish the parameters to use in the NES single shear test.

The preliminary study has been carried out using several traction tests on rubber strips. The test apparatus used to stretch the rubber is the same projected for the NES shear test. The latex bands have a width equal to that of the specimen carbon fabric (10 [cm]) and a length of 120 [cm]. The strip is inserted in the apparatus by passing one of its extremities within the steel cylinder and the support steel plate; both ends of the rubber band are bonded to two steel plates and inserted inside the steel "tongs" (*fig. III.12*).

fig. III.12 - The traction test on rubber.

Before the texture is achieved on the strip surface, various attempts at applying speckle have been carried out on cardboard sized 12x40 [cm^2]. This learning phase has helped acquire the manual skills and to define the technical process necessary to realize the texture.

Two texture typologies (*fig. III.13*) have been achieved using a simple procedure. First, a black cover is splayed on the surface of interest, and a minimum 24 hours later, a cloud of white paint is generated on the sample by directing the spray upward; the white drops falling on the black surface

generate a texture. The speckle pattern achieved is more sensitive to the modality of spraying of white paint; a slight modification of the spray direction creates more different sizes of spots on the surface of interest. The typologies of speckle pattern analyzed in the rubber tests are realized with a technical process which can easily be reproduced. The first kind of texture is characterized by the size of the spots that are very different from one another. The second is featured by more homogeneous spot sizes.

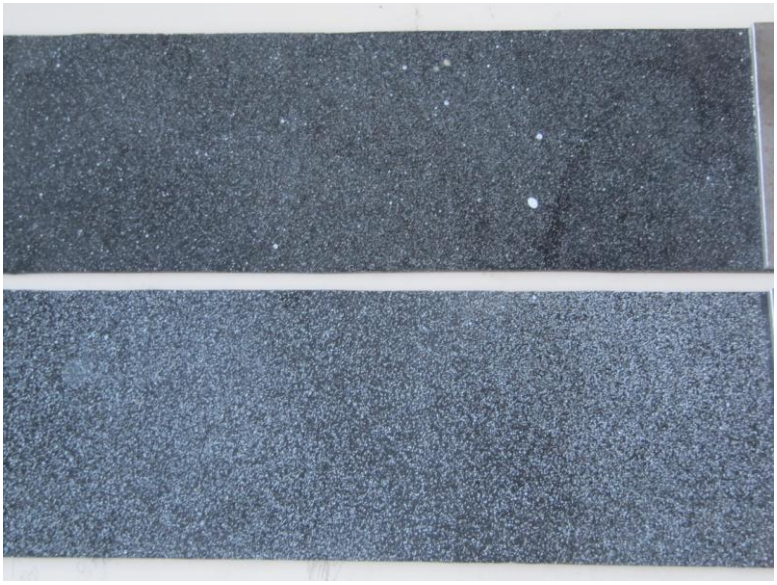

fig. III.13 - The two configurations of speckle: above the texture S1 (heterogeneous size spots), below the texture S2 (homogeneous size spots)

A CCD camera has been placed in front of the specimen at a distance of 120 [cm] (*fig. III.14*). To produce high contrast photos a lamp has been allocated close to the studied surface (*fig. III.14*).

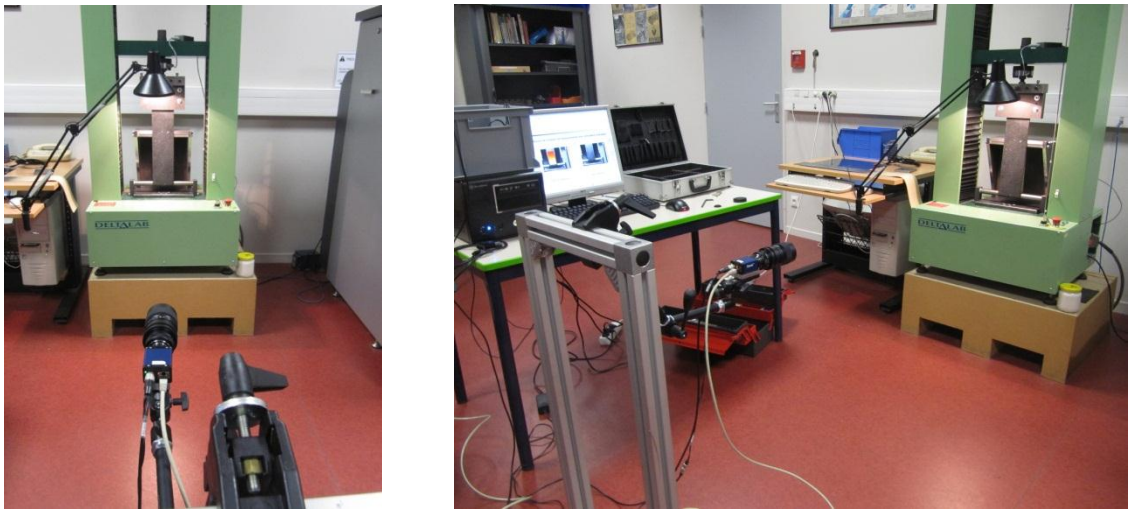

fig. III.14 - The camera and the rubber test

The pictures taken have a size of 1360x1024 [pixel^2]. Two hypotheses of camera orientation have been tested, O1 and O2; the frame is 1360x1024 [pixel^2] in the first one and 1024x1360 [pixel^2] in the second one (camera rotate of 90°). To obtain the side length in [mm] of the pixel square a "scale ratio" (R_z) has been calculated (eq.(3.6)). This is equal to the ratio between the rubber width in [mm] and the same measure in [pixel].

$$R_Z = \frac{Rubber\ Width\ [mm]}{Rubber\ Width\ [pixel]} = \frac{100\ [mm]}{x\ [pixel]} \tag{3.6}$$

The Region Of Interest (ROI) of the rubber surface has dimensions 70x200 [mm^2]. Obviously, if the camera "zooms in" on the rubber, the ratio R_Z decreases and the number of pixels that describe the speckle increases.

The rubber tests have been carried out to answer the following questions.

- Which is the best configuration of speckle pattern (homogeneous or heterogeneous)?
- Once the speckle pattern is established, which is the more efficient ratio [mm]/[pixel]?
- Once the speckle pattern is established and the ratio [mm]/[pixel], what are the Digital Image Correlation parameters that give the most efficient analysis?

The experiments have been carried out applying imposed displacements to the extremities of the rubber strip inserted in the steel tongs. The history of the load applied on the specimen consists in 4 steps of imposed displacement (step of Δu=1 mm); after each one a delay of 30 [s] has been performed to block the displacement traverse and to have time to take frontal pictures.

The Deltalab machine gives the value of the Force [N] applied on the rubber during the test. Once the cross section of the latex bands is known, 660 [mm^2], it is simple to obtain the stress σ [N/mm^2]. More tests have been carried out applying the same loading history described above but modifying: the specimen analyzed (with heterogeneous and homogenous size spot), the orientation of DDC camera (frame of 1360x1024 or 1024x1360 [pixel^2]), the zoom of ROI, the size of ZOI, the shift between the ZOI and the number of iterations.

The strain field obtained by DIC has been used to find the experimental Young modulus of the rubber; this has been compared with the literature value.

The displacement and strain field obtained by the correlations of image have been compared with that of the analytical solutions. In the tests, it is evident that the quality of results is maximized when a good combination between size of speckle, ratio R_Z and size of ZOI is adopted.

The experiments showed that the heterogenic speckle pattern leads to displacement and strain field characterized by local noise restricted to the bigger white spots. By increasing the ZOI size the magnitude of the concentrated noises decreases but still exists. In the tests, the texture characterized by spots of almost homogeneous size leads to displacement and strain field considerably less affected by local noises. The results obtained confirm that the homogeneous speckle pattern is more efficient than the heterogeneous one.

If the frame is 1360 × 1024 the value of x is 374 [pixels], R_z is equal to 0,27 [mm/pixel], and the ROI is defined by 259 × 741[pixel^2]. When the frame is 1024 × 1360 it is possible to "zoom in" on the rubber surface; in this case R_Z is equal to 0,16 [mm/pixel], and the ROI is defined by 424 × 1212 [pixel^2]. In this experimental session optimal results have been obtained by means of the second typology of frame. Finally, the best results (optimal case) have been obtained analyzing digital photos with a R_Z = 0,16 of homogeneous speckle pattern and utilizing the following DIC parameters:

ZOI size = 128 [pixel]
dx = 64 [pixels]
n. iterations = 6

The contour representations of the components D_1 and D_2 of the displacement field obtained using this optimal combination of parameters are reproduced in *figures III.15* and *III.16* for each load step. The reference axis are represented in the same images.

The contour representations of the strain field ε_{11} and ε_{22} are presented in *figures III.17* and *III.18* for each load step

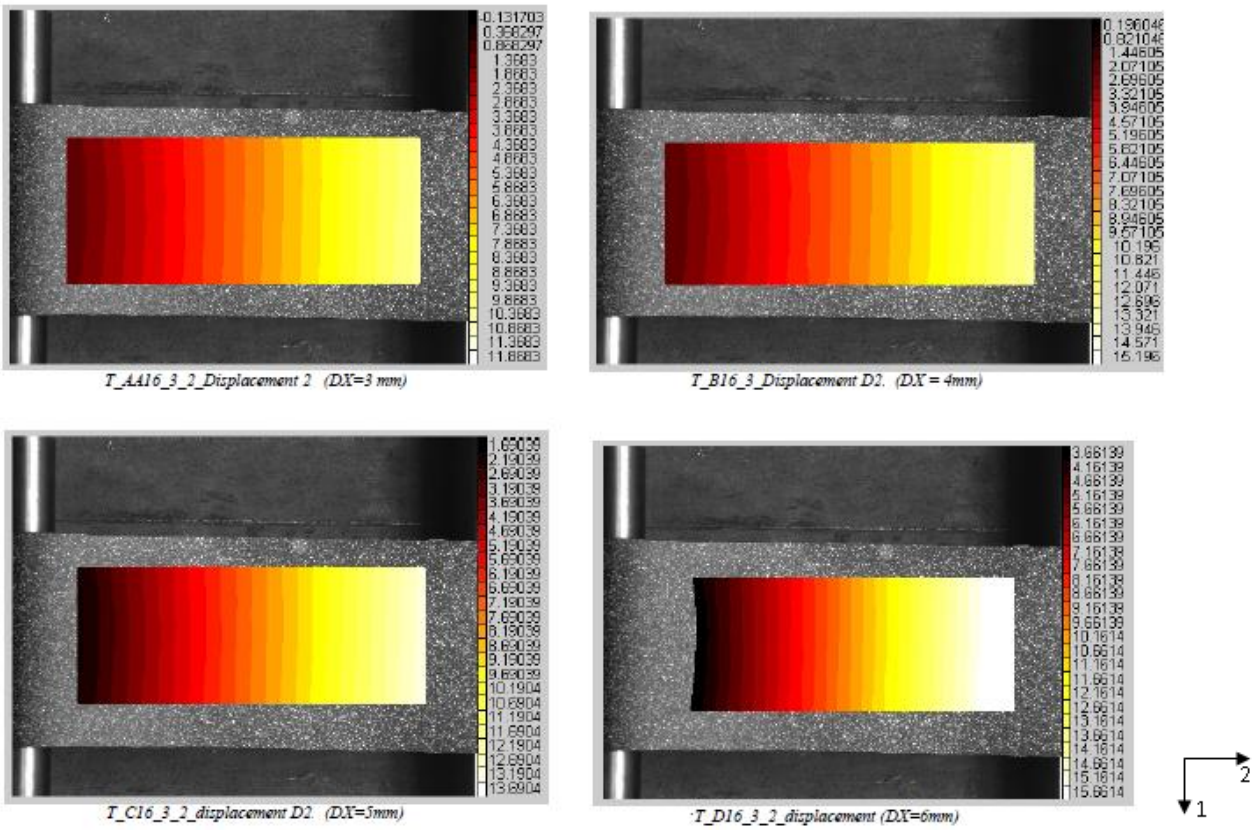

fig. III.15 -The contour representation of the displacement field (D2) in the optimal case for each load step. In the right are reproduced the reference axis.

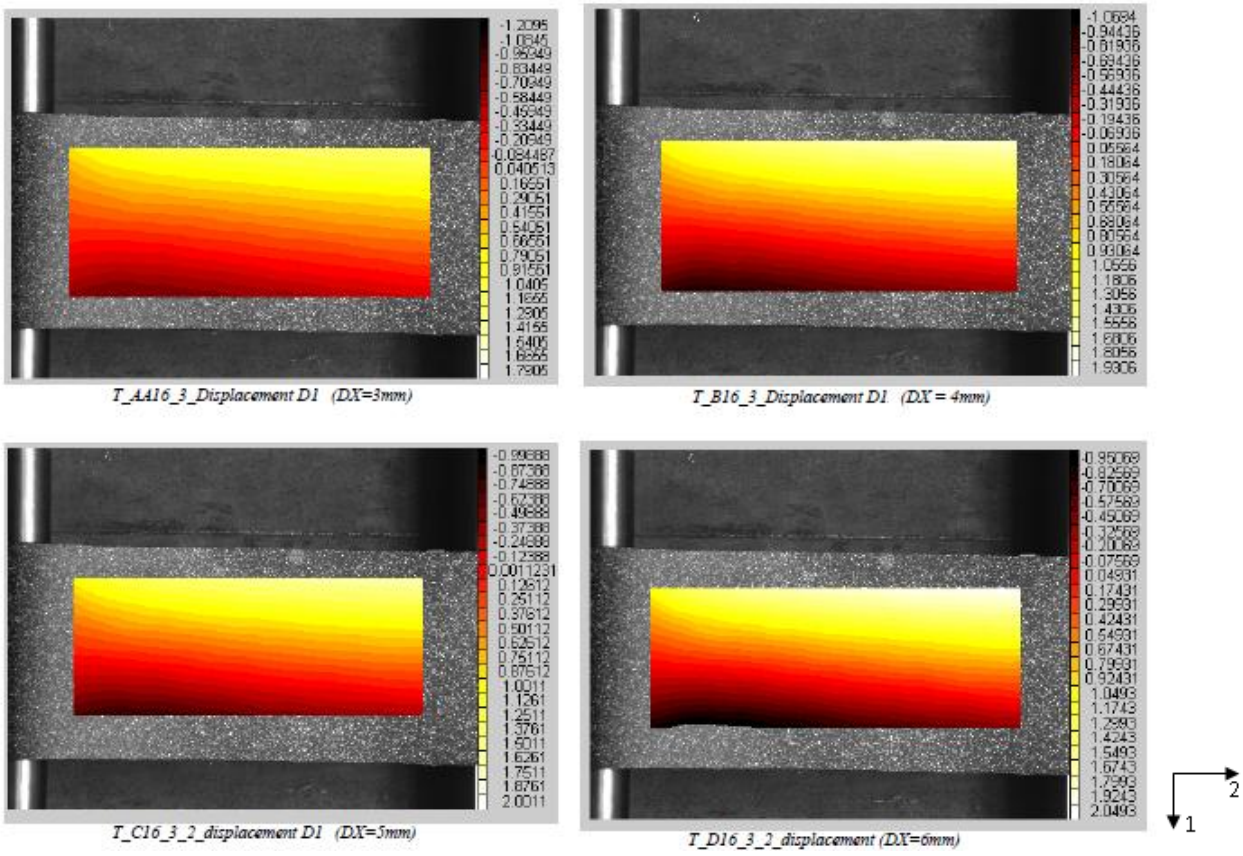

fig. III.16 - The contour representation of the displacement field (D1) in the optimal case for each load step. In the right are reproduced the reference axis.

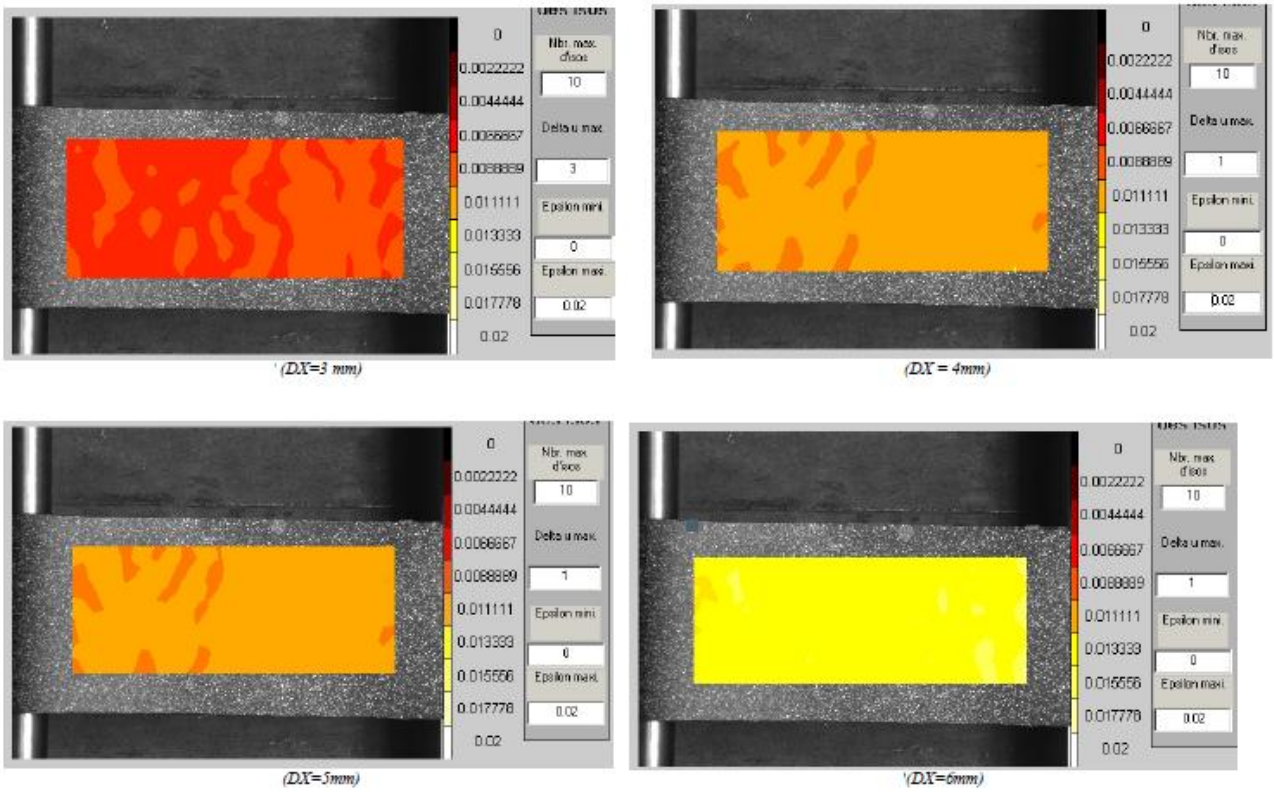

fig. III.17 - The contour representation of the strain field (ε_{22}) in the optimal case for each load step. In the right are reproduced the reference axis.

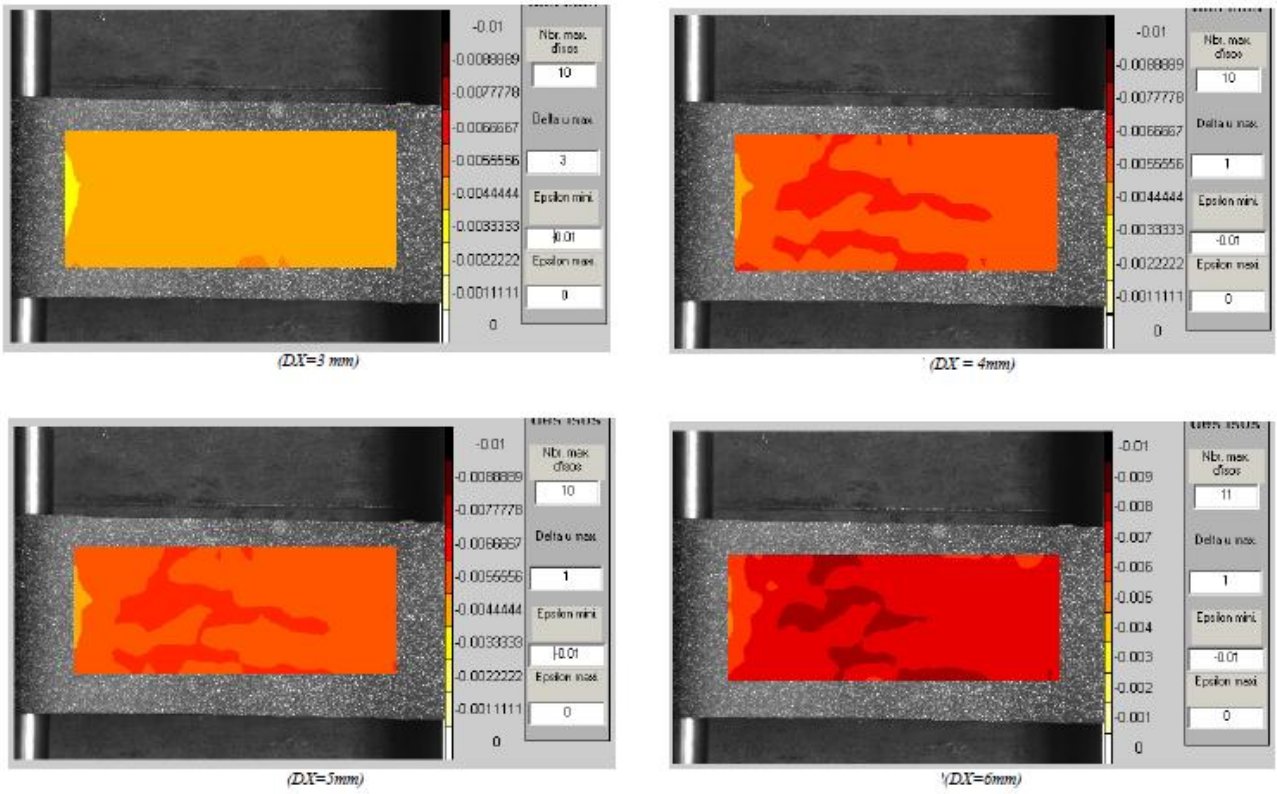

fig. *III.18 - The contour representation of the strain field (ε_{11}) in the optimal case for each load step.*

Dividing the stress σ applied to the rubber to the strain obtained by DIC a value of 0,008 [MPa] has been obtained. This value matches perfectly with the rubber properties found in literature [53].

3.7 The CFRP to fire brick bonded NES shear test and the Digital Image Correlation

During the NES single shear tests, the bidimensional displacement and strain fields of the firebrick reinforced surface have been obtained using Digital Image Correlation.
The speckle pattern on the surface of interest has been drawn on the FRP surface, reproducing the homogeneous size spots tested in the rubber experimental session (*fig. III.20*).

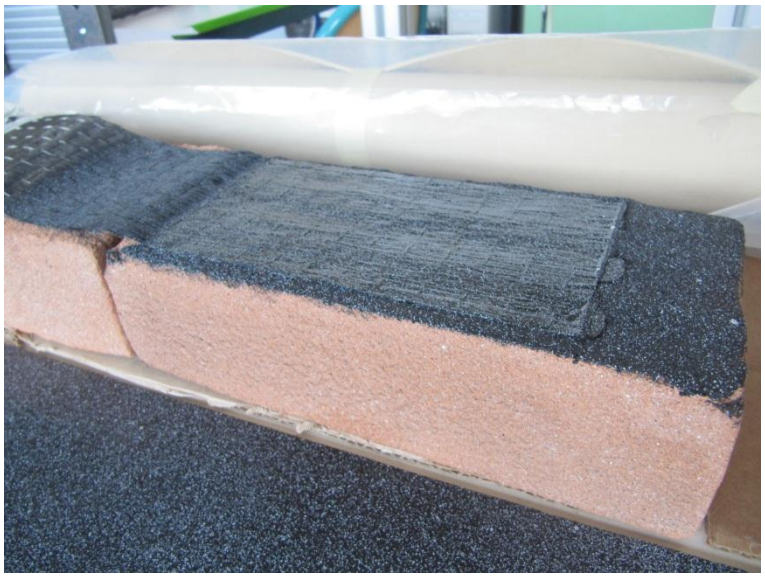

fig. III.20 - The speckle pattern onto the reinforced surface. The fire-brick specimen is drawn near the rubber sample characterized by homogeneous size spots.

During the NES single shear tests the digital images have been taken using a frame of 1024x1360 pixels. The value of R_z of these images is approximately equal to the one chosen for an accurate representation of the strain field in the rubber study.
Unlike the rubber strip surface, the CFRP is bright and reflects the lights. This characteristic generates several problems connected to the impossibility of producing good quality pictures in full ambient light. The nature of the laboratory made it necessary to shade the surface of the specimen from direct light with some devices; an aluminum frame covered with cardboard and blankets were positioned between the camera and the specimen (*fig. III.21*). The images of a CFRP surface before and after assembling the shadow device are presented in *figures III.22* and *III.23*.

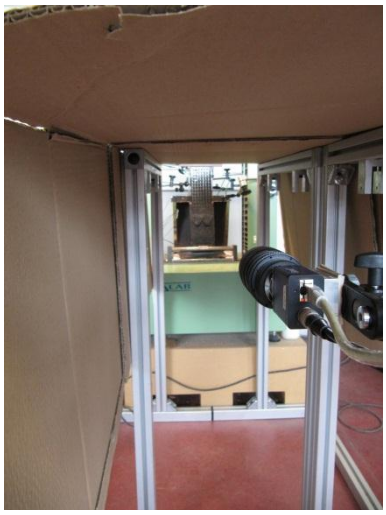

fig. III.21 - The devices used to overshadow the specimen

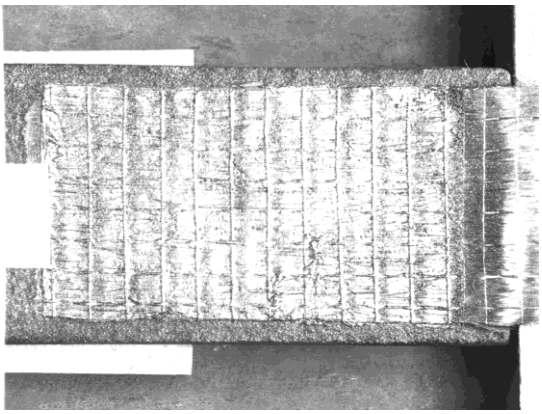

fig. III.22 - The bright CFRP surface

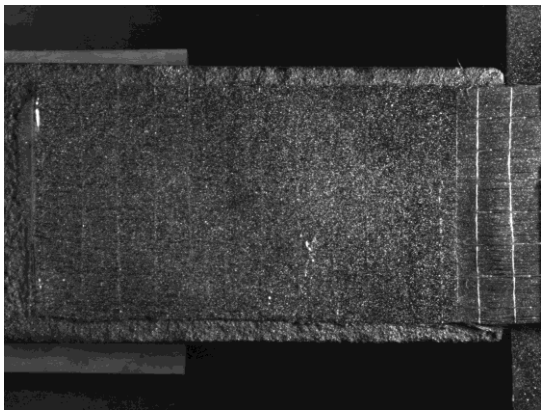

fig. III.23 - The bright CFRP surface shadowed by the cardboards devices

The CORRELI parameters chosen to execute the digital image correlations have been defined according to the optimal case studied in the rubber test session.

Chapter 4

Experimental Results

4 Experimental Results

The main output data of the experimental session are collected in the next pages. The chapter is subdivided in four parts. In the first an overview of the quantity treated is presented; the nomenclature used is defined, the assumptions made and the procedure utilized. A characteristic graph U-L (displacement – load) is presented in the first paragraph to give an idea of the behavior of a generic specimen and guide the reader. In the second part of the chapter all the data related to each series are presented. Specifically, the main data shown for each typology of reinforcement are: the graphs U-L of all the specimens of the series, a master curve representative of the series, the average peaks recorded with the corresponding standard deviation, the energy dissipated during the test, the failure description, the photo of specimens after the failure, graphs y-ε_{yy}, graphs y-τ_{zy} and the chromatic representation of strain fields. In the third part of the chapter a comparison among six reference specimens, one for each typology of reinforcement, has been carried out to analyze the different crack advancement process registered by varying the anchor configuration. At the end of this part the accuracy of the DIC has been verified. The last part of the chapter matches all the average results of each series; in this section a general discussion about the results is presented drawn from all the observations related to the analysis of data.

4.1 Results overview

The results presented in this chapter have been obtained by processing the measures of the instrumental setup.

The values treated and the identification carried out in the experimental analysis for each specimen are as follows:

- The load corresponding to the imposed displacement (graphs U-L);
- The identification of the state of the specimen (elastic behavior – crack advancement – debonding – anchor loading – anchor failure);
- The peak of loads registered (P_1, P_2, P_3);
- The energy dissipated during the test ($\Delta\Gamma$, Γ_{end});
- The fracture mode (cohesive, adhesive, mixed,…);
- The bi-dimensional displacement and strain fields on the reinforced side of the specimen (*u* and ε); and
- The bond stress at the interface.

The considerations formed during the processing of instrumental measures, the treatment procedure and the nomenclature of the results are presented in the next subparagraphs.

4.1.1 Displacement-load graphs, load peaks and energy

The analysis of the *Displacement–Load* graph (U-L) helps gather information about the failure phases of the reinforced system. The characteristic graph U-L obtained in the NES single shear test is shown in *figure IV.1*. In this representation, the linear stroke AB corresponds to the elastic behavior of the firebrick support. A first load peak (**P_1**) is registered in B when the first crack appears in the loaded extremity of the FRP to support bonded joint. The stroke B'C describes the crack advancement phase, in C the total debonding fracture occurs. The load value registered in this point, named P_2, corresponds to the maximum load peak obtained during the test. If no anchors are fastened to the composite sheet the test ends when **P_2** is achieved by the total detachment of the CFRP reinforcement and the simultaneous fall to zero of the load. The experimental study shows that the presence of "CFRP nail" gives the reinforced system, after the peak load in C, a residual resistance and creates a new loading phase in which the load increases (stroke DE). In E a failure of the system *CFRP sheet – CFRP anchor* occurs and, once the peak **P_3** is achieved, the load drops again.

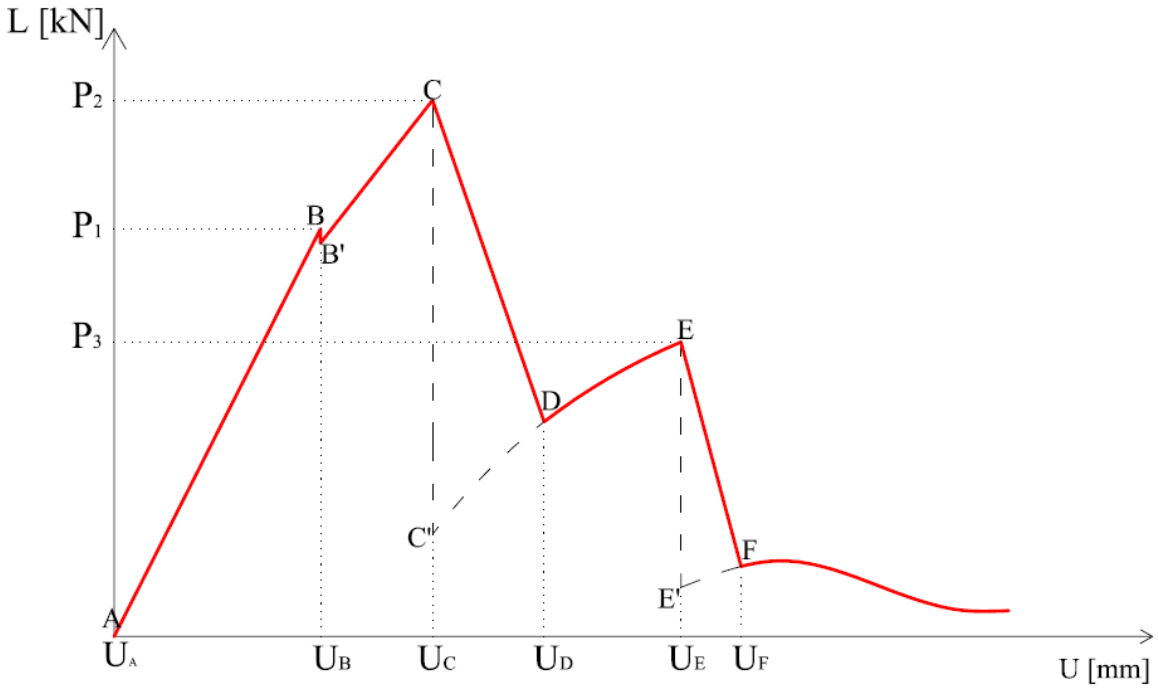

Fig. IV.1 - The characteristic graph U [mm] – L [kN]

fig. IV.2 - The specimen during three test phases; in the left an image of the sample during the crack advancement (strokes BC), in the center a photo of the specimen after the total debonding fracture (strokes DE), finally, in the right a figure of the anchor detached from the CFRP sheet after the achievement of the P3.

U is the imposed displacement applied to the specimen. It is equal to:

$$U = u - D \tag{4.1}$$

As previously described in *par. 2.2.6*, *u* is the displacement of the traverse, and D is the displacement of the steel lock. The displacement u increases linearly with time during all the test (*fig. IV.3*). Instead, the value of D increases linearly with time until the achievement of the debonding failure (*fig. IV.3*); in this instant the load falls, and, due to the spring back of the steel apparatus, a partial drop of D is registered. According to these considerations, the linear increase of the displacement U during time presents a jump at the debonding failure instant (*fig. IV.3*).

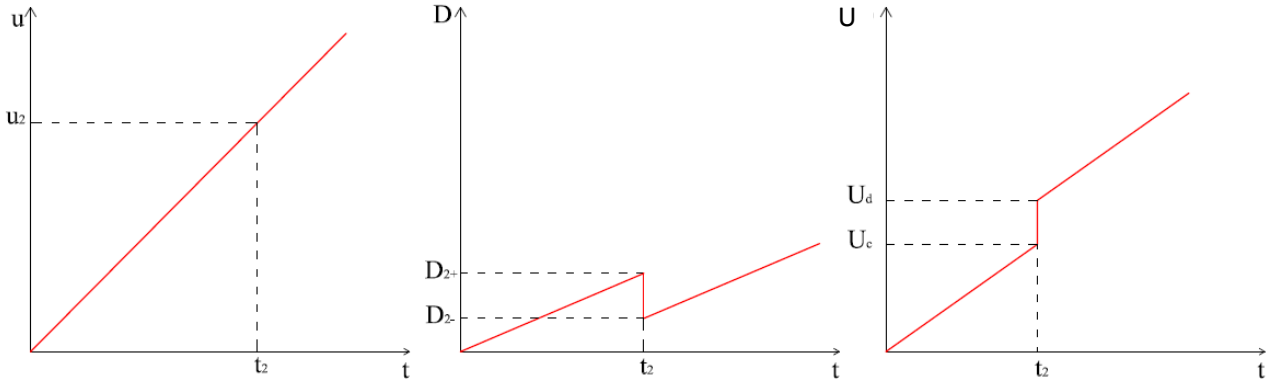

fig. IV.3 - The graphs t-u, t-D and t-U

The graphs displacement-load are presented in *figure IV.4*. In the case of diagram u-L, when the load peak P_2 is reached an almost vertical drop is registered. Considering the graph D-L it is evident that, once the peak P_2 has been achieved, an elastic return of the steel lock occurs; instantly the value of D_{2-} drops to D_{2+} (the nomenclatures $_{2-}$ and $_{2+}$ defines the instant before and after the debonding failure). Therefore, in the diagram U-L, when the peak P_2 is reached an inclined stroke describes the load fall. This slope is due to the springing back of the steel lock.

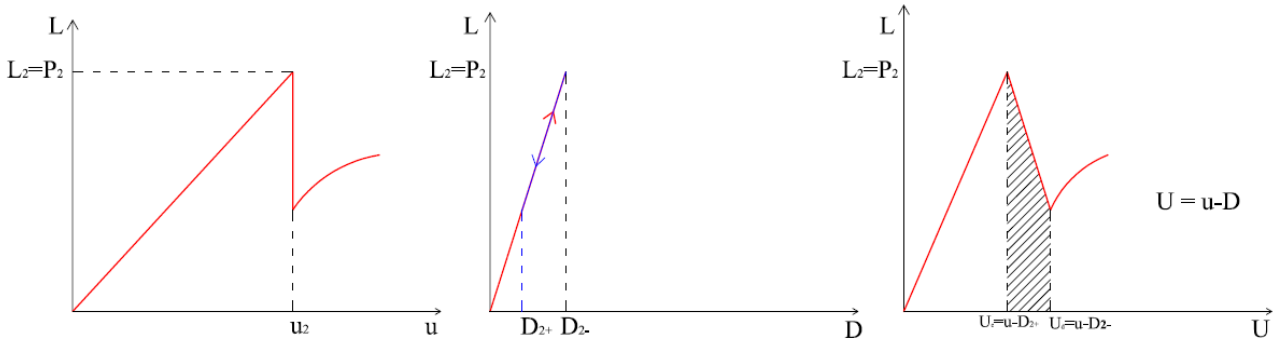

fig. IV.4 - The graphs u-L, D-L and U-L

The energy necessary to lead to failure of the reinforced system is an important parameter to measure the efficiency of the different reinforcement typologies. This energy, named Γ and measured in [J], is equal to the area underlying the U-L curve. It corresponds to the energy dissipated when the system is led to failure. Specifically, the total value Γ has been subdivided in 4 shares. The small dissipation of energy due to the friction between the upper and lower surfaces of the fracture, registered after the anchor fail, has been neglected. The four energy shares are listed and defined below.

– $\Delta\Gamma_1$ is the amount of energy necessary to generate the first crack. It is equal to the area underlying the stroke AB (*fig.IV.5*)

– $\Delta\Gamma_2$ is the amount of energy dissipated during the crack advancement phase, until the total debonding of FRP to fire brick reinforced system. It is equal to the area underlying the stroke BC (*fig. IV.5*).

– $\Delta\Gamma_i$ is the amount of energy dissipated during the load fall and the instant springing back of the steel lock. The assumption made to quantify this $\Delta\Gamma$ is that the drop of D is so fast that the instrumentation setup is incapable of registering it. An almost vertical drop, defined by the stroke CC', and a subsequent loading step, described by the stroke C'D, has been suggested (*fig.IV.5*).

– $\Delta\Gamma_3$ is the amount of energy dissipated during the fiber anchor loading phase. It is equal to the area underlying the stroke DE (*fig. IV.5*).

To compare the energy dissipated during the tests of different series, the *global value of energy* Γ_{END} has been defined (equation (4.2)). Since it is impossible to know exactly the slope of the stroke C'D the value of $\Delta\Gamma_i$ has been evaluated as indicated in *fig. IV.5*, from the slope of the stroke DE. In this way, we can approximately account for the energy absorbed by the system when the displacement U instantaneously jumps from U_{2-} to U_{2+}, which could have been recorded if a much stiffer system had been used.

$$\Gamma_{END} = \Delta\Gamma_1+\Delta\Gamma_2+\Delta\Gamma_i+\Delta\Gamma_3 \qquad (4.2)$$

Obviously, in the specimens of series T0 the fourth component of the sum is equal to 0.

In order to describe the general behavior as recorded in each series a Master Curve (MC) for each reinforcement configuration has been realized defining the points B (U_B, P_B), C(U_C, P_C), D (U_D, P_D), E (U_E,P_E). The coordinates were evaluated from the average values of peaks and corresponding displacements from all the tests of each series. The point B' has the same abscissa as B, U_B, and a ordinate $P_{B'}= P_B- \Delta P_B$ [N]. The value of ΔP_B has been obtained for each series as an average of the fall measured after the peak P_1 in all the tests with the same configuration. The point C' of the Master Curves has been defined intersecting the vertical passing through C and the straight line passing through DE.

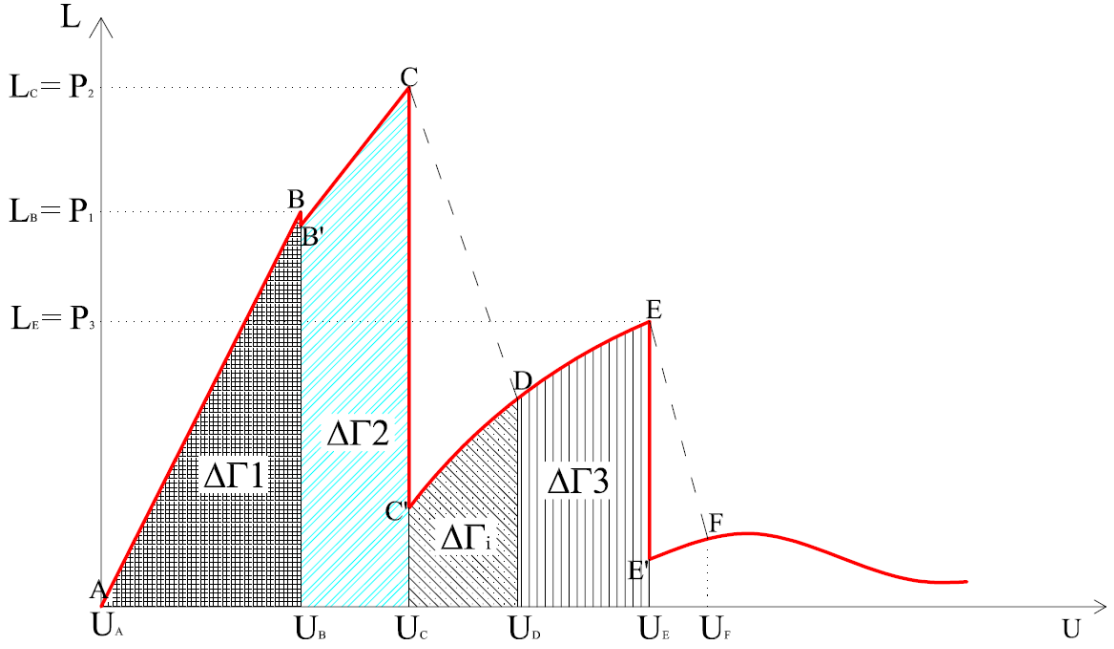

fig. IV.5 - The graph U-L and the dissipated energy shares

4.1.2 Failure modes and fracture definitions

The achievement of the peaks is followed by a fracture development. In this experimental study several fracture typologies have been registered. To permit an easier lecture of the results, the nomenclature used in the chapter for defining the rupture modality is presented herein (*fig. IV.6*)

The *cohesive fracture* (**CF**) , the *adhesive fracture* (**AF**) and the *mixed fracture* (**MF**) have already been presented in the first chapter (par. 1.3.1)[1].

The *prismatic failure* (**PF**) is characterized by the development of a fracture a few centimeters deep inside the fire brick [6]. In this phenomenon a prismatic part of the support, bounded or connected by anchors to the composite sheet, is removed from the fire brick. The experiments have shown that the approximated dimensions of the prism are 4 to 5 [cm] thickness, 12 [cm] width and 20 [cm] length. The prismatic failure takes place in a brittle manner and causes the instantaneous fall to 0 of the load.

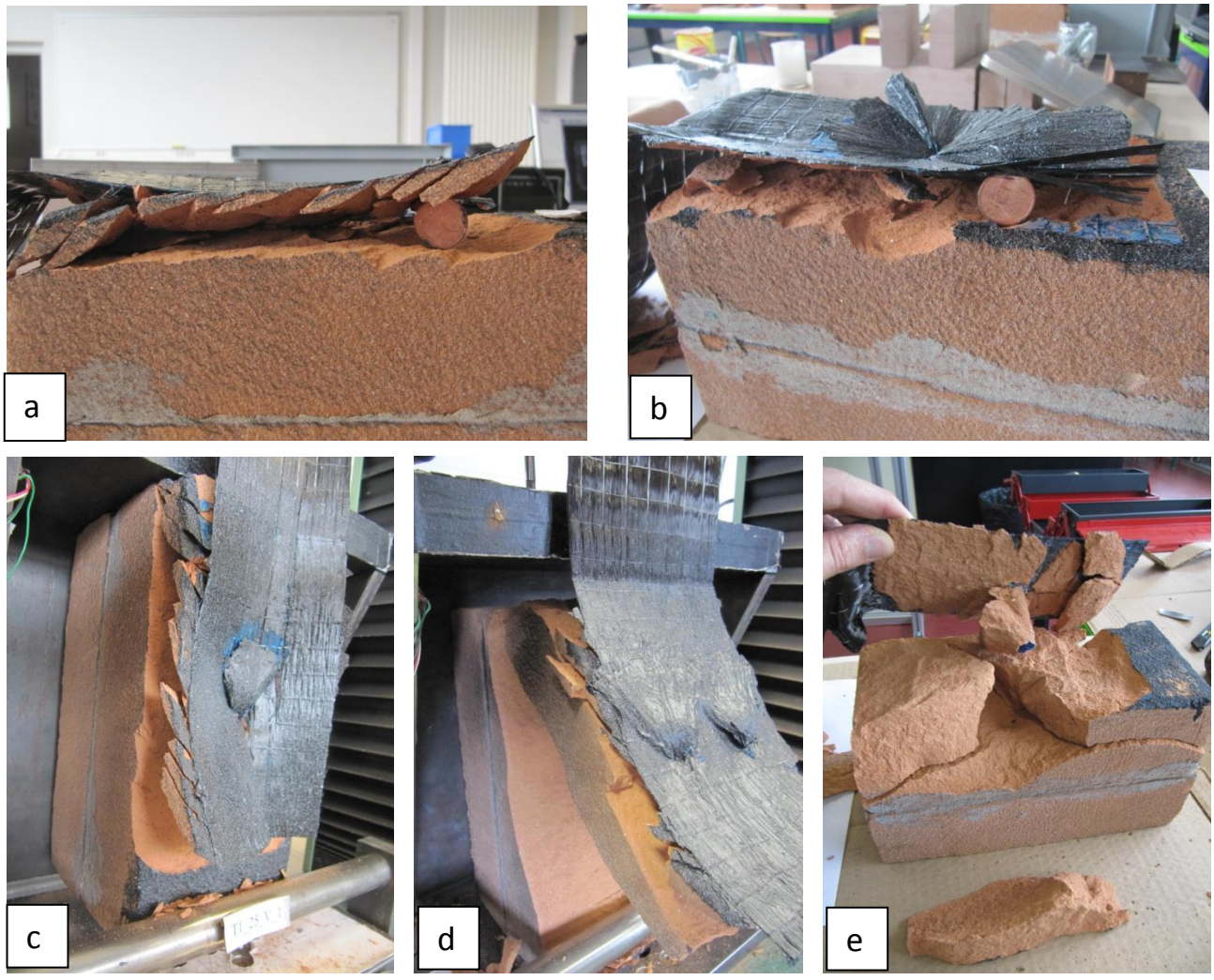

fig. IV.6 - The failure modes; a) Cohesive Fracture (CF), b)Mixed fracture, c) Debonding splay anchor (DSA) allowed after a cohesive fracture, d) Prismatic Failure, e) Pull out nail (PON).

The *Debonding Splay Anchor* (**DSA**) occurs when a delamination between the CFRP sheet and splay anchor is registered. The detachment of the fan anchor permits a consistent slip of the sheet and generates a load drop.

The *Pull Out of the Nail* (**PON**) is a failure modality characterized by the total exit of the anchor from the support; the experimental session has shown that the exit of the carbon nail leads to several prismatic fractures.

4.1.3 Strain field analysis

The displacement fields has been obtained by means of DIC and has been used to calculate the strains. The reference image considered during the correlations corresponds to the frontal photo of the sample subjected to an applied displacement of 0,25 [mm]. The image related to the instant 0 cannot be used as a reference signal because, during the first step of the time history, substantial displacements due to the imperfection of the sample could generate some noise in the results. The displacement and strain fields presented in the following pages are related to some photos taken during the crack advancement phase (stroke B'C).

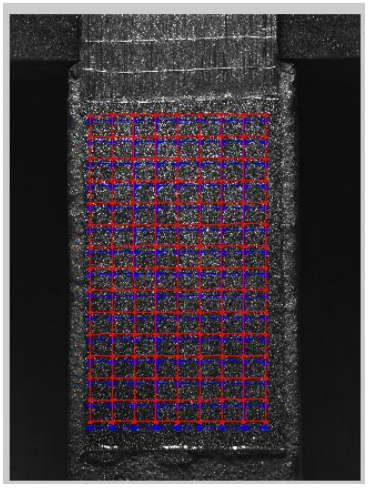

fig. IV.7 - The grid realized onto the Region Of Interest (specimen T0_1)

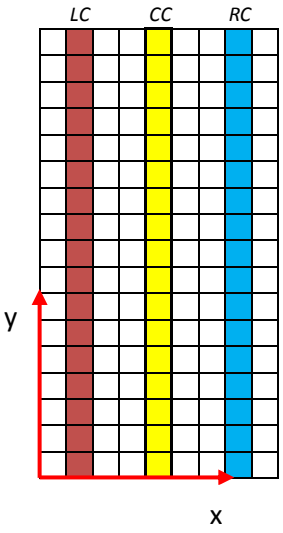

fig. IV.8 - The matrix of values registered in the nodes and the reference axis. The z axis is perpendicular to the plane of the reinforced surface. The left column LC, the central column CC and the right column RC are respectively underlined in red, yellow and blue.

As explained in chapter 3, by using DIC, the values of displacements and strains are obtained for all nodes of a geometrical grid (*fig. IV.7*). This is defined by the correlation parameters illustrated in *par. 3.4*. The values of *u* and *ε* are stored in a matrix made up by *n* lines (i=1, 2, .., n) and *m* columns (j=1,2,…m) (*fig. IV.8*). Each line i corresponds to an ordinate y [mm], likewise each column j corresponds to a coordinate x [mm]. The *figure IV.8* defines the reference axis x, y and z. The latter is perpendicular to the plane of the reinforced surface.

The representation of the curves $y\text{-}\varepsilon_{yy}$ for several load steps reveals the evolution of the strain distribution during the test (*ex. fig. IV.13*). In the next pages the graphs "y-ε" represent the value of the strain along the central column of the matrix defined in *fig. IV.8*. Chromatic bi-dimensional representations in the plane x-y of the fields ε_{yy}, ε_{xx}, u_x, u_y have been realized to present the values registered on all the surfaces analyzed (*ex. fig. IV.14*). A "colorbar" relates each color to a corresponding strain value. Furthermore, tridimensional representations in the space $x\text{-}y\text{-}\varepsilon_{yy}$ and $x\text{-}y\text{-}\varepsilon_{xx}$ have been realized.

4.1.4 The bond stress analysis, the force F_e and the evaluation of the DIC efficiency

The analysis of the bond stress at the interface between the reinforcement and the support enables the description of the stress transfer zone advancement to be made, to verify the displacement of the effective bond length (l_e) and to measure the τ_{zymax} registered during the tests. A study of Carloni et al. [48] underlines that the investigation of the fracture properties of the interface reinforcement-support can be conducted by measuring the strain on the surface of FRP strip. The bond equilibrium law utilized to relate local slip to bond stress at the interface has been defined previously in the equation (3.1) and it has already been used by Corr et al. [47]. This equation helps obtain the matrix of τ_{zy} using the matrix of strain ε_{yy}. The bond equilibrium (3.1) proposed has been developed to study a simple cohesive problem; therefore, it is relevant to analyze the stresses in all the reinforced surface of specimens T0. In the following paragraphs the formula has also been used to evaluate the τ_{zy} on the specimens fastened by anchor/s to define the bond stresses between the CFRP sheet and the support. It should be noted that the method cannot be safely applied to the zone of the nail where the geometry and the stiffness of the reinforcement are different; further studies will be developed to define the stresses in this area.

The bond stress τ_{zy} is represented in the next pages using graphs $y - \tau_{zy}$ (*fig. IV.23*) referred to the Central Column (CC) and 3D representation in the space "$x - y - \tau_{zy}(x,y)$" (*fig. IV.78*).

The matrix of τ_{zy} describes the stress transfer phenomena on all the reinforced surface of specimens T0. Multiplying each τ_{zy} [MPa] of the matrix times the surface of a single square of the correlation grid yields the matrix of the force *f* (eq. (4.3)). The sum of all the elements of this matrix allows for the calculation of the total force F_e transferred between the reinforcement and the support (eq. (4.4)). Therefore, F_e is equal to the volume underlying the surface " x-y-τ_{zy}(x,y)".

$$f(i,j) = \tau_{zy}(i,j) \times (\Delta x \times \Delta y) \tag{4.3}$$

$$F_e = \sum_{\substack{i=1 \\ j=1}}^{\substack{n \\ m}} f(i,j) \tag{4.4}$$

where Δx and Δy are respectively the distance in [mm] between two nodes of the grid along the directions x and y. The comparison of F_e with the load value measured by the universal machine Deltalab (F_D) has enabled the precision of the results obtained by means of Digital Image Correlation to be verified.

4.2 Results of the tests

4.2.1 Series T0

The NES single shear tests executed on specimens T0 have shown a uniform behavior of the samples.

The *figure IV.9* collects the curves U-L obtained testing all the specimens of the series. The slope of the first stroke AB of the curves is almost the same for all the tests T0; it shows that all the specimens of the series have the same stiffness. In all the experiments the behavior of the sample during the application of the load history was the same. In the following the principal phenomenological steps of the tests T0 are described; the underlined values reported herein are "average value". Once the peak P_1 has been achieved (10,30 kN with a standard deviation of 0,83 kN) a first fracture occurs in the loaded side of the specimen; after that, a crack started to advance from loaded to unloaded direction until the attainment of P_2 (12,35 kN with a standard deviation of 1,46 kN**)**. After this peak a brittle fracture was registered. The energy dissipated during the test has been evaluated by computing the surface under each curve. In *figure IV.10* a bar graphs of the dissipated energy is shown.

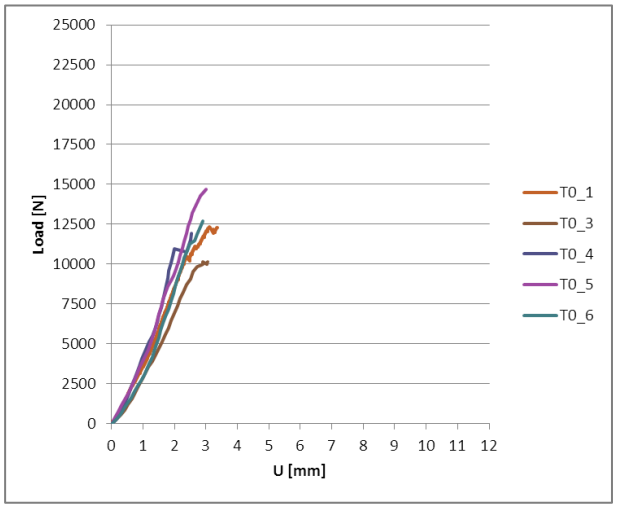

IV.9 - The curves U-L registered during test of series T0

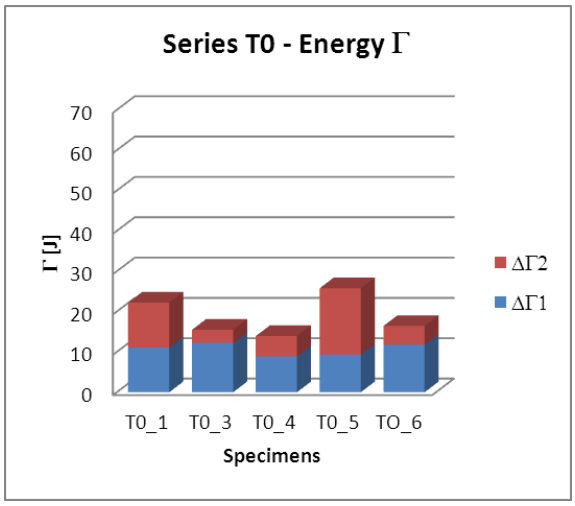

IV.10 The energy dissipated during the tests of series T0

The energy necessary to achieve the fracture in B is on average equal to 10,67 J (standard deviation of 1,32 J). In all the crack advancement phases (stroke B'C) 8,10 J was dissipated (standard deviation of 4,96 J). The value of Γ_{END} up to the debonding failure was on average 18,77 J (standard deviation of 4,49 J). The numerical values and their averages are summarized in *table 4.I*.

table 4.I - Peaks and energy registered during the tests of series T0. The mean values and the standard deviations are also shown.

	u_1 [mm]	P_1 [kN]	$\Delta\Gamma_1$ [J]	u_2 [mm]	P_2 [kN]	$\Delta\Gamma_2$ [J]	$\Delta\Gamma_{end}$ [J]
T0_1	2,38	10,51	11,12	3,36	12,28	11,12	22,23
T0_3	2,72	9,82	12,22	3,05	10,14	3,25	15,47
T0_4	2,00	10,98	8,88	2,53	11,92	5,05	13,92
T0_5	1,89	8,95	9,36	3,00	14,69	16,42	25,78
T0_6	2,50	11,25	11,78	2,89	12,70	4,65	16,43
Average	2,30	10,30	10,67	2,97	12,35	8,10	18,77
St. d.	0,31	0,83	1,32	0,27	1,46	4,96	4,49

Four of the six specimens in series T0 failed with cohesive fractures inside the fire brick. The cracks observed interest a layer under the CFRP of thickness 3-8 mm. The fractures developed during the stroke B'C subdivided the support in more blocks with a "rib" shape.

One of the specimens failed with a mixed fracture characterized by superficial and deep cracks. In all the experiments of series T0 a prism of the support (unloaded extremity), with the approximated dimensions of 1,5 cm thickness and 5 cm length, was removed with the bonded CFRP sheet in the brittle failure. Several photos of the samples T0 after the test are presented in *figure IV.11*. The *table 4.II* attributes a failure mode to each sample.

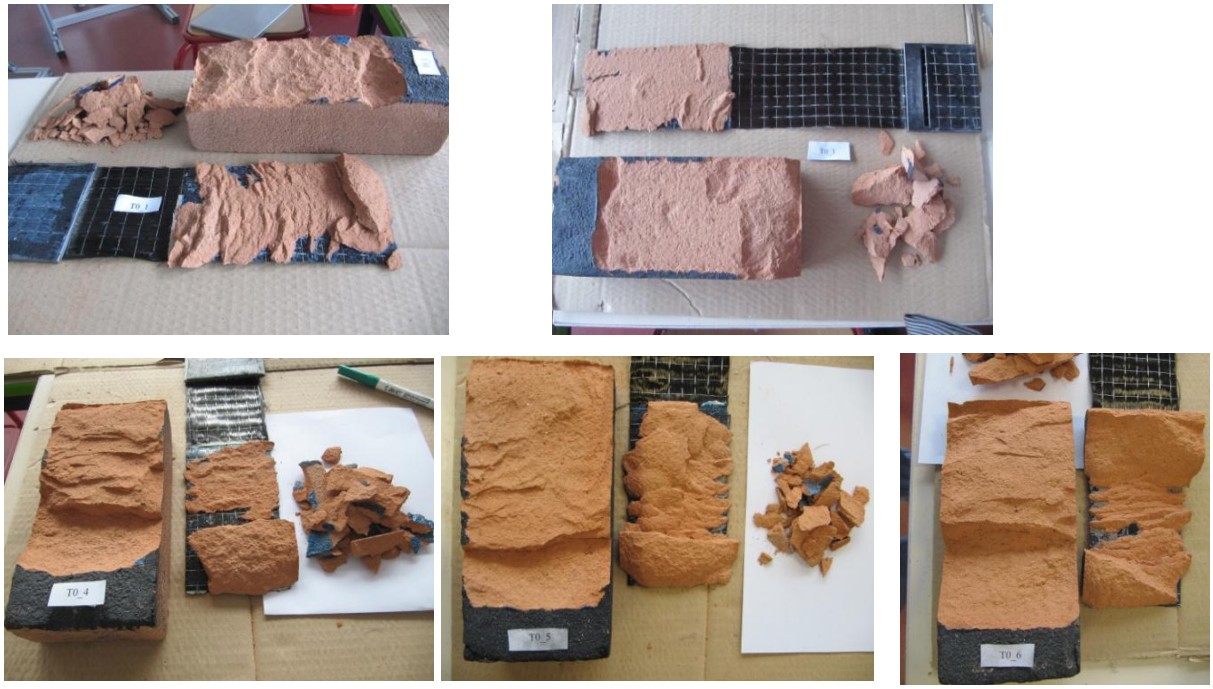

fig. IV.11 - The samples of series T0 after the test (in order T0_1, T0_3, T0_4, T0_5, T0_6)

tab. 4.II - The failure modes of specimens T0

Specimen	*Fracture in C*
T0_1	*CF*
T0_3	*MF*
T0_4	*CF*
T0_5	*CF*
T0_6	*CF*

The strain fields of a representative specimen T0 is presented below (specimen T0_6). These results have been obtained by digital image correlation matching several photos with a reference image. The strain fields presented herein are relative to some instants of the crack advancement process (*fig. IV.12*) and show the migration of the strain transfer zone. The digital image correlation has been realized using a region of interest composed by a grid of squares (128x128 pixel²) composed of 11×17 nodes. The graph of *figure IV.13* shows the values of the strain ε_{yy} in the central column for six different instants of load (tab. 4.I).

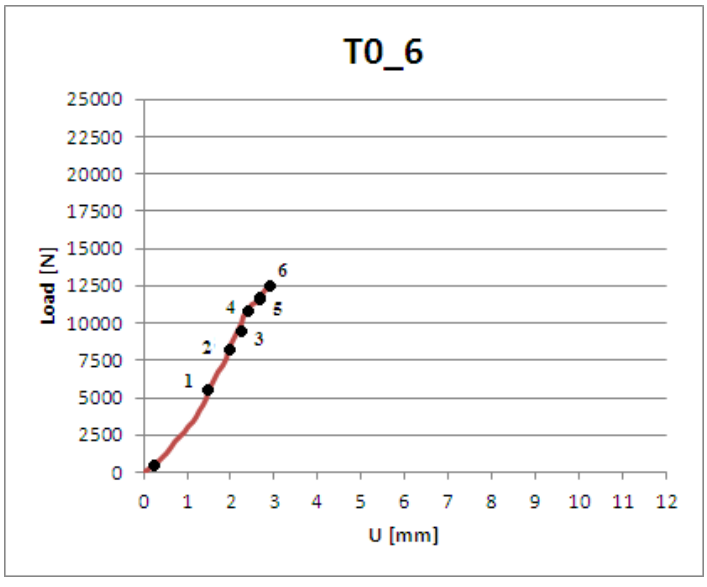

STEP DIC	*L [N]*	*Photo*
refe	*590*	*2*
1	*5400*	*21*
2	*8630*	*29*
3	*9980*	*34*
4	*11250*	*40*
5	*11890*	*43*
6	*12700*	*47*

fig. IV.12 - The graph U-L of the test T0_1. The black points define the instants of load history analyzed by DIC. On the right the table that define the steps (load and corresponding photo) of the analysis reported in this paragraph.

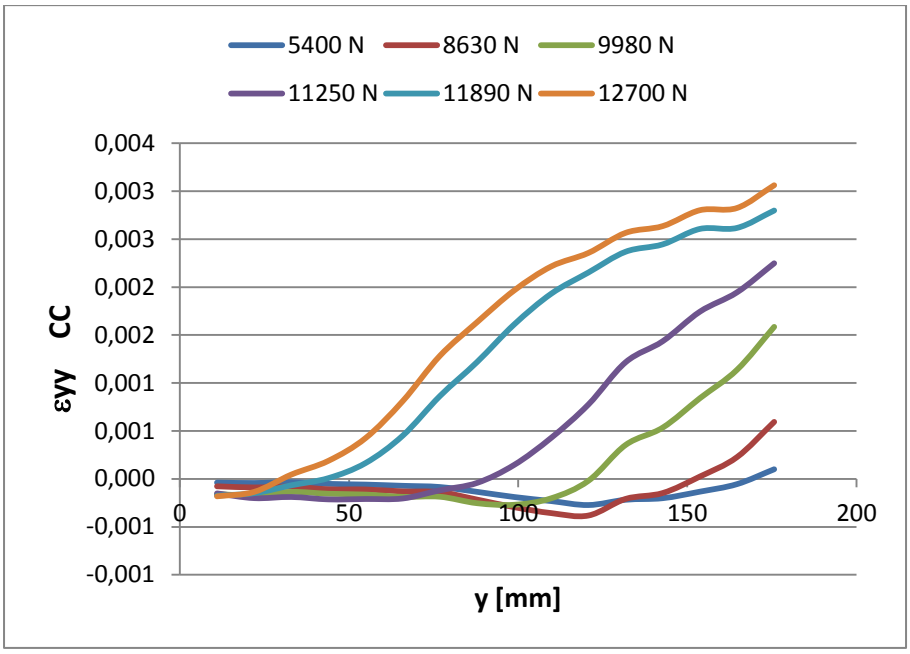

fig. IV.13 - The graphs y[mm]-ε_{yy} of several instants of load history

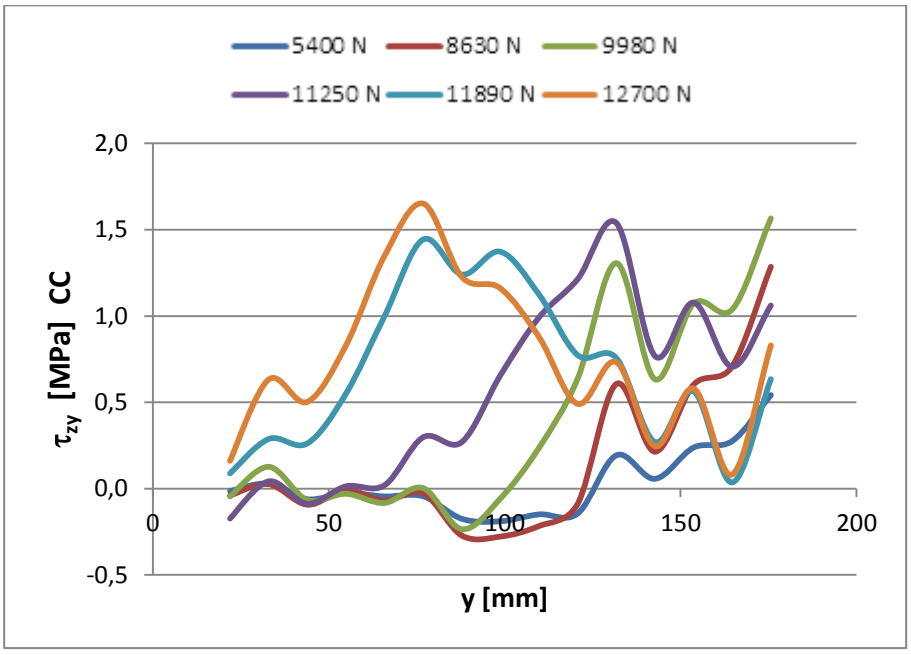

fig. IV.14 - The graphs y [mm] – τ_{zy} of several instants of load history

The *figure IV.13* illustrates the expansion and the migration of the strain transfer zone from the loaded to the unloaded side. This strain field evolution agrees with the literature data presented in the first chapter (*figg. I.26, I.27* and *I.30*). The *figure IV.14* shows the development of the bond stress in the interface CFRP – support. In the first two steps represented the τ_{zy} is localized in a zone close to the loaded side. Once a value of stress approximately equal to 1,5 MPa has been reached

the stress transfer zone moves from the loaded side toward the unloaded side; this is clear as regards the DIC steps 3, 4, 5, 6. It should be noted that the maximum value of t_{zy} registered is approximately equal to the tensile strength of the fire brick. The curves of *figure IV.14* underline that the length, in the y direction, of the stress transfer zone is environ equal to 100 mm; this value could be considered as an approximate experimental measure of the optimal bond length.

The chromatic representations of *figures IV.15* show the ε_{yy} field in four steps of load. In the images the movement of the strain transfer zone is evident. The images highlight a high concentration of strain on the right side. The images related to the ε_{xx} (*fig. IV.16*) show that during the application of the load a contraction of the CFRP sheet in the x direction happens.

A tridimensional representation of the stress bond field during different steps of the test T0_6 is presented in the *paragraph 4.3.3*.

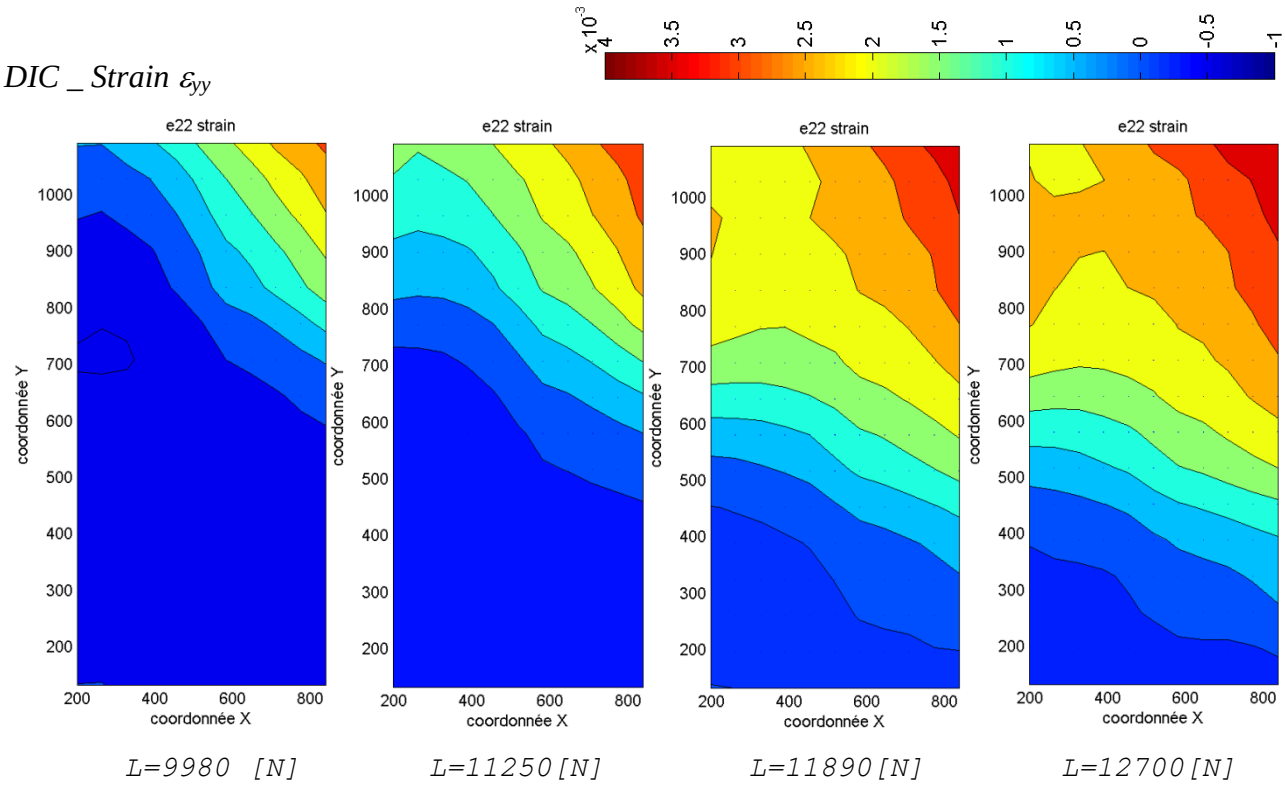

fig. IV.15 - The strain field ε_{yy} of four steps of test T0_6 obtained by Digital Image Correlation

DIC _ Strain ε_{xx}

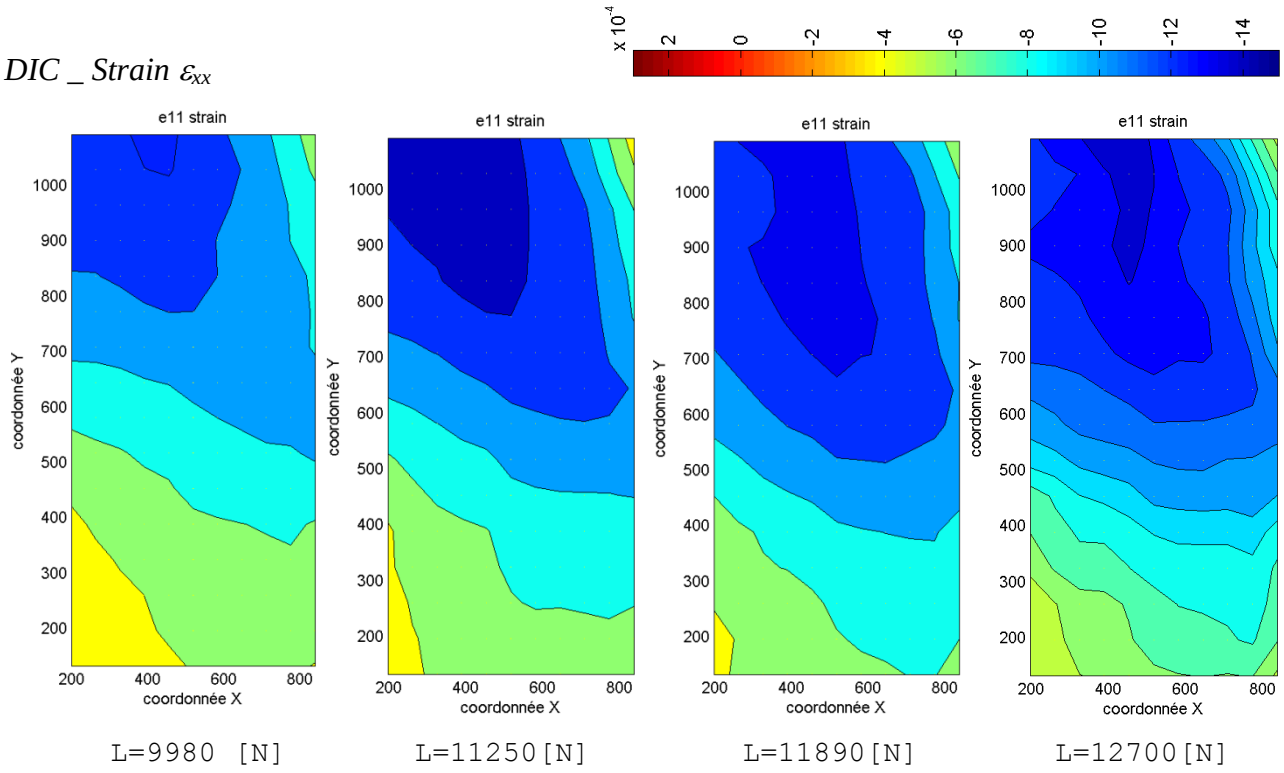

fig. IV.16 - The strain field ε_{xx} of four step of test T0_6 obtained by Digital Image Correlation

4.2.2 Series T1_25_V

The specimens of series T1_25_V present an experimental behavior similar to that exposed in the *fig. IV.1*. As in the series T0 analyzed above, during the tests a first peak P_1 and a second peak P_2 were registered. After the achievement of this second peak, a brittle debonding failure between the CFRP sheet and the fire brick support occurred. In four of six tests of the series T1_25_V the total fall of the load, subsequent to the achievement of P_2, is avoided by the anchor (*fig. IV.17*). In these cases, after the debonding, the anchor remains inserted inside the support and bonded to the surface of the composite sheet. The anchor permits a new increase of load until a peak P_3. When this value was reached the debonding of the CFRP sheet from the anchor splay occurred. Only in the tests T1_25_V_4 and T1_25_V_6 this typology of failure was registered at the same time of the cohesive brittle fracture in C (*fig. IV.1*). It is important to underline that the average value of P_2 registered in this series is equal to 15,49 kN (standard deviation of 0,71 kN); it is 25,46 % higher than that registered in series T0.

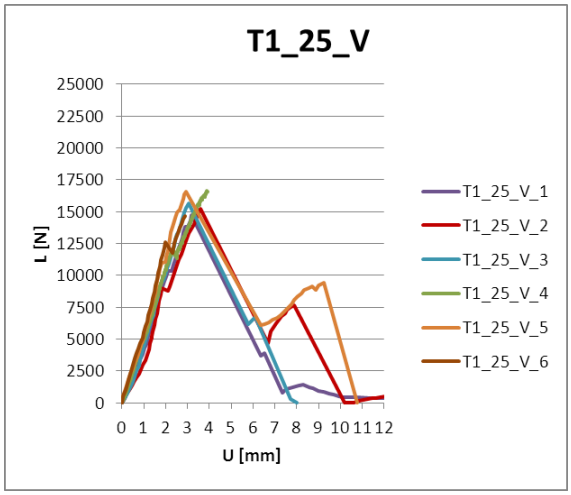

fig. IV.17 - The curves U-L registered during the tests of series T1_25_V

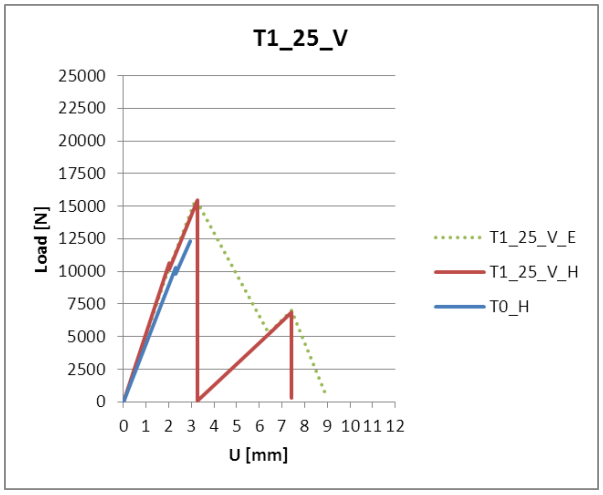

fig. IV.18 - The master curve of specimens T1_25_V compared with that of T0; dotted line is the experimental master curve, red line

The graphs U-L (*fig. IV.17*) show that the first stroke of the curves is almost equal for all the specimens; therefore, all the samples T1_25_V present the same stiffness properties. The "master curve" MC presented in *fig.IV.18* interpolate the curves of the four tests T1_25_V characterized by a residual resistance after peak P_2. The comparison of this master curve with those of T0 shows that the stiffness of the reinforced system fastened by a small anchor is almost equal to that without an anchor. In *figure IV.18* the dotted line represents the interpolation of the experimental data, the red line represents the master curve U-L under the assumption described in *par. 4.1.1*.

The dissipated energy during the tests, subdivided in $\Delta\Gamma_1$, $\Delta\Gamma_2$, $\Delta\Gamma_i$ and $\Delta\Gamma_3$, is represented in the bar graph of *fig. IV.19*. The average energy Γ_{end} is equal to 37,45 J (standard deviation of 10,32 J); it's 99,52 % higher than that of T0.

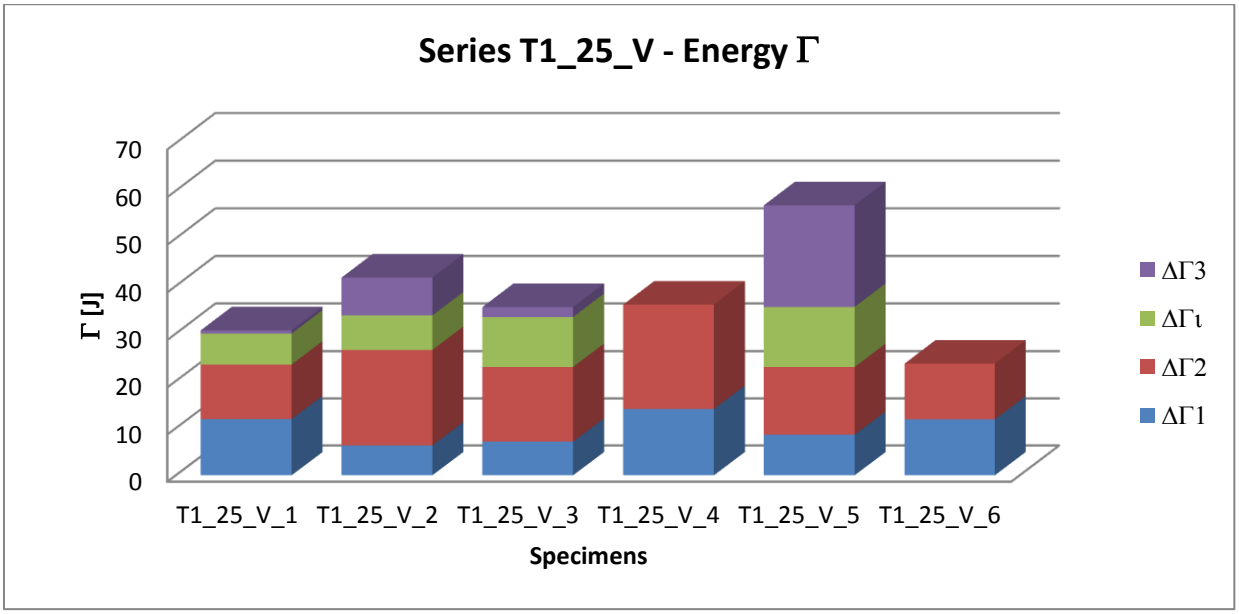

fig. IV.19 - The energy dissipated during the tests of series T1_25_V

The *table 4.III* collects all the numerical values of peaks and energy.

*fig.4.III - Peaks and energy registered during the tests of series T1_25_V. In the table the average and the standard deviation values are also shown. The values signed by a * are obtained considering a population of data composed of only the four tests characterized by a residual resistance.*

	U_1 [mm]	P_1 [kN]	$\Delta\Gamma_1$ [J]	U_2	P_2 [kN]	$\Delta\Gamma_2$ [J]	$\Delta\Gamma_i$ [J]	U_3 [mm]	P_3 [kN]	$\Delta\Gamma_3$ [J]	Γ_{end} [J]
T1_25_V_1	2,29	10,35	11,93	3,20	14,71	11,56	6,51	6,52	3,89	0,69	30,68
T1_25_V_2	1,84	8,99	6,33	3,57	15,18	20,22	7,26	7,89	7,65	7,94	41,75
T1_25_V_3	1,78	9,36	7,14	3,05	15,61	15,85	10,50	6,10	6,74	2,07	35,55
T1_25_V_4	2,34	11,92	14,07	3,91	16,57	22,00	-	-	-	-	36,08
T1_25_V_5	1,81	10,6	8,59	2,95	16,2	14,36	12,64	9,23	9,06	21,33	56,93
T1_25_V_6	2,00	12,59	11,87	2,91	14,67	11,81	-	-	-	-	23,68
average	2,01	10,64	9,99	3,26	15,49	15,97	9,23*	7,44*	6,84*	8,01	37,45
ST.d.	0,23	1,28	2,81	0,36	0,71	3,95	2,48*	1,23*	1,89*	8,16	10,32

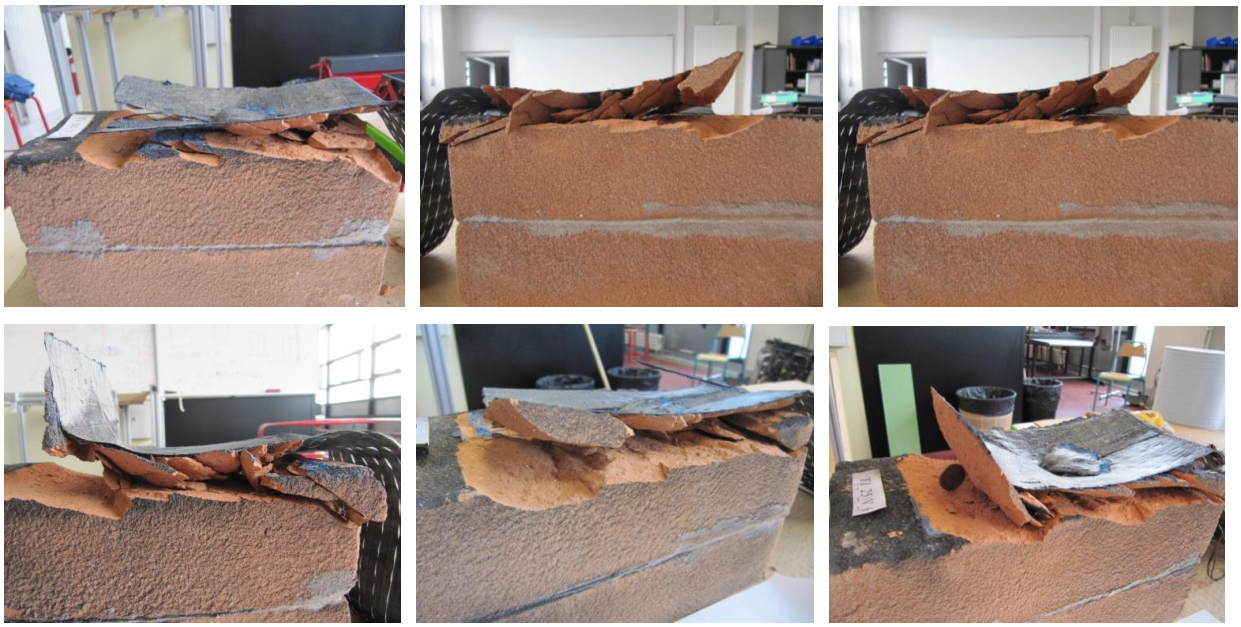

fig. IV.20 - The samples of series T1_25_V after the test (in order T1_25_V_1, T1_25_V_2, T1_25_V_3, T1_25_V_4, T1_25_V_5, T1_25_V_6)

Two principal types of failure have been recorded (*fig. IV.20*); the debonding in point C, and the anchor failure in E (*fig. IV.1*). In the point C a cohesive fracture was observed in all tests; it was characterized by deep cracks in a layer of 5-8 mm tick under the CFRP sheet. As in series T0 a prism was removed by the CFRP from the unloaded end. The anchor failures of all the tests occurred by a brittle debonding between the sheet and the splay anchor (*table 4.IV*).

*Table 4.IV - The failure modes of specimens T1_25_*V

Specimen	*Fracture in C*	*Fracture in E*
T1_25_V_1	CF	DSA
T1_25_V_2	CF	DSA
T1_25_V_3	CF	DSA
T1_25_V_4	CF - DSA	-
T1_25_V_5	CF	DSA
T1_25_V_6	CF - DSA	-

The strain field of a representative specimen of series T1_25_V is analyzed herein. The sample studied below is the T1_25_V_5. The strain values have been obtained by DIC matching more photos corresponding to several load steps (*fig. IV.21*) with a reference signal.

The *figure IV.22* and the chromatic representations of image *IV.27* show that the strain ε_{yy} increases, in a first time, only on the loaded side. When the applied load grows the strained zone moves from

the loaded to the unloaded side. It's interesting to underline that the zone between 0 < y < 5 [cm] is characterized by a ε_{yy} almost equal to zero.

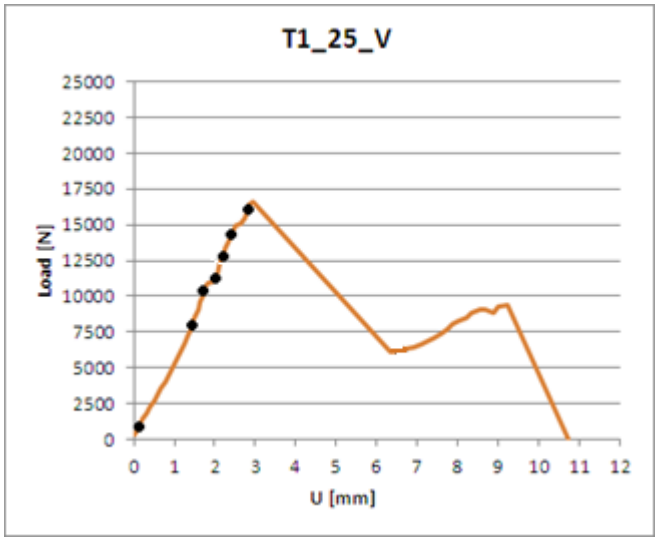

STEP DIC	L [N]	photo
refe	1020	2
1	7790	27
2	10600	36
3	11130	39
4	13010	45
5	14760	50
6	15990	54

fig. IV.21 - The graph U-L of the test T1_25_V_5. The black points define the instants of load history analyzed by DIC. On the right the table that define the steps (load and corresponding photo) of the analysis reported in this paragraph.

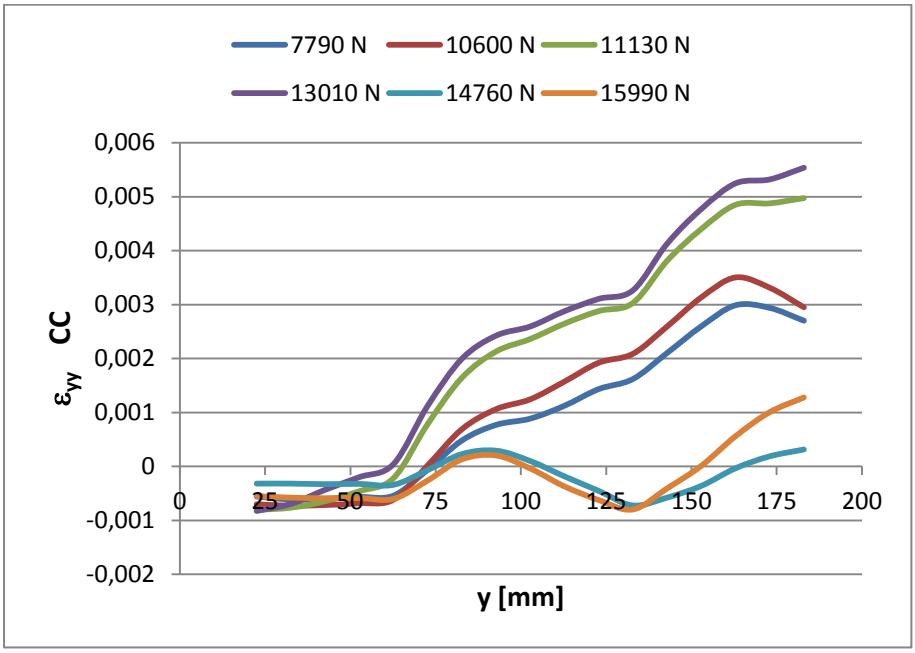

fig. IV.22 - The graphs y[mm]-ε_{yy} of several instants of load history (the results refer to the central column)

The presence of the anchor modifies the classical distribution of the bond stresses shown in the previous case T0 and, consequently, influences the propagation of the stress transfer zone. Regarding the values of $\tau_{zy}(x,y)$ along the central axis of the composite (*fig. IV.23)* it is possible to

define two stress concentration zones; one is before the nail ($y_b \approx 140$ mm), the other after ($y_a \approx 65$ mm). The graphs y - $\tau_{zy}(x,y)$ CC (*fig.IV.23*) shown that in the first steps of load, the peak of the bond stress registered in y_b is bigger than that measured in y_a (see the steps corresponding to 7790 and 10600 N). The increment of the applied load allows an increment of the bond stress in y_a, this last overcome the value of τ_{zy} in y_b (see the steps corresponding to 11130, 13010, 14760 and 15990 N). The contribution of the anchor is less remarkable on the lateral side of the composite surface (columns LC and RC of the matrix of data defined in *par. 4.1.3*). The *fig. IV.24* and *IV.25* show a more homogeneous distribution of the stresses in column LC and RC. A comparison between the distribution of stresses along y in the central, left and right columns is presented in *figure IV.26*. This shows that the nail allows the development of a high stress concentration in front of and behind itself in the central axis of the composite (x = 50 [mm]). On the lateral side of the reinforcement (x = 10 [mm] and x = 90 [mm]) the stresses have values smaller than that registered in the central axis and, moreover, a more homogeneous distribution; here the influence of the anchor is low.

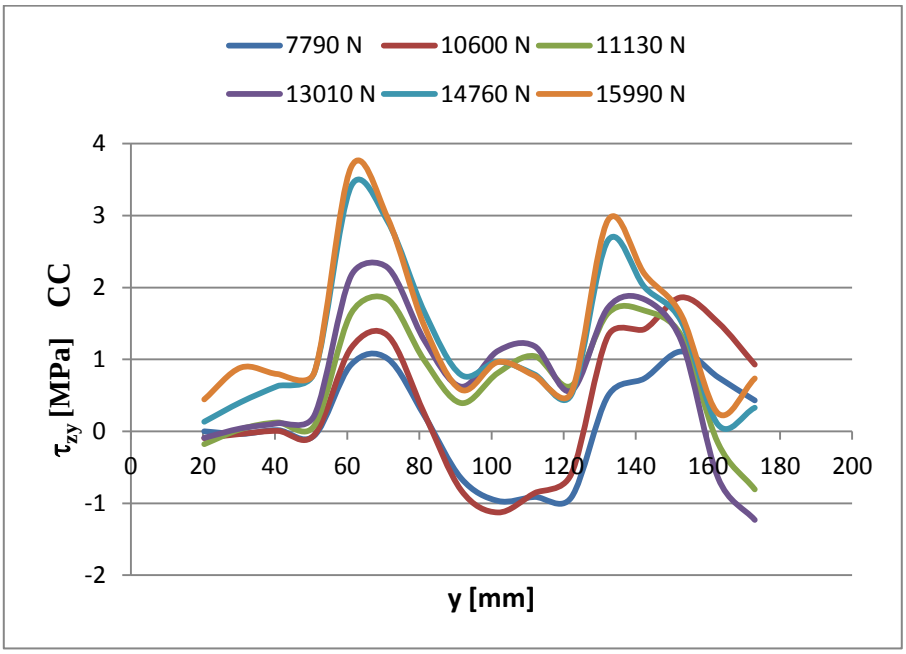

fig. IV.23 - The graphs y [mm] - τ_{zy} of several instants of load history (Central Column, x=50 [mm])

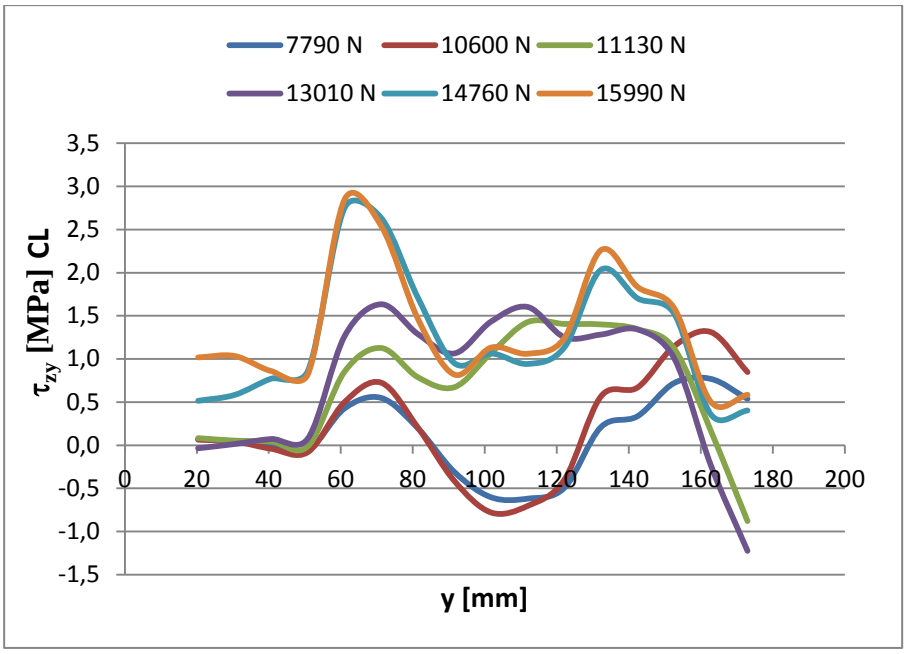

fig. IV.24 - The graphs y [mm] – τ_{zy} of several instants of load history (Left Column, x=10 [mm])

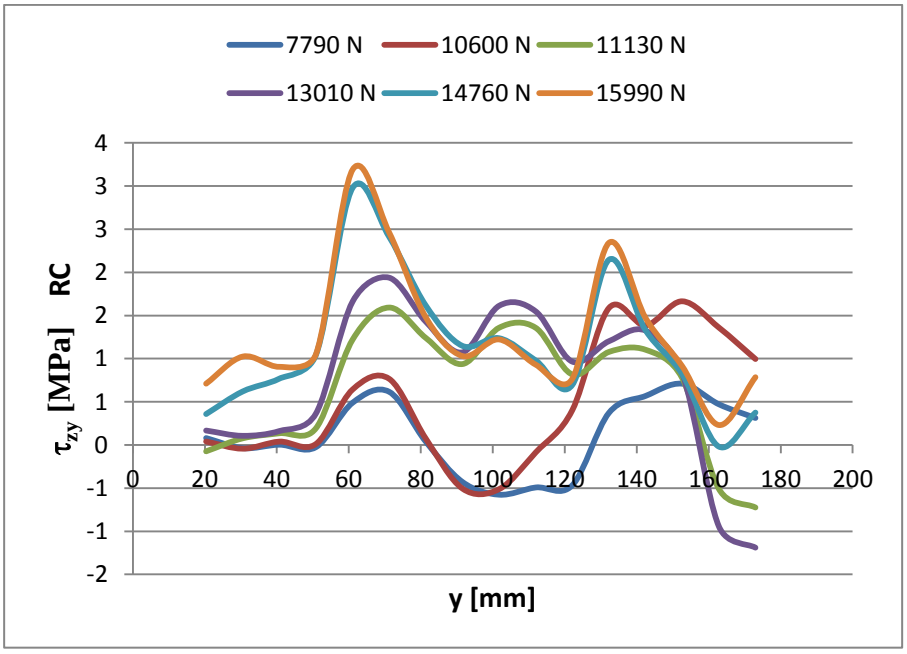

fig. IV.25 - The graphs y [mm] - τ_{zy} of several instants of load history (Right Column, x=90 [mm])

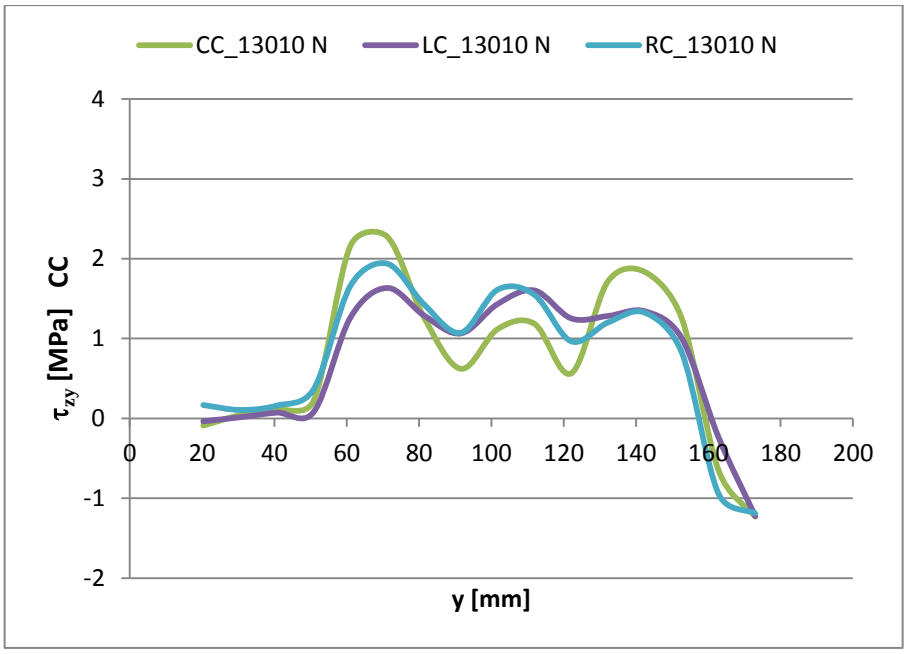

fig. IV.26 - The graphs y [mm] - τ_{zy} in the step L=13010 N for the line x=10 [mm] (Left Column), x=50 [mm] (Central Column) and x=90 [mm] (Right Column)

The chromatic representations of the strain fields ε_{yy} and ε_{xx}, corresponding to four load steps, are presented herein. The images show that in the y direction the strain progressively grows with load remaining almost zero on the unloaded side. In the x direction, a contraction of the composite versus the anchor occurs (*fig. IV.28)*.

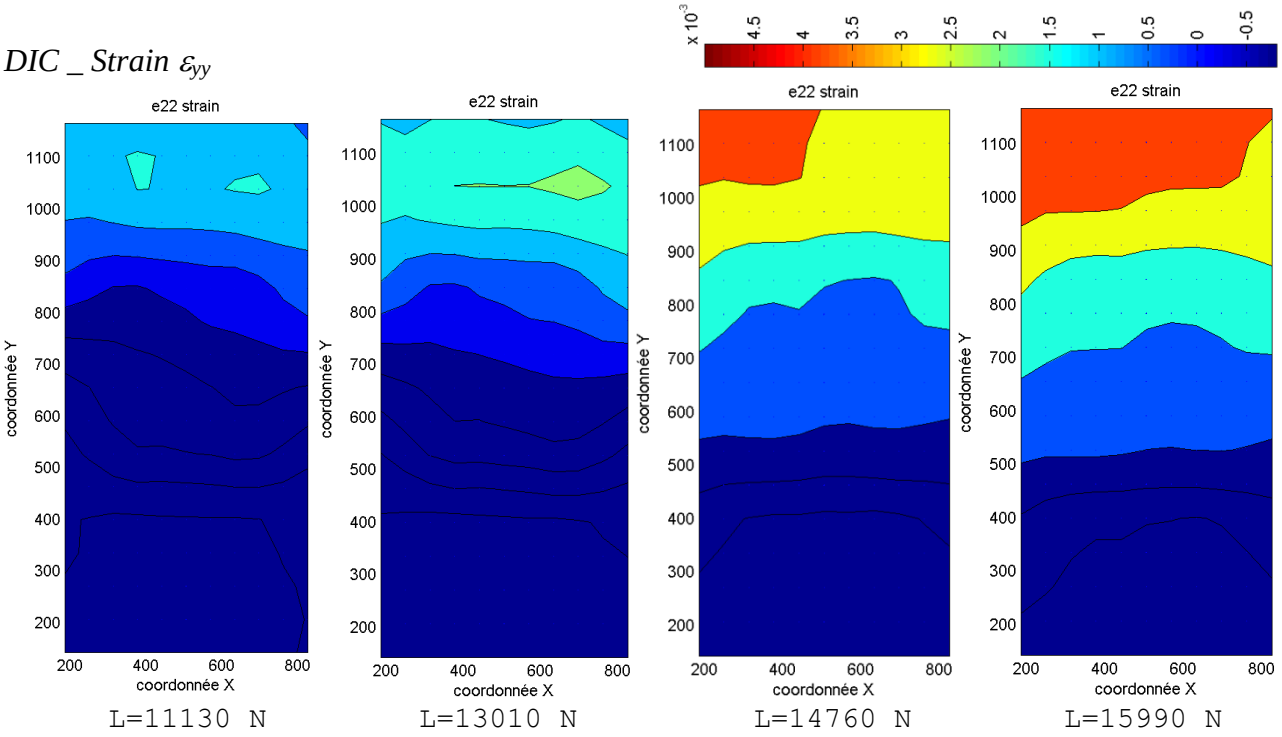

fig. IV.27 - The strain ε_{yy} of four steps of test T1_25_V_5 obtained by Digital Image Correlation

DIC _ Strain ε_{xx} (after "lissage")

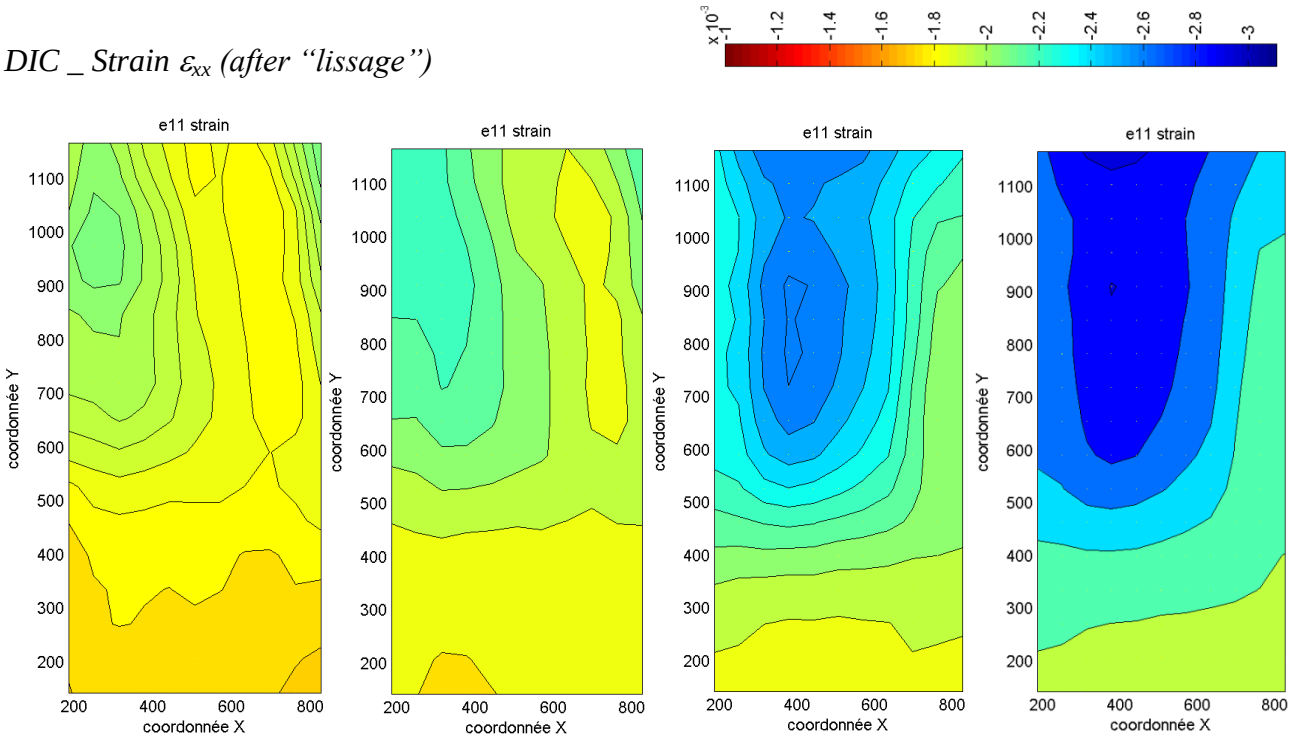

L=11130 N L=13010 N L=14760 N L=15990 N

fig. IV.28 - The strain ε_{xx} of four steps of test T1_25_V_5 obtained by Digital Image Correlation

4.2.3 Series T1_40_O

The test curves U-L of specimens T1_40_O are represented in figure *fig.IV.29*. The average values of the peaks P_1, P_2 are respectively 11,38 kN (standard deviation of 2,05 kN) and 15.66 kN (standard deviation of 0,59 kN). The average value P_3 has been obtained using the data of the statistical population only composed of the four tests T1_40_O_1/3/4/5 that are characterized by an anchor loading phases after the achievement of peak P_2. The average value of P_3 calculated is equal to 8,47 kN (standard deviation of 1,44 kN).

The average peak P_2 registered during the series T1_40_O is 26,83% bigger than that noticed in tests T0. The specimens T1_40_O_2 and T1_40_O_6 do not present a loading anchor phase after the achievement of P_2. The master curve MC represented in *figure IV.30* has been realized by interpolation of the T1_40_O experimental curves neglecting the samples T1_40_O_2/6.

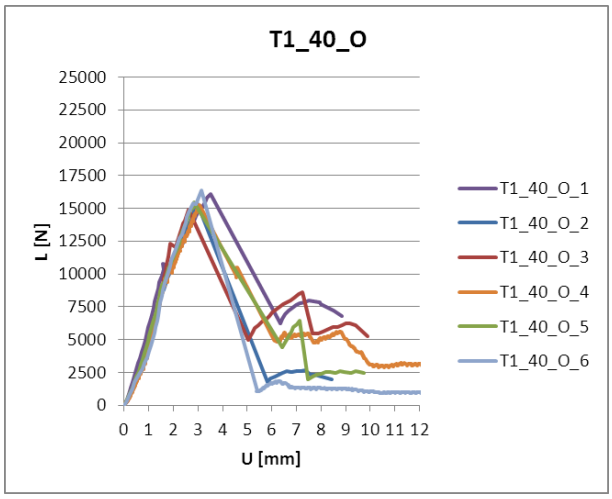

fig. IV.29 - The curves U-L registered during test of series T1_40_O

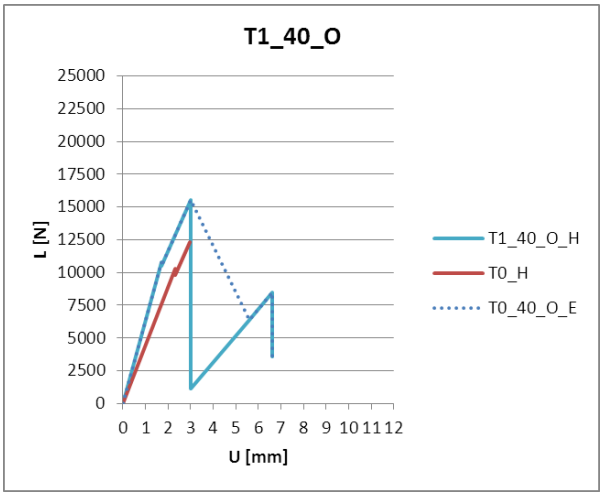

fig. IV.30 - The master curve of specimens T1_40_O compared with that of T0; dotted line is the experimental master curve, the blue line is the MC, the red line is the MC of series T0

The stroke slopes AB of the several tests represented in *figures IV.29* show that the specimens T1_40_O are characterized by the same stiffness properties. Furthermore, the comparison of master curves *(fig. IV.30)* demonstrates that the samples T1_40_O are stiffer than the sample TO. The values of dissipated energy portions are plotted in the *figure IV.31* using bar graphs. The average energy Γ_{END} dissipated to generate the total failure of the reinforcement is equal to 36,19 J, value characterized by a standard deviation of 12,89 J. The average Γ_{END} obtained for the series T1_40_O is 92,80 % greater than that of series T0.

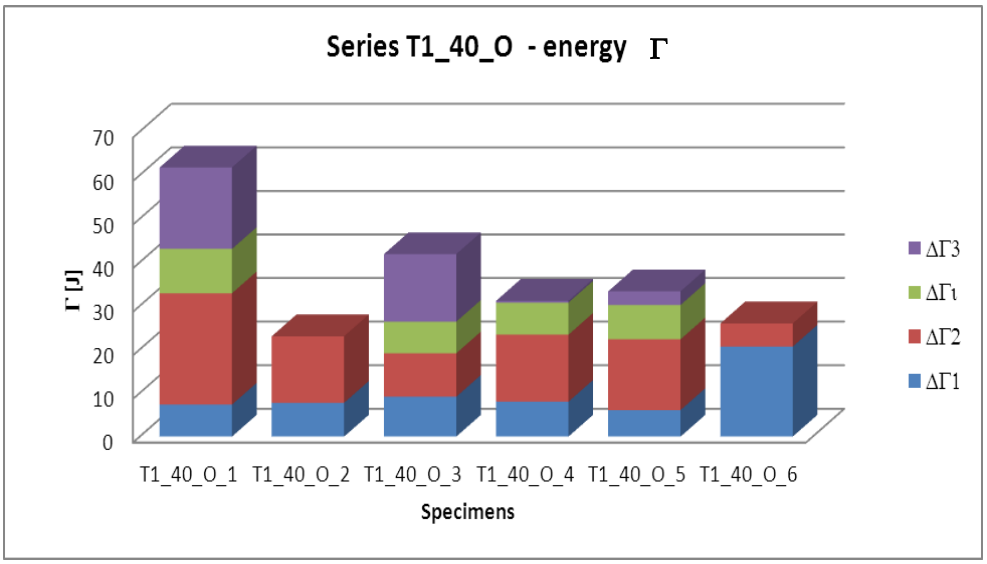

fig. IV.31 - The energy dissipated during the tests of series T1_40_O

The *table 4.V* collects all the numerical values of the peaks and the energy.

*tab. 4.V - Peaks and energy registered during the tests of series T1_40_ O. The values signed by a * are obtained considering a population of data composed of only the four tests characterized by a residual resistance.*

	U_1 [mm]	P_1 [kN]	$\Delta\Gamma_1$ [J]	U_2	P_2 [kN]	$\Delta\Gamma_2$ [J]	$\Delta\Gamma_i$ [J]	U_3 [mm]	P_3 [kN]	$\Delta\Gamma_3$ [J]	Γ_{END} [J]
T1_40_O_1	1,56	11,19	7,34	3,52	16,52	25,55	10,16	7,50	8,40	18,70	61,76
T1_40_O_2	1,75	9,75	7,77	2,97	15,45	15,25	-	-	-	-	23,02
T1_40_O_3	1,87	12,30	9,15	2,63	14,88	9,97	7,26	7,22	8,60	15,50	41,88
T1_40_O_4	1,83	10,46	8,01	3,05	15,28	15,38	7,35	4,58	10,49	0,43	31,17
T1_40_O_5	1,54	9,18	6,10	2,86	15,46	16,24	7,89	7,14	6,41	3,11	33,34
T1_40_O_6	2,81	15,38	20,65	3,15	16,36	5,32	-	-	-	-	25,97
average	1,89	11,38	9,84	3,03	15,66	14,62	8,17*	6,61*	8,47*	9,43*	36,19
St.d.	0,43	2,05	4,92	0,27	0,59	6,21	1,18*	1,18*	1,44*	7,81*	12,89

The failure modes observed after the achievement of the peak P_2 are the cohesive (CF) and the mixed fracture (MF) (*fig. IV.32* and *tab.4.VI*) . The MF was manifested only during the test T1_40_O_2, confirming the hypothesis that during this experiment a peeling load component was developed.

The experiments show that the debonding of 360° splay anchor occurs in a ductile manner. When the peak P_3 was achieved, approximately 150° of the opening anchor fan, splayed in the same direction of load, was detached from the support (*fig. IV.33*). After the load fall registered in E (*fig. IV.1*) a residual resistance was recorded; this is due to the remaining bonded part of the splay anchor and to the friction between the faces of fracture. In this phases, the application of load allows a progressive debonding of the fan anchor and the opening of the CFRP sheet in correspondence with the central longitudinal axis in the unloaded side (*fig. IV.34*).

fig. IV.32 - The samples of series T0 after the test (in order T1_40_O_1, T1_40_O_2, T1_40_O_3, T1_40_O_4, T1_40_O_5, T1_40_O_6)

Tab 4.VI - The failure modes of specimens T1_40_O

Specimen	*Fracture in C*	*Fracture in E*
T1_40_O_1	CF	DSA
T1_40_O_2	MF+DSA	-
T1_40_O_3	CF	DSA
T1_40_O_4	CF	DSA
T1_40_O_5	CF	DSA
T1_40_O_6	CF-DSA	-

fig. IV.33 - The specimen T1_40_O_2 after the achievement of the peak P_3

fig. IV.34 - The specimen T1_40_O_3 during the post P_3 phases

The strains field and the stress bond field analysis of the reference specimen T1_40_O_5 is presented below. The *fig. IV.35* shows the graph U-L and the steps of load history studied by digital image correlation. The reference image used to correlate each deformed images is photo 2.

The graphs y-ε_{yy} (relative to the central column, x=50 [mm]) show that in the first steps the zone interested by the strain is close to the loaded side. The load increment leads ε_{yy} to become higher and to evolve from the loaded to the unloaded side. This phenomenological evolution is evident in *figure IV.36* and in the chromatic representations of *figure IV.39*.

The stress bond field is described by the curves of figures *IV.37* and *IV.38*. The firsts steps are characterized by a stress transfer zone placed close to the loaded side. In the next instants of load history the τ_{zy} increases and a concentration of stresses is recorded in two zones; before (y_b = 50 mm) and after (y_a = 125 mm) the anchor. The difference between the peak registered in y_b and that measured in y_a became smaller as the load applied increases. However, the τ_{zy} measured in y=50 mm is always smaller than that measured in y = 125 mm. The curves τ_{zy} referred to the right column (x = 90 mm), are similar to that traced for the CC (x = 50 mm) - (*figure IV.38 and IV.37)*. Afterward, the bond stress value is almost constant along the x direction.

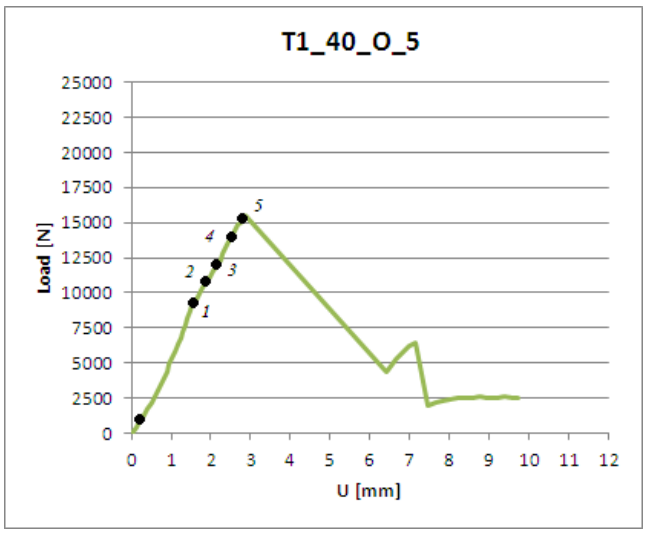

STEP DIC	L [N]	photo
refe	890	2
1	9180	24
2	11160	29
3	12340	32
4	14000	36
5	15070	39

fig. IV.35 - The graph U-L of the test T1_40_O_5. The black points define the instants of load history analyzed by DIC. On the right the table that define the steps (load and corresponding photo) of the analysis reported in this paragraph.

The ε_{xx} are negative during all the test. In the last step represented in the chromatic representation of the strain field ε_{xx} (*fig.IV.40*) the contraction of the composite and, in particular of the fan anchor is remarkable.

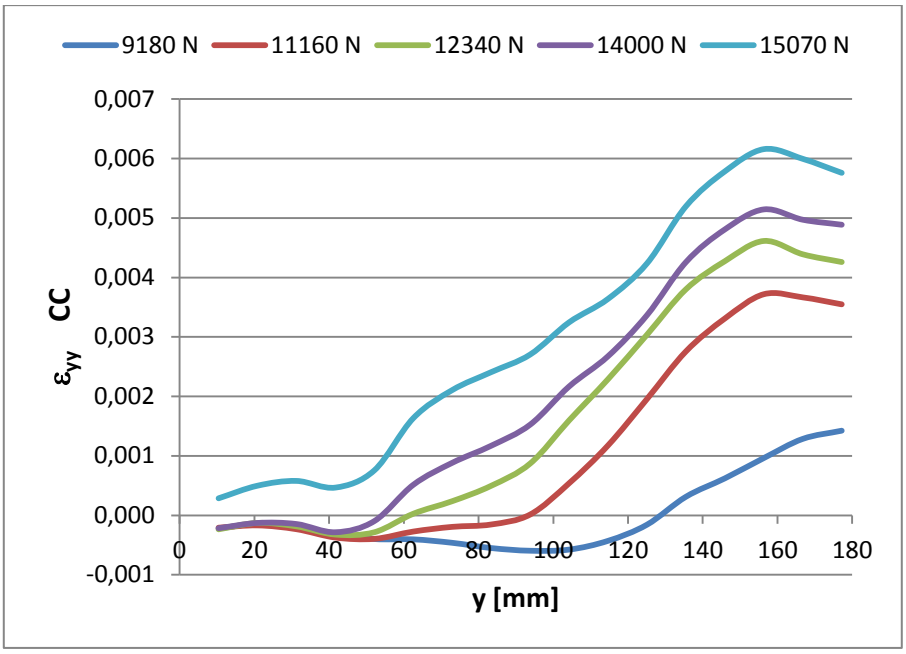

fig. IV.36 - The graphs y-ε_{yy} of several instants of load history (the results refer to the central column)

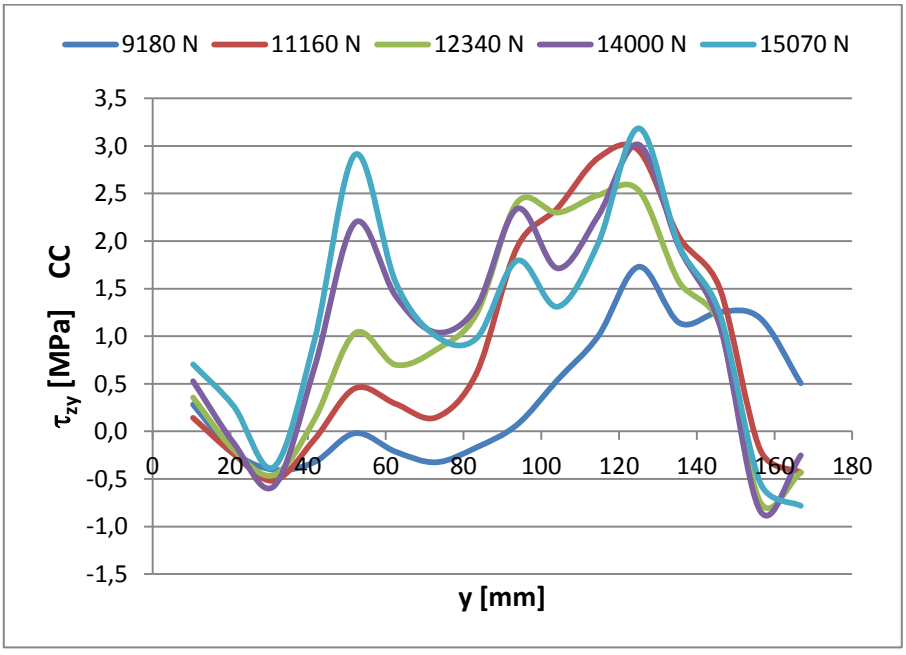

fig. IV.37 - The graphs y-τ_{zy} of several instants of load history (the results refer to the central column, x= 50 mm)

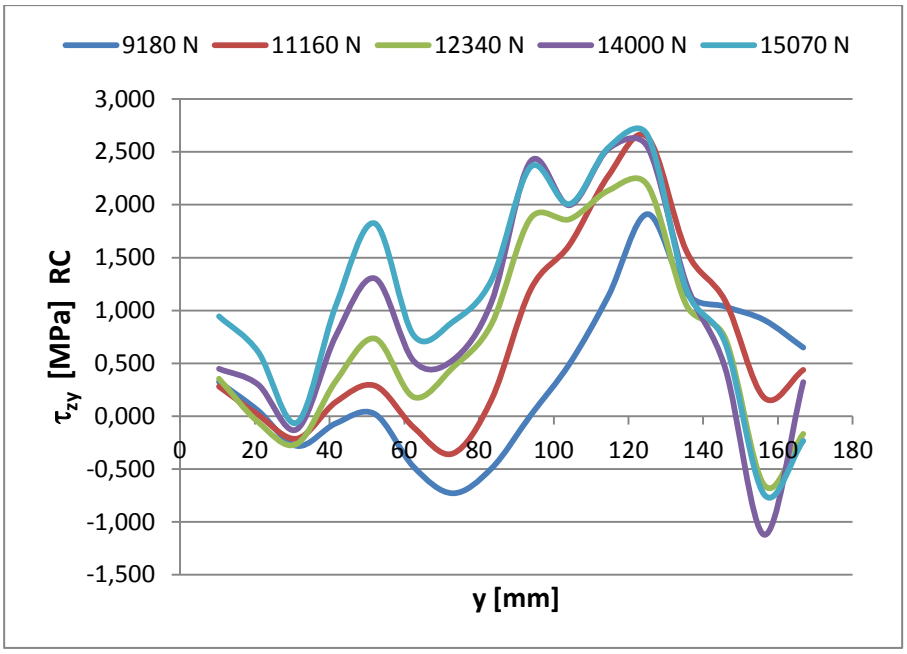

fig. IV.38 -The graphs y-τ_{zy} of several instants of load history (the results are refer to the right column, x=90 mm)

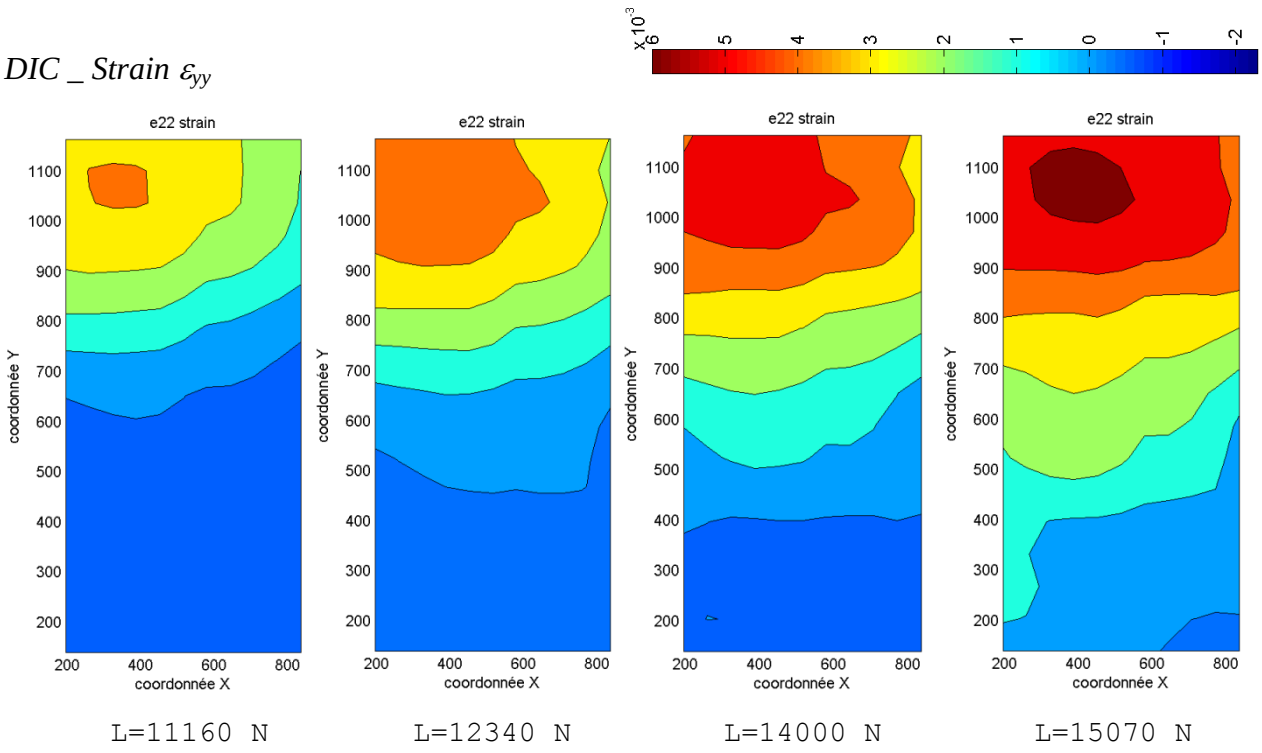

fig. IV.39 - The strain field ε_{yy} measured by digital image correlation in four steps of test T1_40_O_5.

DIC _ Strain ε_{xx}

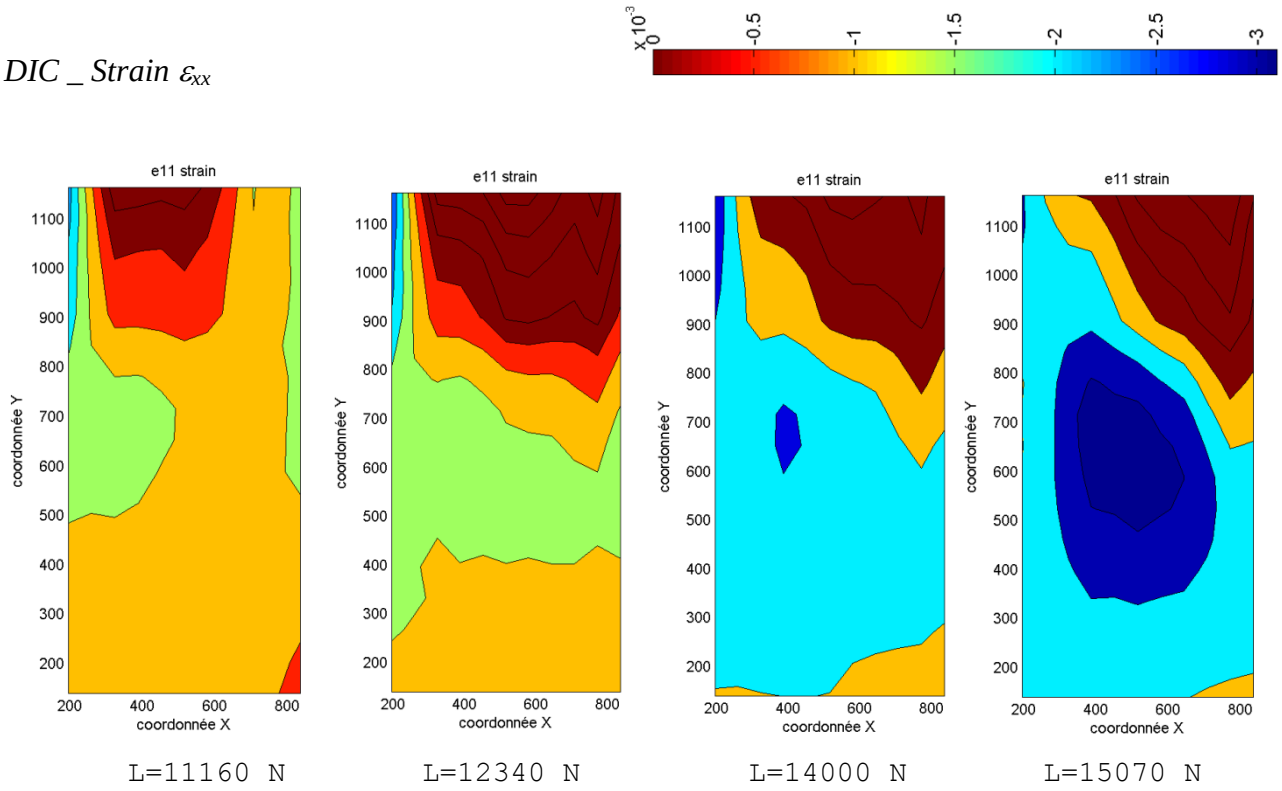

fig. IV.40 - The strain field ε_{xx} measured by digital image correlation in four steps of test T1_40_O_5.

4.2.4 Series T1_40_V

The curves U-L of the series T1_40_V are represented in *fig. IV.41* In four tests of this set a further loading phase after the peak P_2 has been registered. The specimens characterized by this residual resistance (T1_40_V_1/2/3/6) have graphs U-L similar to that presented in the preceding paragraphs referring to fire brick fastened with one anchor. Specifically, after a first stroke AB, and achieving the value P_1, the crack advances from the loaded to unloaded side. Once the value P_2 has been reached, a load fall and a successive anchor loading phase leads to the achievement of the peak P_3. The loading phase DE (*fig. IV.1*) of the tests T1_40_V_1, T1_40_V_2 and T1_40_V_3 shows two peaks; these are produced by a debonding splay anchor which occurred in two successive steps (*figures IV.43*). The specimen T1_40_V_4 achieves the failure in P_2 when a cohesive fracture together with a debonding splay anchor occurs (*fig. IV.41*). The sample T1_40_V_5 fails in a brittle manner; in this test once the maximal peak has been achieved, a prismatic fracture has developed. The average peaks P_1 and P_2 registered in this series are respectively equal to 10,05 [kN] (with a standard deviation of 0,62 kN) and 16,16 [kN] (standard deviation of 0,54 kN). The average of peak P_3 is equal to 10,10 [kN] (standard deviation of 1,69 kN). This value has been calculated considering a statistical population of tests only composed of the four specimens T1_40_V_1, T1_40_V_2, T1_40_V_3 and T1_40_V_6. The values related to the same set of specimens have been utilized to realize the master curve (MC) of *fig. IV.42*.

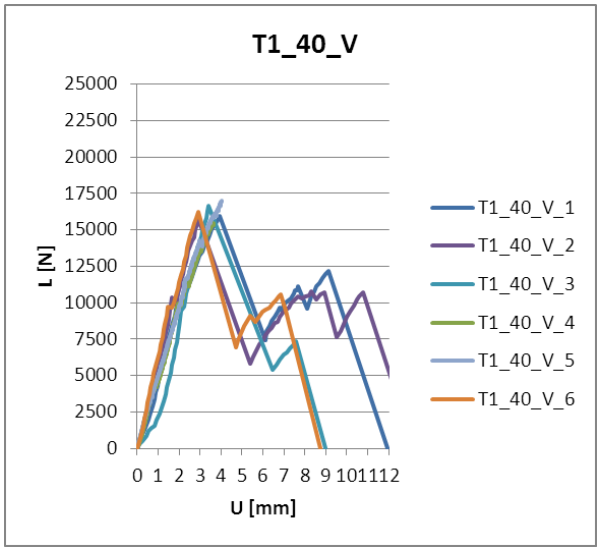

fig. IV.41- The curves U-L registered during test of series T1_40_V

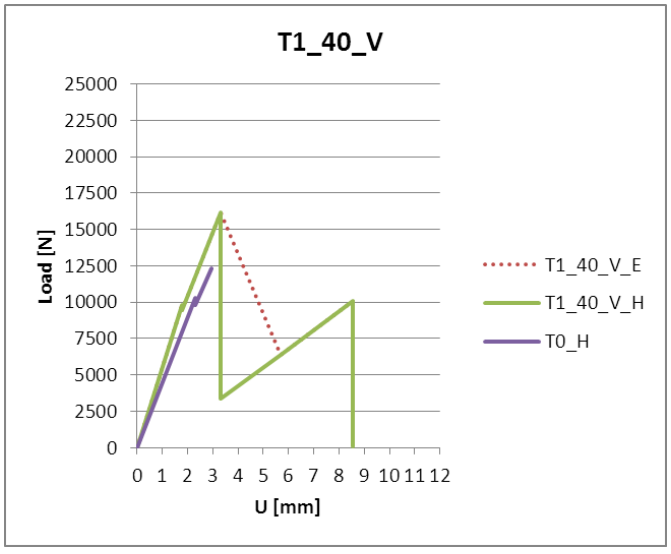

fig. IV.42 - The master curve of specimens T1_40_V compared with that of T0; dotted line is the experimental master curve, the green line is the MC

The stroke slopes AB of the tests (*fig. IV.41)* show that the specimens T1_40_V are characterized by the same stiffness properties K. This value is greater than that registered during the series T0 *(fig.IV.42).*

tab. 4.VII - Peaks and energy registered during the tests of series T1_40_V. In the last two lines the average and standard deviation of the values are tabulated. The numbers marked with an asterisk have been obtained from a population composed of only the specimens T1_40_V_1/2/3/6.

	U_1 [mm]	P_1 [kN]	$\Delta\Gamma_1$ [J]	U_2	P_2 [kN]	$\Delta\Gamma_2$ [J]	$\Delta\Gamma_i$ [J]	U_3 [mm]	P_3 [kN]	$\Delta\Gamma_3$ [J]	Γ_{end} [J]
T1_40_V_1	1,87	9,58	8,24	3,96	15,95	26,68	19,39	9,14	11,92	26,30	80,60
T1_40_V_2	1,68	10,38	7,96	2,92	15,72	15,68	17,15	10,77	10,71	43,87	84,66
T1_40_V_3	2,10	9,44	6,70	3,43	16,64	17,24	16,98	7,58	7,34	7,05	47,97
T1_40_V_4	1,97	9,94	9,33	3,64	15,43	21,11	-	-	-	-	30,44
T1_40_V_5	2,30	11,26	13,04	4,05	17,02	25,22	-	-	-	-	38,26
T1_40_V_6	1,48	9,72	6,85	2,90	16,22	17,80	15,74	6,76	10,44	21,74	62,13
Average	1,90	10,05	8,69	3,48	16,16	20,62	17,31*	8,56*	10,10*	24,74*	57,34
St. d.	0,27	0,62	2,14	0,45	0,54	4,12	1,31*	1,53*	1,69*	13,14*	20,36

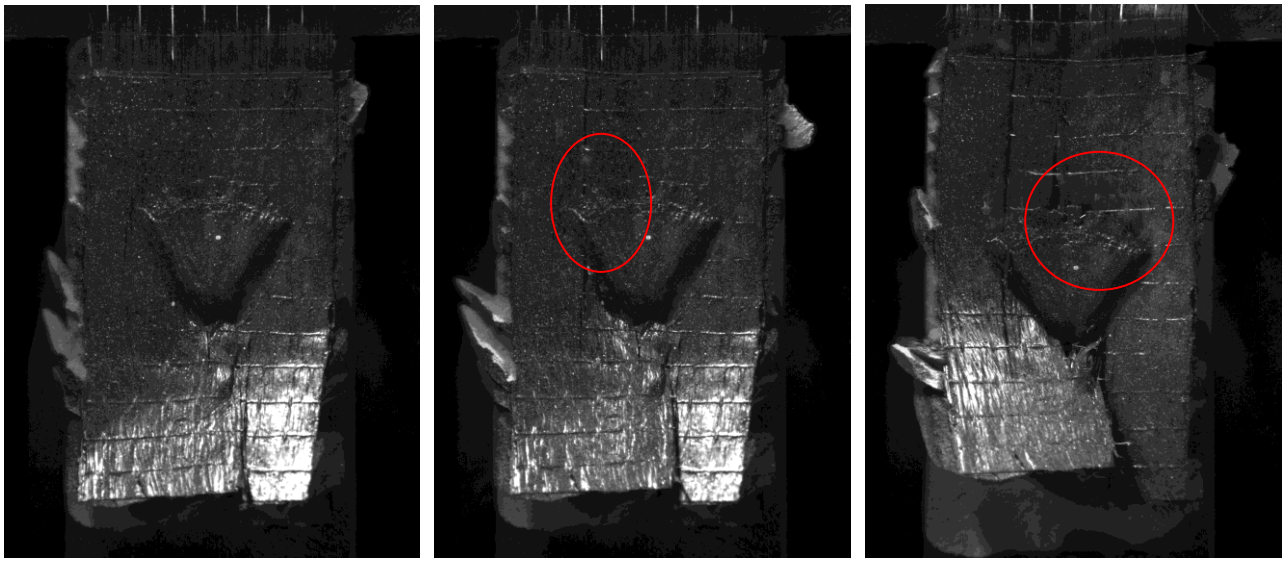

fig. IV.43 - Three frontal images of the specimen T1_40_V_1 during the test. In the first photo the anchor is totally bonded to the CFRP sheet. In second photo the first partial fan debonding is shown. In the third photo the total debonding splay is evident. The "debonding splay anchor" happens in two moments justifying the two peak registered in the phase DE.

The average delta energy $\Delta\Gamma_1$, $\Delta\Gamma_2$ and $\Delta\Gamma_3$ necessaries to achieve the peaks are respectively equal to 8,69 J (with a standard deviation of 2,14 J), 20,62 J (with a standard deviation of 4,12 J) and 24,74 J (with a standard deviation of 13,14 J). The average quantity of energy dissipated at the end of the test (Γ_{END}) is equal to 57,34 J (with a standard deviation of 20,36 J). The *figure IV.44* shows a

bar graph of the amount of energy ΔΓ related to each specimen of the series T1_40_V. The *table 4.VII* collects all the numerical values of peaks and energy.

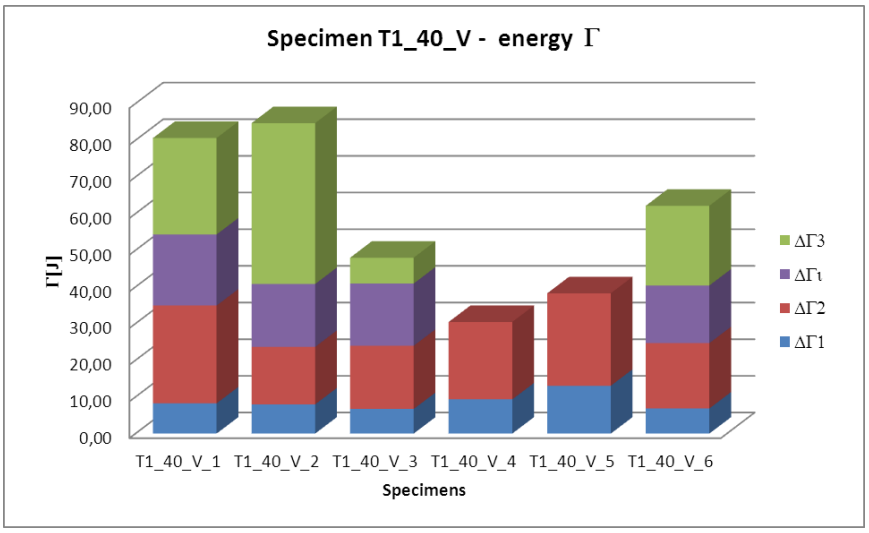

fig. IV.44 - The energy dissipated during the tests of series T1_40_V

Several failure modalities have been observed during the tests (*fig. IV.45* and *tab. 4.VIII*). The experiments T1_40_V_1, T1_40_V_3 and T1_40_V_6 have been characterized by a cohesive fracture in C and an anchor splay debonding in E. The specimen T1_40_V_2 failed by a Mixed Failure in C and a Pull Out of Nail (PON) in E. In this test the anchor was released from the support breaking the fire brick into prisms. The specimen T1_40_V_4 experienced a fall of load in C due to a contemporary cohesive and anchor splay debonding fracture. The sample T1_40_V_5 fails in C with a prismatic failure, in this case no crack advancement phase has been registered.

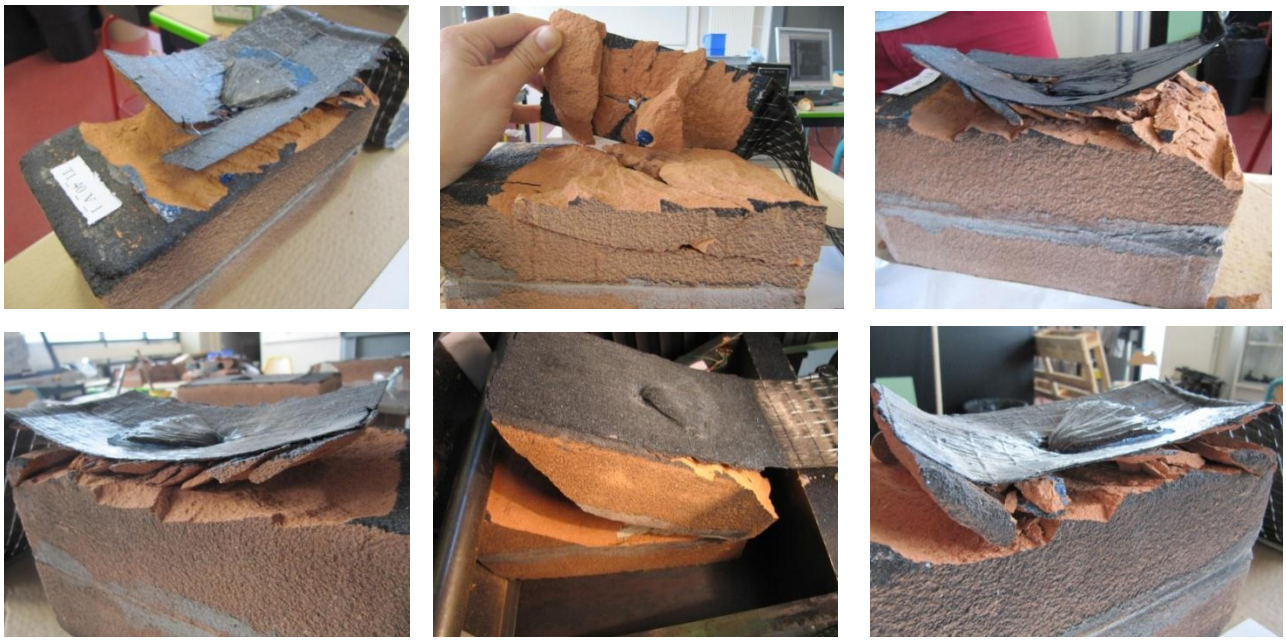

fig. IV.45 - The samples of series T0 after the test (in order T1_40_V_1, T1_40_V_2, T1_40_V_3, T1_40_V_4, T1_40_V_5, T1_40_V_6)

tab. 4.VIII - The failure modes of specimens T1_40_V

Specimen	*Fracture in C*	*Fracture in E*
T1_40_V_1	CF	DSA
T1_40_V_2	MF	PON
T1_40_V_3	CF	DSA
T1_40_V_4	CF - DSA	-
T1_40_V_5	PF	-
T1_40_V_6	CF	DSA

The strain and the stress field of the specimen T1_40_V_6 are reported below. The reference and the deformed photos utilized in the DIC correlation procedure are defined in the U-L graph and in the table of *figures IV.46*.

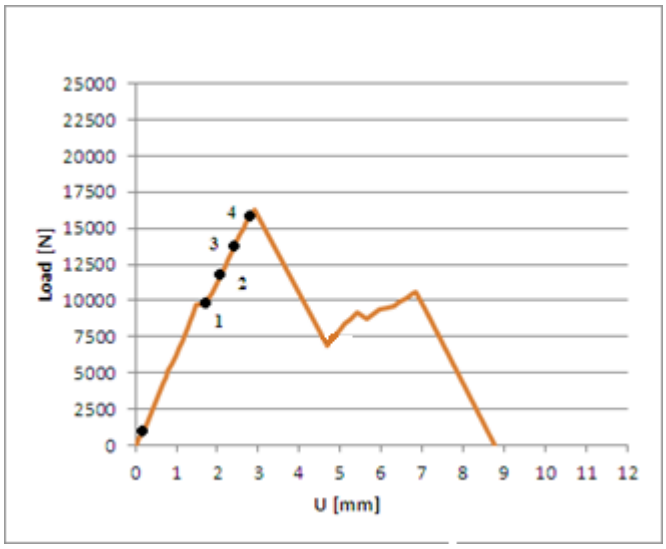

STEP DIC	*L [N]*	*photo*
refe	*1000*	*2*
1	*9680*	*31*
2	*11880*	*38*
3	*13750*	*44*
4	*15830*	*52*
5	*6930*	*54*

Fig. IV.46 - The graph U-L of the test T1_40_V_6. The black points define the instants of load history analyzed by DIC. In the right the table that define the steps (load and corresponding photo) of the analysis reported in this paragraph.

The evolution of the strain values, related to the central column CC (x=50 mm), are represented in *figure IV.47*. The first step (L=9680 N) shows a concentration of strain in the loaded side of the specimen. When the applied load increases, the ε_{yy} CC increase. All the curves represented have a low slope in correspondence to the fastened zone. On the unloaded side of the specimen, a small value of strain has been registered during all the steps represented.

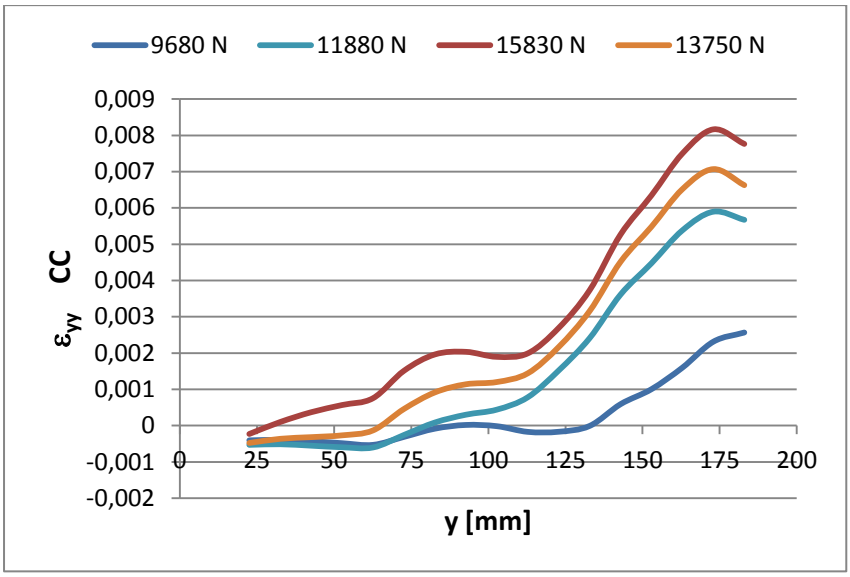

fig. IV.47 - The graphs y-ε_{yy} of several instants of load history (the results refer to the central column)

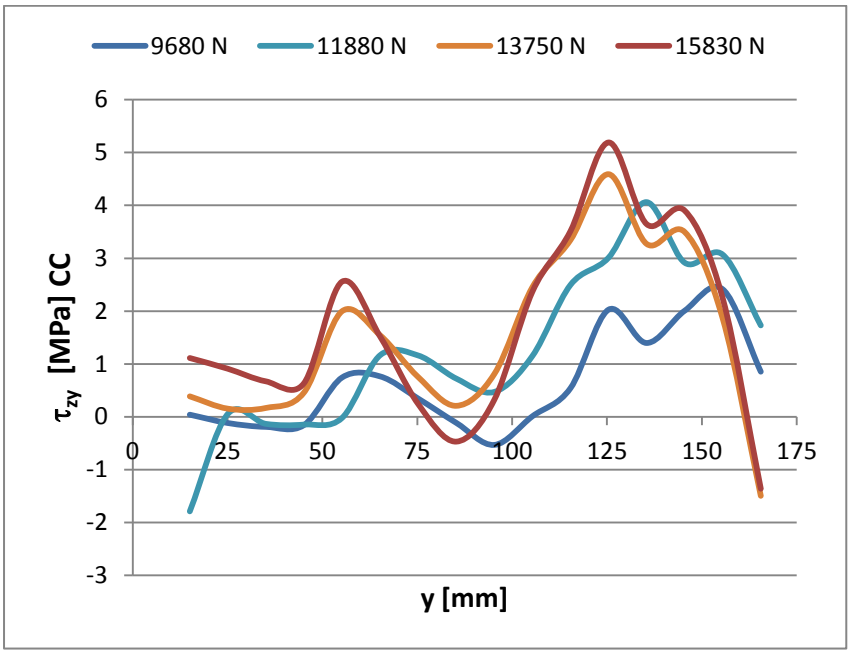

fig. IV.48 - The graphs y-τ_{zy} of several instants of load history (the results refer to the central column)

The *figure IV.48* shows the bond stresses obtained using the equation (3.1). It is evident that initially a concentration of stresses is present in the loaded end of the specimen. The value of τ_{max} increases in the succession of steps, while the stress transfer zone moves from the loaded extremity toward the anchor area. In the unloaded side of the sample, in the zone between the extremity and the anchor, a small stress transfer area has been calculated ($50 < y < 75$ mm).

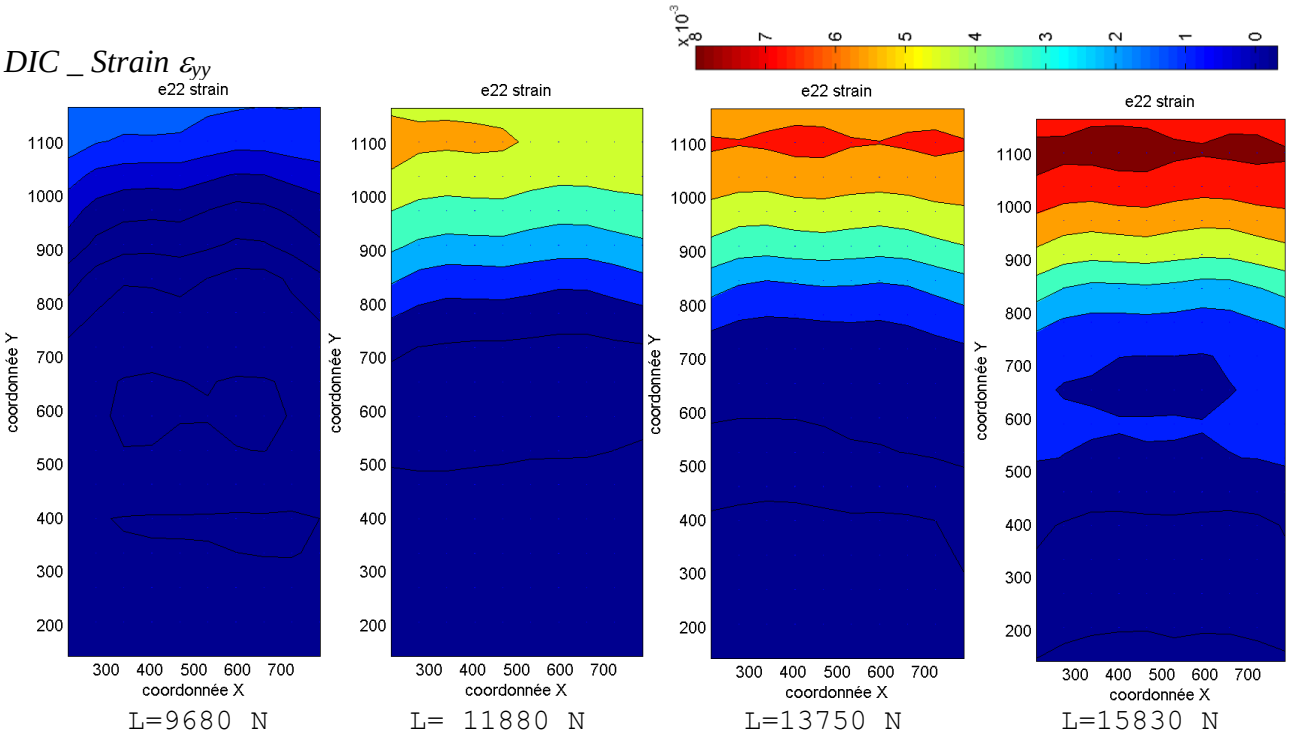

fig. IV.49 - The strain field ε_{yy} measured by means of CORRELI^{GD} in four steps of test T1_40_V_6

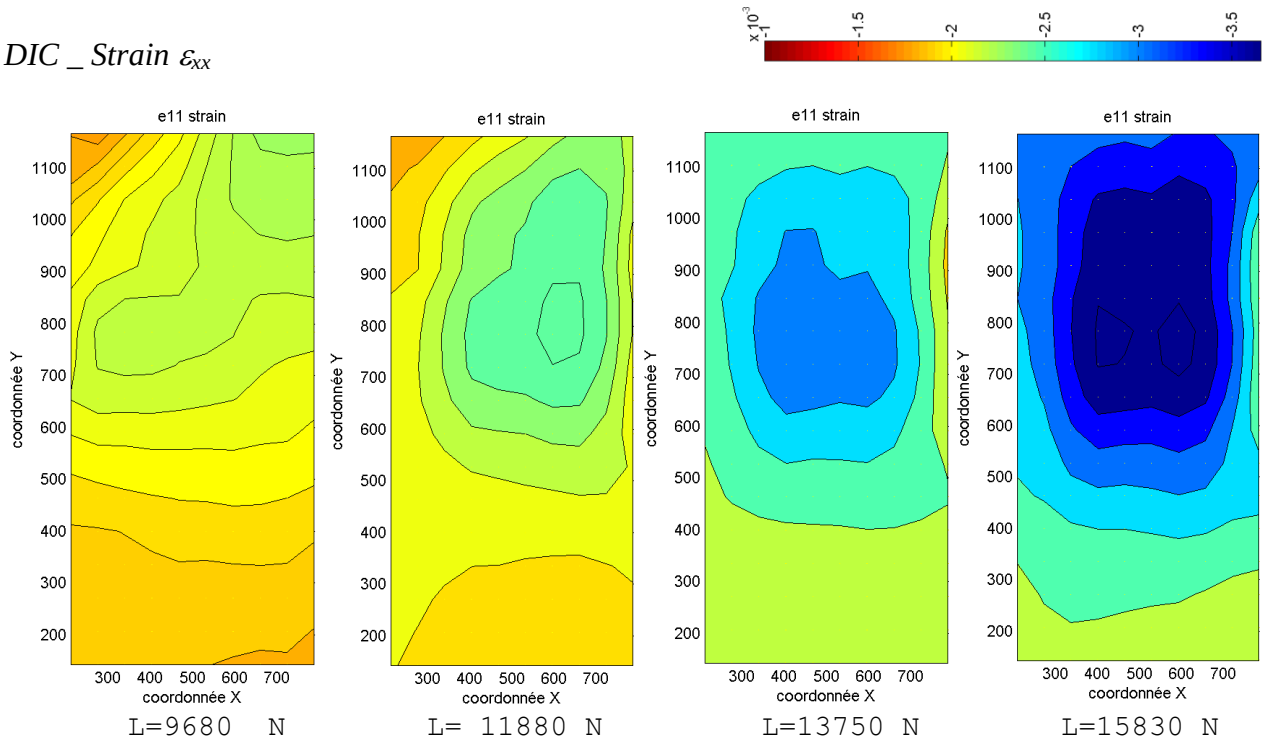

fig. IV.50 - The strain field ε_{xx} measured by means of CORRELI^{GD} in four steps of test T1_ 40_V_6

The chromatic representation of the strain fields ε_{yy} and ε_{xx} is presented above. The analysis of the *figure IV.49* shows the displacement of the strain transfer zone from the loaded to the unloaded side and the evolution of the value of ε_{yy} during the loading process.

The *fig. IV.50* shows the contraction of the composite sheet versus the anchor. The crack advancement process described by this graphs is coherent with that measured by video and photographic camera.

4.2.5 Series T2_40_V

The tests of series T2_40_V are described by curves of figure *IV.51*. In this set, four specimens failed after the achievement of peak P_3 (T2_40_V_1/3/5/6) and two samples experienced a brittle prismatic fracture after the achievement of peak P_2.

The average of peak registered are respectively 11,46 kN (with a standard deviation of 1,14) for P_1 and 20,53 kN (with a standard deviation of 1,22 kN) for P_2. The average value of peak P_3 has been obtained from the population composed of only the tests T2_40_V_3, T2_40_V_5 and T2_40_V_6 and it is equal to 13,73 kN (with a standard deviation of 2,35 kN). The average of P_2 and P_3 is respectively 66,15 % and 11,15 % larger than the maximum load registered in series T0.

All the samples in this series are characterized by an approximately equal stiffness as shown by curves of *figure IV.51*. This stiffness value is greater than that registered in the specimens of series T0. The comparison between the master curves of series T2_40_V and T0 is shown in figure *IV.52*. The MC of series T2_40_V has been realized neglecting the sample T2_40_V_2 and T2_40_V_4. The numerical values of test T2_40_V_1 are not take into account because several problems in the steel lock during the test led to a curve U-L which was anomalous.

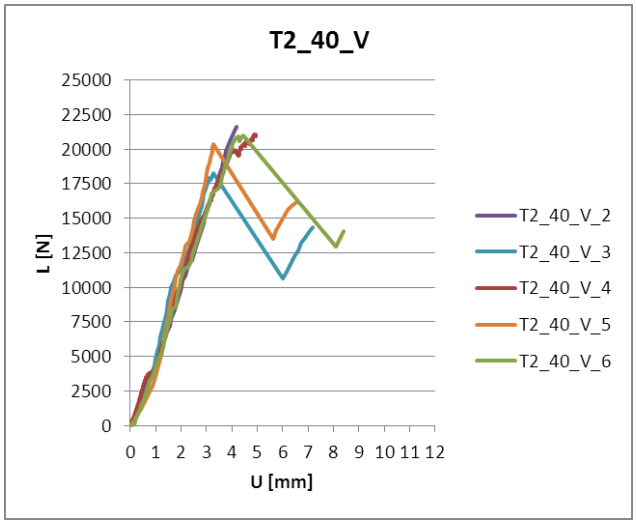

fig. IV.51 - The curves U-L registered during test of series T2_40_V

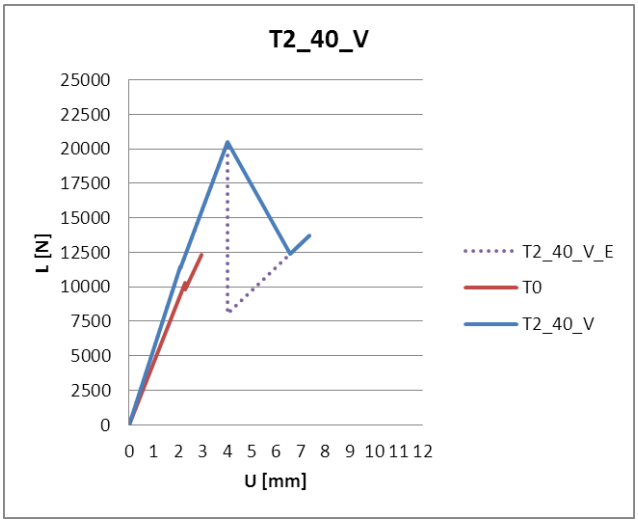

fig. IV.52 - The master curve of specimens T2_40_V compared with that of T0; dotted line is the experimental master curve, the red line is the MC

The partial amounts of energy necessary to achieve the peaks P_1, P_2 and P_3 are shown in the bar graphs of *fig. IV.53*. The average values of $\Delta\Gamma_1$, $\Delta\Gamma_2$ and $\Delta\Gamma_3$ are respectively equal to 10,75 J (standard deviation of 2,28 J), 33,25 J (standard deviation of 12,42 J) and 11,02 J (standard deviation of 4,67 J). The population of the test used to calculate the $\Delta\Gamma 3$ does not take the specimen that fails in a brittle manner after P_2 and the specimen T2_40_V_1 in consideration.

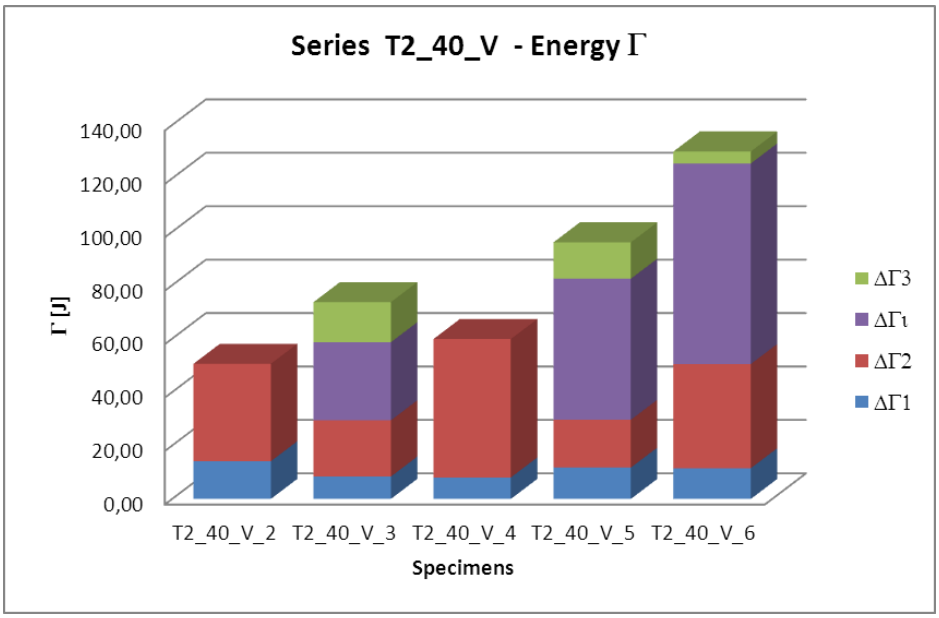

fig. IV.53 - The energy Γ measured during the tests of series T2_40_V

The *table 4.IX* collects all the numerical values of peaks and energy.

tab. 4.IX - Peaks and energy registered during the tests of series T2_40_V. In the last two lines the average and standard deviation of the values are tabulated. The numbers marked with an asterisk have been obtained from a population composed of only the specimens T2_40_V_3/5/6.

	U_1 [mm]	P_1 [kN]	$\Delta\Gamma_1$ [J]	U_2	P_2 [kN]	$\Delta\Gamma_2$ [J]	$\Delta\Gamma_i$ [J]	U_3 [mm]	P_3 [kN]	$\Delta\Gamma_3$ [J]	Γ_{End}[J]
T2_40_V_2	2,44	11,99	14,12	4,17	21,60	36,46	-	-	-	-	50,58
T2_40_V_3	1,78	10,84	8,36	3,26	18,22	21,06	29,10	7,20	10,57	15,00	73,51
T2_40_V_4	1,82	9,67	8,05	4,93	21,07	51,79	-	-	-	-	59,84
T2_40_V_5	2,19	13,04	11,74	3,29	20,35	17,91	52,81	6,52	16,19	13,61	96,06
T2_40_V_6	2,15	11,74	11,50	4,45	21,36	39,01	75,09	8,40	14,42	4,46	130,07
average	2,07	11,46	10,75	4,02	20,52	33,25	52,33*	7,37*	13,73*	11,02*	82,01
St. d.	0,25	1,14	2,28	0,66	1,22	12,42	18,78*	0,78*	2,35*	4,67*	28,49

Several failure modes have been observed during the tests (*tab. 4.IX* and *fig. IV.54*). The specimens T2_40_V_3, T2_40_V_5 and T2_40_V_6 fail with a cohesive fracture after P_2 (point C of the characteristic curve) and a prismatic brittle failure after P_3 (point E of the characteristic curve). The T2_40_V_2 fails in a brittle manner after the achievement of peak P_2 with the development of a prismatic fracture. The sample T2_40_V_4 reaches rupture in C when a cohesive fracture of the sheet and an almost contemporary prismatic failure occur. Finally, the test on specimen T2_40_V_1 is characterized by a cohesive failure in C and an anchor splay debonding in E. The *table 4.X* collects all the failure modes observed.

fig. IV.54 - The samples of series T2_40_V after the test (in order T2_40_V_1, T2_40_V_2, T2_40_V_3, T2_40_V_4, T2_40_V_5, T2_40_V_6)

Tab. 4.X - The failure modes of specimens T2_40_V

Specimen	*Fracture in C*	*Fracture in E*
T2_40_V_1	CF	DSA
T2_40_V_2	CF - PF	-
T2_40_V_3	CF	PF
T2_40_V_4	CF - PF	-
T2_40_V_5	CF	PF
T2_40_V_6	CF	PF

The DIC analysis of test T2_40_V_5 is presented as follows. The photos utilized in the correlation procedure refer to the black points represented in *figure IV.55*. The table presented in the right side of the same figure collects the number of each step and the corresponding load and photo.

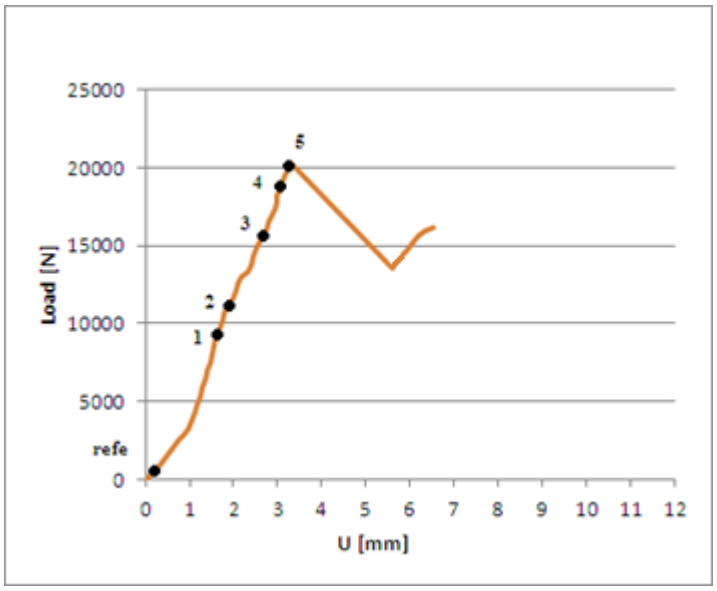

STEP DIC	L [N]	photo
refe	800	2
1	9620	28
2	11600	35
3	15670	51
4	18670	61
5	20130	71

fig. IV.55 - The curve U-L of the specimen T2_40_V_5. The black points in the figure define the instant of photos. The table on the right defines the steps analyzed in this paragraph.

The curves of *fig. IV.56* describe the ε_{yy} evolution. The first steps show a concentration of strain close to the loaded extremity. When the load increase the ε_{yymax} grows. The zone subjected to the high concentration of deformation is localized between the fan anchor and the extremity loaded of the sample.

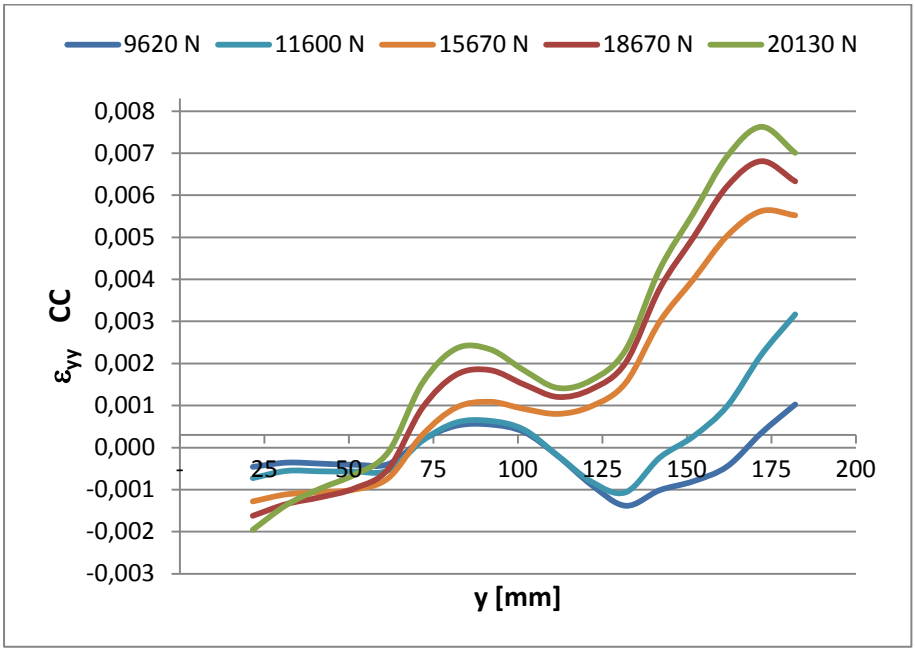

fig.IV.56 - The graphs y-ε_{yy} of several instants of load history (the results refer to the central column)

The *figure IV.57* illustrates the values of τ_{zy} along the y-direction evaluated for each step of analysis. It should be noted that a high concentration of stresses is presented before and after the nail. The peak of τ_{zy} is registered between the fan and the loaded extremity of the sample. A low displacement of the stress transfer zone is registered when the peak move from y=170 mm to y=135 mm.

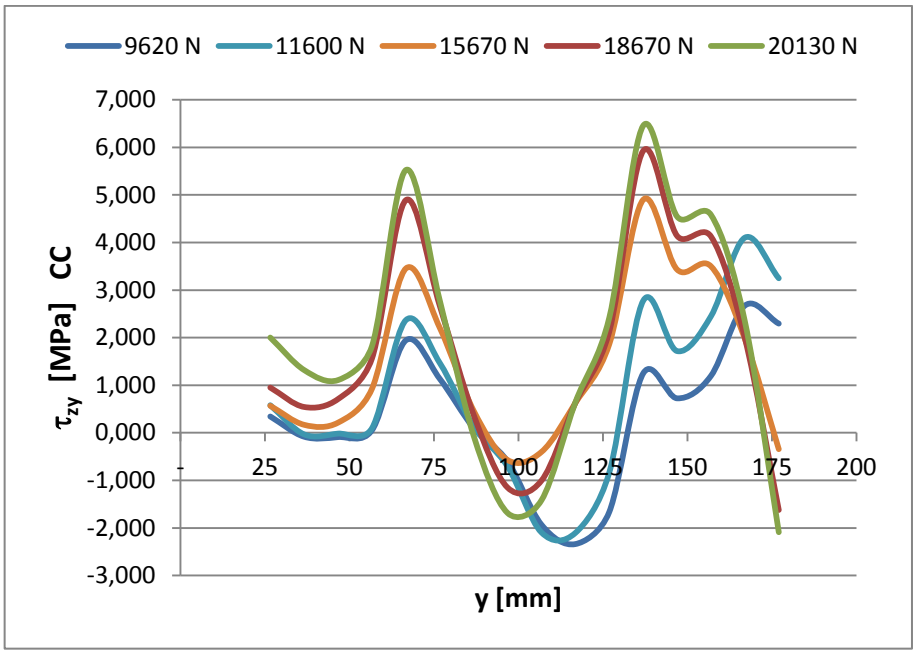

fig. IV.57 - The graphs y-τ_{zy} of several instants of load history (the results refer to the central column)

The *figures IV.58* and *IV.59* illustrate the strain fields ε_{xx} and ε_{yy} in four steps of the load history. The strain in the load direction are concentrated between the border and the fan anchor. The ε_{xx} field presented in *figure IV.59* shows a contraction of the sheet from the two lateral borders versus the two anchors.

DIC _ Strain ε_{yy}

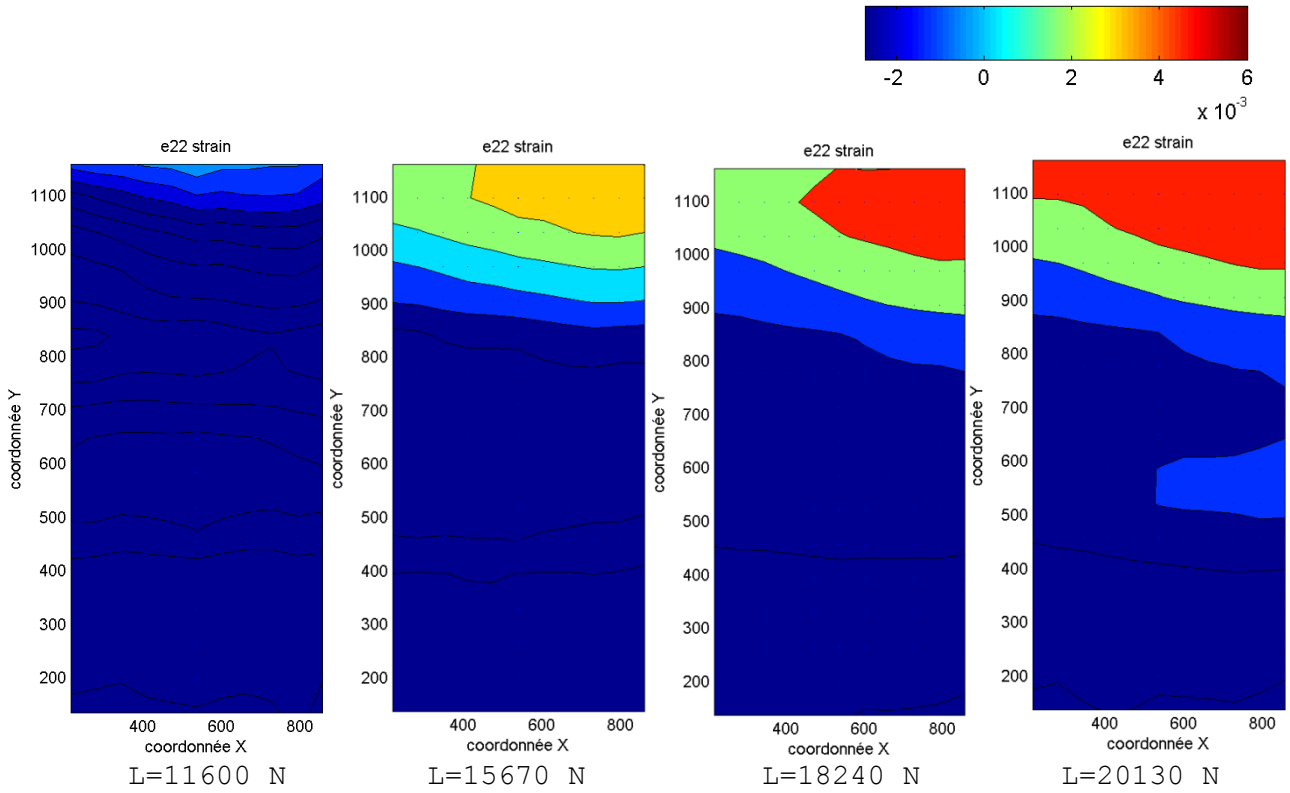

fig. IV.58 - The strain field ε_{yy} measured by means of CORRELI^{GD} in four steps of test T2_40_V_5

DIC _ Strain ε_{xx}

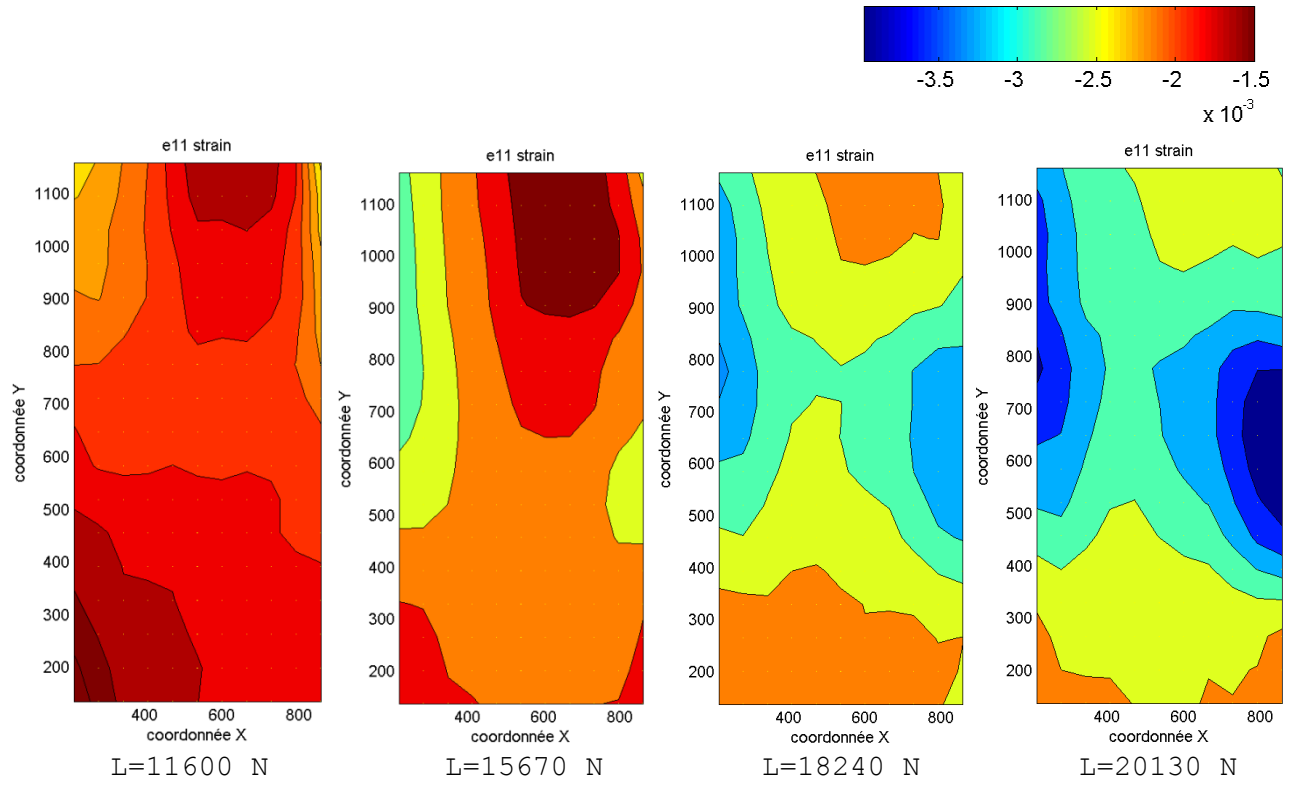

fig. IV.59 - The strain field ε_{xx} measured by means of CORRELI^{GD} in four steps of test T2_40_V_5

4.2.6 - Series T3_25_V

The curves that describe the tests T3_25_V are shown in *fig IV.60*. The graphs U-L underline the achievement of high maximal peaks and the successive failure. The anchor loading phases, defined by stroke DE of fig. *IV.1*, occurred only twice. Two experiments of the series has been invalidated because a technical problem in the steel apparatus occurred.

The average peaks P_1 and P_2 are respectively 9,67 kN and 23,01 kN. The average maximal peak is the 86,15 % higher than that of the series T0. The peaks P_3 registered during the tests T3_25_V_3 and T3_25_V_6 are respectively 18,77 kN and 16,71 kN.

It should be noted that the stroke slopes AB of the test curves T3_25_V is almost constant for all the specimens. As well shown in *figure IV.61* the stiffness of the reinforced system T3_25_V is higher than that of series T0. The master curve realized for the series T3 neglects the stroke of anchor loading phase, which occurred only twice.

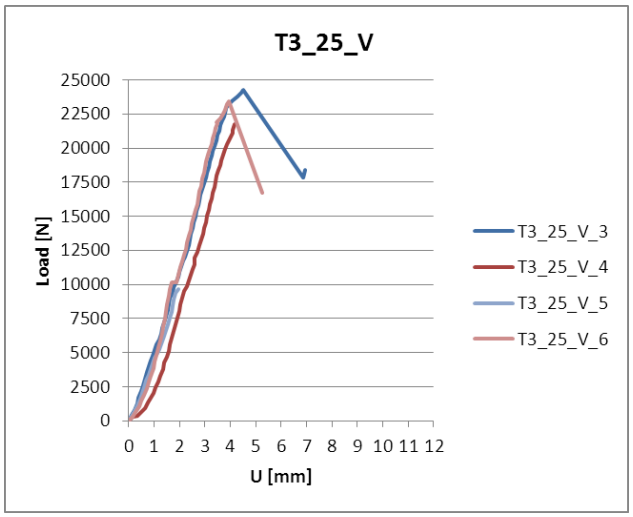

fig. IV.60 - The curves U-L registered during test of series T3_40_V

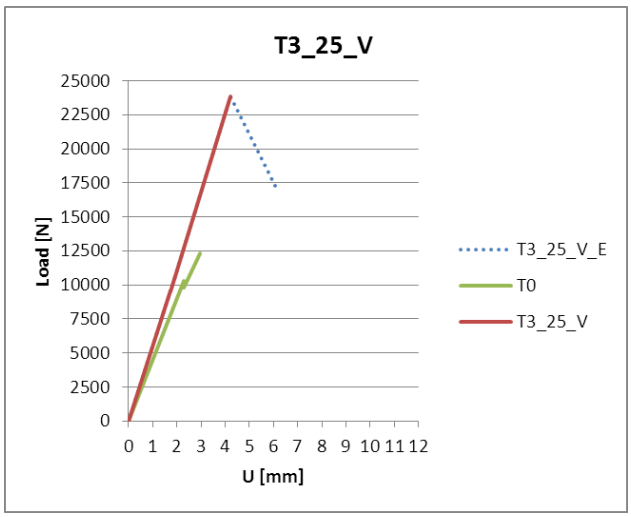

fig. IV.61 - The master curve of specimens T3_40_V compared with that of T0; dotted line is the experimental master curve, the red line is the MC

The energy dissipated during the tests are described by the bar graphs of *figure IV.62*. The average value of energy necessary to achieve the maximal peak ($\Delta\Gamma_1+\Delta\Gamma_2$) is equal to 47,50 J. This value is the 153% higher than that registered during the T0 series. The *table 4.XI* collects all the numerical values of peaks and energy.

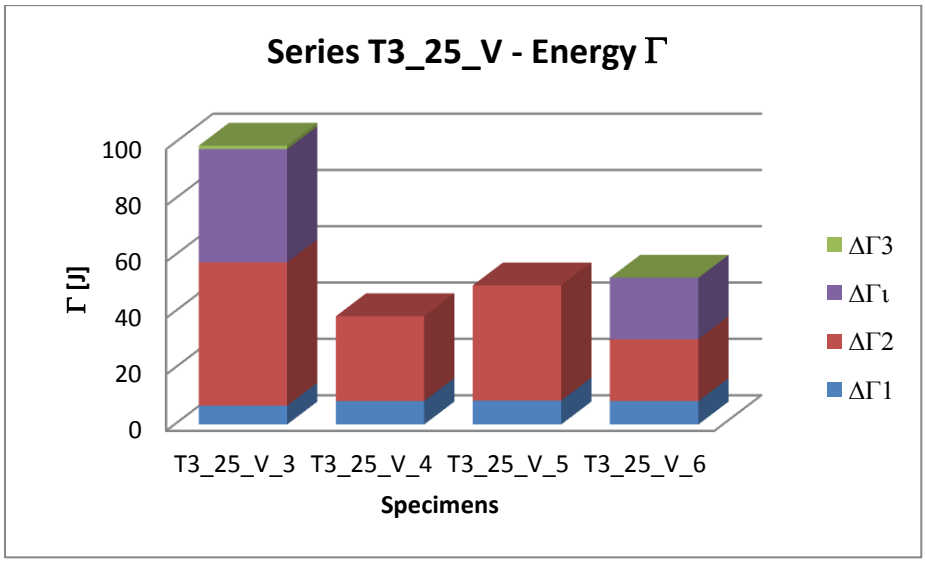

fig. IV.62 - The energy dissipated during the tests of series T3_40_V

tab. 4.XI - Peaks and energy registered during the tests of series T3_25_ V. In the last two lines the average and standard deviation of the values are tabulated. The numbers marked with an asterisk have been obtained from a population composed of only the specimens T3_25_V_3/6.

	U_1 [mm]	P_1 [kN]	$\Delta\Gamma_1$ [J]	U_2	P_2 [kN]	$\Delta\Gamma_2$ [J]	$\Delta\Gamma_i$ [J]	U_3 [mm]	P_3 [kN]	$\Delta\Gamma_3$ [J]	$\Delta\Gamma_{End}$[J]
T3_25_V_3	1,63	9,06	6,69	4,52	24,29	50,87	40,23	6,95	18,39	1,25	99,04
T3_25_V_4	2,28	9,85	8,32	4,17	21,73	30,08	-	-	-	-	38,40
T3_25_V_5	1,94	9,63	8,48	4,37	22,58	40,87	-	-	-	-	49,36
T3_25_V_6	1,87	10,13	8,29	3,95	23,42	36,41	21,96	5,26	16,71	0,01	66,66
average	1,93	9,67	7,95	4,25	23,01	39,56	31,09*	6,10*	17,55*	0,63*	51,76
St. d.	0,23	0,39	0,73	0,21	0,95	7,57	9,14*	0,85*	0,84*	0,62*	25,70

The failure modes registered during this series are shown in *figure IV.63* and defined in *table 4.XII*. Two specimens (T3_25_V_3/6) failed with the development of a cohesive fracture between the sheet and the support after the achievement of P_2, and with a brittle prismatic failure after a short anchor loading phase. The remaining samples, reached the peak P_2, failed with a brittle prismatic failure.

tab. 4.XII - The failure modes of specimens T3_40_V

Specimen	*Fracture in C*	*Fracture in E*
T3_25_V_3	CF	PF
T3_25_V_4	PF	-
T3_25_V_5	PF	-
T3_25_V_6	CF	PF

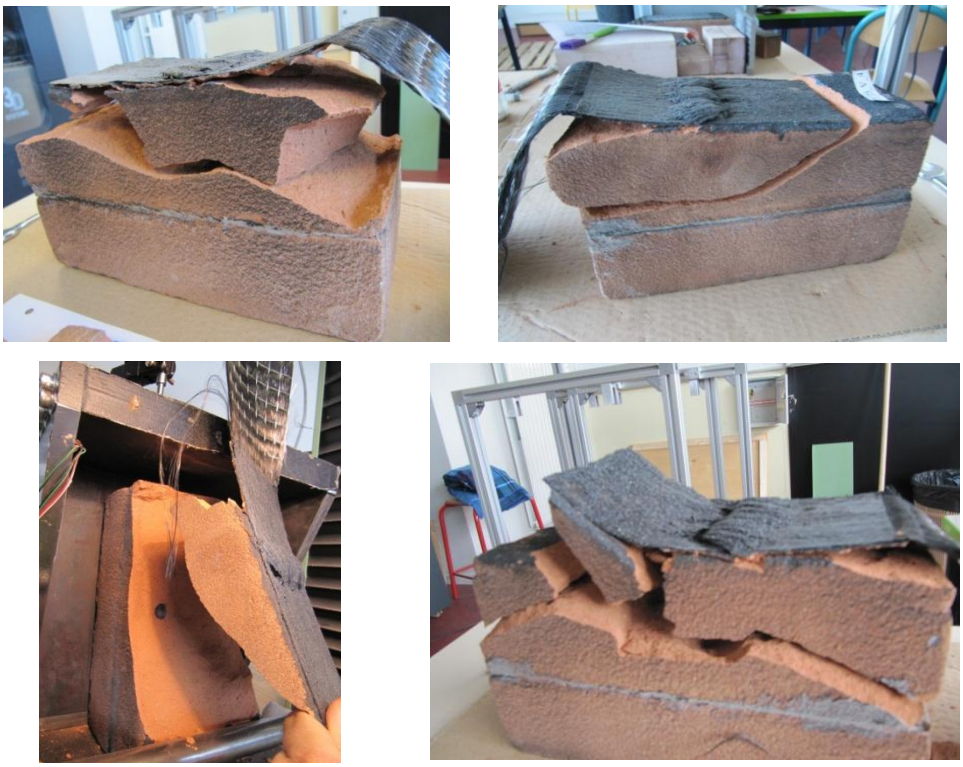

fig. IV.63 - The samples of series T3_25_V after the tests (in order T3_25_V_3, T3_25_V_4, T3_25_V_5, T3_25_V_6)

A Digital Image Correlation has been executed to analyze the strain fields ε_{yy} and ε_{xx}. The results reported follows are been obtained studying the representative specimen T3_25_V_3. The graph U-L of the test and the photos utilized in the correlation are presented in the *figure IV.64*.

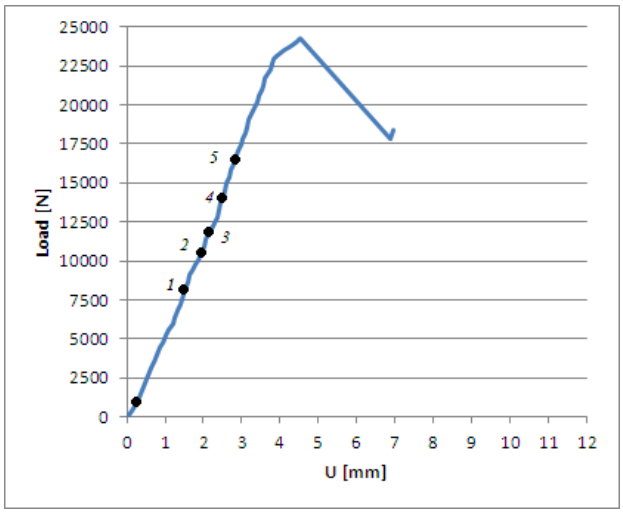

STEP DIC	L [N]	photo
refe	810	3
1	8127	34
2	10940	46
3	12060	51
4	14110	61
5	16610	72

fig. IV.64 - The graph U-L of the test T3_25_V_3. The black points define the instants of load history analyzed by DIC. On the right the table that define the steps (load and corresponding photo) of the analysis reported in this paragraph.

The *figure IV.65* represents the values of ε_{yy} along the y-direction in the central column of the matrix of data (x=5 cm). It should be noted that a high concentration of stresses is registered, already in the first steps, in the zone between the loaded extremity and the fan anchor. In correspondence of the splay a value of ε_{yy} almost constant has been registered in all the steps analyzed; in the unloaded side the values of strain are close to zero.

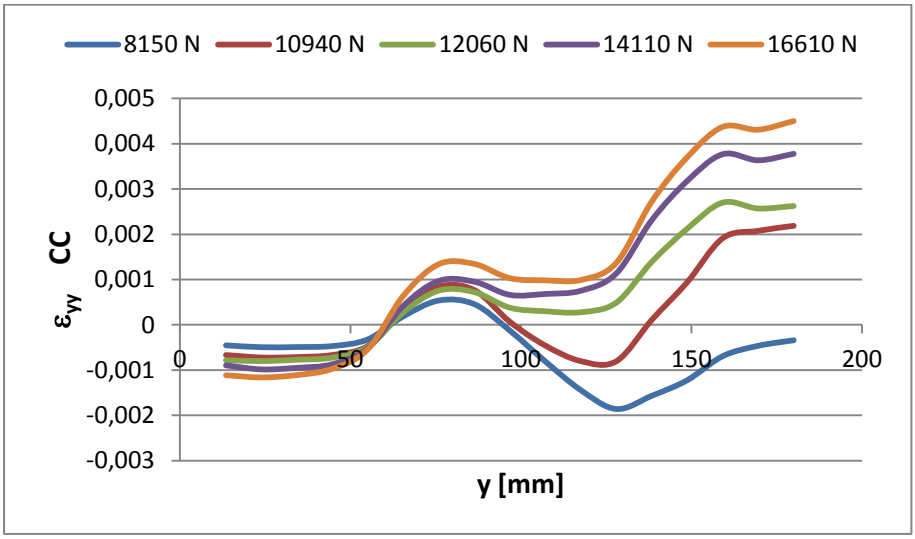

fig. IV.65 - The graphs y-ε_{yy} of several instants of load history (the results refer to the central column)

The bond stresses evaluated using the equation (3.1) are represented for the central column of the matrix of data (*fig. IV.66*). It should be noted that the distribution of stresses of specimens with 3 anchors is similar to that of samples fastened with two anchors. Specifically, a high concentration of stresses is registered between the loaded border and the fan anchor. In the unloaded side another peak of stress is registered. The increment of load allows to an increment of the maximal stress. A low displacement of the stress transfer zone is evident analyzing the displacement of the peak from the loaded side versus the anchor.

The chromatic representations referring to the strain fields are reported follows. The *figures IV.67* show that the strain ε_{yy} interest the zone between the loaded extremity and the fan anchor. The increment of load allows the ε_{yy} to grows and to expand versus the anchor.

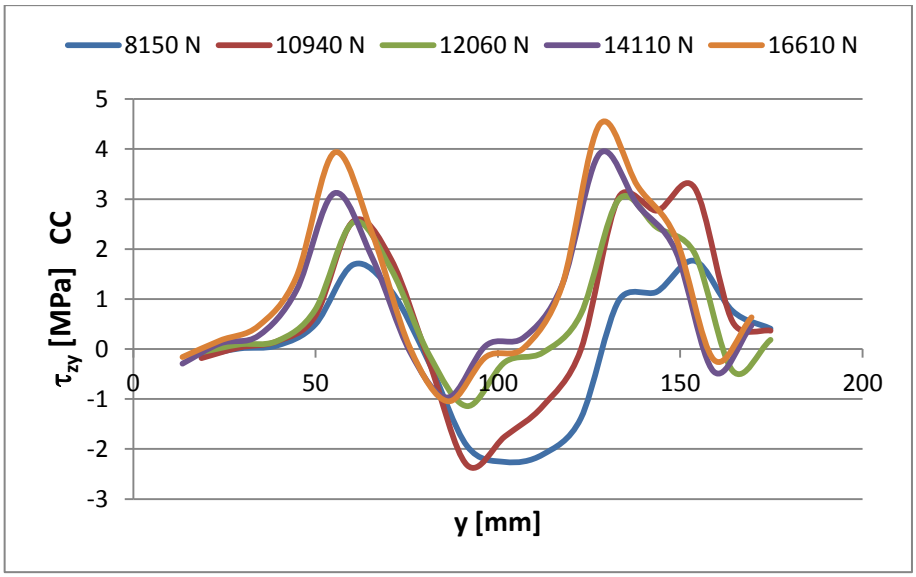

fig. IV.66 - The graphs y-τ_{zy} of several instants of load history (the results refer to the central column)

The *figures IV.68* shows a contraction of the sheet in the x-direction, specifically, a concentration of negative ε_{xx} has been registered in proximity of anchors fastened on the right side of the specimen.

DIC _ Strain ε_{yy}

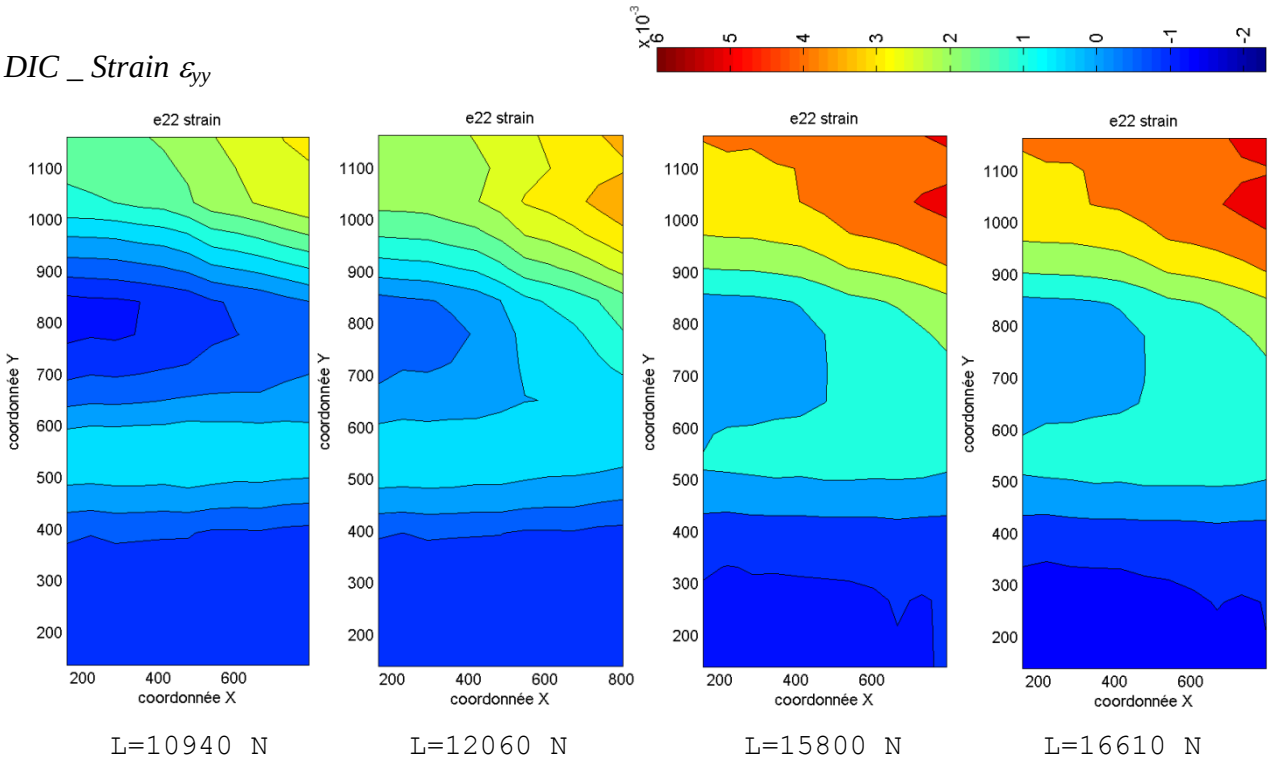

fig. IV.67 - The strain field ε_{yy} measured by means of CORRELI^{GD} in four steps of test T3_25_V_3

DIC _ Strain ε_{xx}

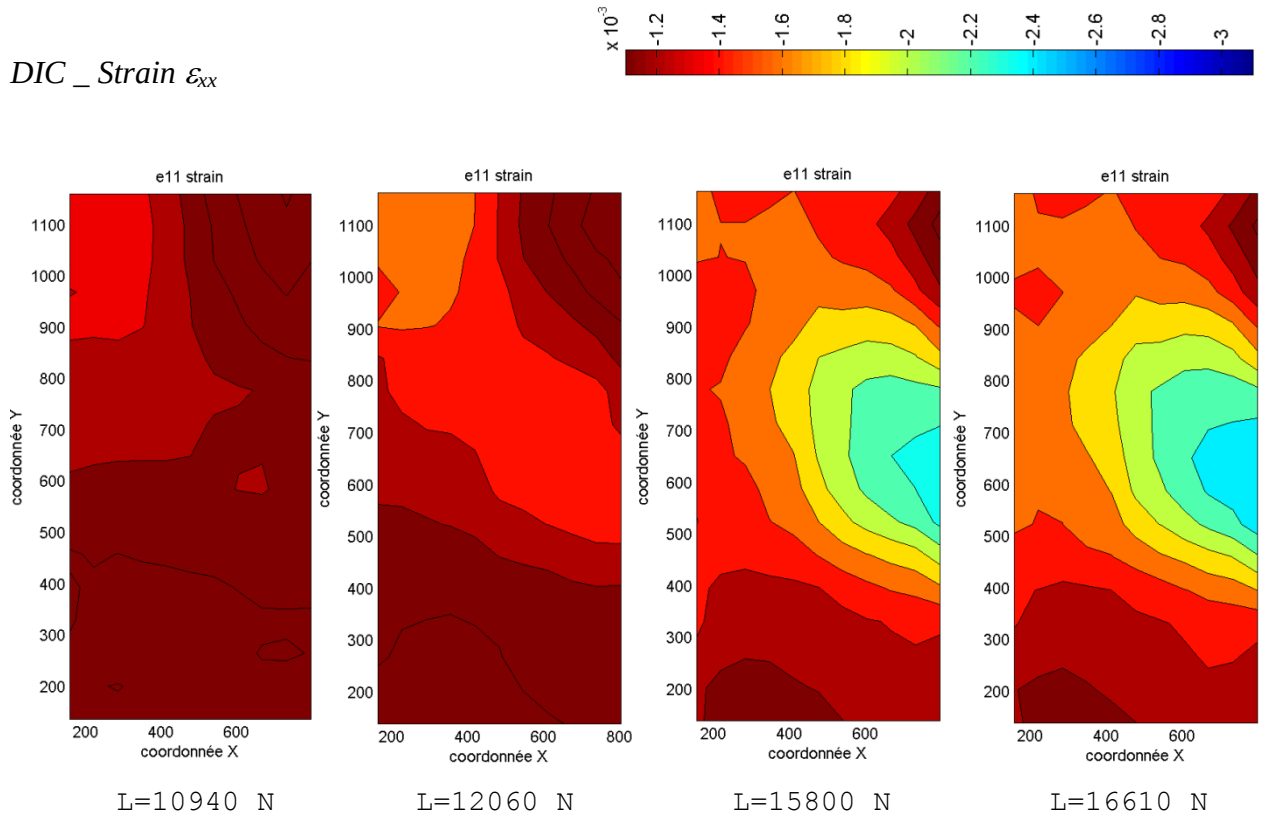

fig. IV.68 - The strain field ε_{xx} measured by means of CORRELI^{GD} in four steps of test T3_25_V_6

4.3 Comparison between the series

The failure behaviors in each of the six different configurations of reinforcement are now compared using the six tests selected as reference tests. The strain and the bond stress fields of the samples T0_6, T1_25_V_5, T1_40_O_5, T1_40_V_6, T2_40_V_5 and T3_25_V_3 have been analized and illustrated in bi-dimensional and tri-dimensional chromatic representations.

Since the specimens have been subjected to displacement controlled test, the photos have been taken at fixed value of u. For this motivation it has been chosen to compare the strain and stress fields at six fixed displacement steps. They have been selected for specifically describing the crack advancement phases between the peak loads P_1 and P_2. The curves U-L of the six reference tests and the fixed steps of displacement used for the comparison are shown in *figure IV.69*. The numerical values of U [mm] of each step and the corresponding measures of load and energy of the all tests cited above are presented in *table 4.XIII* and *4.XIV*. The cells in grey denote the steps after the attainment of the peak P_1. The interpretation of the results must take into account that the specimen T0_6 is less stiff than the others, therefore, for this sample, the value of load corresponding to a fixed displacement step is lower than that of other reference specimens.

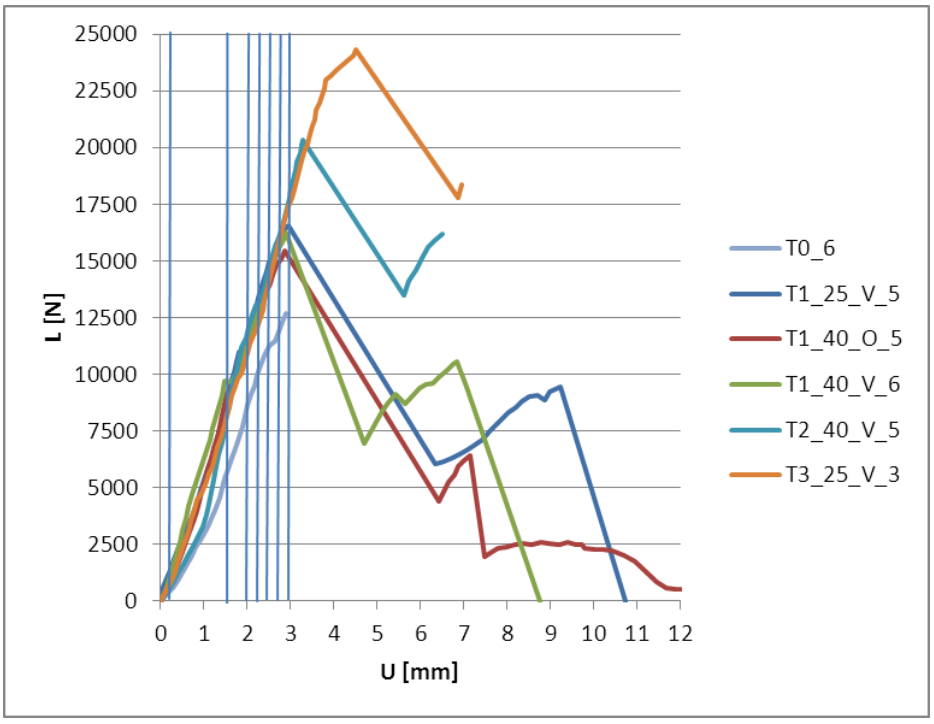

fig. IV.69 - The curves U-L of the six reference tests. The vertical line define the steps of load

The six tables presented herein (*4.XV, 4.XVI, 4.XVII, 4.XVIII, 4.XIX* and *4.XX*) show the property of the photos used in the DIC and the values of parameters utilized to carry out the correlations. In the

tables the distances between the nodes of the grids (Δx), the surface A_τ of each grid square, the number i of nodes in the y direction and the number j of nodes in the x direction are specified.

The *figures* from *IV.70* to *IV.75* illustrate the grid that define the Region Of Interest (ROI) of each specimen analyzed. It's important to underline that the factor R_z of the six groups of photos (one for each reference test) is almost equal ($0{,}16 < R_z < 0{,}17$); it's crucial to realize the comparison using a ZOI size and a distance between ZOI constants for all the correlations.

The strain fields ε_{yy} of the different specimens recorded during the load steps are presented in *paragraph 4.3.1*. Likewise the strain fields ε_{xx} of the reference samples recorded during the load steps are presented in *paragraph 4.3.2*. The stress bond fields is discussed in *paragraph 4.3.3*.

Tab. *4.XIII - The comparison steps and the corresponding values of load and energy (specimen T0_6, T1_25_V_5, T1_40_O_5)*

		T0_6			T1_25_V_5			T1_40_O_5		
Step	**U [mm]**	**L [N]**	**Γ [J]**	**Photo**	**L [N]**	**Γ [J]**	**Photo**	**L [N]**	**Γ [J]**	**Photo**
refe	0,25	590	0,09	2	1020	0,34	2	890	0,09	2
1	1,50	5400	3,93	21	8260	6,32	28	9180	6,10	24
2	2,00	8630	8,55	29	11130	11,74	39	11160	10,46	29
3	2,25	9980	11,16	34	13010	14,34	45	12340	13,74	32
4	2,50	11250	14,46	40	14590	18,17	49	14000	17,48	36
5	2,75	11890	17,45	43	15190	21,47	52	15070	21,32	39
6	3,00	12700	19,85	47	16200	24,90	55	failure		
7	3,25	failure			failure					

Tab. 4.XIV - The comparison steps and the corresponding values of load and energy (specimen T1_40_V_6, T2_40_V_5, T3_25_V_3)

		T1_40_V_6			T2_40_V_5			T3_25_V_3		
Step	**U [mm]**	**L [N]**	**Γ [J]**	**Photo**	**L [N]**	**Γ [J]**	**Photo**	**L [N]**	**Γ [J]**	**Photo**
refe	0,25	1000	0,10	2	800	0,10	2	810	0,09	3
1	1,50	9720	6,85	30	8050	4,49	22	8150	5,77	34
2	2,00	10000	9,37	33	10650	7,22	31	10940	10,44	46
3	2,25	11390	12,38	37	13040	11,74	41	12060	12,92	51
4	2,50	12280	14,19	40	14810	16,31	48	14110	16,64	61
5	2,75	15830	23,13	52	16030	19,72	53	15800	19,92	69
6	3,00	failure			18240	24,02	61	16610	21,63	72
7	3,25				20130	28,80	71	19420	29,14	84

Tab. 4.XV - Photo and DIC parameters (specimen T0_6)

T0_6		
b_{FRP}	583,00	pixel
R_z	0,17	mm/pixel
ZOI size	128	pixel
Δx	64	pixel
Δx	10,98	mm
A_τ	120,51	mm²
i	17	nodes
J	11	nodes

fig. IV.70 - A photo of the specimen T0_6 and the corresponding grid of ZOIs

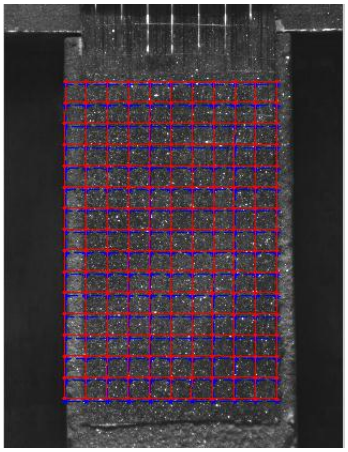

Tab. 4.XVI - Photo and DIC parameters (specimen T1_25_V_5)

T1_25_V_5		
b_{FRP}	629	pixel
R_z	0,159	mm/pixel
ZOI size	128	pixel
Δx	64	pixel
Δx	10,176	mm
A_τ	103,551	mm²
i	17	nodes
J	11	nodes

fig. IV.71 - A photos of the specimen T1_25_V_5 and the corresponding grid of ZOIs.

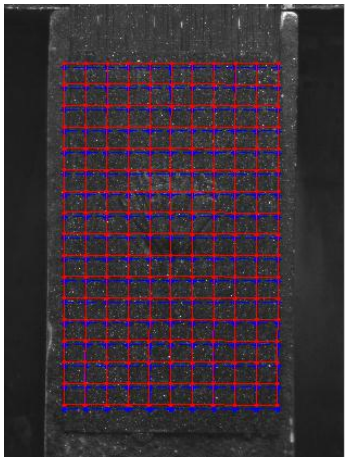

Tab. 4.XVII - Photo and DIC parameters (specimens T1_40_O_5)

T1_40_O_5		
b_{FRP}	614	pixel
R_z	0,16	mm/pixel
ZOI size	128	pixel
Δx	64	pixel
Δx	10,42	mm
A_τ	108,65	mm²
i	17	nodes
J	11	nodes

fig. IV.72 - A photos of the specimen T1_40_O_5 and the corresponding grid of ZOIs.

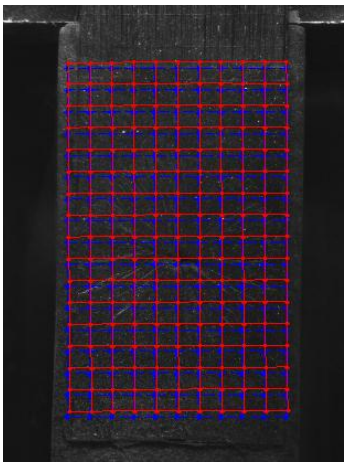

Tab. 4.XVIII - Photo and DIC parameters (specimens T1_40_V_6)

T1_40_V_6		
b_{FRP}	603	pixel
R_z	0,17	mm/pixel
ZOI size	128	pixel
Δx	64	pixel
Δx	10,61	mm
A_τ	112,65	mm²
i	17	nodes
J	10	nodes

fig. IV.73 - A photos of the specimen T1_40_V_6 and the corresponding grid of ZOIs.

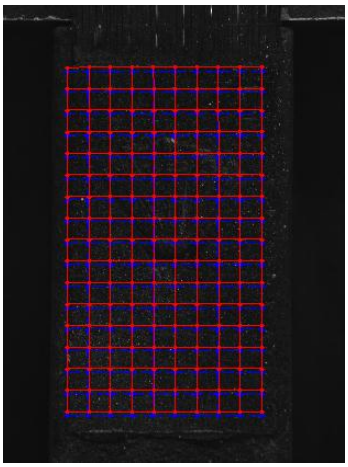

Tab. 4.XIX - Photo and DIC parameters (specimen T2_40_V_5)

T2_40_V_5		
b_{FRP}	630	pixel
R_z	0,16	mm/pixel
ZOI size	128	pixel
Δx	64	pixel
Δx	10,16	mm
A_τ	103,20	mm²
i	17	nodes
J	11	nodes

fig.IV.74 - A photos of the specimen T2_40_V_5 and the corresponding grid of ZOIs.

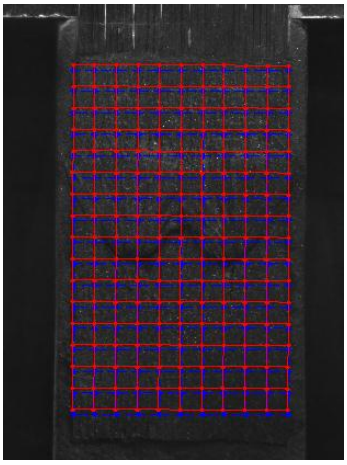

Tab. 4.XX - Photo and DIC parameters (specimen T3_25_V_3)

T3_25_V_3		
b_{FRP}	615	pixel
R_z	0,16	mm/pixel
ZOI size	128	pixel
Δx	64	pixel
Δx	10,41	mm
A_τ	108,30	mm²
i	17	nodes
J	11	nodes

fig. IV.75 - A photos of the specimen T3_25_V_3 and the corresponding grid of ZOIs.

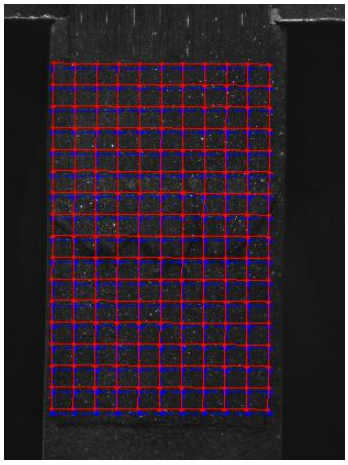

4.3.1 The strain fields ε_{yy}

The comparison of the strain fields ε_{yy} gives some information about the influence of the anchors on the crack advancement process (*see the results sheet A*). In order to evaluate the maximum length of the strain transfer zone, a parameter, named L_s, has been defined. L_s is the distance in mm, along the y axis, between the loaded extremity of the surface and the furthest point characterized by a $\varepsilon_{yy} > 0{,}001$ (*fig. IV.76*). The *table 4.XXI* collects the values of L_s registered in the comparison steps.

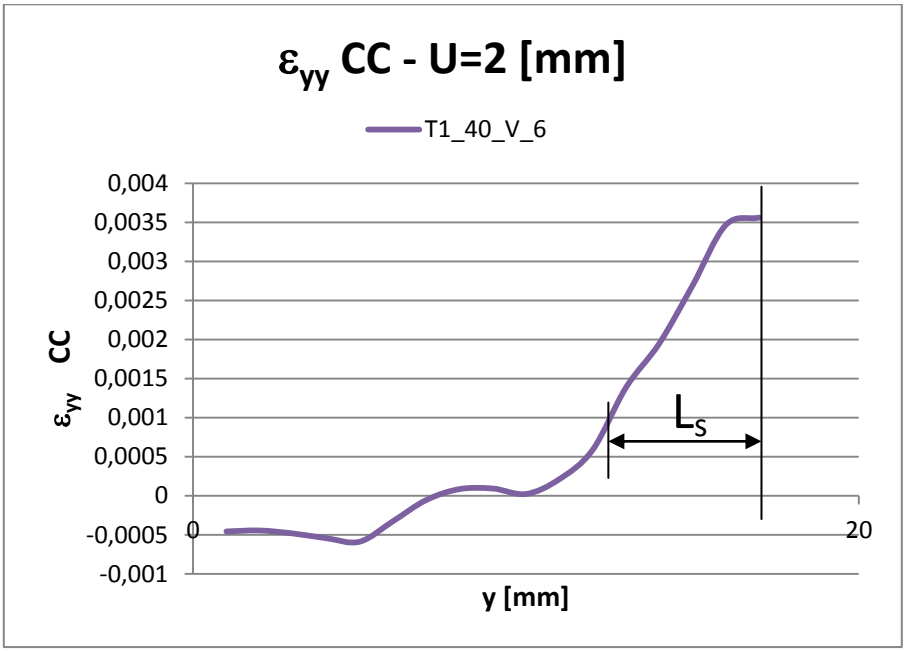

fig. IV.76 - The definition of the parameter L_s in a load step of test T1_40_V_6.

Table 4.XXI - The values of L_s measured in each load step for each reference specimen.

L_s	T0_6	T1_25_V_5	T1_40_O_5	T1_40_V_6	T2_40_V_5	T3_25_V_6
Step 2	10,98	81,41	62,54	53,07	10,16	31,22
Step 3	54,89	91,58	83,39	74,30	30,48	72,85
Step 4	65,87	101,76	104,23	74,30	50,79	93,66
Step 5	109,78	101,76	156,35	95,52	91,43	104,07
Step 6	109,78	142,46			101,59	104,07

The comparison shows that the crack advancement phase of the specimen T0 starts at step 4, while, for other specimens it starts immediately after step 2. This is due to the lower stiffness of the specimen without nail; the load applied to the sample T0_6, for a fixed displacement, is lower than that applied to the fastened specimens.

The strains registered at first step are close to zero in all the analyzed surfaces. When the applied displacement is 2 [mm] (second step) the specimens T1_25_V_5, T1_40_O_5, T1_40_V_6 and T3_25_V_3 have exceeded their peak P_1 (*tab. 4.XIII* and *4.XIV*). This corresponds in the chromatic representation of "step 2" to the "orange" area that implies a concentration of positive strain in the zone of crack development. Among the fastened specimens, the sample that presents the highest value of L_s, in the step two, is the T1_25_V_5 (L_s = 81 mm). When U=2 mm the specimen T1_40_O_5 and T1_40_V_6 are characterized by a L_s equal to 62,5 and 53 mm, respectively. The specimens with two and three nails have a value of L_s smaller than 35 mm. In third step the crack advancement process interests all the samples fastened by one nail. In the same step, the value L_s of specimen T3_25_V_6 achieves the value of 73 mm. In the step four the specimens T0_6 exceed its peak P_1. In the specimen not fastened the crack process starts from a corner of the loaded extremity. In the same step the strain zone with $\varepsilon_{yy} > 0{,}001$ evolves toward the unloaded side and overpasses the anchor in the specimens T1_25_V_5 and T1_40_O_5. When U=2,75 mm (step 5), L_s is equal to 110 mm in the specimen T0, 156 mm in the specimen T1_40_O_5, 102 mm in the sample T1_25_V_5, 95 mm in the specimen T1_40_V_6. The specimens with two and three anchors present a high concentration of strain between the loaded extremity and the nails. In the last step a further increment of the strained zone has been registered for the four specimen analyzed (two have failed before).

These results confirm the role of the nails in stiffening the connection, this reducing substantially the length L_s before debonding failure.

Results sheet A

The strain field ε_{yy}

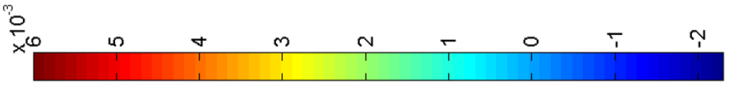

Step 1: U=1,5 [mm]

T0_6 T1_25_V_5 T1_40_O_5 T1_40_V_6 T2_40_V_5 T3_25_V_3

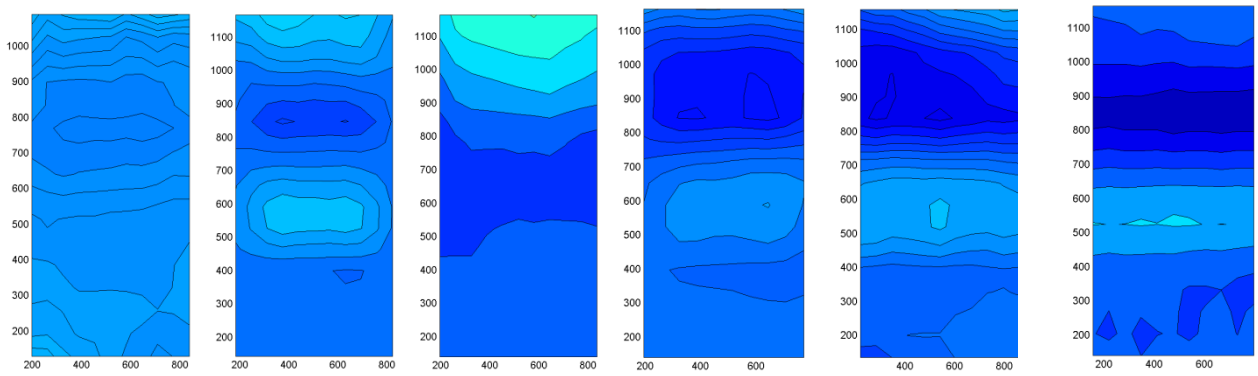

Step 2: U = 2 [mm]

T0_6 T1_25_V_5 T1_40_O_5 T1_40_V_6 T2_40_V_5 T3_25_V_3

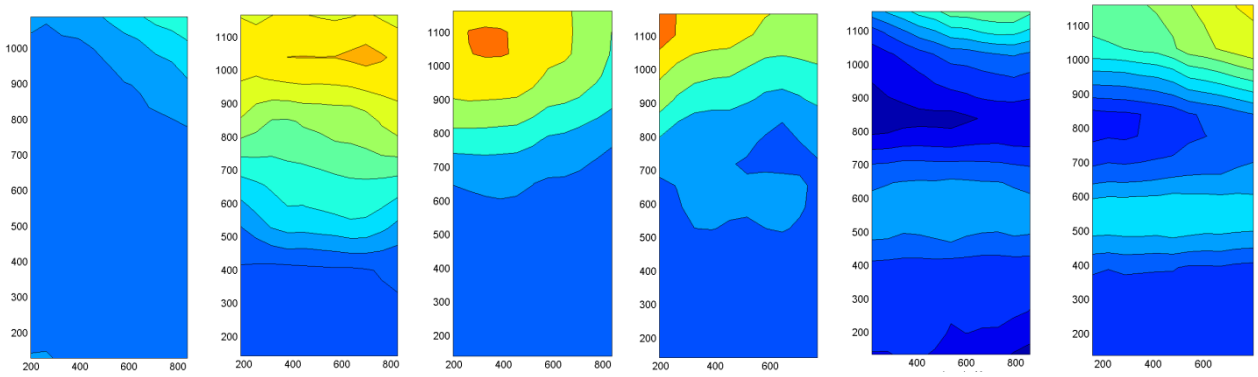

Step 3: U = 2,25 [mm]

T0_6 T1_25_V_5 T1_40_O_5 T1_40_V_6 T2_40_V_5 T3_25_V_3

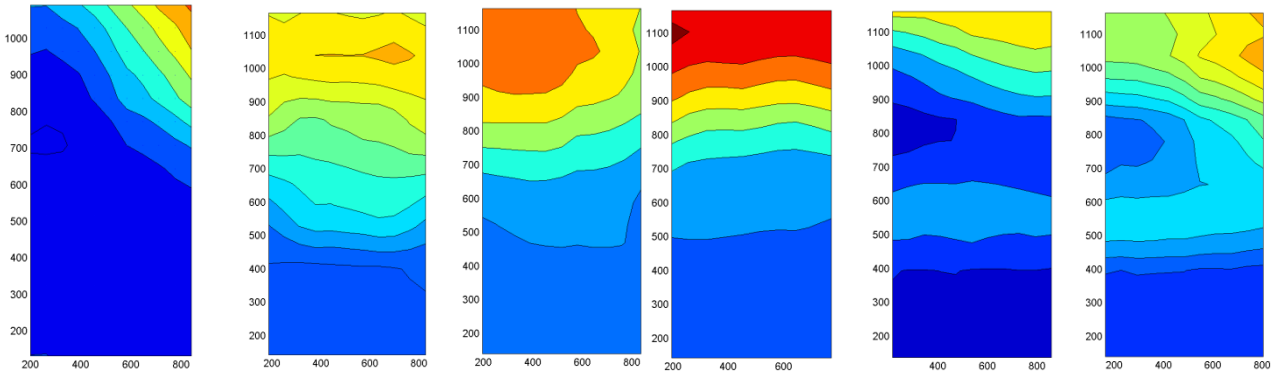

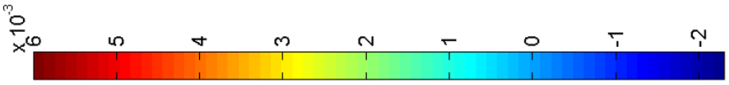

Step 4: U = 2,50 [mm]

T0_6 T1_25_V_5 T1_40_O_5 T1_40_V_6 T2_40_V_5 T3_25_V_3

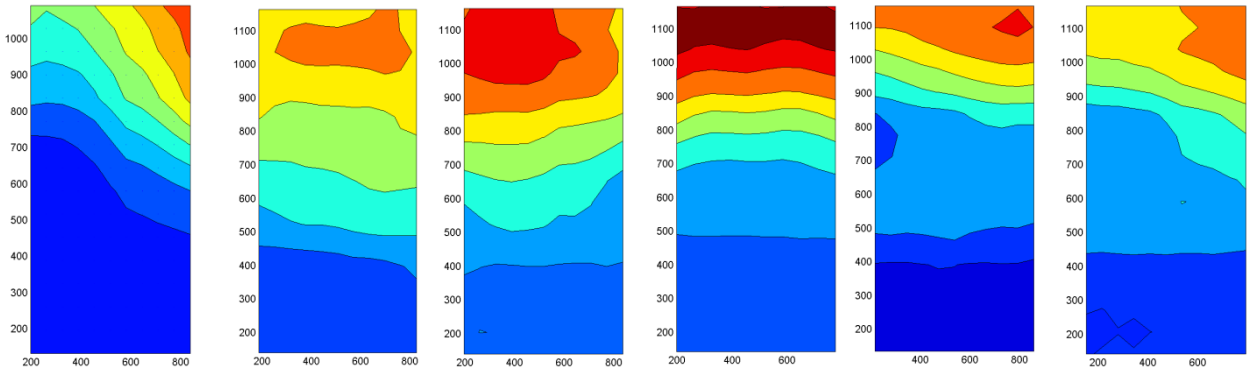

Step 5: U = 2,75 [mm]

T0_6 T1_25_V_5 T1_40_O_5 T1_40_V_6 T2_40_V_5 T3_25_V_3

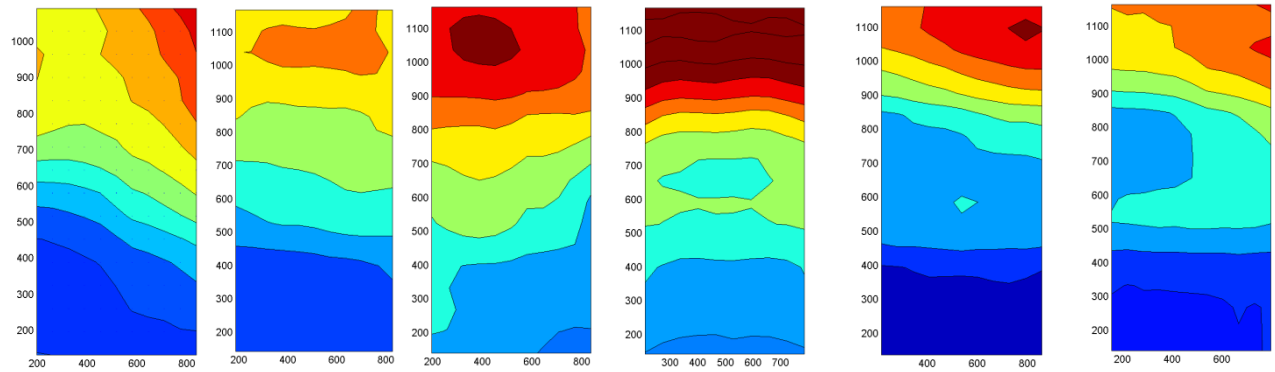

Step 6: U = 3 [mm]

T0_6 T1_25_V_5 T1_40_O_5 T1_40_V_6 T2_40_V_5 T3_25_V_3

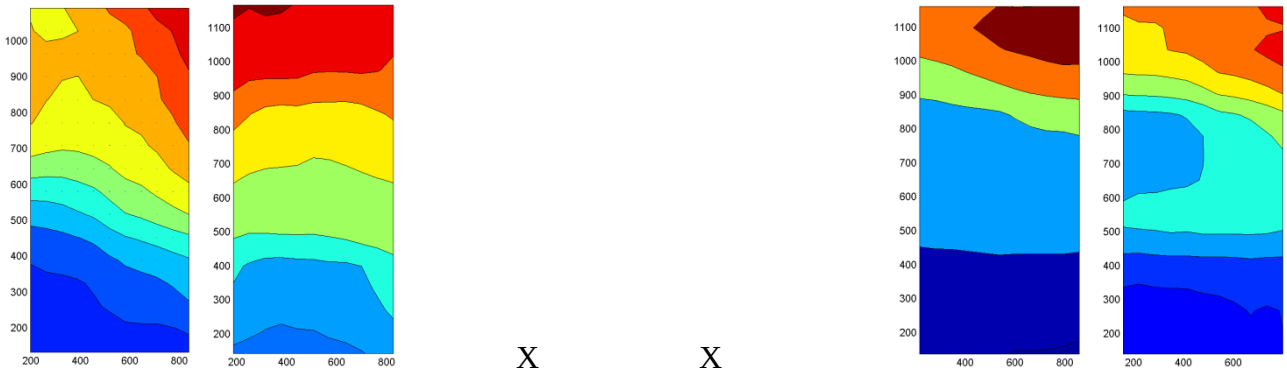

X X

4.3.2 The strain fields ε_{xx}

The strain fields developed in the x direction are represented in the *results sheet B;* this shows the chromatic representations of ε_{xx} recorded during the six load steps on each reference specimen. The bi-dimensional graphs underlines the increment of the maximal negative values of ε_{xx} with the crack advancement process (see in parallel the values of ε_{xx} and ε_{yy}). In the specimen of series T0 the CFRP sheet is subjected to a contraction versus the central axis y; specifically, the zone interested by high negative strain (zone blue in the images) increases from the loaded to the unloaded side. During the test T1_25_V_5 the zone characterized by the high value of negative strain is concentrated in the y center axis in the zone between the anchor and the loaded extremity; this is evident in the images relative to steps 4, 5 and 6. The splay angle of 360° (specimen T1_40_O_5), allows to a concentration of the strain ε_{xx} in the largest zone interested by the fan (see steps 3, 4 and 5). The distribution of strain ε_{xx} recorded in specimen T1_40_V_6 is characterized by a contraction of the sheet versus the central axis of the specimen; this contraction occurs in the zone between the anchor and the loaded border. The strain distribution is similar to that described for the sample T1_25_V_5 in steps 4 and 5, but now the zone interested by high negative values of ε_{xx} is largest because the radius of the splay anchor is biggest (40 mm). In the specimens T2_40_V_6 and T3_25_V_3 the high negative value of strain has been registered in the lateral side of the reinforcement; specifically it has been recorded in the band between the anchors and the lateral border of the sample. The anchors localized in the same line avoid the development of high ε_{xx} between the fastened points (see steps 4, 5 and 6 of specimen T2). The strain field ε_{xx} presented for specimen T3 underlines a specific asymmetrical failure of the specimen.

Results sheet B

The strain field ε_{xx}

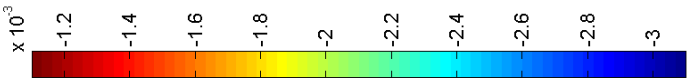

Step 1: U=1,5 [mm]

T0_6 T1_25_V_5 T1_40_O_5 T1_40_V_6 T2_40_V_5 T3_25_V_3

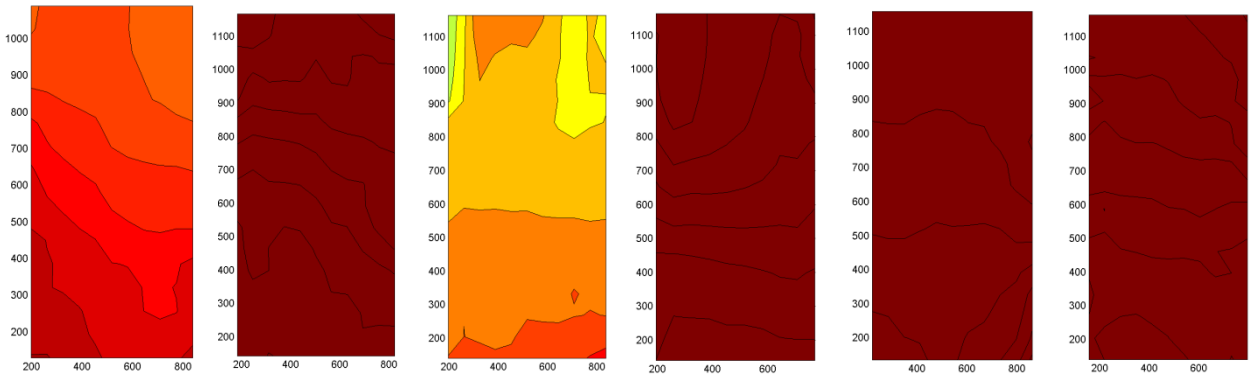

Step 2: U=2 [mm]

T0_6 T1_25_V_5 T1_40_O_5 T1_40_V_6 T2_40_V_5 T3_25_V_3

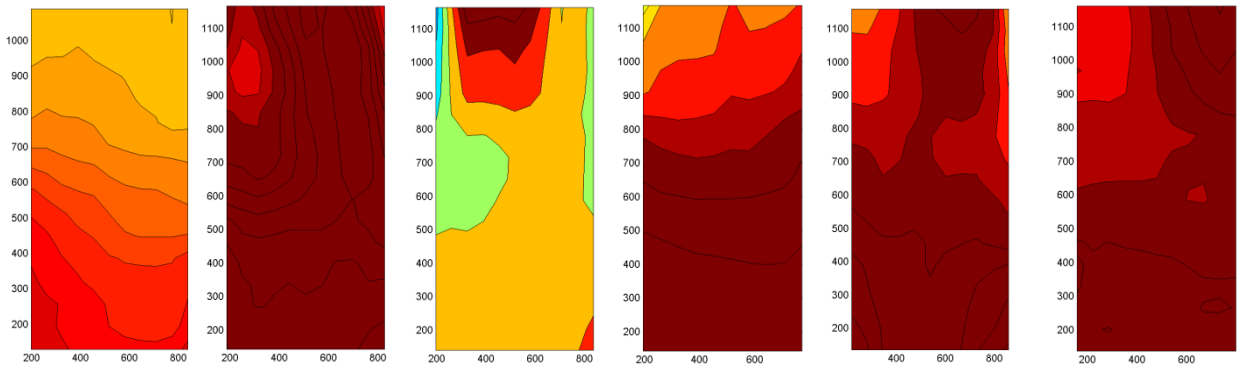

Step 3: U=2,25 [mm]

T0_6 T1_25_V_5 T1_40_O_5 T1_40_V_6 T2_40_V_5 T3_25_V_3

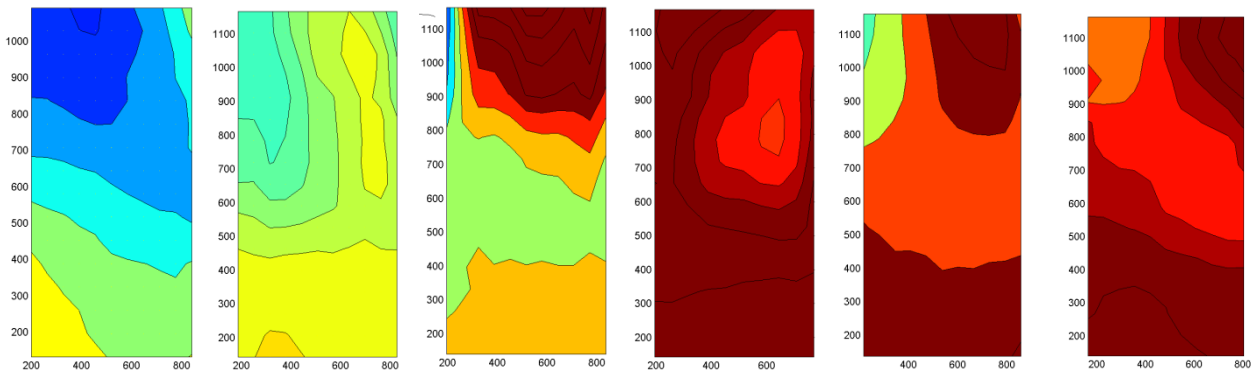

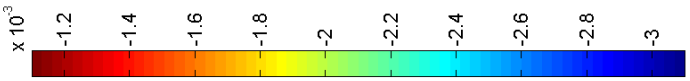

Step 4: U=2,25 [mm]

T0_6	T1_25_V_5	T1_40_O_5	T1_40_V_6	T2_40_V_5	T3_25_V_3
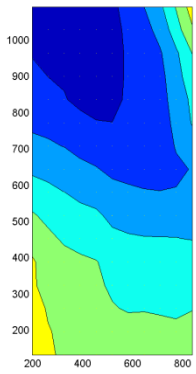	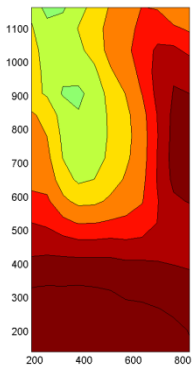	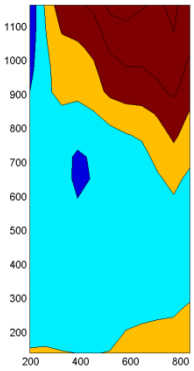	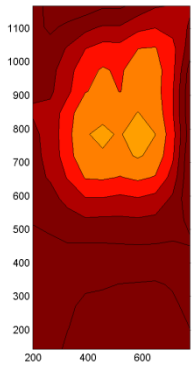	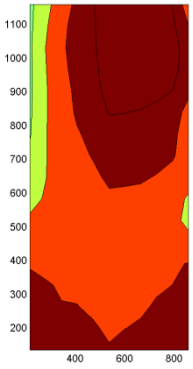	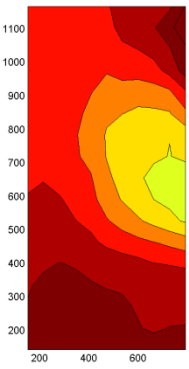

Step 5: U=2,75 [mm]

T0_6	T1_25_V_5	T1_40_O_5	T1_40_V_6	T2_40_V_5	T3_25_V_3
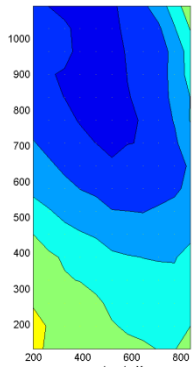	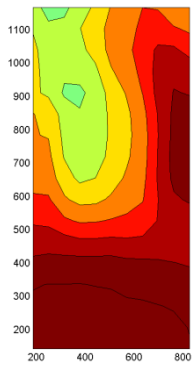	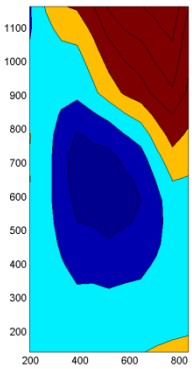	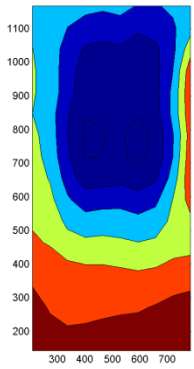	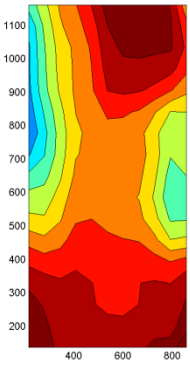	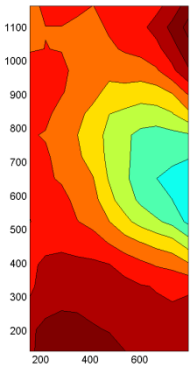

Step 6: U=3 [mm]

T0_6	T1_25_V_5	T1_40_O_5	T1_40_V_6	T2_40_V_5	T3_25_V_3
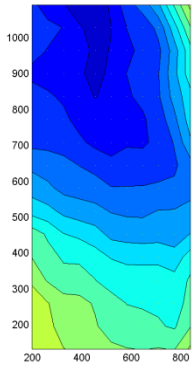	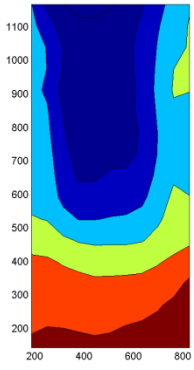	X	X	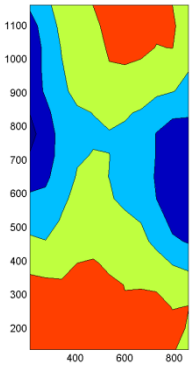	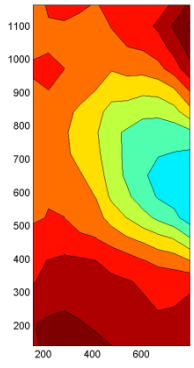

4.3.3 The bond stress τ_{zy}

The qualitative analysis of the tridimensional graphs "*x – y – τ_{zy} (x,y)*" permits to localize and to describe the stress transfer zone between the composite and the support during the tests.

It's important to remember that the equation used to calculate the stresses is the (3.1). This equation relates the ε_{yy} to the stress values. Specifically τ_{zy} is proportional to the slope of curve U-ε_{yy}. The *figure IV.77* shows the curve of strain ε_{yy} overlapped to the curve of stresses τ_{zy}/1000 [MPa], during the firth step of test T3_25_V_3. The curves refer to the central column (x=50 mm).

As previously anticipated the value obtained by using the formula (3.1) has been developed to describe a simple cohesive problem. It is the case of test T0_6. In the next pages the bond stress equation has been also used to evaluate the τ_{zy} on the reinforced face of the specimens fastened by anchor/s. The stresses obtained in the zone of the nail/s must not be taken into account. Indeed formula (3.1) has been developed for a homogeneous FRP sheet. On the contrary in the area where the nails are placed, the presence of the splays substantially, modifies the stiffness of the reinforcement, so that the axial stress in it cannot be simply deduced from the data relative to the axial strain. Moreover, the nail itself represents a constraint that influences the deformation of the sheet and that transmits a significant part of the force to the brick. Further future studies will permit to define accurately the τ_{zy} also in these complex stress transfer area.

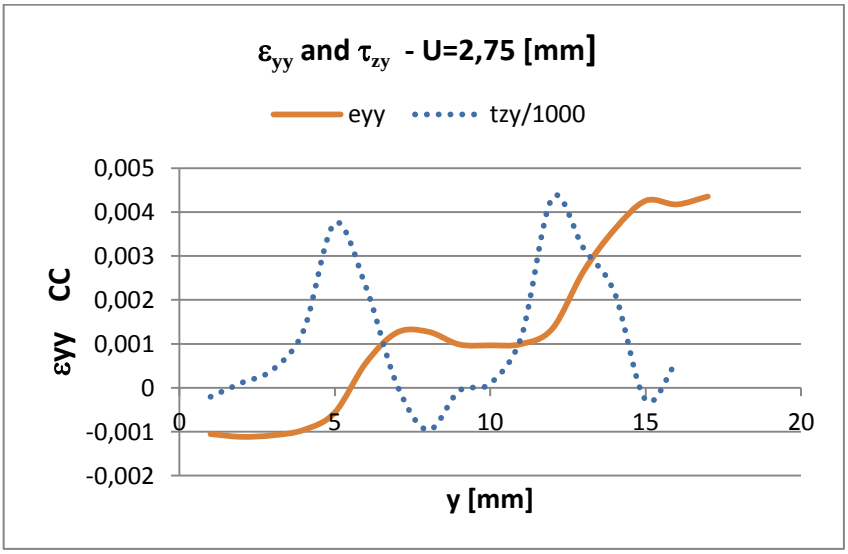

fig. IV.77 - The curves of strain and stresses (CC) referred to the specimen T3_25_V_3 in step 5

When the imposed displacement is U=1,5 [mm] the specimen T0_6 presents only a concentration of low stresses close to the loaded extremity of the reinforced surface (*fig. IV.78*). The tridimensional graphs *x – y – τ_{zy} (x,y)* of the samples characterized by "V" anchors (angle splay of 75°) (*fig.IV.79, IV.81, IV.82, IV.83*) present extended stress transfer zones; the bond stresses registered onto and

close the splay anchors are almost equal to zero. The *fig. IV.80* shows that the bond stresses of the specimen T1_40_O_5 are localized mainly in the loaded extremity for a y length almost equal to 40 mm.

All the figures related to the second step of load (U=2 mm) show an increment of the stress bond peak. The *figure IV.84* illustrates a concentration of τ_{zy} in the right corner of the loaded extremity. The bond stress field of the specimen T1_25_V_5 shows stresses between 1-2 MPa around the nail. In the step 2 the stress transfer zone of the specimen T1_40_O_5 and T1_40_V_6 moves from the loaded side toward the anchor (*fig. IV.86 and IV.87*). The *figures IV.88* and *IV.89* (specimen T2_40_V_5 and T3_25_V_3) shows a higher increase of the τ_{zy} peaks and a smaller movement of the stress transfer zones.

In the third step an extension of the stress transfer zone of the specimen T0_6 has been registered (*fig. IV.90*). The analysis of the images *IV.91, IV.92* and *IV.93* shows an increment of the stresses values without any important displacement of the stress transfer zone. The *figure IV.94* shows an increase of the tangential stress transfer zone (95 < y < 165). In the specimen T3_25_V_3 the main stress transfer zone moves from the loaded side toward the anchors (*fig. IV.95*).

In the step four a displacement of the stress transfer zone from the loaded extremity to the unloaded side has been registered in the specimen T0_6 without increment of the maximal stress peak (fi*g. IV.96*). The figures *IV.97, IV.98, IV.99* show an enhancement of the bond stresses in the zone defined by 40 < y < 75 [mm]. When the imposed displacement was U=2,50 the stresses registered in the specimens T2_40_V_5 and T3_25_V_3 increase (*fig. IV.100* and *IV.101*).

The stresses registered in the fifth step are illustrated by the figures from *IV.102* to *IV.107*. In this step a further displacement of the stress transfer zone toward the unloaded side has been registered in the sample T0_6 (*fig. IV.102*). The bond stress increase in the zone 40 < y < 75 in all the test fastened by anchor (*fig. IV.103, IV.104* and *IV.105*). The peaks stresses registered in the tests T1_40_V_6, T2_40_V_5 and T3_25_V_3 increase; however in correspondence of the anchor the values of τ_{zy} are almost zero (*fig. IV.106 and IV.107*).

The graphs $x - y - \tau_{zy}$ *(x,y)* related to the step 6 are only four; the specimen T1_40_V_6 and T1_40_O_5 have achieved the peak P_2 at U<3 mm. The *figure IV.108* shows the further displacement of the stress transfer zone to the unloaded side (specimen without nail). The stress fields described in figure *IV.109* illustrates an increment of the peak stresses and a lower displacement of the stress transfer zone toward the unloaded side. A lower value of stress is registered in the fastened zone. The graphs of specimens T2_40_V_5 and T3_25_V_3 describe an augment of the stress peaks; the stresses localized in correspondence to the anchors are always almost null (*fig. IV.110 and IV.111*).

The tridimensional graphs presented in this paragraph are ideal to analyze the crack advancement process in the six reference specimens. A high concentration of stresses allows the development of cracks and a subsequent movement of the stress transfer zone.

In the test T0_6, achieved the peak value $\tau \approx 1{,}8$ [MPa], the stress transfer zone moves from the loaded to the unloaded side of the reinforced surface without any increment of the τ_{max}. It is interesting to notice that the τ_{max} recorded is almost equal to the tensile strength of the support. This last has been evaluated dividing the compressive strength of fire brick San Marco (experimentally obtained in Florence - tab. 2.IV) by 10 [1].

In the test T1_25_V_5 the zone interested by high concentration of stress overstep the anchor already in the first step of comparison. The crack advancement occurs from the loaded to unloaded side of the specimen surrounding the nail.

The T0_40_O_5 is the specimen that shows the most similar stress distribution to the sample T0_6. Specifically the stress transfer zone moves from the loaded versus the opposite side interesting also the splay anchor zone. In the last step the highest value of stress has been recorded between the splay anchor and the loaded border.

The specimen T1_40_V_6 shows a high concentration of stress in the zone between the anchor and the loaded border. Small values of stress have been registered in the unloaded side of the sample.

The sample T2_40_V_5 is characterized by a concentration of stress in the area between the anchor and the loaded extremity of the specimen. In the test small displacement of the stress transfer zone has been recorded.

The test T3_25_V_3 shows, as the precedent, that a high concentration of stress is developed in the zone between the anchors and the loaded border of the sample.

The overall analysis of the results shows that:

- The anchor affects the distribution of stress in the “cohesive interface” CFRP-support;
- The stiffness of the anchor affects the crack advancement process;
- The specimen with the most similar behavior to T0_6 is the sample characterized by the smaller tickness of splay (T1_40_O_5); and
- The anchors allow the achievement of stress higher than the tensile strength of the support.

Step 1 (U = 1,5 mm)

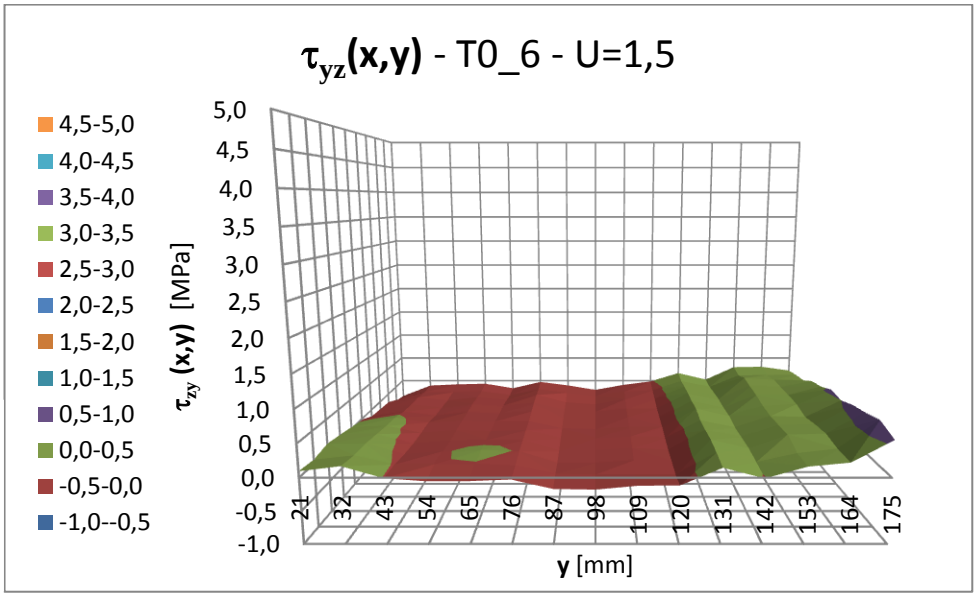

Fig. IV.78 - The bond stress field [MPa] calculated at U=1,5 [mm] for the specimen T0_6

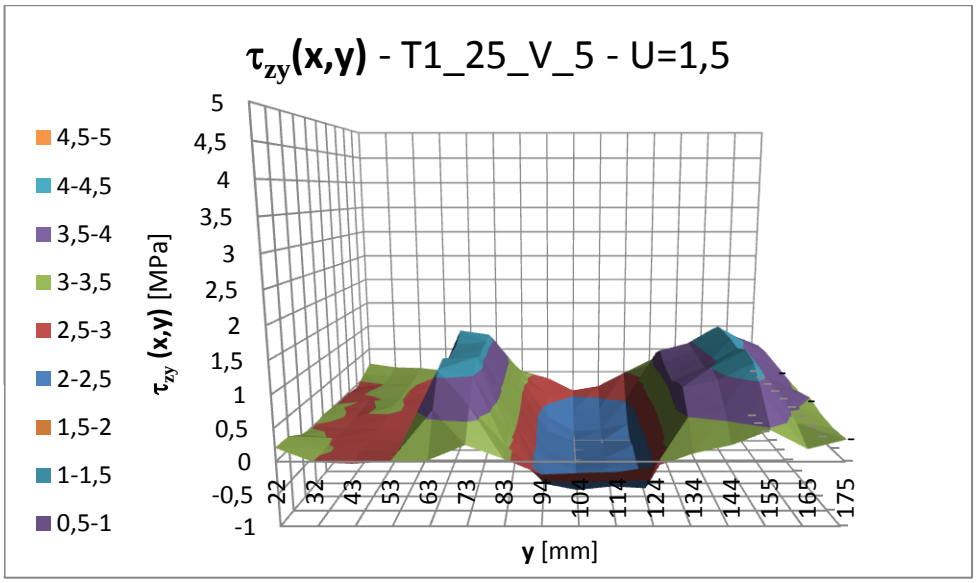

fig. IV.79 - The bond stress field [MPa] calculated at U=1,5 [mm] for the specimen T1_25_V_5

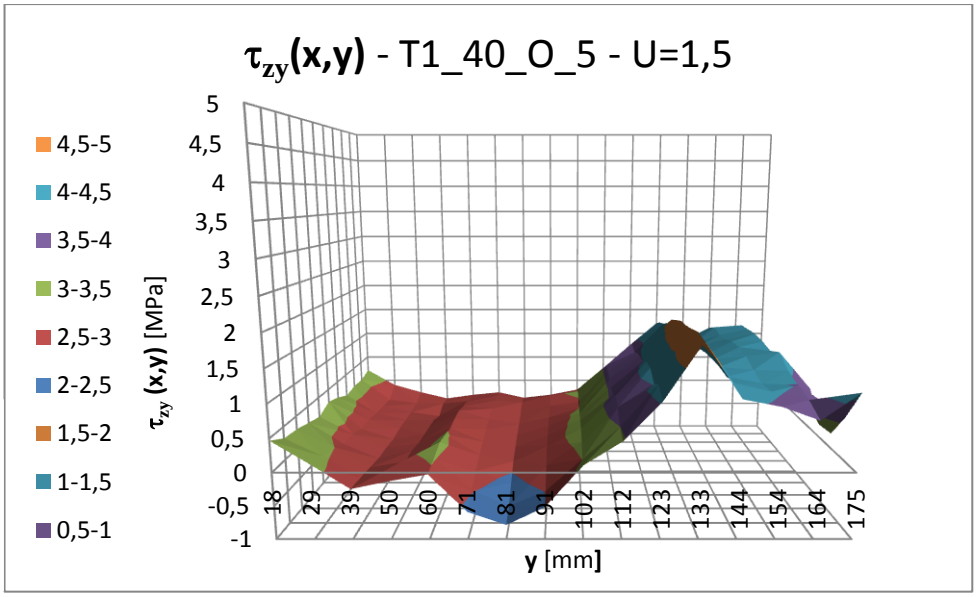

fig. IV.80 - The bond stress field [MPa] calculated at U=1,5 [mm] for the specimen T1_40_O_5

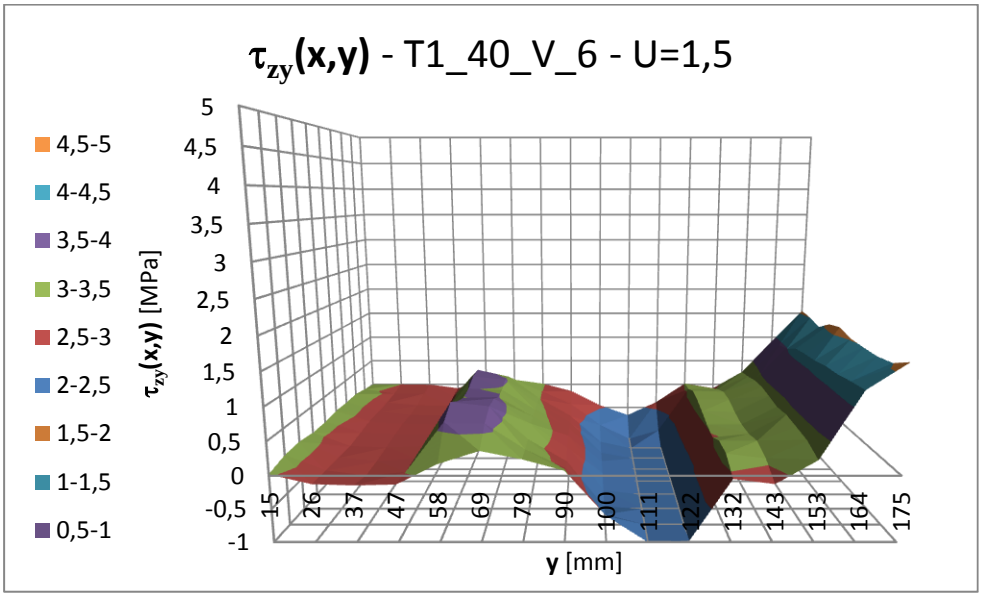

Fig.IV.81 - The bond stress field [MPa] calculated at U=1,5 [mm] for the specimen T1_40_V_6

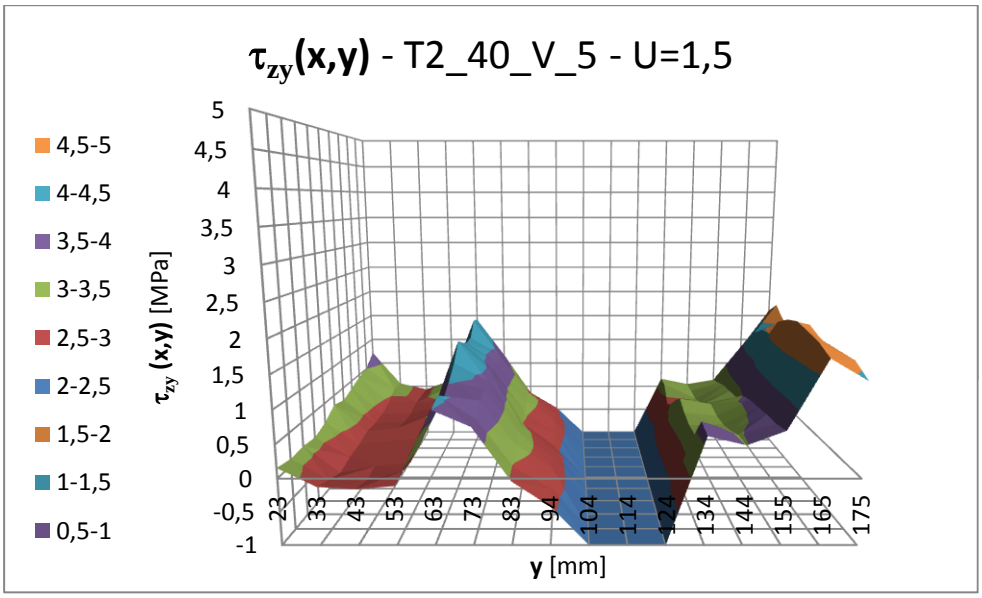

Fig.IV.82 – The bond stress field [MPa] calculated at U=1,5 [mm] for the specimen T2_40_V_5

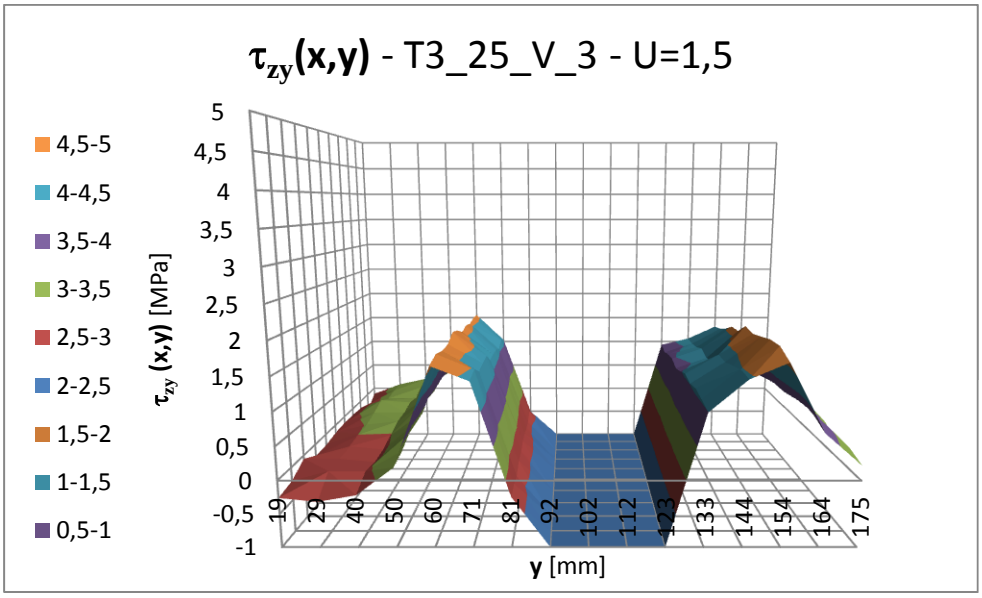

Fig.IV.83 - The bond stress field [MPa] calculated at U=1,5 [mm] for the specimen T3_25_V_3

Step 2 (U = 2 mm)

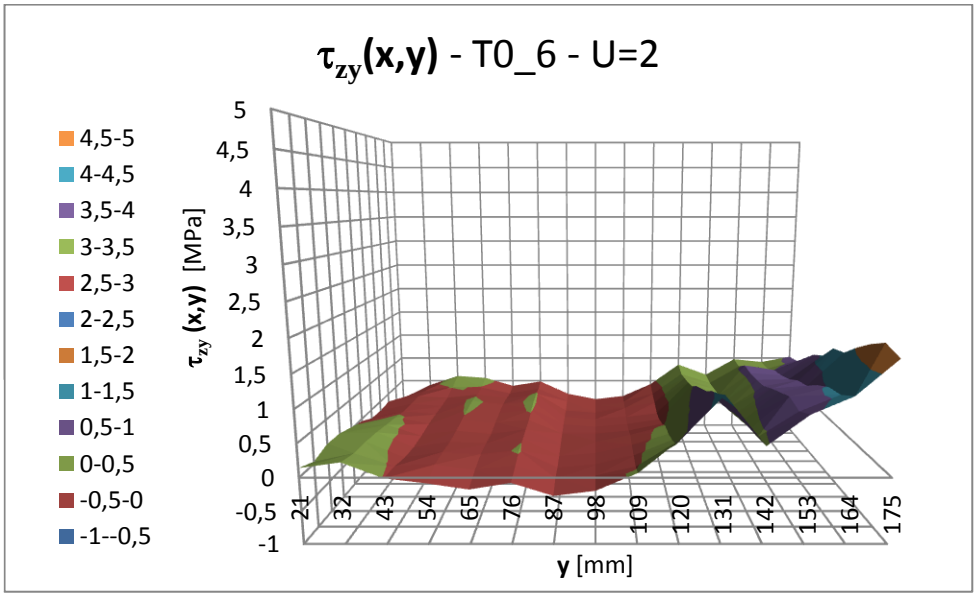

fig. IV.84 - The bond stress field [MPa] calculated at U=2 [mm] for the specimen T0_6

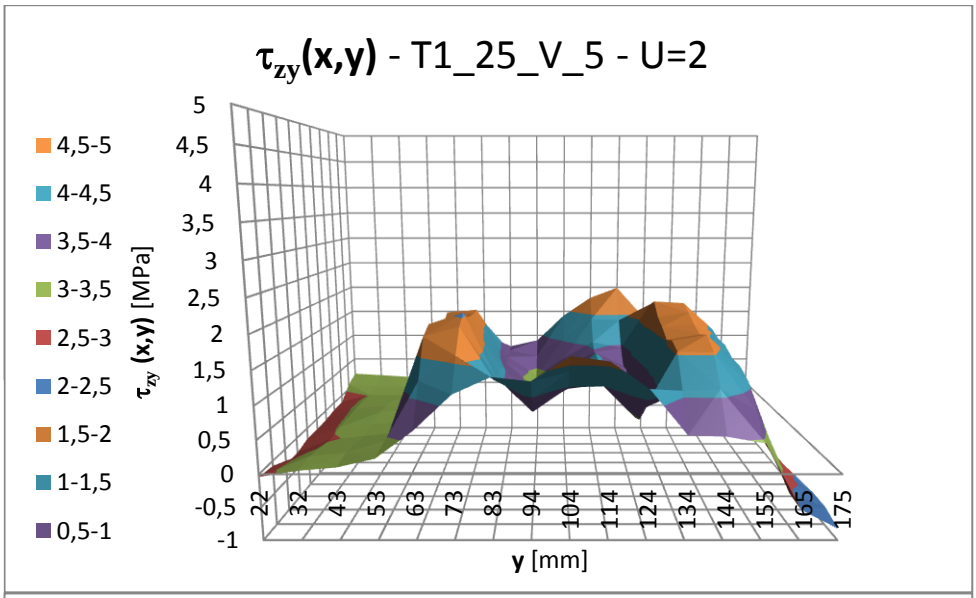

Fig. IV.85 - The bond stress field [MPa] calculated at U=2 [mm] for the specimen T1_25_V_5

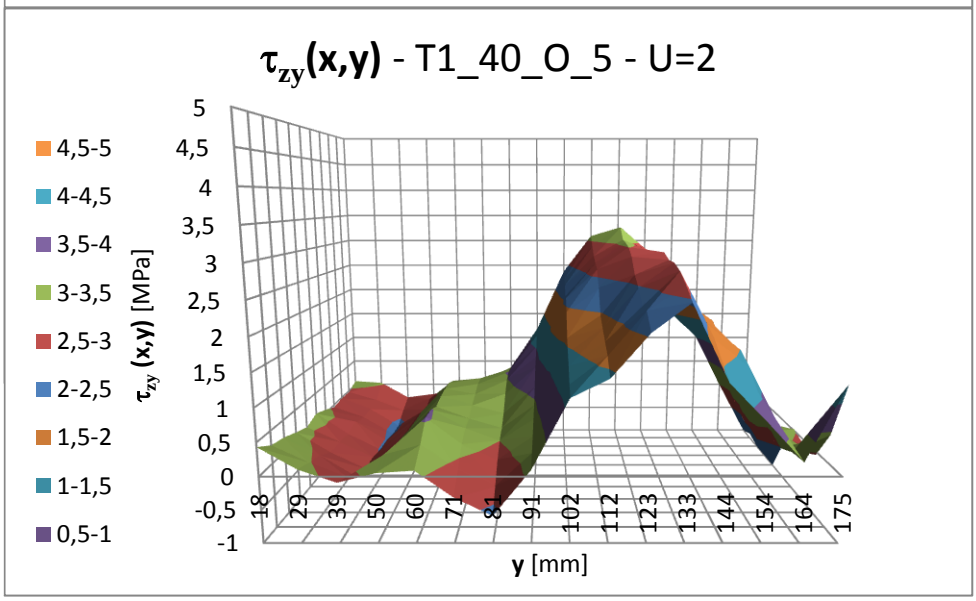

Fig. IV.86 - The bond stress field [MPa] calculated at U=2 [mm] for the specimen T1_40_O_5

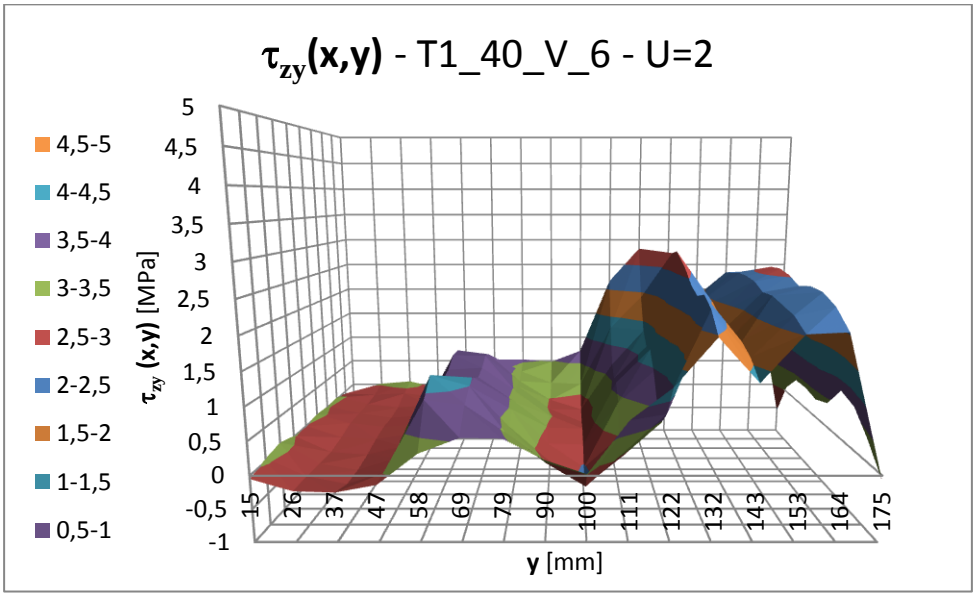

Fig. IV.87 - The bond stress field [MPa] calculated at U=2 [mm] for the specimen T1_40_V_6

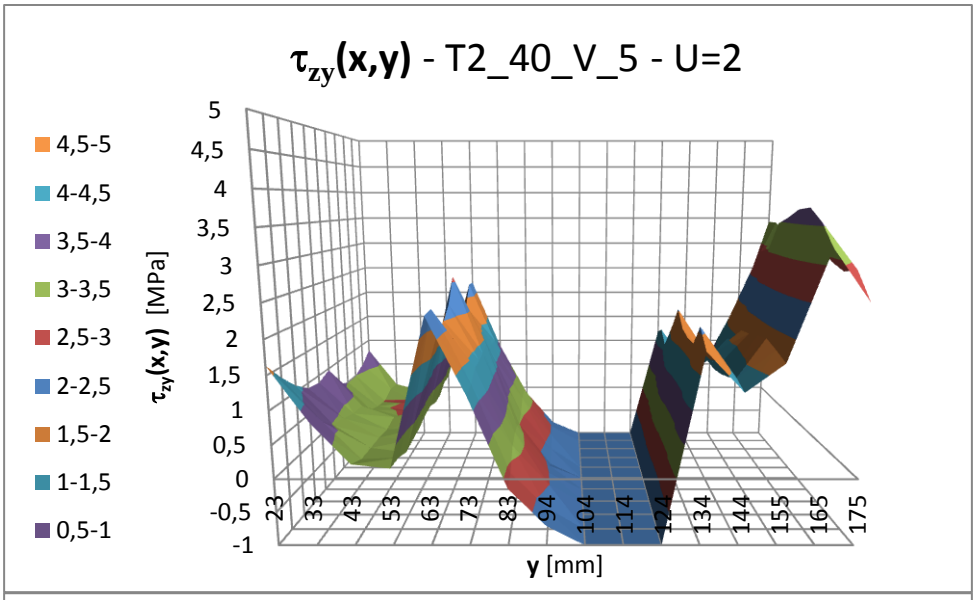

Fig.IV.88 - The bond stress field [MPa] calculated at U=2 [mm] for the specimen T2_40_V_5

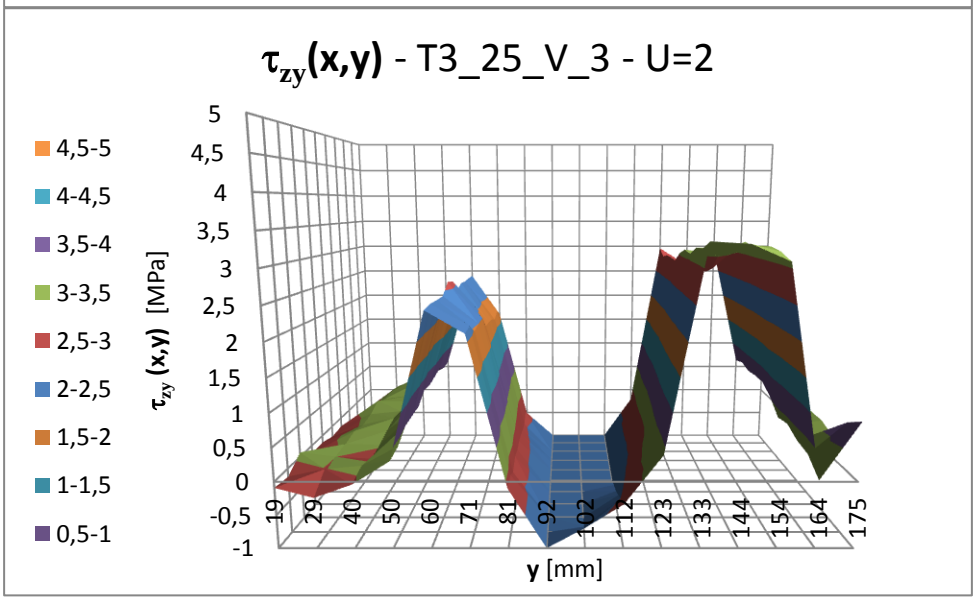

Fig. IV.89 - The bond stress field [MPa] calculated at U=2 [mm] for the specimen T3_25_V_3

Step 3 (U = 2,25 mm)

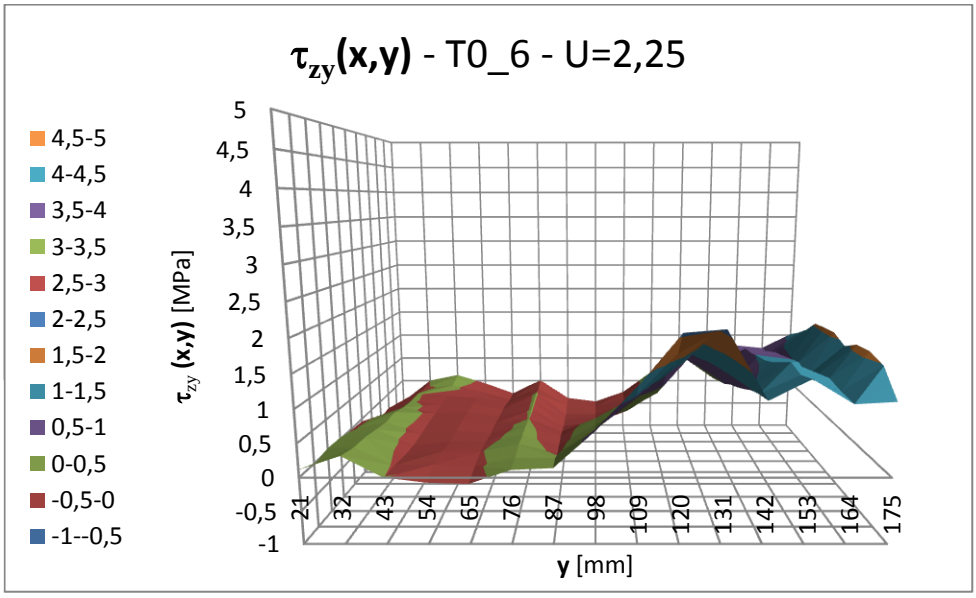

Fig. IV.90 - The bond stress field [MPa] calculated at U=2,25 [mm] for the specimen T0_6

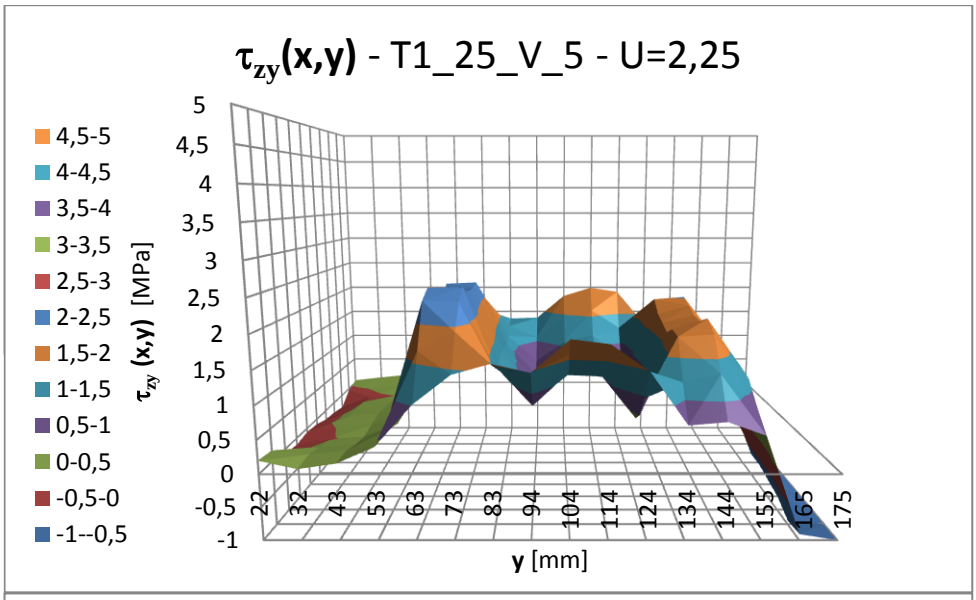

Fig. IV.91- The bond stress field [MPa] calculated at U=2,25 [mm] for the specimen T1 25 V 5

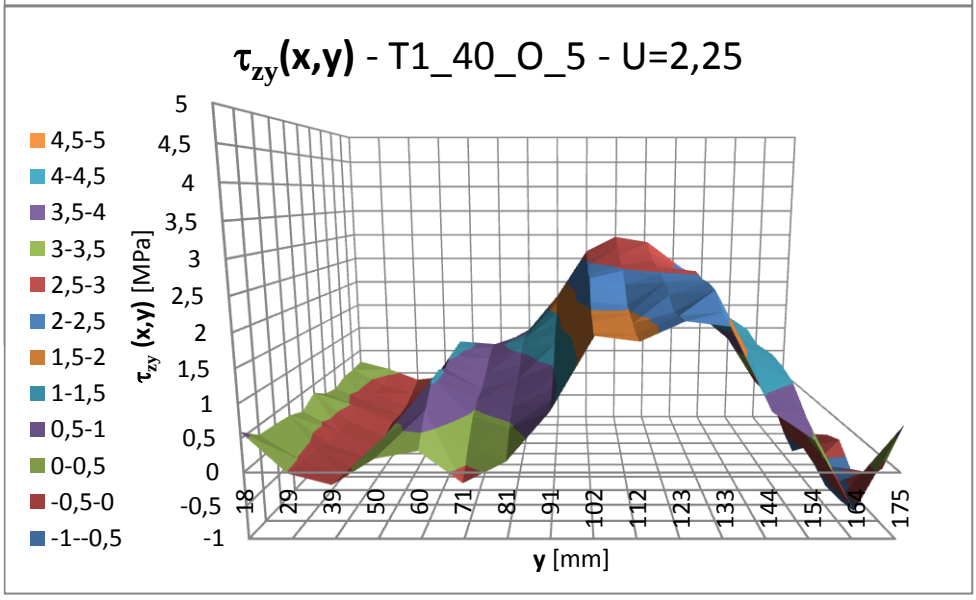

Fig. IV.92- The bond stress field [MPa] calculated at U=2,25 [mm] for the specimen T1_25_V_5

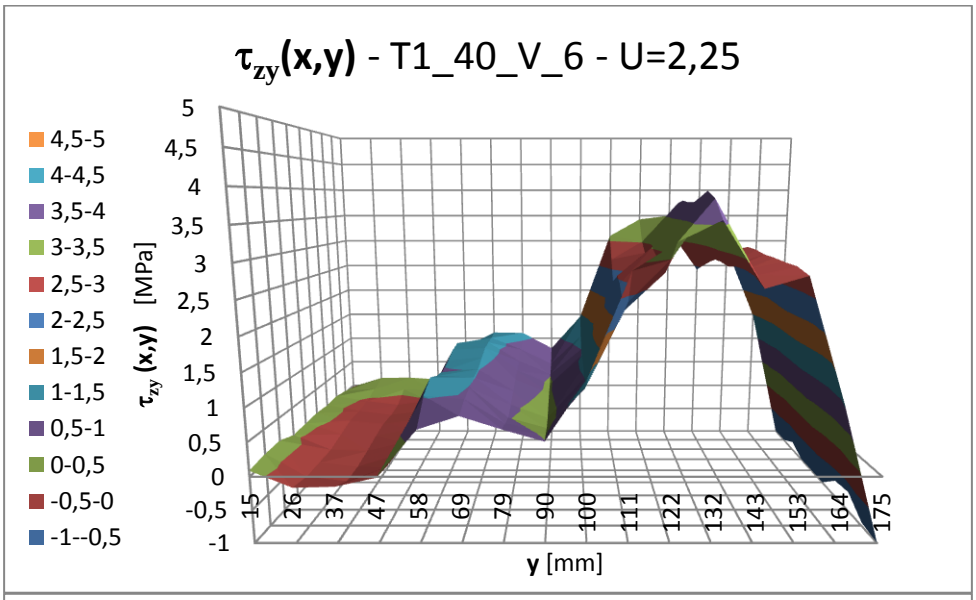

fig. IV.93 - The bond stress field [MPa] calculated at U=2,25 [mm] for the specimen T1_40_V_6

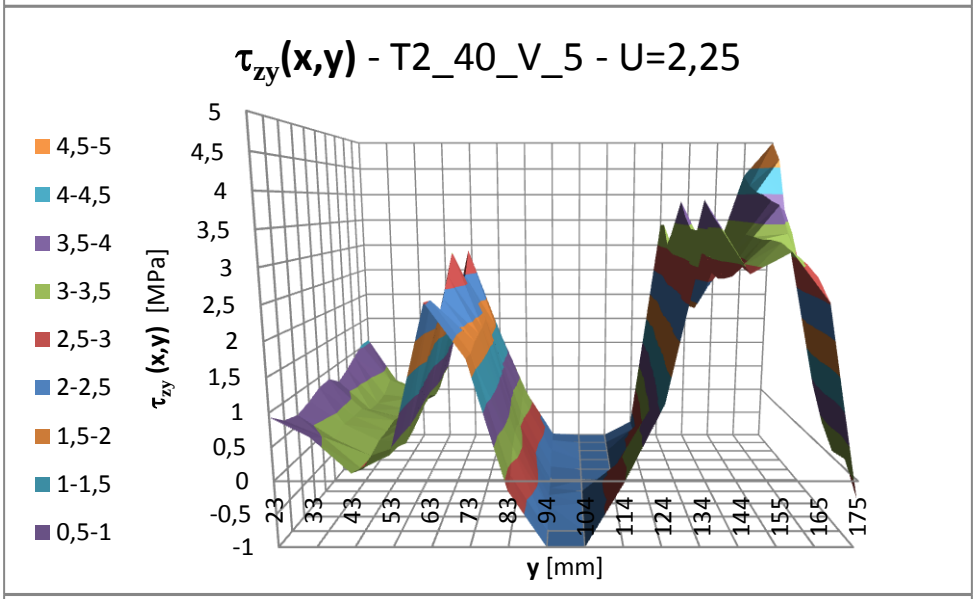

Fig. IV.94 - The bond stress field [MPa] calculated at U=2,25 [mm] for the specimen T2_40_V_5

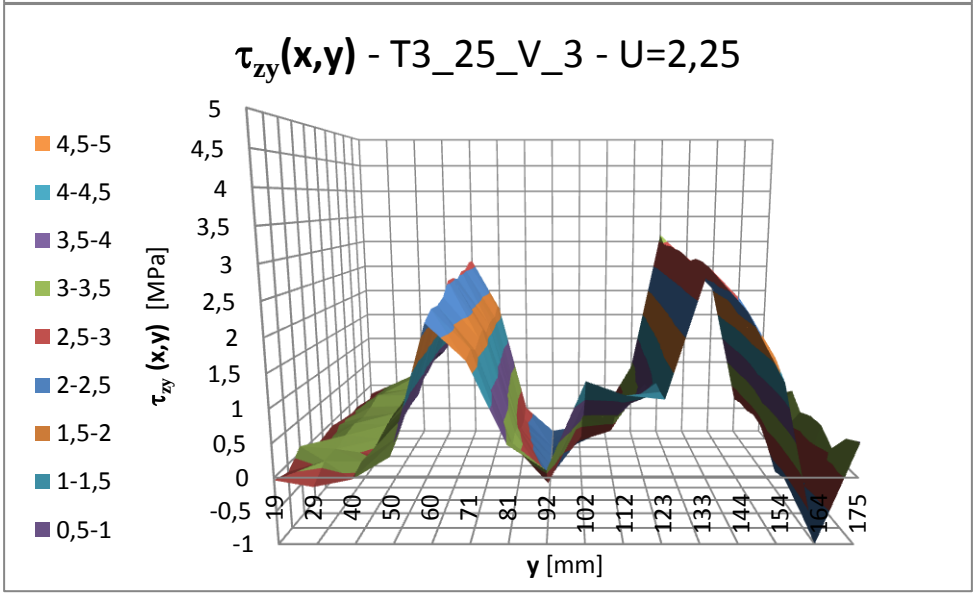

Fig. IV.95 - The bond stress field [MPa] calculated at U=2,25 [mm] for the specimen T3_25_V_3

Step 4 (U = 2,50 mm)

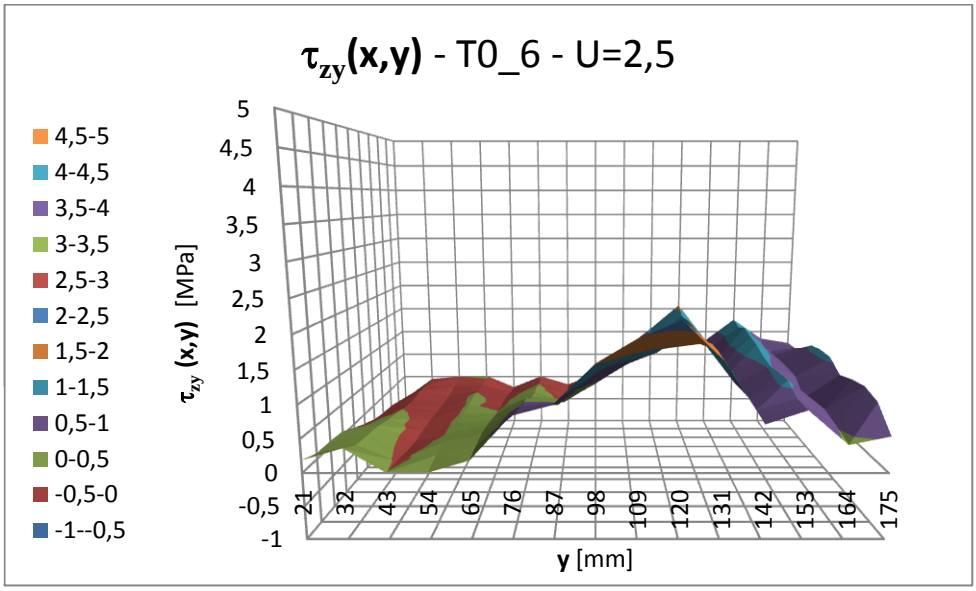

Fig. IV.96 - The bond stress field [MPa] calculated at U=2,50 [mm] for the specimen T0_6

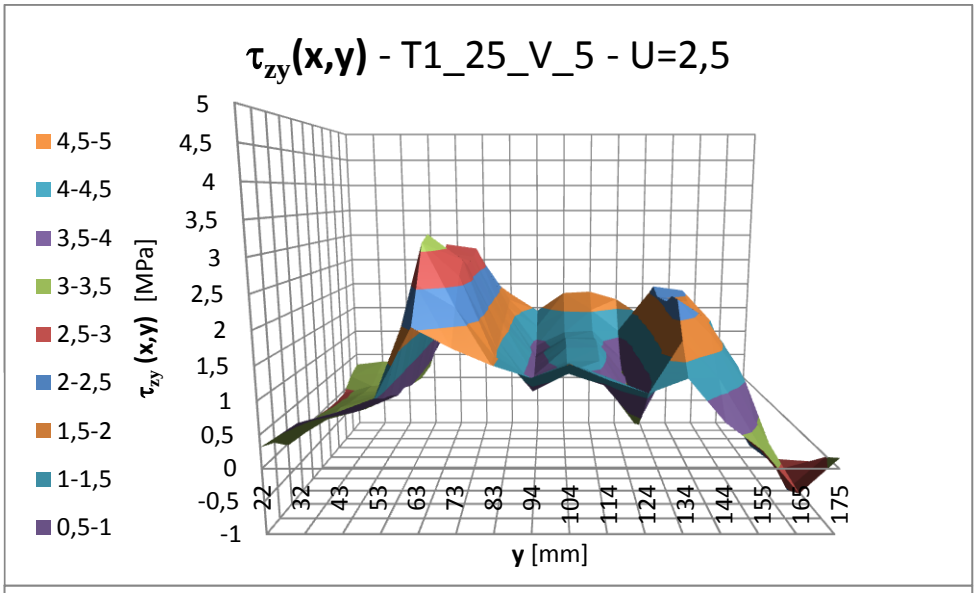

Fig. IV.97 - The bond stress field [MPa] calculated at U=2,50 [mm] for the specimen T1_25_V_5

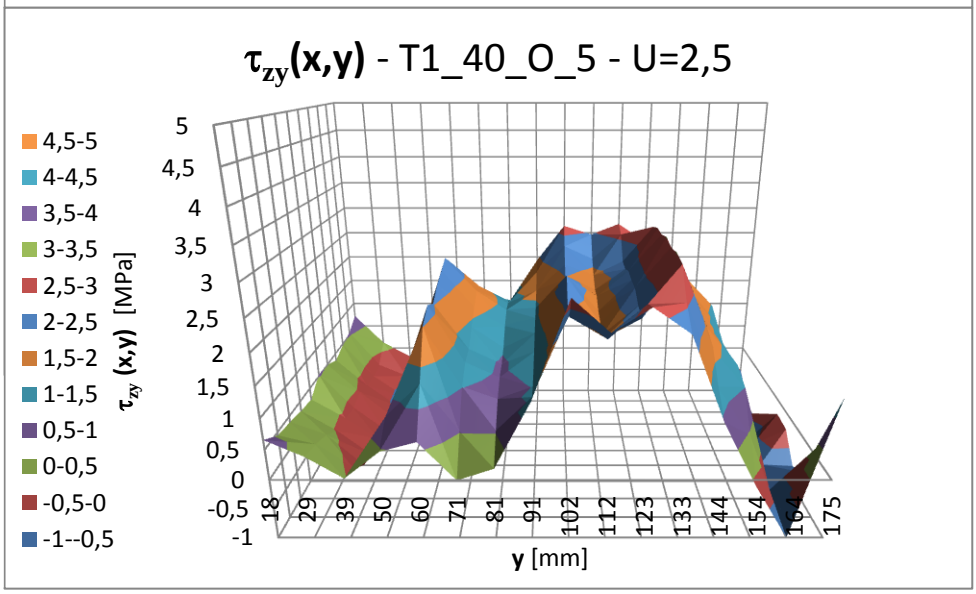

Fig. IV.98 - The bond stress field [MPa] calculated at U=2,50 [mm] for the specimen T1_40_O_5

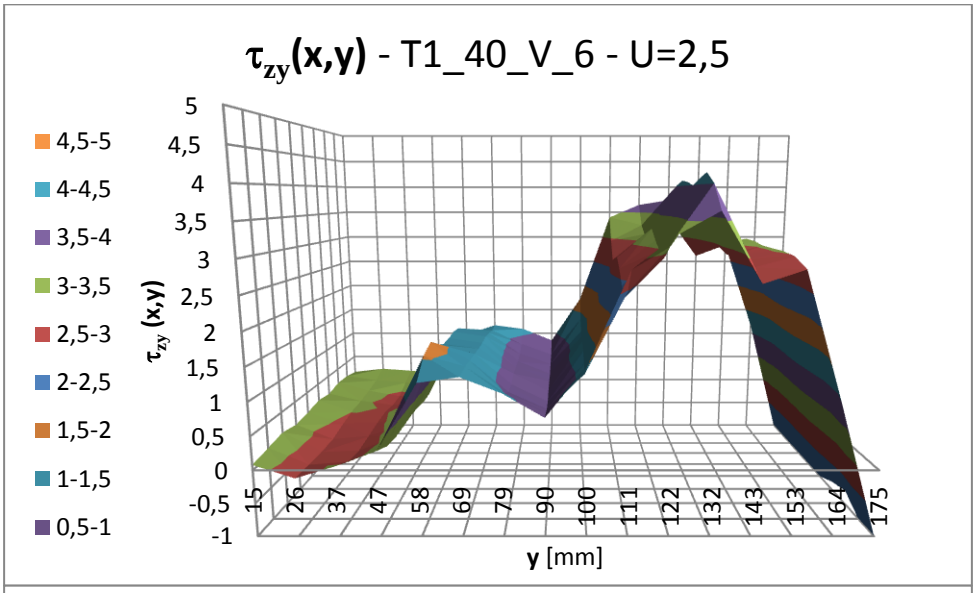

Fig. IV.99 - The bond stress field [MPa] calculated at U=2,50 [mm] for the specimen T1_40_V_6

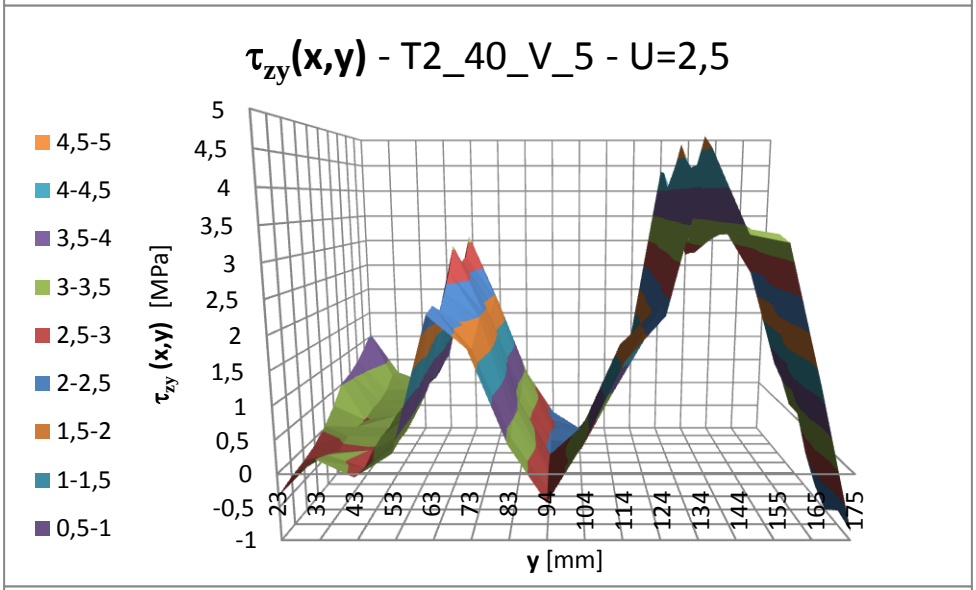

Fig. IV.100 - The bond stress field [MPa] calculated at U=2,50 [mm] for the specimen T2_40_V_5

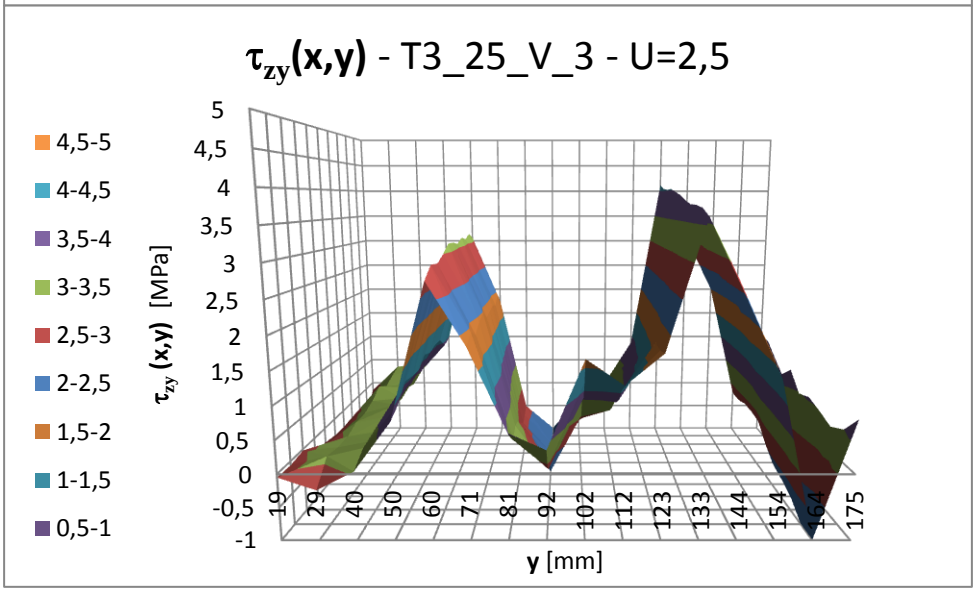

Fig. IV.101 - The bond stress field [MPa] calculated at U=2,50 [mm] for the specimen T3_25_V_3

Step 5 (U = 2,75 mm)

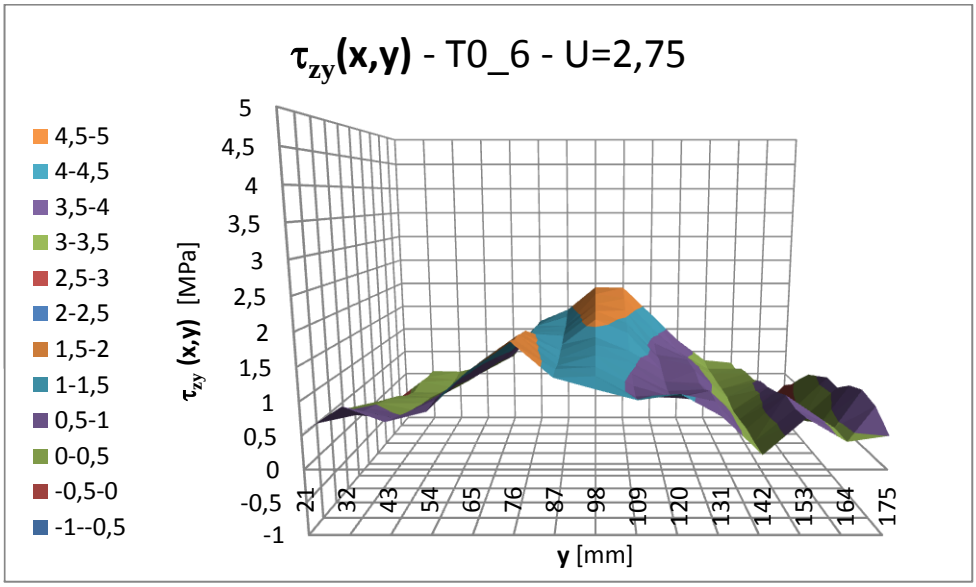

Fig. IV.102 - The bond stress field [MPa] calculated at U=2,75 [mm] for the specimen T0_6

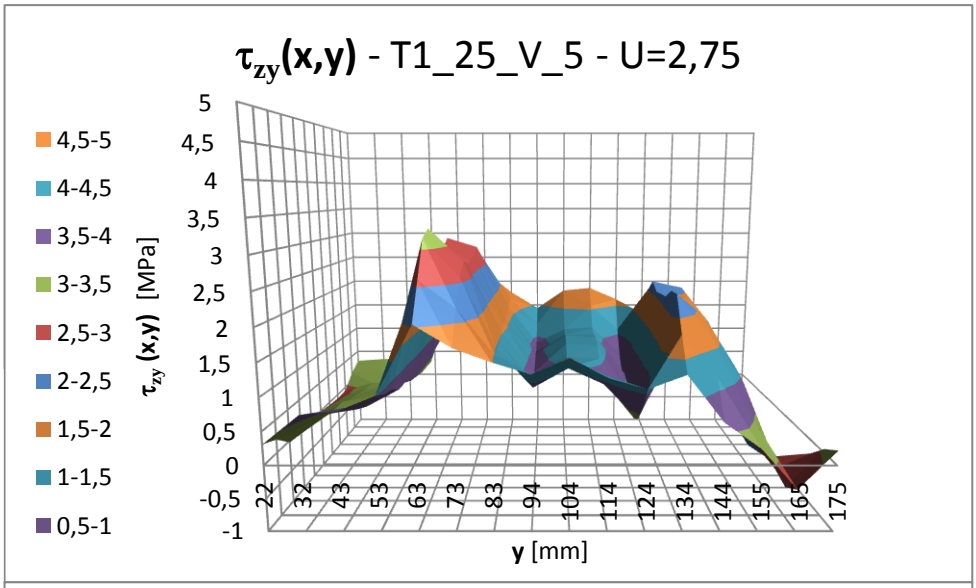

Fig. IV.103 - The bond stress field [MPa] calculated at U=2,75 [mm] for the specimen T1_25_V_5

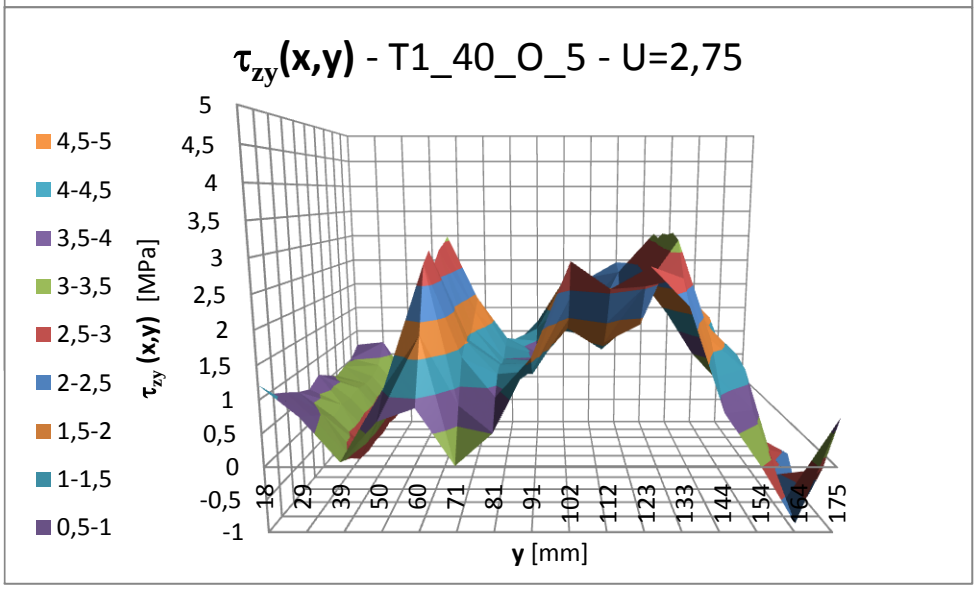

Fig. IV.104 - The bond stress field [MPa] calculated at U=2,75 [mm] for the specimen T1_40_O_5

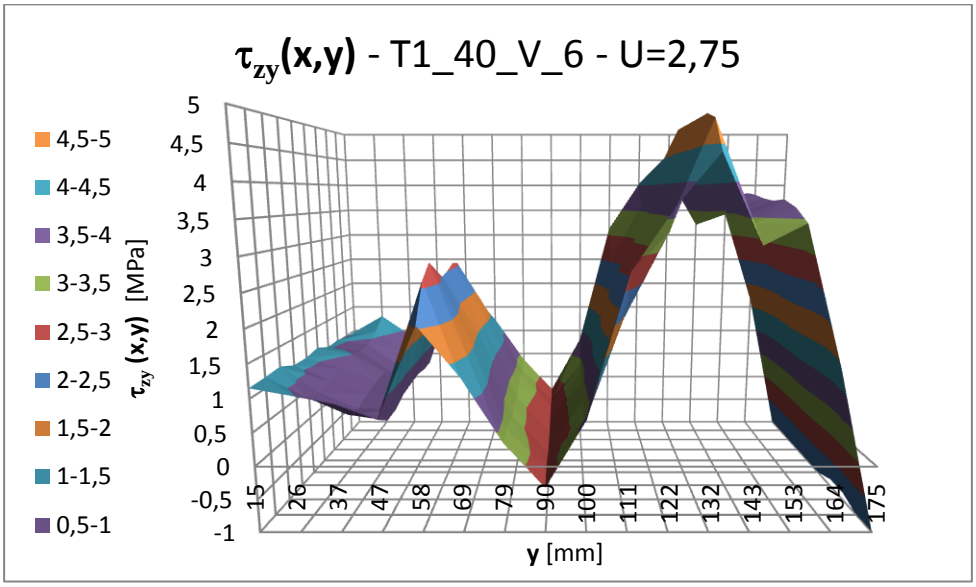

Fig. IV.105 - The bond stress field [MPa] calculated at U=2,75 [mm] for the specimen T1_40_V_6

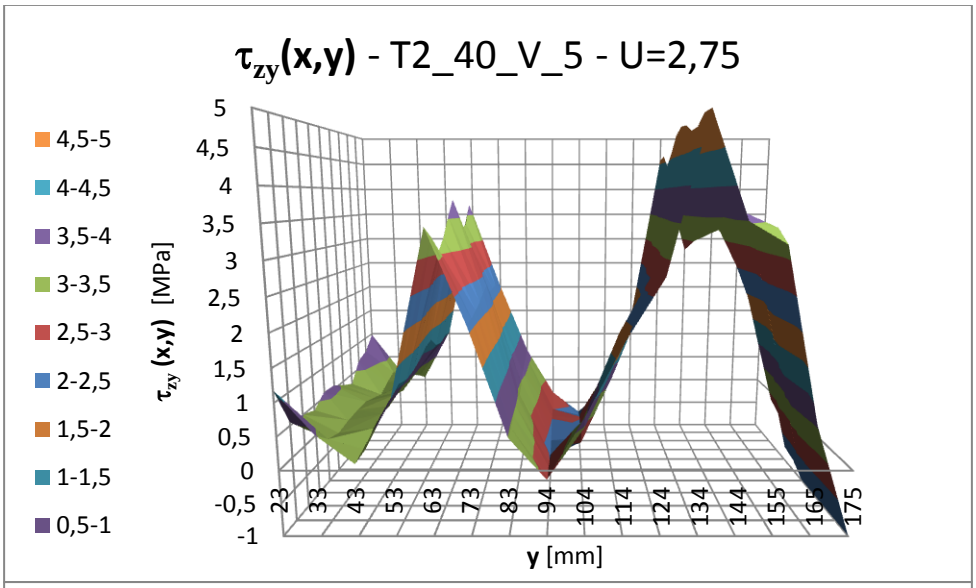

Fig. IV.106 - The bond stress field [MPa] calculated at U=2,75 [mm] for the specimen T2_40_V_5

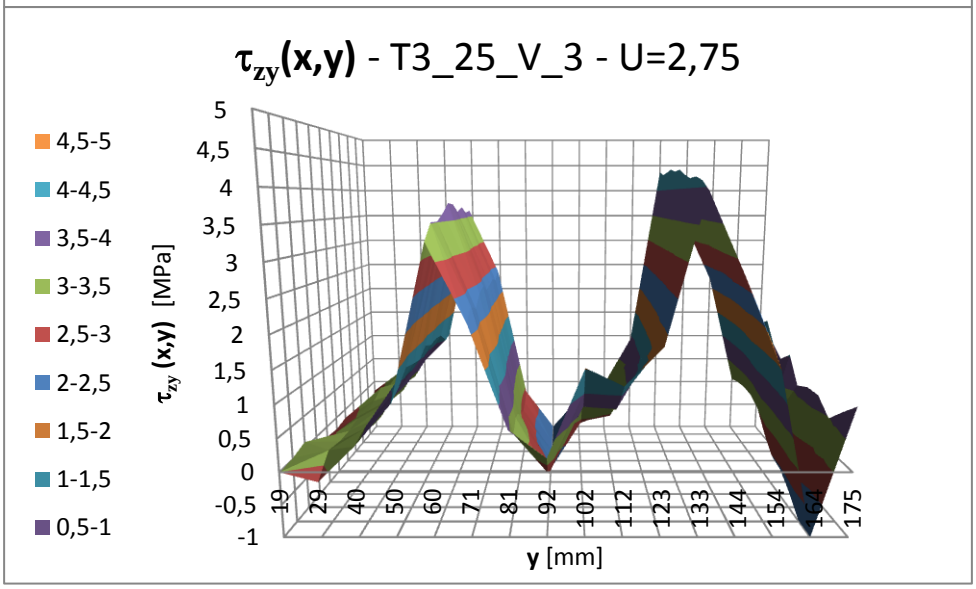

Fig. IV.107 - The bond stress field [MPa] calculated at U=2,75 [mm] for the specimen T3_25_V_3

Step 6 (U = 3 mm)

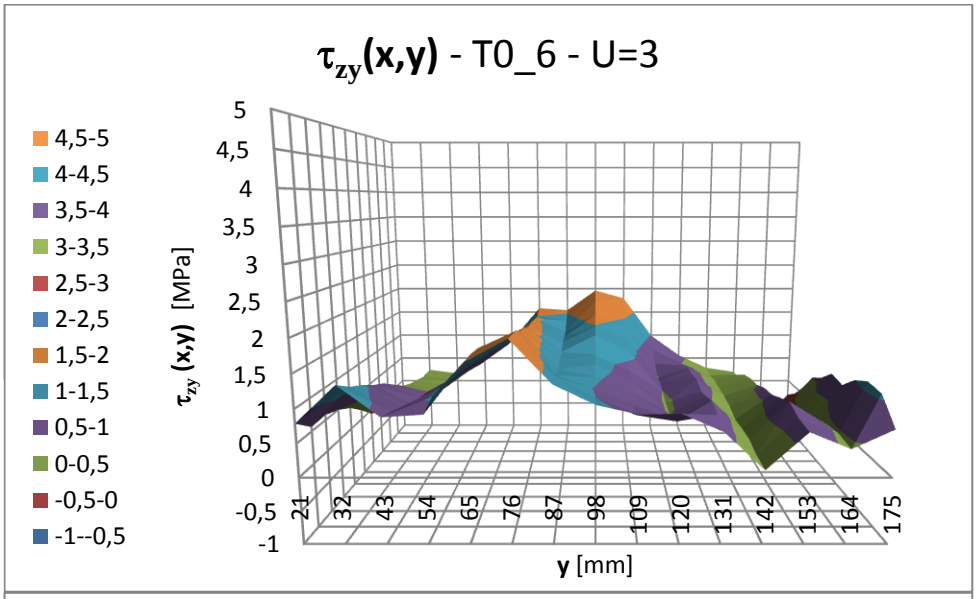

fig. IV.108 - The bond stress field [MPa] calculated at U=3 [mm] for the specimen T0_6

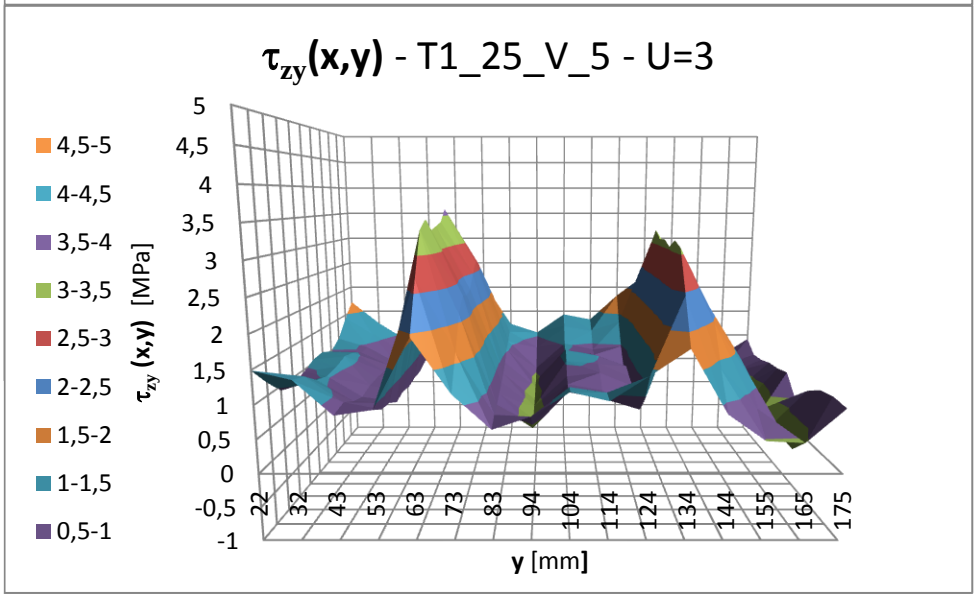

fig. IV.109 - The bond stress field [MPa] calculated at U=3 [mm] for the specimen T1_25_V_5

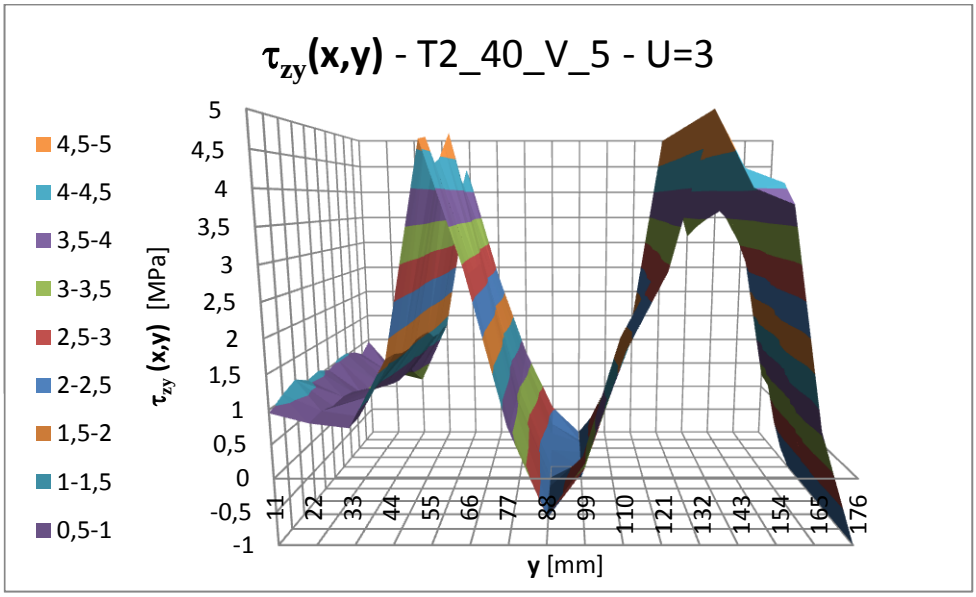

Fig. IV.110 -The bond stress field [MPa] calculated at U=3 [mm] for the specimen T2_40_V_5

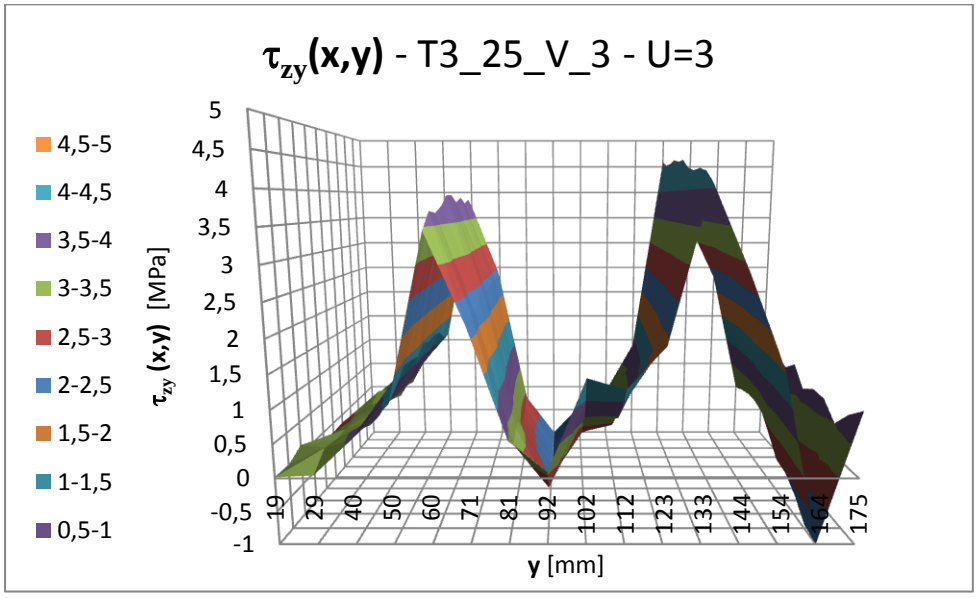

Fig. IV.111 - The bond stress field [MPa] calculated at U=3 [mm] for the specimen T3_25_V_3

4.3.4 The accuracy of the strain and stress fields

To verify the accuracy of the strain and stress fields the equilibrium between the force registered by the universal machine Deltalab (F_d) and the force (F_e), obtained by evaluating the resultant of the tangential stresses, has been checked. The force F_e is defined in equation (4.4). The comparison between the two forces has been carried out in the six load steps, defined and discussed in the previous pages, of the reference test T0_6. The numerical values of F_d and F_e are presented in *table 4.XXII*.

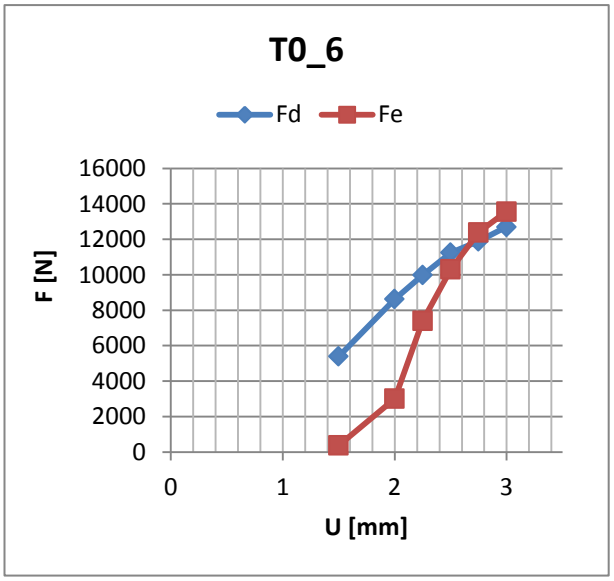

fig. IV.112 - The graphs U-F_d and U-F_e refer to the specimen T0_6

	T0_6	
U [mm]	F_d [N]	F_e [N]
1,50	5400	381
2,00	8630	3014
2,25	9980	7397
2,50	11250	10306
2,75	11890	12398
3,00	12700	13571

Tab. 4.XXII - The numerical values of Fd and Fe recorded in each step of imposed displacement

The graph of *figure IV.112* shows the curves U-F_d and U-F_e. Specifically, in the first three steps, the value of force F_e is lower than that of F_d. In the graph the curve U-F_e intersects the curve U-F_d for a load value almost equal to P_1 (P_1=11,25 kN). In the last three load steps the values of F_e are approximately equal to those of F_d.

The differences between the curves U-F_e and U-F_d have been interpreted on the basis of the following hypothesis:

1. The low stiffness of the steel lock
2. Imperfections on the surface of the specimen

The low stiffness of the steel lock is the principal reason of the underestimation of F_e before the achievement of the peak P_1 and of the overestimation of the same value after P_1. Since the displacement computed by Digital Image Correlation has been obtained comparing a reference

photo (taken at U=0,25 mm) to the deformed photos, all the phenomena that allow a rotation of the analyzed surface during the test generate noises in the results. The photo of reference has been taken when the specimen was perfectly aligned with the load. In this position we can suppose that the angle between the axis of the camera and the specimen reinforced surface is 90° (*fig. IV.113-a*). In this configuration the distance between two points of the texture in the reference image is CD. When the applied load increases the steel lock rotates around the bolts in A (*fig. IV.113-b*) together with the surface of the specimen; in this step the angle between the camera axis and the surface is equal to 90° + α; the distance between the reference point, upon the surface of specimen, is equal to CD+ε_{yy}CD. The value computed by means of DIC is smaller than that of reality, specifically it is equal to cosα(CD+ε_{yy}CD). This assumption justifies the underestimation of strain, stress and force registered before the apparition of the cracks.

When the crack advancement phase starts a detachment of the composite from the support is registered (*fig.IV.113-c*). The rotation of the steel lock could leads to a peeling effect due to the non-planarity between the axis of load and the reinforced surface. This configuration allows the DIC analysis to measure a value of strain in correspondence to the crack advancement different to that of the real one. This hypothesis justifies the higher value of F_e compared to F_d after the peak P_1.

The natural imperfection of the surface of fire brick (steel cylinder) leads to a rotation of the specimen and, therefore, it produces noises in the displacement estimation of DIC.

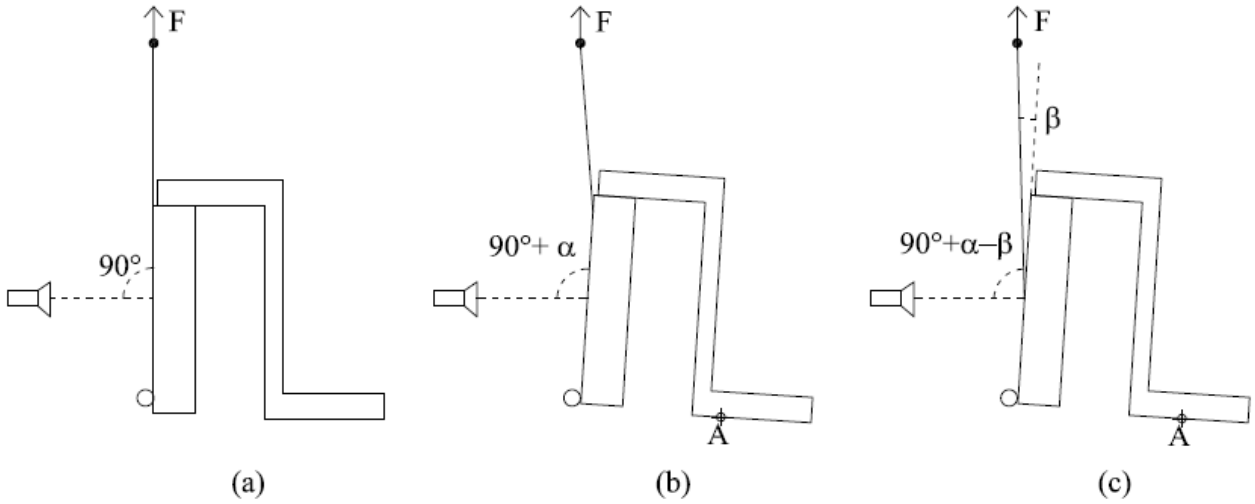

fig. IV.113 - Three steps of hypothetical test; (a) the step corresponding to the reference image, (b) a phase of load before the achievement of peak P_1, (c) crack advancement phase characterized by peeling (after the achievement of P_1). Three steps of hypothetical test; (a) the step corresponding to the reference image, (b) a phase of load before the achievement of peak P1, (c) a hypothesis of crack advancement phase characterized by peeling (after the achievement of P1).

The comparison between F_e and F_d referred to the test T0 shows the good performance of the bi-dimensional DIC analysis. The remarks presented in this paragraph underline that the accuracy of the Digital Correlation analysis is also connected to the boundary condition and to the imperfections of the specimen. Indeed it has been demonstrated that the equation (3.1), defined by Corr et al. [47], is suitable to be used to calculate the bond stresses in simple adhesion problems.

The same procedure used to verify the accuracy of the DIC and the relevance of the equation (3.1) has been developed to study the fastened specimens. In this framework the results obtained show a difference between F_e and F_d. A new detailed analysis of the experimental data and a specific mechanical model will be developed in the future to define the stresses transferred in the anchor zone. Finally the strain and stresses fields analysis about the fastened specimens described in the previous paragraph are coherent with the phenomena registered during the tests. However, for the specimen reinforced with anchor, the comparison between F_e and F_d shows that the values obtained by DIC analysis and using the bond stress equilibrium (3.1) should only be considered as qualitative data.

4.4 Discussion about the global results

The analysis of the results of the tests has led to the definition of the average value and the standard deviation of the peak loads, of the energy and of the displacement corresponding to each series.

As shown in the graphs U-L presented above, almost all specimens belonging to the same group have a similar behavior. The exceptions registered are correlated to several main causes: 1) the mechanical property of each firebrick (par. 2.2.2.1.1), 2) the imperfect alignment of the specimen in the test apparatus due to the geometrical imperfection of each firebrick. 3) the amount of epoxy resin used in the manufacturing process.

The characterization study carried out in Florence showed that the main value of the compressive strength of the fire brick has a coefficient of variation that ranges between 5,13% and 9,02%. Since the cohesive fracture occurred inside the support the mechanical features of the brick influence the results.

When the surfaces of the specimen in contact with the steel lock are characterized by imperfections the correct alignment of the sample might not be achieved. In this case a load peeling component could be developed leading to a premature debonding of anchor splay from the support.

Since the failure of the system sheet-anchor occurs frequently with a debonding fracture (DSA), the amount of epoxy resin used to bond the anchor fan to the CFRP sheet influences the value of peak P_3 and the correlated modality of failure.

The comparison of the six master curves described in the previous paragraphs (one for each series) underlines the differences between the specimen configurations. These curves are represented in *fig. IV.114*. Several observations can be made:

1) All the series characterized by the application of one or more fiber anchors have an average peak load bigger than those of series T0;
2) The master curve of series T1 and T2 present a residual loading phase after the load fall registered in P_2. This phase increases the ductility of the system;
3) The stiffness of the master curve T0 is smaller than that registered for the other series; and
4) The master curves related to series with anchor/s splay of 75° are characterized by an almost identical slope of the first stroke.

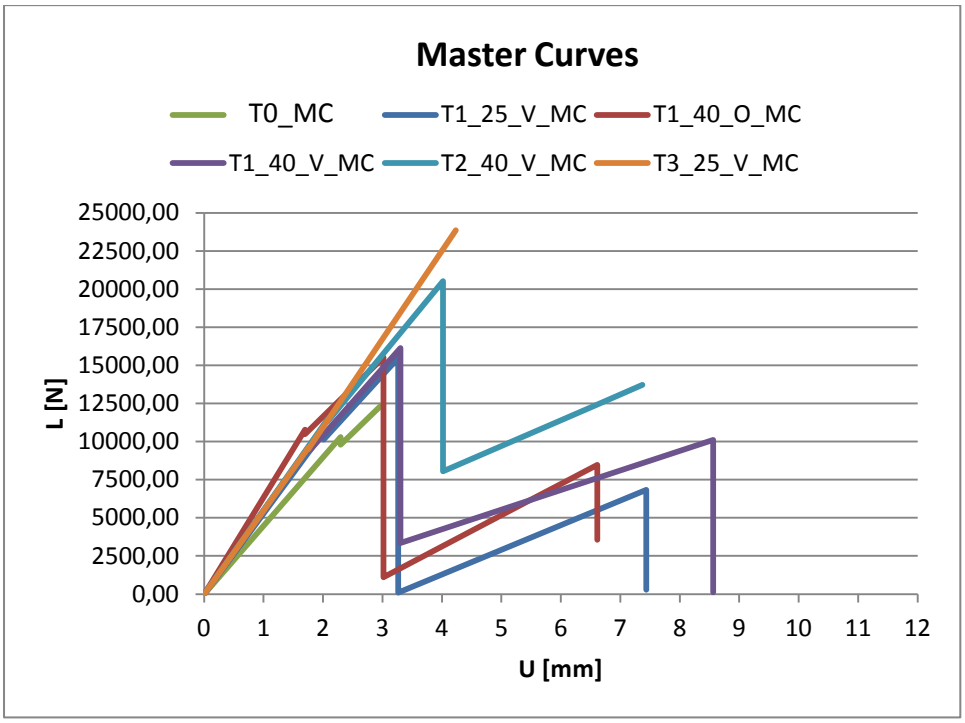

fig. IV.114 - The comparison between the master curve of the six series.

The average value of the peak P_1 is shown in *fig. IV.115* with the corresponding standard deviation. This value is correlated to the development of the first crack in the fire brick. The results show an almost uniform behavior in the different series tested.

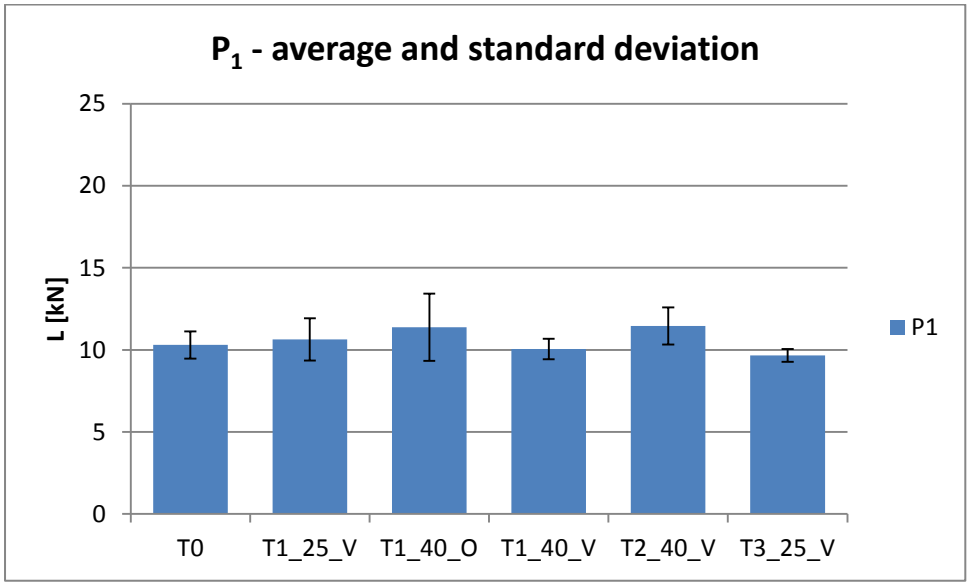

fig. IV.115 - The average peak P_1 registered in the different series

The bar graph of *figure IV.116* presents the average values of P_2 and the corresponding standard deviation of each series tested. P_2 is the peak of load in the test. The tests show that the maximum

load achieved is linked to the number of anchors. The typology of anchor splay does not affect the value of P_2; in fact, the bars that represented the peak load of specimen T1_25_V, T1_40_O and T1_40_V show almost the same value. Therefore, the experiments underline that the crack advancement is influenced by the number of anchor dowels fastened inside the fire brick. In this context, the "nail" diameter and the amount of fiber used to realize the anchor have a central role.

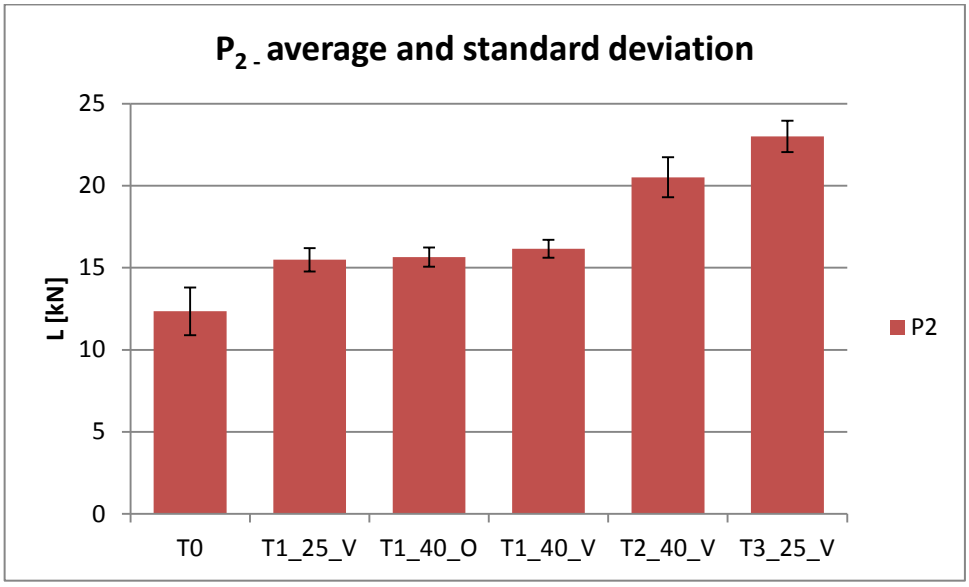

fig. IV.116 - The average peak P_2 registered in the different series

The rate of the maximal load increment has been obtained comparing each series of fastened specimen with the reference series T0 (*tab. 4.XXIII*). It should be noted that the percentage increase almost linearly with the anchor number.

tab. 4.XXIII - The % of increase of the maximum load P_2 correlated to each fastened series. The value of P_2 reported in the first line is the average peak obtained in the series T0 used as term of comparison.

	P_2		
P_{2T0}	12,35		[kN]
T1_25_V	+	25,47	%
T1_40_O	+	26,83	%
T1_40_V	+	30,92	%
T2_40_V	+	66,21	%
T3_25_V	**+**	**86,34**	**%**

The peak P_3 has been recorded twelve times in the tests of series T1_25_V, T1_4O_O and T1_40_V. In those experiments the failure of the system CFRP sheet – fiber anchor has occurred almost always with an adhesive debonding between the splay anchor and the sheet. The peak P_3 is recorded in 4 experiment of the series T2_40_V. In three of these the failure is not linked to the detachment of the fan anchor but to a prismatic failure. The peak P_3 registered during two of 4 tests T3_25_V have not been considered in this study. The value of the average peaks P_3 are shown in *fig. IV.117*.

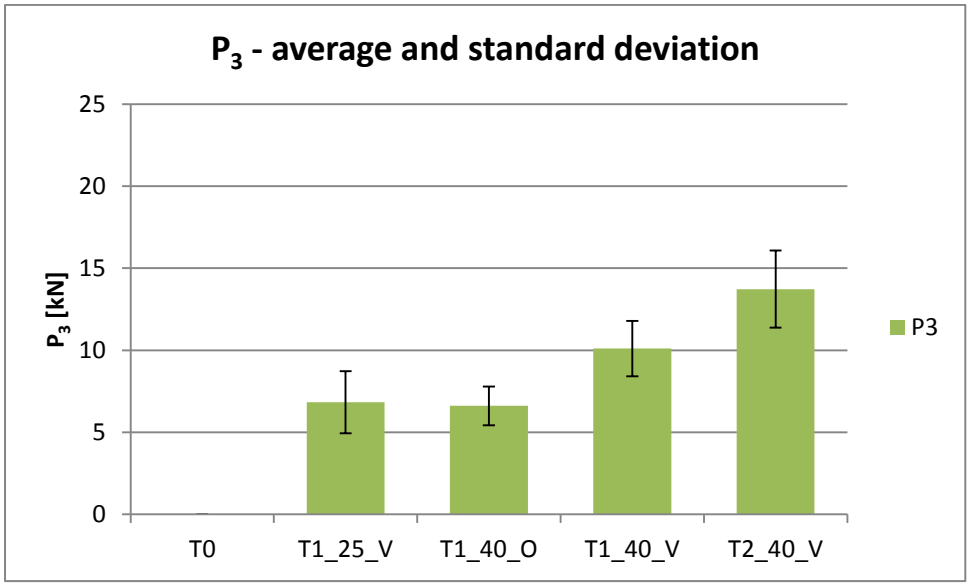

fig. IV.117 - The average peak P_3 registered in the different series

Between the series T1, the specimens T1_40_V are the most ductile. It is important to underline that the average value of P_3 of the series T2_40_V is higher than the P_2 of series T0.

The energy Γ [J] has been calculated to measure the ductility of the different reinforced system (tab. 4.XXIV). The sum of average values $\Delta\Gamma 1+\Delta\Gamma 2$ of each series (*fig. IV.118*) has been compared with the average of energy dissipated by the specimens T0 once the ultimate load is achieved (*tab. 4.XXIV*). The increment of this amount of energy is considerable; it ranges from +25,96 % (series T1_40_O) to +47,5 % (series T3_25_V). The bar graphs represented in *fig. IV.118* refer to the average values of $\Delta\Gamma_1$ and $\Delta\Gamma_2$ obtained from a population constituted by all the specimens of each series. The data of *figure IV.119* refer to the average of energy $\Delta\Gamma_i$ and $\Delta\Gamma_3$. It must be underlined that these average values have been obtained from a population composed only of the tests characterized by residual loading phase (stroke CD). The *fig. IV.118* and *IV.119* show that the splay anchor influence the ductility of the reinforced system. Indeed, the only parameter that

justifies the different ΔΓ of the series characterized by one nail is the fan anchor. The high ductility of series T1_40_V is evident.

Tab. 4.XXIV - The data of the average energy ΔΓ. The values signed by an asterisk have been obtained from the population of tests characterized by residual loading phase. The % of increment is referred to the average energy dissipated by the specimen T0.

Γ [J]	T0	T1_25_V	T1_40_O	T1_40_V	T2_40_V	T3_25_V
$\Delta\Gamma_1$	10,67	9,99	9,84	8,69	10,75	7,95
$\Delta\Gamma_2$	8,10	15,97	14,62	20,62	33,25	39,56
$\Delta\Gamma_i$		9,23*	8,17*	17,31*	52,33*	31,12*
$\Delta\Gamma_3$		8,01*	9,43*	24,74*	11,02*	0,63*
$\Delta\Gamma_1+\Delta\Gamma_2$	**18,77**	25,96	24,46	29,31	44,00	47,50
% increment		+38,30	+30,31	+56,15	+134,44	+153,11
$\Delta\Gamma_i+\Delta\Gamma_3$	0	17,24	17,60	42,05	63,35	31,75

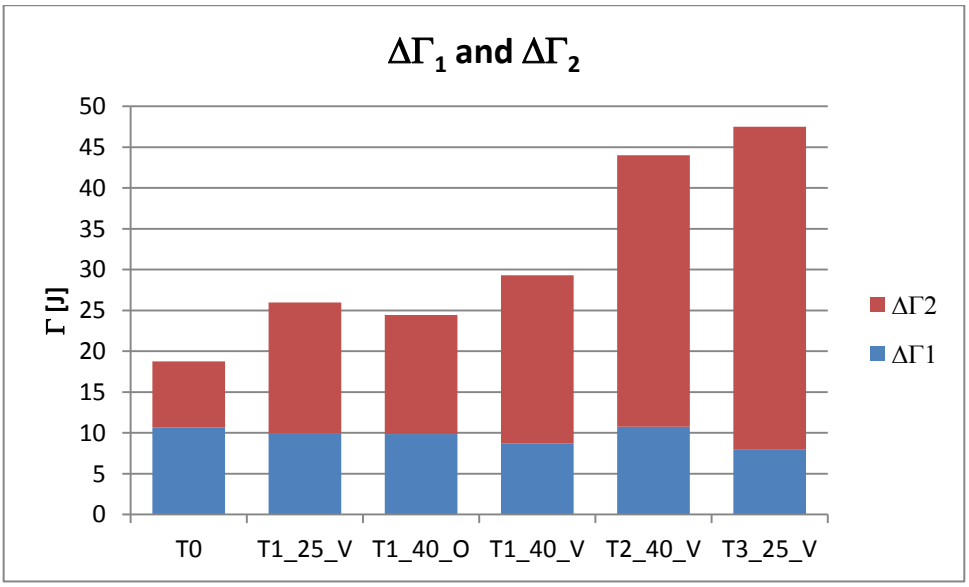

Fig. IV.118 - The average amount of energy $\Delta\Gamma_1$ and $\Delta\Gamma_2$ registered in the different series.

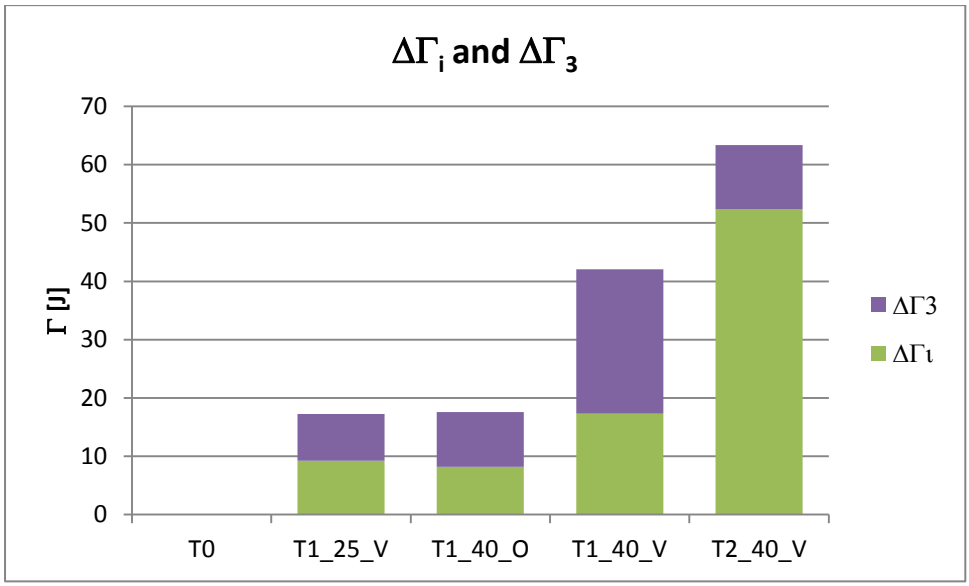

fig. IV.119 - The average amount of energy $\Delta\Gamma_i$ and $\Delta\Gamma_3$ registered in the different series. The population of data used to evaluate these quantities is constituted by only the specimens characterized by a residual loading phase (stroke CD)

If no anchor is present the crack advances progressively from the loaded side to the unloaded side. In the specimens fastened with FRP anchor, the number of nails and the corresponding splay anchor affect the classical evolution of the crack. The strain field ε_{yy} of the five reference specimens fastened at fixed load L=11,9 [kN] shows a strain concentration in the zone between the extremity loaded and the fan anchor (*fig. IV.120*) . The value of L_s related to each specimen in this load step is reported in *table 4.XXV*. The curves y-ε_{yy} of the six specimens, referring to L=12 [kN], are reported in *fig. IV.121*.

ε_{yy} (x,y) L=11,9 kN

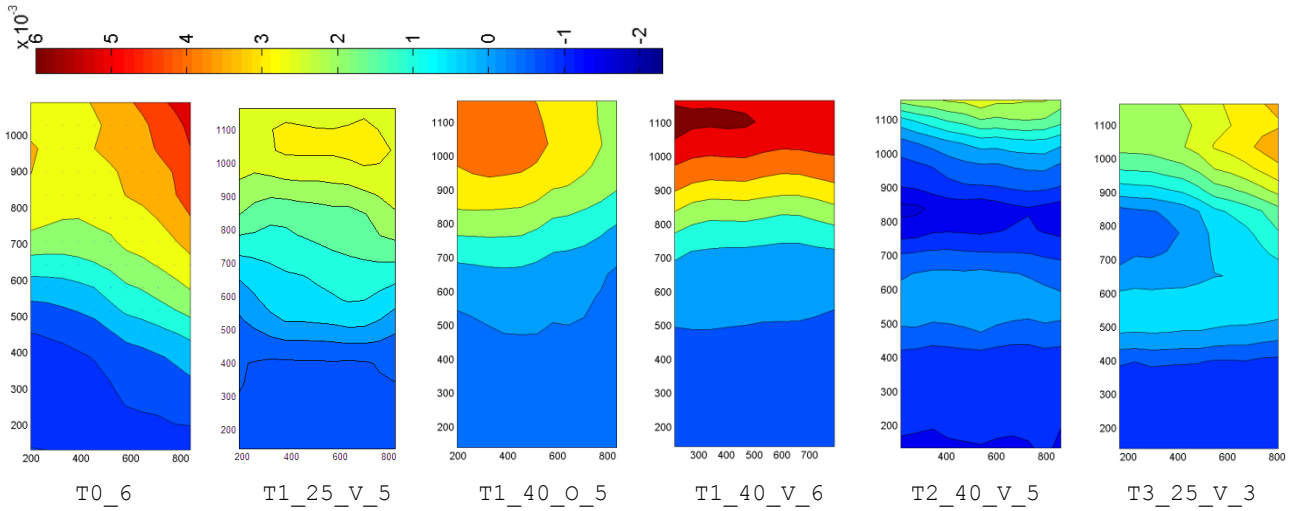

Fig. IV.120 - The strain field $\varepsilon_{yy}(x,y)$ related to six reference specimen at L=11,9 [kN]

Tab. 4.XXV - The value of length Ls recorded in the six different reference specimen when the applied load is equal to L=11,9 kN.

L = 11,9 [kN]	***T0_6***	***T1_25_V_5***	***T1_40_O_5***	***T1_40_V_6***	***T2_40_V_5***	***T3_25_V_3***
L_s [mm]	*111,98*	*101,8*	*72,94*	*74,27*	*20,32*	*72,87*

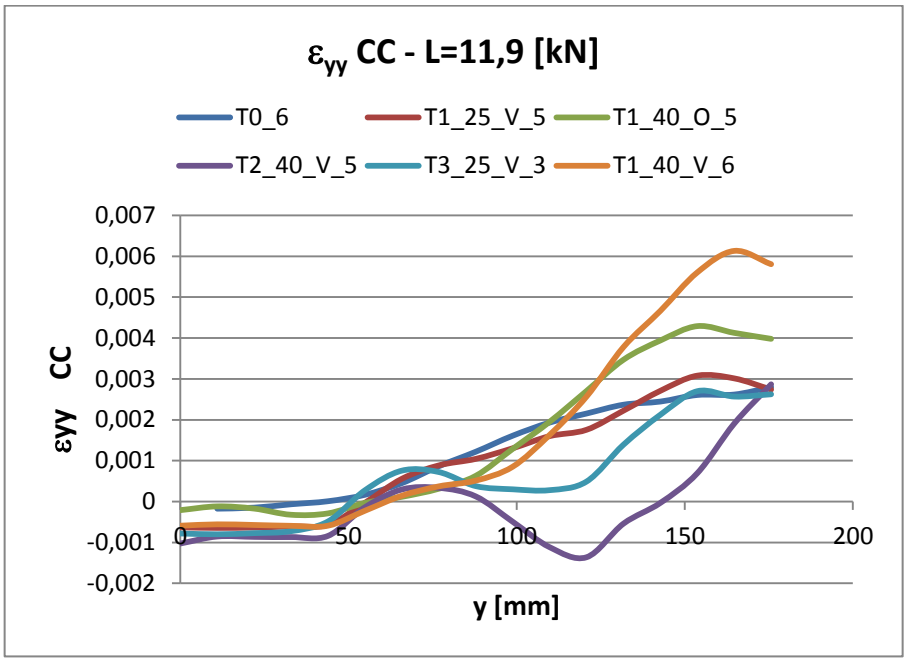

fig. IV.121 - The curves ε_{yy} related to the central column (x=50 mm)when L=11,9 [kN]

The data shown above underline that the fastened configuration T1_25_V_5 leads to a crack advancement process similar to that of series T0. It is evident in the chromatic representation of *figure IV.120*, in the comparison between the curves T1_25_V_5 and T0_6 of *figure IV.121* and in the table of values L_s (L_{ST0_6} =112 mm and $L_{sT1\_25\_V\_5}$ =101,8 mm). The other fastened specimens characterized by only one anchor present a concentration of strain between the loaded border and the anchor ($L_s \approx 73$ mm). The specimens of series T2 and T3 show different values of L_s attributable to the different fan radius.

The *table 4.XXVI* collects the modalities of failure recorded in all the tests. In the majority of specimens of series T0 and T1, the load fall registered after the achievement of peak P_2 is due to a cohesive fracture between the CFRP sheet and the support. The majority of specimens of series T1 that present a further loading phase (stroke DE) fail, once the peak P_3 is achieved, when the debonding between the splay anchor and the CFRP sheet occurs. In the tests of series T_2 a prismatic failure has been recorded in four out of six experiments. The cohesive fracture between the CFRP and the support developed in all the six specimens tested. Twice the prismatic failure has

been registered immediately after the CF, another two times during the residual loading phase. All the tests of series T3_25_V fail with a development of a prismatic failure. On two occasions this failure is verified before the crack advancement affects all the reinforced surface (indeed, before the CF). The residual resistance after the achievement of load peak has been recorded 18 times in a population of 28 fastened specimens (64%).

Tab. 4.XXVI - The modality of failure registered in C and D. The next nomenclature has been used: CF-cohesive fracture, MF-mixed fracture, DSA-debonding splay anchor, PF-Prismatic fracture, PON-Pullout of nail.

Specimen	***Fracture in C***	***Fracture in E***	***Specimen***	***Fracture in C***	***Fracture in E***
T0_1	CF	-	T1_40_V_1	CF	DSA
T0_2	MF	-	T1_40_V_2	MF	PON
T0_3	MF	-	T1_40_V_3	CF	DSA
T0_4	CF	-	T1_40_V_4	CF - DSA	-
T0_5	CF	-	T1_40_V_5	PF	-
T0_6	CF	-	T1_40_V_6	CF	DSA
T1_25_V_1	CF	DSA	T2_40_V_1	CF	DSA
T1_25_V_2	CF	DSA	T2_40_V_2	CF - PF	-
T1_25_V_3	CF	DSA	T2_40_V_3	CF	PF
T1_25_V_4	CF - DSA	-	T2_40_V_4	CF - PF	-
T1_25_V_5	CF	DSA	T2_40_V_5	CF	PF
T1_25_V_6	CF-DSA	-	T2_40_V_6	CF	PF
T1_40_O_1	CF	DSA	T3_25_V_1	*1	
T1_40_O_2	MF-DSA	-	T3_25_V_2	*2	
T1_40_O_3	CF	DSA	T3_25_V_3	CF	PF
T1_40_O_4	CF	DSA	T3_25_V_4	PF	-
T1_40_O_5	CF	DSA	T3_25_V_5	PF	-
T1_40_O_6	CF-DSA	-	T3_25_V_6	CF	PF

Chapter 5

Conclusions and perspectives

5 Conclusions

In this chapter the conclusions drawn from the analysis of the experimental results are presented. Some preliminary questions that have prompted this work have found answers. Namely, these answers are given by the NES single shear tests and offer a general idea of the fiber anchors potentialities in the masonry framework.

The analysis of the experimental results lead to the conclusion that:

- The use of fiber anchors allows the increment of the load peak of the reinforcement
- The presence of the nail gives the system a residual resistance post peak. The anchors avoid the brittle failure of the reinforcement.
- The anchors influence the stress distribution of the reinforced systems before the achievement of the peak load.
- The detachment of the CFRP sheet from the fire brick occurs almost always by cohesive fracture (inside the support).
- The crack advancement is affected by the presence of an anchor.
- The anchors allow a concentration of strain in the area between the anchor and the loaded side of the specimen
- The stress transfer zone (STZ) moves from the loaded to unloaded side. The anchors delay the “classical” evolution of the STZ.
- The Digital Image Correlation procedure is a suitable instrument to study the displacement and the strain fields of the reinforced surface of the specimen.
- The optimal bond length evaluated using the formula of CNR DT200/2004 (1.12) is approximately equal to that recorded during the test of series without anchors.
- The design debonding strength (mode 2) proposed by the CNR DT200/2004 corresponds to the average debonding strength measured in the reinforced specimens without the nail.

The series of reference used to measure the increase of resistance is the T0. The specimens of T0, subjected to a Near End Single Shear test, fail in a brittle manner when the peak P_2 is reached. The average value of P_{2T0} registered during the T_0 tests is 12,35 kN. The average of energy dissipated to achieve this maximum load is 18,77 J.

The experimental analyze proves that the application of fiber anchors generate a considerable enhancement of the maximal peak P_2. The maximal loads registered in each series lead to the conclusion that the increment of the P_2 range between +25% and +86% (these limits are average values corresponding to series T1_25_V and T3_25_V). Once the length and the diameter (amounts of fibers) of the nail are fixed, it has been noted that the increase of the maximum load is correlated mainly to the number of anchors used to fasten the CFRP sheet and not much to the splay characteristics.

Twelve out of eighteen tests carried out on specimens fastened by only one anchor, show a reserve of resistance after the load fall in P_2. In fact, a further loading phase has been registered until the achievement of a peak P_3. The average values of P_3 of series T1_25_V, T1_40_O and T1_40_V are respectively equal to the 55%, 68% and 84% of the P_{2T0}. The characteristic failure observed in P_3 during these series is a debonding between the anchor fan and the CFRP sheet (DSA). The results of the series T1 show that the splay anchor characteristic affects the resistance post peak of the specimen. The series with the fan anchor characterized by a radius of 40 mm and an angle splay of 75° is the most efficient among the series T1 because it allows the highest peak P_3 and the highest dissipation of energy.

The specimens with more than one nail have a different characteristic behavior. The series T2_40_V shows a reserve post peak during four tests; the failure DSA occurs only once while in the other three experiments the CFRP sheet remains attached with the anchor to the support and the failure occurred inside the fire brick with a prismatic fracture. In these tests the average value of P_3 is equal to the 111% of the P_{2T0}. In the series T3_25_V no specimen fails with a debonding of splay anchor. The two specimens that are characterized by a post peak reserve fail by a prismatic fracture after the achievement of peak P_3. The average of P_3 measured in the tests T3 is equal to the 142% of the P_{2T0}. Therefore, the experimental tests show that when the anchors are more than one, collocated and designed in the geometrical configurations of series T2_40_V and T3_25_V, the reinforced system fails because the firebrick fails; the CFRP remains attached to the anchor and, consequently, also to the support. It should be underlined the high ratio between the width of the CFRP sheet and the width of the fire brick support (b_f/b=0,83), it is bigger than the limit fixed experimentally by Yao et al. [6] to avoid the concrete prism failure.

In the experimental study the highest value of P_2 has been obtained for the specimens of series T3_25_V. However, the tests show that this configuration of reinforcement is frequently exposed to

a brittle failure. The tests prove that the series T2_40_V ensures high performances. It is interesting to underline that the value of P_3 reached by the specimens with two anchors is bigger than P_{2T0}. Within the test configurations with one nail the most efficient is the series T1_40_V because it is characterized by the longest ductile phases (the biggest value of $\Delta\Gamma_3$) and the highest value of P_3.

The efficiency of the different configurations has also been measured analyzing the dissipated energy (Γ_{end}). The average value of Γ_{end} registered in series T0 is 18,77 J. The specimens T1_40_V and T2_40_V achieves an average value of Γ_{end} respectively equal to 57,34 J and to 82,01 J. The increment of the ductility due to the anchors is evident.

The differences between the stiffness of the specimens of series T0 and that of series with anchors (illustrated in the graph U-L) show that the anchor influences the stress distribution already in the first phase of the load history. The increment of the peak load allowed by the anchors underline the role of the nails before that the fracture between CFRP sheet and support is verified.

The displacement and strain fields on the reinforced surface of specimens have been detected using the Digital Image Correlation (DIC). This method, for the first time used to study the CFRP reinforcement fastened with anchors, has led to an accurate description of the "strain transfer zone" during the tests. The DIC shows that the evolution of strain occurs from the loaded to unloaded side according to the crack advancement phenomenon registered by means of a video camera and in accordance with the literature studies carried out with strain gauges.
The strain field obtained by DIC has been used to calculate the τ_{zymax} recorded between the reinforcement and the support in the specimen of series T0. Specifically, it is approximately equal to the tensile strength of the fire brick support. It has been noted that in the first load step the stresses are concentrated in the loaded extremity of the specimen. When the bond stresses achieve the value τ_{zymax} the stress transfer zone moves gradually toward the unloaded side of specimen. The comparison between the force applied by the universal machine and the resultant of the tangential stresses shows that the DIC evaluates with good accuracy the strain fields onto the specimen of series T0. At the same time this comparison has underlined the limits of the correlation method. Indeed, more errors affect the results if during the test the specimen moves or rotates so that the analyzed surface departs from the original loading plane.
The analysis of the strain fields of specimens fastened with anchors has led to several observations about the characteristic crack advancement process that affects each specimen typology. The analysis of the curves y-ε_{yy} has demonstrated that in correspondence to the anchor an almost

constant strain has been recorded. It should be remembered that the slope of the curve y-ε_{yy}, referring to the CFRP sheet, is proportional to the bond stress developed at the interface. The stress transfer phenomena developed in correspondence to the multilayer zone of the nail (support-sheet-splay) is more complex to obtain and will be studied in the future with mechanical models.

The anchors of series T1_25_V and T1_40_O decrease the velocity of the crack advancement process but do not avoid the evolution of fracture on the lateral side of the reinforcement. In these specimens the anchor zone is subjected to a low strain that is constant only in a small zone. In the specimen T1_40_V a concentration of strain has been recorded between the loaded extremity and the fan anchor. The value of ε_{yy} decreases rapidly in correspondence with the nail splay; here a high concentration of stresses has been calculated also in advanced phases of load history. Indeed, the nail 40_V slows the development of the crack locking the movement of the stress transfer zone. In the specimen with two and three nails the strain evaluated in the loaded side decreases drastically close to the anchors. These anchors give rise to a high $\Delta\varepsilon_{yy}$, and therefore, to a high concentration of stresses.

The presence of the anchor/s retards the crack advancement and increases the resistance of reinforcement; also in the elastic phases the resistance of the system is not attributable only to the interface CFRP-support, the anchor augments the global resistance.

The strain fields ε_{xx} show that during the test a contraction of the sheet occurs. When an anchor is present the zone characterized by the high negative strain is concentrated close the center axis y in the zone between the anchor and the loaded extremity of the specimen.

The Digital image Correlation is able to study the strain field on all the reinforced surfaces of specimens fastened with anchors while a similar extensive analysis is impossible to obtain by strain gauges.

The determination of the stress transfer zone evolution during the tests T0 has led to the evaluation of the optimal bond length. It is equal to around 100 mm. This value is in accordance with the formula proposed by CNR DT200/2004 [1] (see par. 2.2.2.2 of this thesis).

The average debonding strength (σ_{2max}) of the CFRP reinforcement measured in the series T0 is 739,52 MPa (it is equal to the ratio $P_2/(t_f \times b_f)$). This value is almost identical to the design debonding strength of the FRP reinforcement proposed by the CNR DT200/2004 for the second mode of debonding. The formula used to define the $f_{fdd,2}$ is the (1.10); it is reported as follows with the numerical value of the design strength obtained.

$$f_{fdd,2} = \frac{K_{cr}}{\gamma_{f,d}\sqrt{\gamma_M}}\sqrt{\frac{2E_f\,\Gamma_{FK}}{t_f}} = \frac{3}{1{,}2\,\sqrt{2}}\sqrt{\frac{2\times 203000\times 0{,}07}{0{,}167}} = 742{,}43[MPa] \quad (5.1)$$

The *table 5.I* shows the ratio $R_{\sigma 2}$ between the average maximal stress (σ_{2max}), registered in each series tested, and the design debonding strength ($f_{fdd,2}$) defined by CNR [1]. The $R_{\sigma 2}$ of the different fastened series ranges between 1,25 (for the series T1_25_V) and 1,86 (for the series T3_25_V).

The ratio $R_{\sigma 3}$ has been obtained dividing the average stress measured in peak P_3 (σ_{3max}) to the value of design debonding strength ($f_{fdd,2}$). The values $R_{\sigma 3}$ presented in *table 5.II* shows that the residual average strength of the reinforcement ranges between the 53% (series T1_40_O) and the 111% (series T2_40_V) of the design strength $f_{fdd,2}$.

The factors $R_{\sigma 2}$ and $R_{\sigma 3}$ could be used to obtain an "indicative" value of design strength, and of the design residual strength for all the reinforced system fastened by anchors and characterized by similar geometrical configuration and mechanical features of those tested in this research. The statistical population presented in this thesis is not extended; a more exact value of the ratios $R_{\sigma 2}$ and $R_{\sigma 3}$ will be evaluate adding the results obtained in Paris (36 specimens) with those obtained in Florence (36 specimens).

Tab. 5.I - The maximal average stress σ_{2max} and the ratio $R_{\sigma 2}$

	T0	***T1_25_V***	***T1_40_O***	***T1_40_V***	***T2_40_V***	***T3_25_V***
P_2[kN]	12,35	15,49	15,66	16,16	20,52	23,01
σ_{2max} [Mpa]	739,28	927,55	937,61	967,85	1228,74	1377,54
$R_{\sigma 2}=\sigma_{2max}/f_{fdd,2}$	1,00	1,25	1,26	1,30	1,66	1,86

Tab. 5.II - The maximal average stress σ_{3max} and the ratio $R_{\sigma 3}$

	T0	***T1_25_V***	***T1_40_O***	***T1_40_V***	***T2_40_V***	***T3_25_V***
P_3[kN]	-	6,84	6,61	10,10	13,73	-
σ_{3max} [Mpa]	-	409,28	395,90	604,94	821,96	-
$R_{\sigma 3}=\sigma_{3max}/f_{fdd,2}$	-	0,55	0,53	0,81	1,11	-

The research demonstrates that the use of the CFRP anchor increases the resistance and the ductility of the reinforcement. The latter are important to augment the mechanical features of the structural members and, especially, to increase the safety of people during earthquakes by avoiding the brittle collapse of the strengthened elements.

The results presented in this thesis are coherent with those obtained by the research group Fagone - Ranocchiai - Briccoli Bati. Ongoing scientific articles will present the general results of all the 72 specimens realized and compare the DIC results to those of strain gauges.

The research presented in this thesis lays the ground work for a study of the CFRP in masonry bonded joint fastened with fiber anchors. The second step of the research will provide the realization of NES single shear tests on pillars, composed of fire bricks and mortar. The specimen will be reinforced bonding a CFRP sheet onto a surface and applying the anchors reproducing the configuration T2_40_V and T1_40_V. The study will be carried out using the same methodology and the same steel apparatus projected and realized in this research work. Several tests will be performed to evaluate the influence of the anchors when a mortar layer is juxtaposed between the CFRP sheet and the pillar. The successive step will be the realization of the flexural tests on masonry reinforced walls. The DIC will be used to analyze the displacement and strain field. Mechanical models will be developed to evaluate the stresses in the anchor area.

The experimental analysis will be executed in parallel with a numerical analysis. This will be based on damage mechanics.

The fruitful collaboration among the Universities of Catania, Paris Est and Florence will be continued.

Bibliography

[1] CNR-DT 200/2004, *Istruzioni per la Progettazione, l'Esecuzione ed il Controllo di Interventi di Consolidamento Statico mediante l'utilizzo di Compositi Fibrorinforzati-Materiali,strutture in c.a. e in c.a.p., strutture murarie*, Versione Sottoposta ad Inchiesta Pubblica, Roma-CNR 13 luglio 2004.

[2] Morphy R. D., *Behaviour of fibre reinforced polymer (FRP) stirrups as shear reinforcement for concrete structures*, Thesis, University of Manitoba, 1999.

[3] Liberatore D., Gambarotta L., Beolchini G.C., Binda L., Magenes G., Cocina S., Lo Giudice E., Scuderi S., *Tipologie edilizie in muratura del comune di Catania*, web site I.N.G.V.

[4] D.M. 14 gennaio 2008, *Norme Tecniche per le costruzioni, Cap. 11 "materiali e prodotti per uso strutturale",* January 2008.

[5] Chen JF, Teng JG. *Anchorage strength models for FRP and steel plates bonded to concrete.* J.Struct. Eng. 2001; 127: 784-791.

[6] Yao J, Teng JG, Chen JF. *Experimental study on FRP-to-concrete bonded joints*. Composites: Part B. Engineering. 2005; 36 : 99-113.

[7] Jongsma J. E., *Etude de Structures Adhésives de Polymères en Couches Minces, PhD thesis*, Ecole Doctoral Mécanique, Thermique et Génie Civil de Nantes, 2008.

[8] Cottone A, Giambanco G, *Minimum bond length and size effects in FRP-substrate bonded joints*, Engineering Fracture Mechanism. 2009; 76: 1957-1976.

[9] Fedele R. , Milani G. *A numerical insight into the response of masonry reinforced by FRP strips*. *The case of perfect adhesion*. Composite Structures. 2010; 92: 2345-2357.

[10] Pham K., Marigo J.J., *Approche variationnelle de l'endommagement: les concepts fondamentaux.* J. Comptes Rendus Mécanique, 2010, 191-198.

[11] Lemaitre J., Chaboche J.L., Benallal A., Desmorat R., *Mécanique des matériaux solides*, Ed. Science Sup DUNOD, 2009.

[12] Manuel Code_Aster, M. Bottoni, *Loi de comportement ENDO_ORTH_BETON*, R7.01.09, 2011.

[13] Contrafatto L, Cuomo M., *A new thermodynamically consistent continuum model for hardening plasticity coupled with damage*. Int. Journal of Solids and Structures. 2002; 39: 6241-6271.

[14] Pensée V., Kondo D., Dormieux L., *Micromechanical analysis of anisotropic damage in brittle materials*. J. Eng. Mech. 2002: 128: 889 – 897.

[15] Briccoli Bati S., Fagone M., *An analysis of CFRP-brick bonded joints*, XVIII Conference of the Italian Group of Computational Mechanics (GIMC) – Siracusa 22-24 September 2010.

[16] Briccoli Bati S., Fagone M., *Caratterizzazione della modalità di rottura di elementi in laterizio fibrorinforzati: test sperimentali e simulazioni numeriche*. Conference "Materiali e Metodi innovativi nell'Ingegneria Strutturale", Catania 4-6 July 2007.

[17] Capozzucca R. *Experimental FRP/SRP-historic masonry delamination*, Composite Structures. 2010; 92: 891-903.

[18] Giacquinta C., *Analisi sperimentale sotto carichi ciclici di pannelli murari rinforzati in CFRP*, PhD Thesis, University of Catania (Italy), December 2005.

[19] Milani G., *3D FE limit analysis model for multi-layer masonry structures reinforced with FRP strip*. International Journal of Mechanical Sciences. 2010; 52: 784-803.

[20] Grande E., Milani G., Sacco E., *Modelling and analysis of FRP-strengthened masonry panels*, Engineering Structures. 2008; 30: 1842-1860.

[21] Ha Lee J, Lopez MM, Bakis CE., *Slip effects in reinforced concrete beams with mechanically fastened FRP strip*. Cement & Concrete Composites, 2009; 31: 496-504.

[22] Martin JA, Lamanna AJ., *Performance of mechanically fastened FRP strengthened concrete beams in flexure*. J. Compos. Constr. 2008; 12: 257-265.

[23] Ascione L., Berardi V. P., D'Aponte A., *Anchorage device for FRP laminates in the strengthening of concrete strunctures close to beam-column joints*, Composites. Part B Engineering. 2011; Vol. 42 (7): 1840-1850.

[24] Bramblett, R. M., *Flexural Strenghtening of reinforced concrete beam using carbon fiber reinforced composites.* Master of Sciences thesis, The University of Texas at Austin, 2000.

[25] Orton SL, Jirsa OJ, Bayrak O. *Design considerations of carbon fiber anchors*. J. Compos. Constr. 2008; 12: 608-616.

[26] Le Tuan Pham, *Development of a quality control test for Carbon Fiber Reinforced Polymer Anchor*., Thesis of master of Sciences in Engineering, University of Texas at Austin, May 2009.

[27] Niemitz C.W., *Anchorage of carbon fiber reinforced polymers to reinforced concrete in shear application.* Thesis of master of Science, University of Massachusetts, February 2008.

[28] Zhang HW, Smith ST, Kim SJ., *Optimisation of carbon and glass FRP anchor design.* Construction and Building Materials. 2012; 32:1–12.

[29] American Concrete Institute (ACI). (2002). *Guide for design and construction of externally bonded FRP systems for strengthening concrete structures*, ACI 440.2R-02, Farmington Hills, Mich.

[30] S. T. Smith, S. Hu, S.J. Kim, R. Seracino, *FRP-strengthened RC slabs anchored with FRP anchors*, Engineering Structures. 2011; 33: 1075-1087.

[31] BASF Construction Chemicals Italia SPA, technical sheet *MBrace Primer: Primer a base epossipoliamminica del sistema MBrace FRP (Fiber Reinforced Polymer),* December 2009.

[32] BASF Construction Chemicals Italia SPA, technical sheet *MBrace Adesivo: adesivo a base epossidica del sistemaMBrace FRP (Fiber Reinforced Polymer),* January 2011.

[33] BASF Construction Chemicals Italia SPA, technical sheet *MBrace fibre CFRP: rinforzo fibroso unidirezionale in fibra di carbonio del sistema MBrace FRP (Fiber Reinforced Polymer),* June 2009.

[34] BASF Construction Chemicals Italia SPA, technical sheet *MBrace fibre: rinforzo fibroso a base di tessuti unidirezionali in fibra di carbonio, aramide e vetro del sistema MBrace FRP (Fiber Reinforced Polymer)*, December 2009.

[35] OTUA (Office technique pour l'utilisation de l'acier), *Dossier technique OTUA*; internet web link "*www.otua.org/Prop_Physiques/FicheOTUA/OTUA1.html"*.

[36] Henan BEBON international, internet web link "*www.steel-plate-sheet.com"*.

[37] Sika, Product Data Sheet, *Sikadur 300,* edition 21.04.10.

[38] Chevalier L. *Mécanique des systèmes et des milieu déformables: course, exercise et problèmes corrigès*, Ellipses, 2004.

[39] Peters WH, Ranson WF. 1981. *Digital image techniques in experimental stress analysis*. Opt. Eng. 1981 ; 21 : 427–441.

[40] Chu TC, Ranson WF, Sutton MA, Petters WH, *Applications of digital-image-correlation techniques to experimental mechanics*. Exp. Mech. 1985; 3: 232–244.

[41] Hild F., Roux S., Guerrero N., Marante M. E., Flòrez-Lòpez J., *Calibration of constitutive models of steel beams subject to local buckling by using digital image correlation*. Eur. J. Mech. A/Solids. 2011; 30: 1-10.

[42] Hild F, Périé JN, Coret M. *Mesure de champs de déplacements 2D par intercorrélation d'images : CORRELI*. Internal report 230, LMT-Cachan, 1999.

[43] Chevalier L, Calloch S, Hild F, Marco Y., *Digital image correlation used to analyze the multiaxial behavior of rubber-like materials.* Eur. J. Mech. A/Solids. 2001; 20: 169-187.

[44] Hild F., "*CORRELI^{LMT}: a software for displacement field measurement by digital image correlation*". Rapport interne n°254 LMT-CACHAN, 2002.

[45] Besnard G, Hild F, Roux S. *Finite-element displacement fields analysis from digital images: application to Portevin-Le Chatelier bands*. Experimental Mechanics 2006; 46: 789-804.

[46] Hild F, Roux S. *Digital image correlation: from displacement measurement to identification of elastic properties* – a review. Strain 2006; 42:69–80.

[47] Corr D, Accardi M, Graham-Brady L, Shah S. *Digital image correlation analysis of interfacial debonding properties and fracture behavior in concrete*. Engineering Fracture Mechanics. 2007; 74: 109-121.

[48] Carloni C, Subramaniam KV., *Direct determination of cohesive stress transfer during debonding of FRP from concrete*. Composite Structures. 2010; 93: 184-19.

[49] Carloni C, Subramaniam KV, Savoia M, Mazzotti C., *Experimental determination of FRP-concrete cohesive interface properties under fatigue loading*. Composite Structures 2012; 94: 1288-1296.

[50] Ali-Ahmad M, Subramaniam KV, Ghosn M., *Experimental investigation and fracture analysis of debonding between concrete and FRP*. J. Eng. Mech. ASCE 2006; 132: 914-923.

[51] Boyle W. S., Smith G. E., *Charge Coupled Semiconductor Devices*. Bell Sys. Tech. J. 1970; 49: 587–593.

[52] Martinez P., Klotz A., *A practical guide to CCD astronomy*, Cambridge University Press, 1998.

[53] Web site: "*http://www.matbase.com/material/polymers/elastomers/styrenebutadiene-rubber/properties"*.